2012

All-optical terahertz generation from semiconductors: materials and mechanisms

Krunal Radhanpura
University of Wollongong

All-Optical Terahertz Generation from Semiconductors: Materials and Mechanisms

by

Krunal Radhanpura, M.Sc.

A thesis submitted in fulfilment of the requirements for the award of the degree

Doctor of Philosophy

from the

Institute for Superconducting and Electronic Materials
University of Wollongong

2012

Supervisors: Professor Roger Lewis, Associate Professor Rodney Vickers

THESIS CERTIFICATE

I, Krunal Radhanpura, declare that this thesis, submitted in fulfilment of the requirements for the degree of Doctor of Philosophy from the Institute for Superconducting and Electronic Materials, University of Wollongong, is wholly my own work unless otherwise referenced and/or acknowledged. This work has not been previously submitted for qualifications at any other academic institution.

Krunal Radhanpura

18 December 2012

ABSTRACT

Terahertz frequency (10^{12} Hz) electromagnetic radiation possesses many exciting cross-disciplinary applications in the fields of astronomy, telecommunications, biology, physics, chemistry, and industry. Recent advancements in the field with the availability of high power sources, sensitive detectors, and efficient scanning systems, make it possible to use the terahertz (THz) radiation very effectively for applications such as biomedical imaging, security screening, and material property analysis. The real-world applications, however, are still limited by the lack of compact and cost effective systems, which can be achieved by having better sources and detectors working in this range.

In this thesis, I will focus on the examination of semiconductor materials as potential sources of THz generation without having any need of external bias voltage. Coherent, pulsed THz radiation may be generated under excitation of ultrashort near-infrared pulses from different semiconductor materials such as InAs, GaAs, InP, GaBiAs, InGaAsN, and ZnTe. The mechanisms behind THz generation from these materials will be discussed in detail. Terahertz time-domain spectroscopy (THz TDS) is used in order to measure both the amplitude and phase of THz generated from these materials. Information about different material parameters can be attained by investigating their response as THz emitters.

In the absence of external bias, the THz radiation from a semiconductor sample may be generated due to mechanisms such as optical rectification (OR) and transient current (TC) effects depending on the material properties, incident excitation fluence, and experimental geometry. There are different ways to extract the information about the mechanism responsible for THz generation. These include effect of angular rotation of the crystal, the effect of magnetic field on the generated THz, and the effect of varying the optical fluence of the excitation radiation. Here I will present the general theory of optical rectification for zincblende $\bar{4}3m$ structures for any arbitrary crystallographic direction, along with experimental results for high-index GaAs (11*N*) crystal planes for different experimental geometries. Using this, it is possible to extract information about the intrinsic surface field of the material and the contribution of it to

the THz generation. External magnetic fields enhance the THz radiation efficiency of transient current emitters. The theory of the effect of in-plane magnetic field rotation on THz generation for TC emitters is presented and the results for the (100) InAs emitter are compared with theory. Heavy noble gas ion irradiation can improve the THz emission efficiency of InP bulk and honeycomb nanoporous samples. Epilayer growth of GaBiAs layers on GaAs substrates increases the surface field contribution in THz emission which in turn increases the overall THz radiation from these samples. On the other hand, epilayer growth with dilute nitride doping in GaAs quenches the overall THz signal with an exponential decay with nitrogen content. The post-growth annealing of the semiconductors up to a critical temperature improves the THz emission efficiency.

LIST OF PUBLICATIONS

The work presented in this thesis has appeared in a number of peer-reviewed journal articles and conference proceedings:

Journal articles

1. K Radhanpura, S Hargreaves, R A Lewis, and M Henini. "The role of optical rectification in the generation of terahertz radiation from GaBiAs", *Applied Physics Letters*, **94** (25), 251115 (3 pages) 2009. **(Chapter 7)**

2. S Hargreaves, K Radhanpura, and R A Lewis. "Generation of terahertz radiation by bulk and surface optical rectification from crystal planes of arbitrary orientation", *Physical Review B*, **80** (19), 195323 (16 pages) 2009. **(Chapter 3)**

3. K Radhanpura, S Hargreaves, R A Lewis, L Sirbu, and I M Tiginyanu. "Heavy noble gas (Kr, Xe) irradiated (111) InP nanoporous honeycomb membranes with enhanced ultrafast all-optical terahertz emission", *Applied Physics Letters*, **97** (18), 181921 (3 pages) 2010. **(Chapter 6)**

4. K Radhanpura, S Hargreaves, and R A Lewis. "Bulk and surface field-induced optical rectification from (11*N*) zincblende crystals in a quasireflection geometry", *Physical Review B*, **83** (12), 125322 (6 pages) 2011. **(Chapter 4)**

Submitted

K Radhanpura, R A Lewis, M O Lemine, and M Henini. “Nitrogen quenches terahertz emission in dilute GaAsN” **(Chapter 8)**

Conference papers and proceedings

1. K Radhanpura, S Hargreaves, and R A Lewis. "The generation of terahertz frequency radiation by optical rectification", *presented at 33rd Annual Condensed Matter and Materials Meeting, Wagga Wagga, Australia,* (4 pages) Feb. 2009. **(Chapter 3)**

2. K Radhanpura, S Hargreaves, and R A Lewis. "THz generation by optical rectification involving high-index planes", *presented at the 34th International Conference on Infrared, Millimeter and THz Waves Busan, Korea, (IRMMW-THz 2009),* (2 pages) Sep. 2009. **(Chapter 3 and 4)**

3. K Radhanpura and R A Lewis. "Characterization of semiconductor materials as terahertz emitters under the effect of in-plane magnetic field", *presented at the 35th International Conference on Infrared, Millimeter and THz Waves, Rome, Italy, (IRMMW-THz 2010),* (2 pages) Sep. 2010. **(Chapter 5 and 6)**

4. J C Knott, K Radhanpura, and R A Lewis. "Annealing of Sb-doped GaAs to optimize for terahertz emission", *presented at the 19th Australian Institute of Physics Congress, Melbourne, Australia,* (3 pages) Dec. 2010. **(Chapter 2)**

5. K Radhanpura, S Hargreaves, and R A Lewis. "Terahertz generation from high index GaAs planes at different angles of incidence", *presented at 35th Annual Condensed Matter and Materials Meeting, Wagga Wagga, Australia,* (4 pages) Feb. 2011. **(Chapter 3 and 4)**

ACKNOWLEDGEMENTS

This thesis would not have been possible without motivation, support, and guidance from a number of people.

First of all, I would like to thank my principal supervisor Professor Roger Lewis. I owe my deepest gratitude to him for his invaluable support and help during my research. I would also like to thank my co-supervisor Associate Professor Rodney Vickers for his support.

I would like to thank my former colleague Dr. Stuart Hargreaves for helping me to learn about the terahertz time-domain spectroscopy system. Much of the work presented in this thesis could not have been done without his helpful assistance. I would like to thank Peter Ihnat for his help regarding all technical issues.

I would like to thank our collaborators Professor Mohamed Henini from the University of Nottingham, Professor Ion Tiginyanu from the Technical University of Moldova, and Professor Hans Hartnagel from Technical University of Darmstadt for providing the samples which have been used for the research work presented in this thesis.

Finally, I would like to thank my family - *Bhai*, *Bhabhi*, *Mummy*, and *Papa* for their continuous encouragement and support during these years.

TABLE OF CONTENTS

LIST OF FIGURES

LIST OF TABLES

Chapter 1

1 Introduction

1.1 Basics of terahertz electromagnetic radiation

Terahertz (THz) frequency electromagnetic radiation lies between infrared and millimeter wave radiation in the electromagnetic spectrum with frequency range of 100 GHz to 10 THz[1], corresponding to submillimeter wavelengths. The position of THz frequencies in the electromagnetic spectrum along with specifications about frequency, wavelength, and other important parameters are given in Figure 1.1. Many materials have their characteristic energies in the THz frequency region. Also the energy of vibrational and rotational modes of molecules lies in this range. Hence, THz radiation can be very useful to characterize materials based on their intrinsic properties. However, the field has not been exploited fully in comparison to the surrounding electronics and optics fields, due to previous scarcity of generation and detection systems which can operate at these frequencies[2], underlining the inaccessibility of the THz regime known as "THz gap"[3].

The field has seen major advancement in last two decades. Newly developed ultrafast optical techniques, fabrication of materials with ultrashort carrier lifetimes, and solid state lasers such as quantum cascade laser are bringing a revolution in the field with the technology quickly approaching the "Tera-Era"[4].

There are many different approaches for the generation and detection of THz radiation which include both coherent and incoherent systems. Incoherent thermal emission from blackbody radiation sources such as the mercury arc lamp and the SiC globar and detectors such as the bolometer were among the first used in Fourier transform spectroscopy which enabled material characterization from THz frequencies to infrared wavelength[1,5]. However, these sources have weak emission at longer wavelengths. Also, the bolometer needs to be operated at liquid-helium temperatures. Other commonly used but less sensitive incoherent detectors are Golay cell and pyroelectric detectors[6].

Coherent systems can be divided into two parts depending on the nature of generated THz radiation being continuous wave or pulsed.

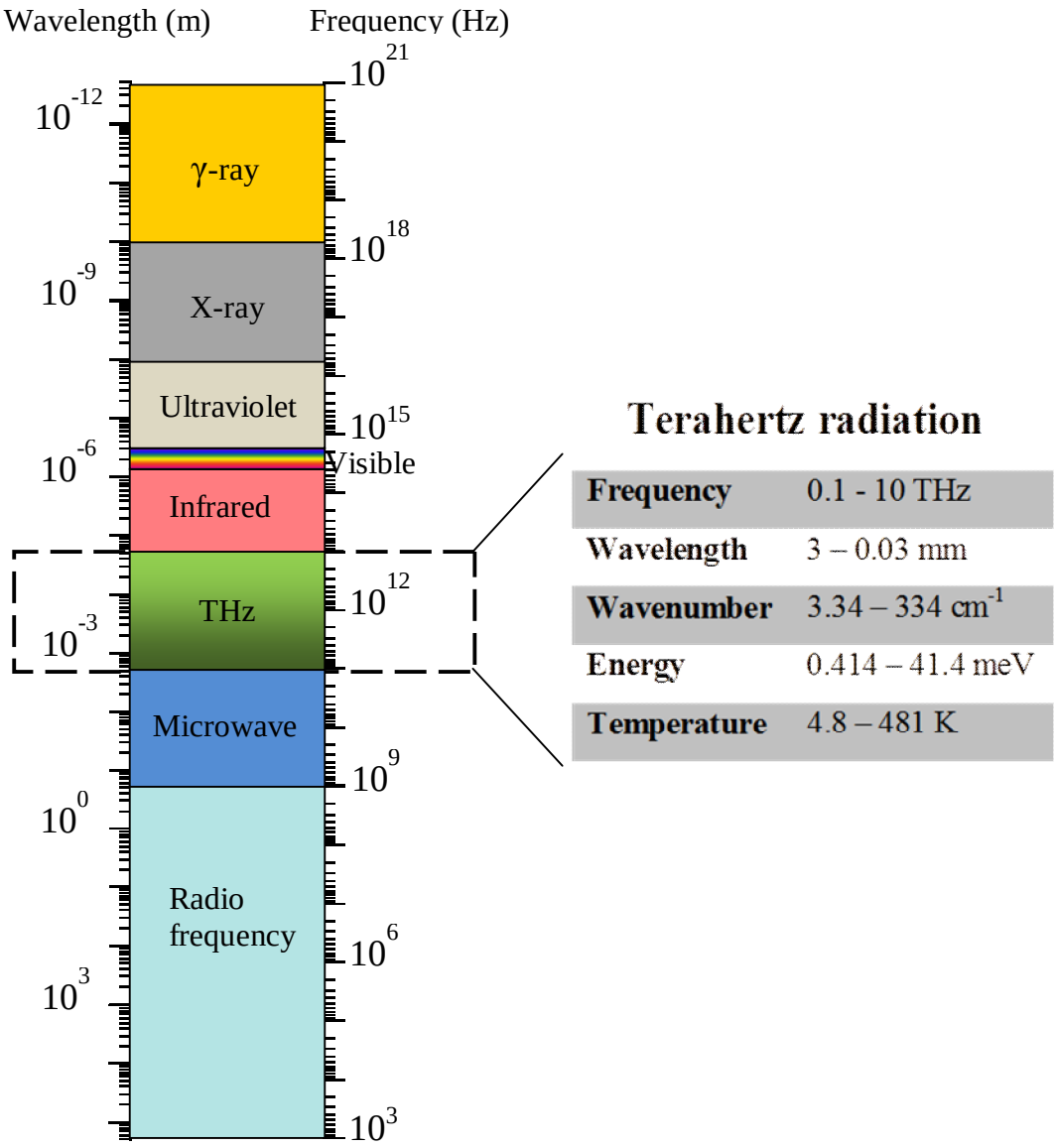

Figure 1.1 A representation of the electromagnetic spectrum from radio frequency to γ-rays, along with specifications about frequency, wavelength, energy and temperature for terahertz range.

1.1.1 Continuous wave (CW) THz systems

A range of different techniques are available for CW THz generation and detection.

The solid state quantum cascade laser[7] (QCL) works on the principle of intersubband transitions in semiconductor hetrostructures. It can be used in both pulsed and CW systems with output powers of a few hundred mW. However, these lasers need to be operated below room temperature[8]. Recently, a study on room-temperature detection in a QCL using antenna-coupled field-effect transistors in InAs nanowires and graphene channel material have been presented[9], indicating the possibility of room-temperature operation of QCL in the near future. Other solid state lasers, such as p-type germanium lasers[10,11], are also used for narrowband CW THz generation. However, they have low THz generation efficiency, low output power, and need cryogenic cooling. Free electron lasers (FEL) and backward-wave oscillators (BWO) are high-power THz sources able to generate both CW and pulsed coherent THz radiation. The principle of THz generation in both these systems is similar. The FELs occupy a large space and are very expensive, while BWOs are small laboratory sized equipment[12].

Gas vapor lasers such as methanol lasers[13] and HCN lasers[14] work on the principle of rotational and vibrational resonances of molecules in the THz range. Such lasers use carbon dioxide lasers as the excitation. Gas vapor lasers are high-power lasers with mW THz output, but have finite THz bandwidth and cover limited THz frequencies. Photomixing methods based on two laser sources with slightly different wavelengths combined in a nonlinear material are also used. The beat frequency corresponds to the THz range and can be observed using appropriate laser sources such as diode lasers which operate between 800 nm and 850 nm and an appropriate nonlinear material for photomixing[12].

1.1.2 Pulsed THz systems

Pulsed THz radiation enables coherent, broadband THz radiation spectroscopy and imaging systems which can be operated at normal atmospheric conditions without any need of cryogenic cooling. They are used quite extensively for the majority of current THz applications. Pulsed THz emission under excitation of ultrashort laser pulses has been observed from different materials such as metals, semiconductors, superconductors, organic and inorganic materials, and air plasmas. The emission of

pulsed THz radiation can be attributed to various effects. Notably among these are the photoconductive antenna structure[15], optical rectification[16,17], transient current effect[18], coherent polarization oscillations, coherent phonons[19-21], coherent plasmon oscillations[22,23], transitions in coupled quantum wells[24], intersubband transitions in quantum wells[25], and ultrafast modulation of the superconductivity in high T_c superconductors. More recently, the THz generation and detection with laser-induced gas plasmas has attracted much attention[26-29].

The commonly used excitation wavelength for THz generation is near-infrared pulses with center wavelength around 800 nm. Other possible excitation wavelengths such as 1550 nm and 1030 nm have also been a point of research interest[30,31] due to the availability of inexpensive and compact lasers working at these wavelengths. It can be also useful for applications in telecommunications[32].

1.2 Pulsed terahertz generation mechanisms

The most common mechanisms for broadband pulsed THz emission from semiconductor materials using ultrashort excitation pulses are photoconductivity, optical rectification, and the transient current effect.

1.2.1 Photoconductive (PC) mechanism

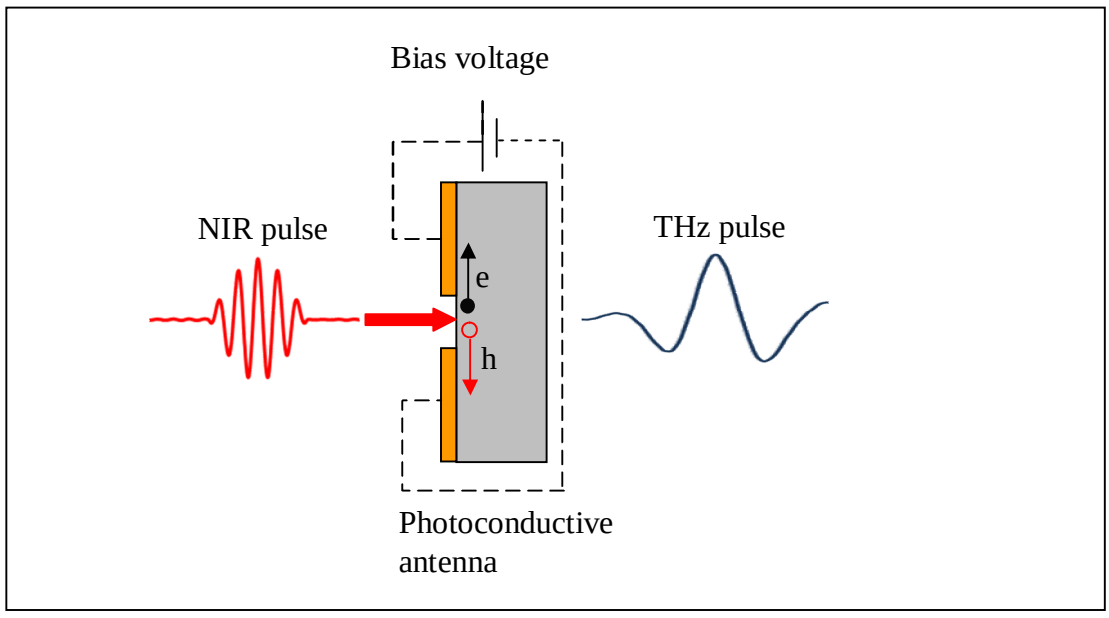

Figure 1.2 Photoconductive emission mechanism. Photocarriers, generated from the antenna substrate under excitation of NIR pulses, are accelerated by the external bias voltage and emit transient THz pulses.

In this mechanism, electrode structures with a micron scale antenna gap are fabricated on a semiconductor substrate. The substrate is photoexcited with above bandgap ultrashort laser pulses at the antenna gap which cause electron-hole pairs to be generated in the semiconductor. These photocarriers are then accelerated by the applied external DC bias voltage, which creates a transient current gradient and radiates THz pulses.

In the far-field approximation, the THz electric field $E_{\mathrm{THz}}(r,t)$ emitted from a PC antenna at the observation point r and observation time t can be represented as[33]

$$E_{\mathrm{THz}}(r,t) = -\frac{1}{4\pi\varepsilon c^2}\int\left[\frac{\partial j(r',t')}{\partial t'}\right]_{t'=t_r}\frac{\sin\theta}{|r-r'|}d^3x', \qquad 1.1$$

where, ε and c are the dielectric constant of the medium and the speed of light, respectively. The time-derivative is taken at the retarded time, $t_r = t - |r-r'|/c$. θ is the angle between the generated photocurrent and the direction of detection. $j(r,t)$ is the current density on the photoconductive antenna, which is related to the applied bias voltage E_{bias} as

$$j(t) = \frac{\sigma(t)E_{\mathrm{bias}}}{\frac{\sigma(t)Z_0}{1+n_d}+1}, \qquad 1.2$$

where $\sigma(t)$ is the conductivity, Z_0 is the characteristic impedance of vacuum, and n_d is the refractive index of the substrate.

Interference of field components generated from different points on the antenna produce the overall pattern of THz radiation. The first demonstration of pulsed THz generation and detection was using a PC antenna[15] and is still used very effectively due to its high conversion efficiency from optical to THz power and relatively high stability in comparison to other emission mechanisms[33].

Generation of THz radiation through the PC mechanism depends on various factors such as antenna geometry, optical pulse duration, applied bias voltage, along with properties of the PC substrate such as bandgap, carrier lifetime, and carrier mobility[34]. The efficiency of the PC mechanism strongly depends on the type of antenna structure. Different antenna structures such as "Auston switch"[35], Hertzian dipoles, strip-line antenna[36], logarithmic-periodic antenna[37], Ag-paint dots[6], and bow-tie antenna have been reported. The typical antenna gap size is of the order of few micrometers. It

can be further reduced. However, doing so causes a decrease in the effective active region where the THz electric field is generated. The applied bias voltage can be increased only up to the damage threshold of the material.

Low-temperature grown (LT) GaAs is the most commonly used photoconductive emitter due to its ultrashort carrier lifetime, high carrier mobility and high breakdown field[37]. A THz bandwidth up to 30 THz using a LT-GaAs PC emitter[38] and THz power of the order of 40 μW using a semi-insulating GaAs as PC antenna[39] have been observed. Radiation-damaged silicon-on-sapphire (RD-SOS), prepared by implanting argon, silicon, or oxygen into SOS samples, is another frequently used as PC emitters[40]. Many other materials, such as ion-implanted GaAs, InGaAs, GaAsN, GaAsBi, and GaAsSb, have been studied as PC emitters[41,42].

1.2.2 Optical rectification (OR) mechanism

There are some mechanisms which do not rely on external bias voltage to produce THz radiation[43,44]. Among them, the most commonly used mechanism is optical rectification[16,17].

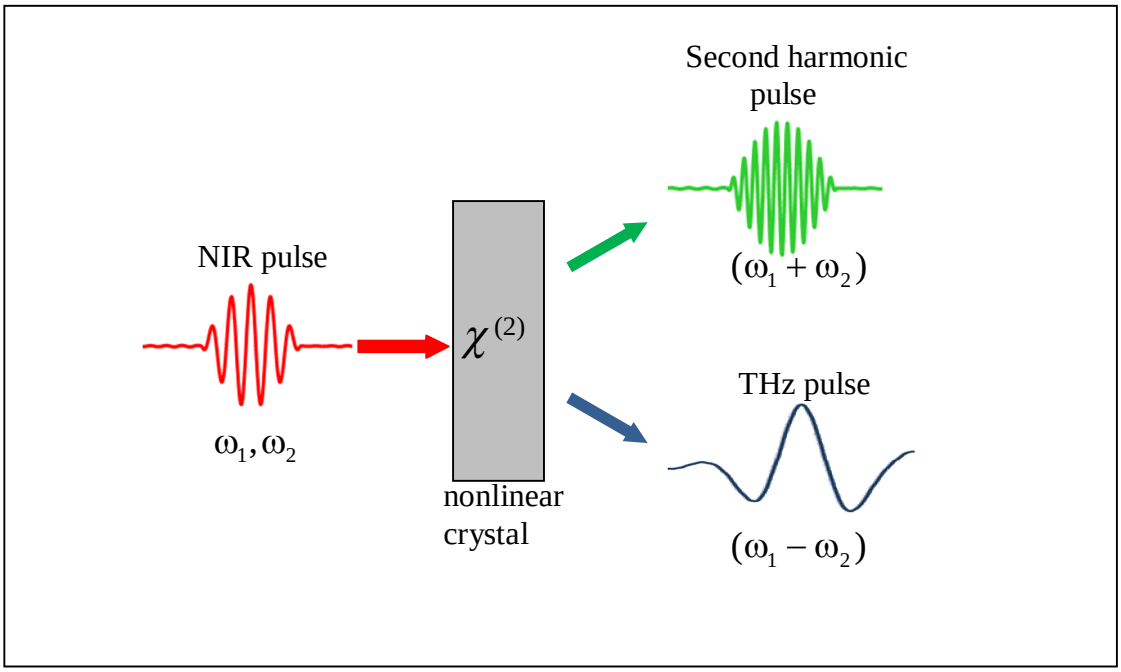

Figure 1.3 Optical rectification mechanism. The incident NIR pulse exploits the nonlinearity property of the crystal and generates sum frequency (second harmonic) and difference frequency (THz) components.

In this mechanism, the optical excitation causes a change in the polarization of the crystal by exploiting the nonlinearity of the material to produce sum-frequency and difference-frequency polarization components. For ultrashort NIR pulses, the polarization components with difference frequencies are in the THz range while the sum frequency components correspond to second-harmonic generation are in the visible or ultra-violet range. The OR effect can be second order bulk OR effect[45] or higher order surface-electric-field induced OR effect[46,47], also known as Franz-Keldysh effect[48].

The THz field in terms of second-order nonlinear polarization components can be written as[49]

$$E_i^{\mathrm{THz}}(\Omega) \propto \frac{\partial^2 P_i^{(2)}(\Omega)}{\partial t^2} = \frac{\partial^2}{\partial t^2}\chi_{ijk}^{(2)}(\Omega = \omega_1 - \omega_2; \omega_1, -\omega_2) E_j^{\mathrm{NIR}}(\omega_1) E_k^{\mathrm{NIR}}(\omega_2), \quad 1.3$$

where $\chi_{ijk}^{(2)}$ is the second-order susceptibility tensor, E_j^{NIR} and E_k^{NIR} are the incident excitation electric field components at frequencies ω_1 and ω_2, respectively; and $P_i^{(2)}(\Omega)$ and $E_i^{\mathrm{THz}}(\Omega)$ are the i^{th} component of induced second-order polarization at frequency $\Omega = \omega_1 - \omega_2$ and corresponding THz field, respectively.

Since THz generation through the OR effect relies on the nonlinearity property of the material and not on generation of electron-hole pairs, the THz radiation can be observed even with below bandgap excitation via this mechanism. This makes it distinct from other mechanisms involved in THz generation. However, nonlinear coefficients of a material can be enhanced by above bandgap excitation, which can effectively improve THz output power[50,51].

The OR emitters are used quite extensively due to simplicity of operation and broadband nature of generated THz radiation. The efficiency of optical rectification mechanism depends on the incident excitation pulse properties, non-linear coefficient of the material, crystal orientation, the crystal damage threshold, THz absorption in the material, and the phase-matching conditions[37,45,50].

Many nonlinear materials have been investigated for THz emission via the OR mechanism. This include semiconductors such as GaAs[52], ZnTe[53], InP[45], InAs[54], InSb[54], GaSe[55,56], CdTe[57], CdZnTe[58]; dielectric crystals such as lithium niobate ($LiNbO_3$)[59-61], lithium tantalate ($LiTaO_3$)[60,62]; organic materials such as DAST[63,64]; polymers; and metals such as gold[65,66].

1.2.3 Transient current (TC) effect

The transient current or current surge mechanism is a linear effect which can be further divided into the surface-field effect[18,67] or photo-Dember effect[54,68].

(a) Surface-field (SF) effect

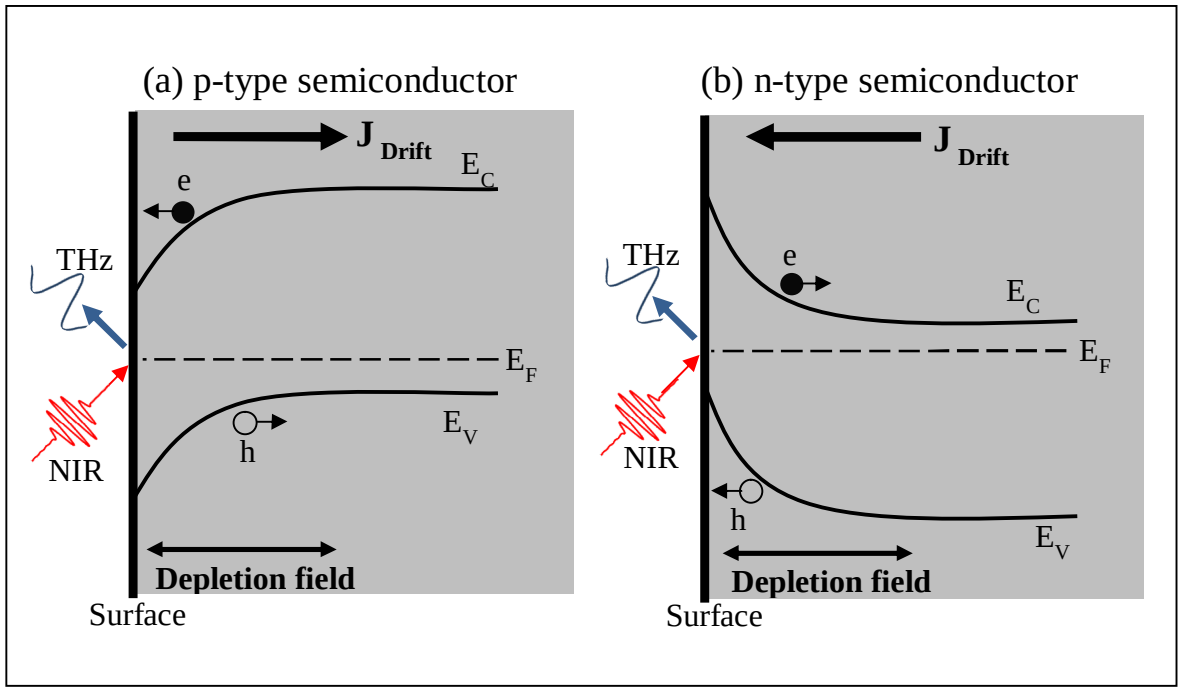

Figure 1.4 Surface-field effect for p-type and n-type semiconductors. The photocarriers generated due to excitation of NIR pulses are accelerated by the internal surface-depletion field and emit THz pulses.

For many semiconductors, a surface-depletion field is present due to Fermi level pinning and band bending of the conduction band and valence band at the surface. In the event of above bandgap ultrafast photoexcitation, electron-hole pairs are liberated in the semiconductor. The intrinsic surface-field drives the two kinds of carriers in opposite direction and produces a photocurrent with formation of the dipole in the direction of the surface normal. This transient dipole emits THz pulses.

Thus, the surface-field effect relies on the intrinsic field as opposed to the external bias in the case of photoconductive emission. Furthermore, in the case of PC effect, the current flow is in the surface plane, while for surface-field effect the current flow is in the direction of surface normal. The direction of the surface-depletion-field depends on the doping type and the position of the surface states with respect to the

Fermi level. In general, the band bending at the p-type and n-type materials are downward and upward, respectively[18].

The surface depletion field $E_d(x)$ as a function of the distance x perpendicular to the surface can be represented as[18]

$$E_d(x) = (eN/k)(W - x), \tag{1.4}$$

where N is the impurity concentration and W is the depletion width, which can be given as

$$W = \sqrt{(2k/eN)\left[V - (kT/e)\right]}, \tag{1.5}$$

where V is the potential barrier and kT/e is the thermal energy.

The generated drift current of photoexcited carriers due to this surface field and corresponding THz radiation field can be represented as[69]

$$J_{\text{drift}} = eE(n\mu_n + p\mu_p) \tag{1.6}$$

and

$$E_{\text{THz}} \propto \frac{\partial J_{\text{drift}}}{\partial t}. \tag{1.7}$$

The surface-field effect is more pronounced in wide-bandgap semiconductors, such as GaAs and InP, due to the presence of a strong depletion field and a relatively long absorption depth[54,70].

(b) Photo-Dember (PD) effect

In the photo-Dember mechanism, following the excitation by above bandgap optical pulses, a strong spatial gradient is formed near the semiconductor surface, caused by difference in the diffusion rates of electrons and holes. The higher mobility electrons tend to diffuse rapidly away from the surface, while holes remain in the vicinity of the surface due to their comparatively lower mobility. The resulting transient dipole, generated along the surface normal direction, emits THz pulses.

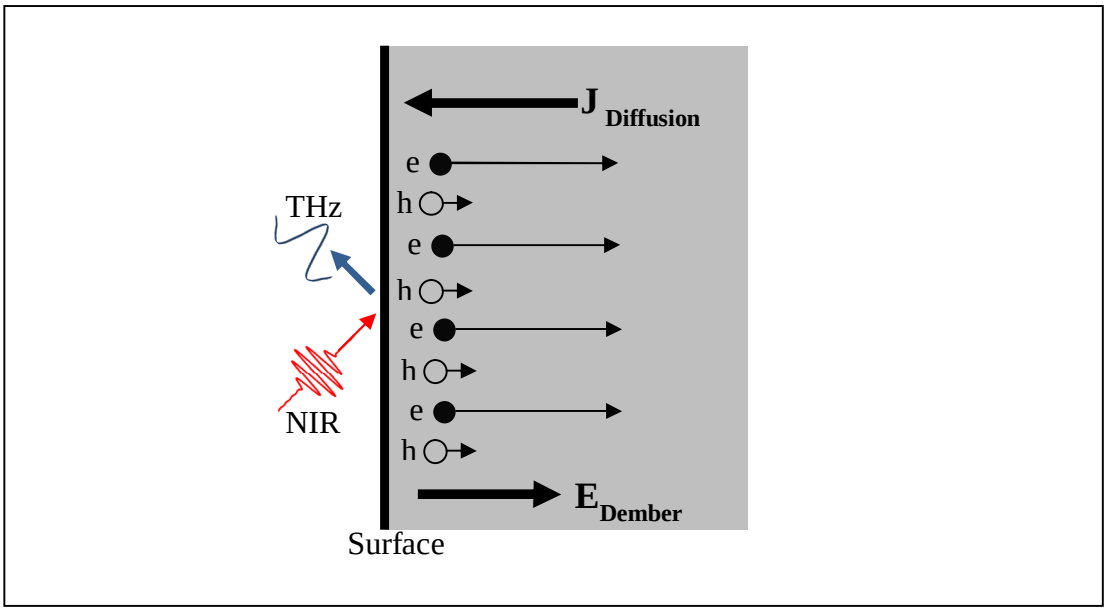

Figure 1.5 Photo-Dember effect. THz is generated by above bandgap excitation due to different rates of diffusion of electrons and holes.

The diffusive currents of the electrons (J_n) and the holes (J_p) can be represented as[68]

$$J_n \propto eD_e \frac{d\Delta n}{dx} \text{ and } J_p \propto -eD_h \frac{d\Delta p}{dx}. \quad 1.8$$

Here e is the electron charge, Δn and Δp are the densities of photo-excited electrons and holes, respectively. D_e and D_h are the diffusion coefficients of electrons and holes, respectively.

Also,

$$D = k_B T \mu / e, \quad 1.9$$

where k_B is the Boltzmann constant, T is the carrier temperature, and μ is the mobility of the carriers.

The diffusion current $J_{\text{diffusion}} = J_n + J_p$, hence, is proportional to the carrier mobility.

Further, the diffusion current of the electrons is much larger than holes due to large mobility and kinetic energy of electrons compared to that of holes. Hence, the THz radiation amplitude is approximately proportional to the electron mobility

$$E_{\text{THz}} \propto \frac{\partial J_n}{\partial t} \propto \mu_e(T). \quad 1.10$$

The photo-Dember effect is more pronounced in narrow-bandgap semiconductors, such as InAs and InSb, due to the higher electron mobility, weak depletion field, and short absorption depth[54,70].

Among different pulsed THz generation mechanisms, the PC emission has highest THz conversion efficiency. However, PC emitters saturate at high excitation densities due to screening of the applied DC bias. Also, high bias voltage increases the dark-current[71]. The OR emitters, on the other hand, can be used at high excitation power so can be stronger than PC emitters. Further, in order to observe high emission efficiency, PC emitters often require proper focusing due to finite size of the antenna gap. On the other hand, the focusing may not be a crucial requirement for the OR and TC mechanisms. OR and TC emitters are easy to use as they do not require external biasing. The OR emitters are better at high optical fluence of the excitation beam compared to TC emitters as TC emission may saturate at high excitation power.

In order to distinguish the linear TC mechanism and non-linear OR mechanism, geometrical parameters may be used. For OR emitters, a change in the THz signal is observed by rotating the emitter azimuthally about its surface normal, while TC emitters are invariant with azimuthal rotation. On the other hand, the TC emission changes with application of an external magnetic field, while OR emitters are not affected by an external magnetic field.

For many semiconductor materials the THz is generated by more than one mechanism, depending on material properties and the experimental set up. One such example is GaAs. Along with LT-GaAs as PC emitter, bulk GaAs is also capable of generating THz in the absence of external bias. Further the mechanism can be a mixture of both linear transient current and non-linear optical rectification mechanisms and either of the mechanisms can dominate under appropriate experimental conditions[69].

1.3 Pulsed terahertz detection methods

The most commonly used pulsed THz detection methods are photoconductive detection and electro-optic detection.

1.3.1 Photoconductive detection

In this detection method, an unbiased photoconductive antenna is placed in the THz beam path. The excitation probe beam, which initially splits from the pump beam, is incident on the antenna gap and excites photocarriers. The THz electric field biases the antenna and accelerates the charge carriers, so generating current proportional to the THz field. The resultant current, flowing through the antenna gap, is measured using high-sensitivity current amplifier. By employing a substrate with subpicosecond time response and scanning the excitation beam relative to the THz beam, the entire electric field profile of the THz pulse can be mapped.

The averaged THz current, $i_{\mathrm{THz}}(\tau)$, detected with the PC antenna for a relative time delay τ can be represented by convolution of the transient photoconductance of the PC antenna, $G(t)$ and the incident THz field, $E_{\mathrm{THz}}(t)$ as[33]

$$i_{\mathrm{THz}}(\tau) \propto \int G(t-\tau) E_{\mathrm{THz}}(t) dt \,. \qquad 1.11$$

For a substrate with extremely short carrier lifetime, $G(t)$ can be approximated as a delta function, and the current $i_{\mathrm{THz}}(\tau)$ is proportional to THz electric field $E_{\mathrm{THz}}(t)$. For a substrate with long carrier lifetime, $G(t)$ can be approximated as a step function and the current $i_{\mathrm{THz}}(\tau)$ is proportional to the time-integrated waveform of $E_{\mathrm{THz}}(t)$[33].

Earlier PC antennas suffered from lower THz bandwidths[72]. However, with the development of ultrashort laser sources and better antenna structures, the detection bandwidth has been improved to be comparable to electro-optic detection[73,74]. LT GaAs and ion-implanted silicon on sapphire[75] are the most commonly used materials for photoconductive THz detection.

1.3.2 Electro-optic detection (Pockels effect)

In this detection method, the THz beam and excitation probe beam propagate collinearly through an electro-optic crystal. The incident THz field modulates the birefringence of the crystal, via Pockels effect, and causes a rotation of the polarization of the optical probe pulse.

The detected THz output in terms of the change in the probe beam polarization can be represented as

$$E_i^{\text{out}}(\omega_1) \propto \frac{\partial^2 P_i^{(2)}(\omega_1)}{\partial t^2} = \frac{\partial^2}{\partial t^2} \chi_{ijk}^{(2)}(\omega_1; \omega_2, \omega_1 - \omega_2) E_j^{\text{NIR}}(\omega_2) E_k^{\text{THz}}(\omega_1 - \omega_2), \quad 1.12$$

where E_j^{NIR} is the j^{th} electric field component of the probe pulse at a frequency ω_2, E_k^{THz} is the electric field component of the terahertz pulse at frequency $\omega_1 - \omega_2$, $P_i^{(2)}(\omega_1)$ and $E_i^{\text{out}}(\omega_1)$ are i^{th} components of the effective second-order polarization at frequency ω_1 and corresponding THz output, respectively.

The THz detection using EO effect depends on the nonlinear coefficient $\chi^{(2)}$ of the detector crystal and the quality of phase matching between THz and optical pulses. Many EO materials such as ZnTe[76], GaP[77], GaAs[78], multilayered EO polymer films[79], poled polymers[80], and DAST crystal[81] have been used for THz detection. For commonly used 800 nm optical excitation, ZnTe is the most suitable nonlinear crystal for emission and detection of THz radiation, due to its large nonlinear coefficient, excellent phase matching, and high transparency at optical and THz frequencies[4,45].

EO detection is widely used due to its broad-bandwidth capacity and ease of implementation. OR emission and EO detection provides coherent broadband THz generation with bandwidth of the order of 100 THz[82]. However, there is a trade-off between the output power and bandwidth determined by the crystal thickness. A thicker crystal generates higher THz output because of a greater interaction length, however it reduces the detection bandwidth due to mismatch between group velocity of optical pulses and phase velocity of THz pulses[34].

1.4 Applications of terahertz radiation

The THz emission ability of semiconductor materials allows one to obtain information about material properties such as transient carrier mobility, impurity concentration, doping type, strength and polarity of the static internal field, and crystal orientation[18,43].

THz radiation transmits through many packaging materials such as paper, plastic, clothing, and cardboard, while it shows distinctive absorption features for explosives such as TNT, RDX, HMX[16] and drug-of-abuse such as cocaine, heroin, morphine[2] concealed within packaging materials. Hence, THz radiation can be very useful in security screening[83-85]. THz spectroscopy is used for quality control in pharmaceutical products[86,87] and food inspection[88]. It can also be used for air pollution

detection and gas sensing as many polar molecules, such as H_2O, C, N_2, O_2, O_3, HCl, CO, CH_3CN, and SO_2, have absorption peaks in the THz frequency range[34,37].

THz radiation provides a low power, non-ionizing, and non-destructive method of material characterization. Hence, it can be used very effectively for personnel scanning and biomedical applications[89]. Many medical applications such as diagnostics of skin burns[90,91], teeth[92] and cancer[93-95] using THz spectroscopy and imaging have been reported. Dielectric properties of biological molecules such as DNA, RNA, nucleogases, proteins, polypeptides, and biological liquids can also be investigated using THz spectroscopy[5,95,96].

THz spectroscopy and imaging provide useful way for investigating the history of artwork[97] and cultural heritage related materials[98]. Also, reproduction of three-dimensional structure of objects can be obtained using THz tomography[99,100].

Chapter 2

2 Terahertz Time-Domain Spectroscopy Apparatus

2.1 Introduction

Terahertz time-domain spectroscopy is one of the most efficient and widely-used system for THz spectroscopy and imaging. The principle of this system is based on using a medium which generates coherent THz pulses by the means of ultrashort pulses of excitation radiation. The THz field amplitude with femtosecond (fs) time resolution can be obtained by using part of the excitation beam as gating pulses and mapping the change in the field amplitude by scanning the excitation probe beam relative to the THz beam. The time-domain system can measure electric field rather than power and hence provide information about both phase and amplitude simultaneously.

Time-domain THz equipment can be broadly divided into three different types, based on its applications: THz time-domain spectroscopy (TDS), THz imaging, and THz time resolved time-domain spectroscopy (TRTS), also known as optical pump terahertz probe spectroscopy[101,102]. All of these systems can be obtained in a single experimental set up with some modifications in the system components.

In a conventional THz-TDS system, the time-domain THz signal is measured with the sample (sample scan) and without the sample (reference scan) in the THz beam path. Different properties of the sample can be obtained from analysis of these scans[2,89,103].

THz imaging provides two-dimensional image of the sample under investigation. In conventional imaging set up, the sample is placed on two crossed motorized translation stages which translate the sample in the plane perpendicular to the incident THz beam. The THz time-domain scans are obtained at different positions of the sample by translating the sample[104]. Current imaging techniques enable real-time imaging of the sample using CCD camera for detection. Such systems can be used very effectively for security screening and tomography study[105,106].

TRTS works on the principle of studying the photoconductivity of material excited by above bandgap excitation in the subpicosecond timescale using THz pulses as the probe beam. The carrier dynamics properties of many nanomaterials such as GaAs nanowires[101], ZnO nanowires[107], CdSe nanoparticles[108], TiO_2 nanoparticle

films[109], single-walled carbon nanotubes[110], and InP quantum dots and arrays[111] have been studied using this method.

Other time-domain setups are also in use such as differential THz time-domain spectroscopy (DTDS)[112] and the double modulated DTDS technique[113] which are particularly used for spectroscopy of thin film materials.

2.2 THz-TDS system specifications

The free space THz time-domain apparatus used in this thesis is shown in Figure 2.1.

The visible laser (Spectra Physics - Millennia Pro 6sJ diode pumped laser) produces continuous wave output with the fundamental wavelength of 532 nm (564 THz). With the capacity of maximum power output of 6.0 W, the laser is usually operated at 3.5 to 4.0 W. The beam path of visible laser is covered with a box in order to avoid laser exposure. This laser is used as pump laser for Ti-Sapphire oscillator based laser (Femto Lasers - Femtosource Compact CPRO laser), which generates <12-fs near-infrared (NIR) pulses with 80 MHz repetition rate and 790 nm center wavelength (frequency 379 THz; photon energy 1.57eV). The laser is capable of producing both continuous wave and mode locked signals. For pulsed THz measurements, the mode locked signal, with average power of 400 mW, is used as the excitation radiation. The beam is horizontally polarized.

In the free space path, the NIR beam first passes through a mirror pair in order to reduce dispersion, followed by a 98:2 beam splitter which splits a small fraction of beam towards the spectrum analyzer (Avantes - AvaSpec 2048 fiber optic spectrometer) for continuous monitoring of the beam profile. The beam is then split into two parts using a second beam splitter in order to divide the beam into pump beam (for THz generation) and probe beam (for gating) with 85:15 ratio.

On the pump beam side, the NIR beam is modulated by an optical chopper (Stanford Research Systems - SR540) in order to allow phase sensitive detection. The chopper frequency is set at 1 kHz and connected to lock-in amplifier (Stanford Research Systems - SR830). A variable power attenuator maybe placed in the beam path in order to vary optical fluence. The manual delay stage is used in order to adjust the pump beam path length.

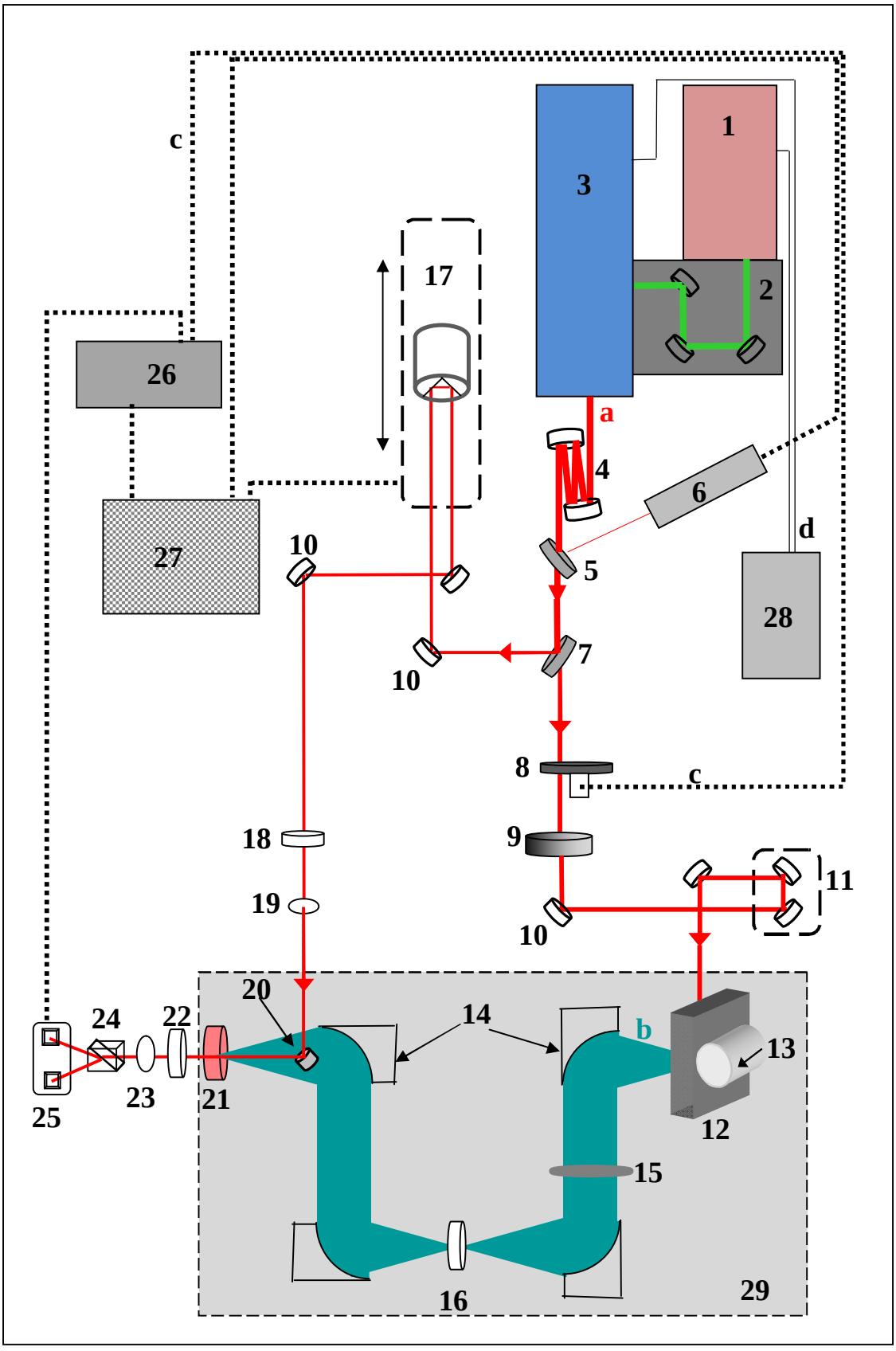

Figure 2.1 Terahertz time-domain spectroscopy - quasireflection geometry set up

Components used in THz TDS set up as shown in Figure 2.1

1. Visible laser: 532 nm wavelength (564 THz frequency)
2. Cover box for visible laser
3. Near-infrared laser: 790 nm wavelength (380 THz frequency)
4. Near-infrared dielectric mirror pair
5. Beam splitter 1: 98:2 power ratio
6. Near-infrared spectrometer
7. Beam splitter 2: 85:15 power ratio
8. Optical Chopper: 1 kHz chopping frequency
9. Variable power attenuator
10. Near-infrared dielectric mirrors
11. Manual optical delay stage
12. THz emitter
13. Permanent magnet
14. Parabolic mirrors
15. Wire-grid polarizer
16. Sample for THz spectroscopy
17. Mechanical optical delay stage
18. Polarizing filter
19. Lens: 15 cm focal length
20. Metallic mirror
21. Detector: (110) ZnTe electro-optic detector
22. Quarter-wave plate
23. Lens: 10 cm focal length
24. Wollaston prism
25. Balanced photo detector
26. Lock-in amplifier
27. Computer screen
28. Water coolant
29. Purging box

NIR beam path — THz beam path

Electrical connections — Water coolant tubes

The NIR beam is then incident on the THz emitter, which generates THz pulses by different mechanisms. The angle of incidence of the excitation beam to the emitter crystal is either 45^o (quasireflection geometry) or 0^o (transmission geometry) with respect to the surface normal. A permanent magnet (0.15-T magnetic field strength) may be placed on the back of the emitter mount in order to observe the effect of an in-plane magnetic field. The generated THz beam is then propagated and collimated using four off-axis gold-coated parabolic mirrors.

A wire-grid polarizer may be placed between first and second parabolic mirrors in order to observe only horizontal or vertical THz polarization components. The sample for THz spectroscopy study is placed between second and third parabolic mirrors at the common focal point of these two mirrors. For analyzing different emitter and detector responses, a NIR filter (polystyrene) is placed at the sample position in order to block any NIR beam leaking through with the THz beam. After the fourth parabolic mirror, the THz beam is focussed onto the THz detector. A 1 mm thick (110) ZnTe electro-optic crystal is used for THz detection.

On the probe beam side, the NIR beam passes through a mechanical optical delay stage (Oz-optics ODL300) which can be scanned with minimum step size of 719 nm, corresponding to the double transit time of 4.8 fs for the NIR excitation beam. A polarizing filter is placed in the probe beam path in order to allow only the horizontally polarized components to pass through to the detector. A 15-cm focal length lens focuses the NIR gating beam on the small metallic mirror placed between the fourth parabolic mirror and the ZnTe detector. The metallic mirror is placed in such a way that the THz beam and gating NIR beam copropagate inside the detector crystal.

The THz beam changes the polarization of the gating pulse due to the birefringence property of the ZnTe detector. A quarter-wave plate is placed after the detector which produces two orthogonally polarized components. A 10-cm focal length lens is used in order to focus the beam further. The Wollaston prism splits the two orthogonally polarized components. A balanced photodetector, consists of two photodiodes (BPW34, SIEMENS) connected to OPA655 with 47 kΩ resistor, is used to measure the differential voltage across these components, which is proportional to the THz field at a particular pump-probe delay.

The output of the photodetector is fed into the lock-in amplifier. The mechanical delay stage is operated using a Labview program. The THz time-domain signal is

obtained by scanning the probe beam delay stage with small steps and measuring the photodiode response at each step. In normal operation, the lock-in amplifier is used with 100 ms time constant, which may be increased to a higher value for better sensitivity and higher signal to noise ratio, if required. The Fourier transform of this signal gives the frequency response in the THz range.

The visible and near-infrared lasers are connected to a water cooler (Thermotek - T255P recirculating chiller) in order to keep a constant flow of cool water circulating in both laser units. The temperature is maintained at 20 ^{o}C in the water coolant. The purging box may be placed over the THz beam path, covering from THz emitter to detector, in order to purge the system with dry air or nitrogen and remove any water vapor absorption components present in THz signal.

2.3 Effect of different components used in the system

2.3.1 Near infrared excitation beam

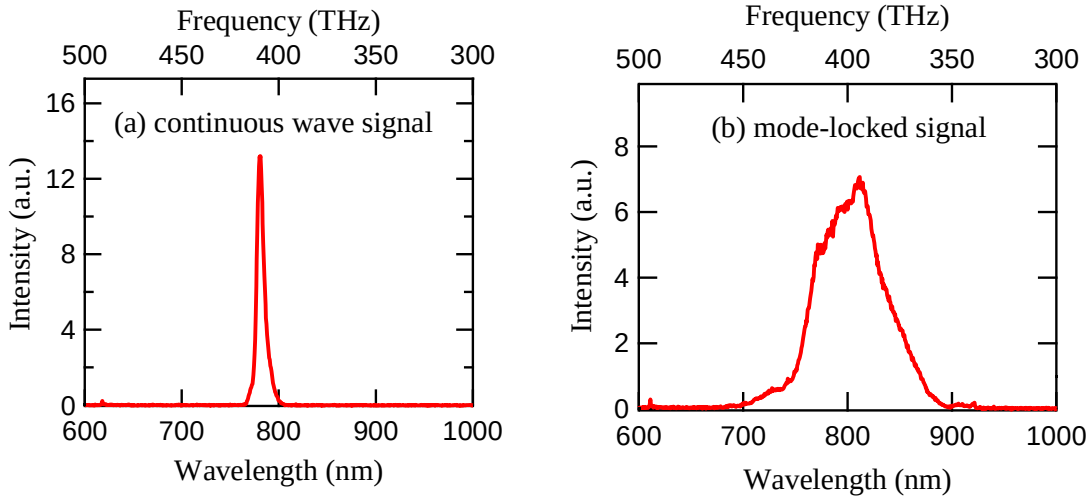

Figure 2.2 Continuous wave and mode-locked near-infrared signal measured by Avantes spectrometer. The mode-locked signal with output power of 400 mW is used as excitation radiation.

Figure 2.2 represents the response of Avantes spectrometer to the NIR beam. The mode-locked signal is used for pulsed THz measurements. The spectral range of 700-900 nm wavelength with 790 nm centrer wavelength is observed. The NIR beam is continuously monitored while taking measurements on the TDS system.

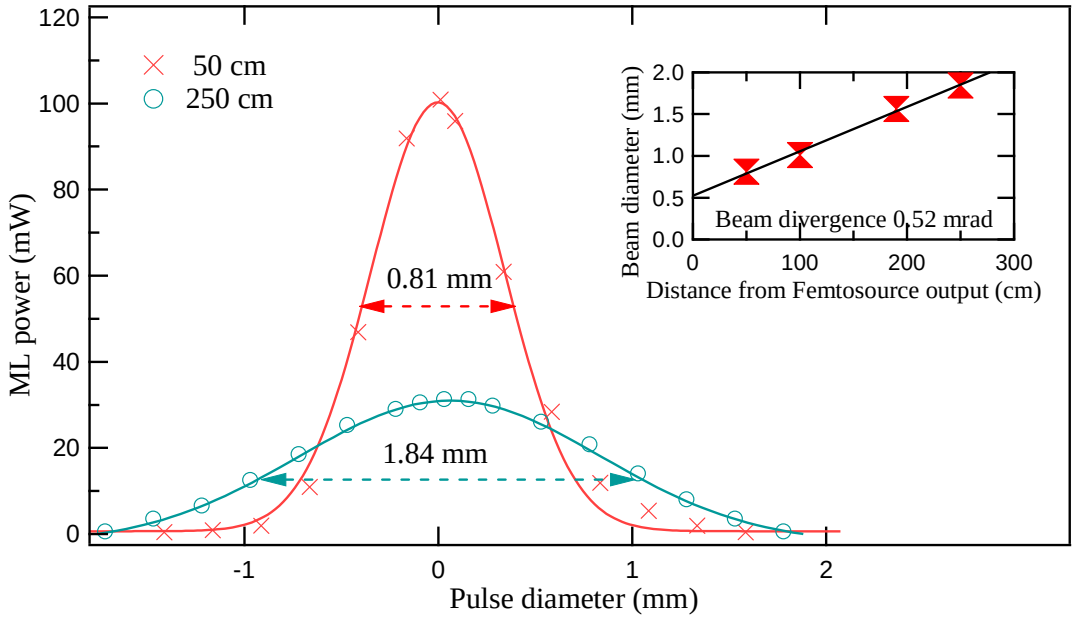

Figure 2.3 Near-infrared beam diameter and divergence. Beam diameter FWHM of 0.81 mm and 1.84 mm is measured at distances of 50 cm and 250 cm from the Femtosource output, respectively. The inset shows the overall beam divergence of the beam which is 0.52 mrad. The beam waist at the Femtosource output is roughly 0.5 mm

The beam diameter is affected considerably by the divergence of the laser beam. This is calculated to be about 0.52 mrad. The diameter of the beam at the emitter position is ~2 mm, which can be reduced to 0.2 mm using proper focusing.

2.3.2 Terahertz time-domain signal and corresponding frequency and phase spectra

Figure 2.4 shows terahertz time-domain signal for p-type Zn-doped (100) InAs (MTI Corporation, USA) in quasireflection geometry. The peak-to-peak voltage observed is 9.8 mV with typical signal to noise ratio of 800, measured over 25 ps scan with 100 ms time constant. The corresponding frequency spectrum and phase response can be obtained by taking the Fourier transform of this signal. The observed frequency range is 0.1 to 1.2 THz. The estimated absolute THz power is of the order of nano Watts.

Small oscillations after the main peak in time-domain signal and sharp features in frequency spectrum at frequencies 0.56 THz, 0.75 THz, and 0.95 THz are results of absorption of the water vapor present in the atmosphere. These absorption lines may serve as references for the THz frequency spectrum. However, these lines can cause

difficulty for spectroscopy of materials which show characteristic features around these frequencies. In order to eliminate these absorption lines, an enclosed system can be used which covers THz beam path as shown in Figure 2.1. The system is then purged with dry air or nitrogen. It is also possible to remove water vapor absorption features using numerical calculations[114].

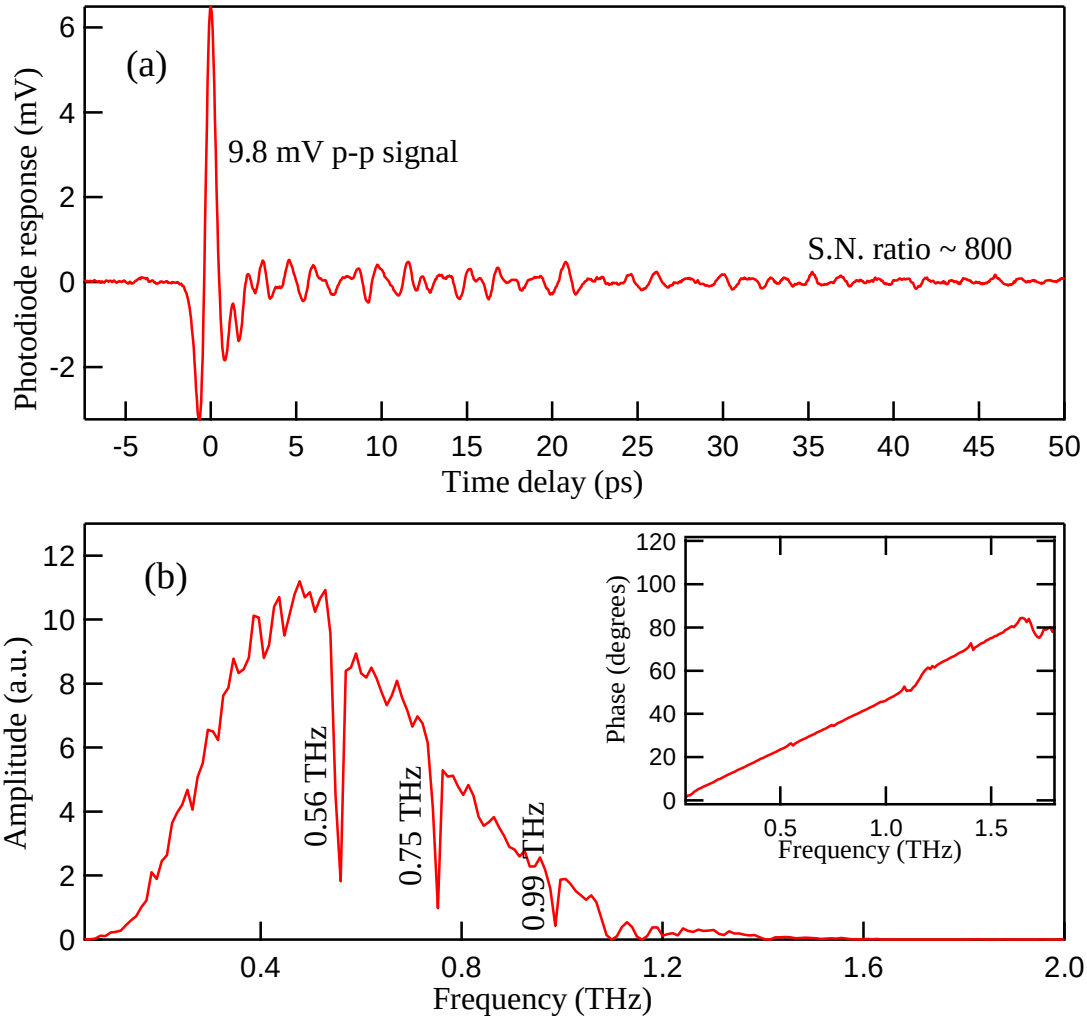

Figure 2.4 (a) THz time-domain signal from (100) p-type InAs emitter. The signal is obtained by measuring photodiode response at different time delays between pump beam and probe beam with step size of 48 fs. (b) Corresponding frequency spectrum. The observed frequency is in the range of 0.1 to 1.2 THz. The absorption lines at 0.56 THz, 0.75 THz, and 0.99 THz arise from the water vapor molecules present in the air. The inset in figure (b) represents phase Fourier transform for this signal

The THz output of 9.8 mV does not represent actual THz electric field amplitude but depends on experimental parameters such as type and thickness of the detector, the balanced photodetector used and the intensity of probe beam on two photo diodes.

The actual THz electric field amplitude E_{THz} can be obtained from[39]

$$\frac{\Delta P}{P_{\mathrm{probe}}} = \frac{\omega n^3 E_{\mathrm{THz}} r_{41} L}{c} \qquad 2.1$$

where

$\Delta P = P_1 - P_2$ is the difference in the intensity of the two photodiodes of the balanced photo detector,

$P_{\mathrm{probe}} = P_1 + P_2$ is the intensity of the probe beam

r_{41} is the electro-optic coefficient of the ZnTe detector = 3.9 pm/V

L is the length of the ZnTe detector crystal = 1 mm

n is the near-infrared refractive index for ZnTe detector = 2.8

ω is the near-infrared angular frequency

and c is the speed of light in vacuum

For the particular experimental measurement of InAs presented here, the value of $\Delta P / P_{\mathrm{probe}}$ is around 3×10^{-3}. Hence, the peak THz electric field can be calculated to be 44 V/cm.

Although, the THz electric field obtained this way shows the absolute THz radiation fields generated from the emitter, THz output for various semiconductors presented in this thesis are shown in terms of signal measured by balanced photodetector. Since, the local experimental parameters are kept constant for all sample measured as emitters, the THz signals can be represented directly in terms of photodiode response for convenience,

2.3.3 THz emitter geometries

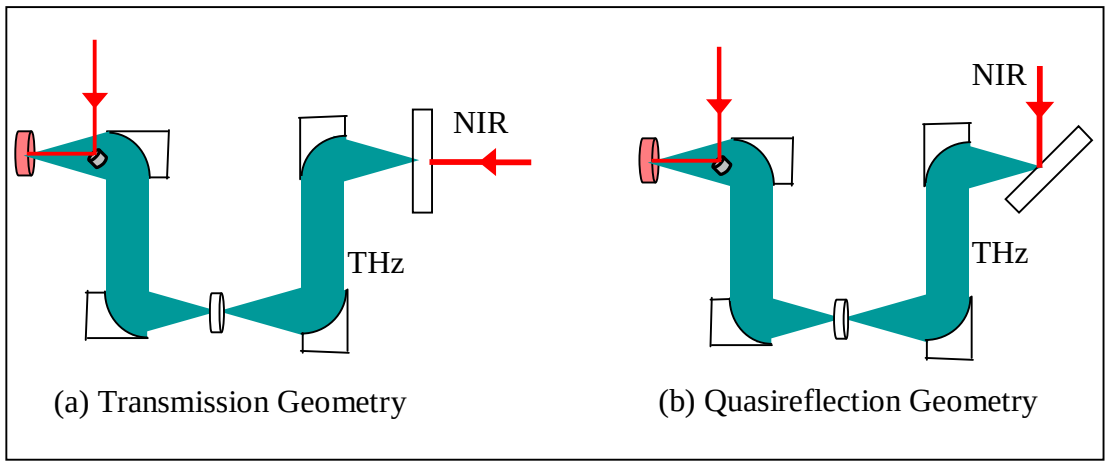

Figure 2.5 Emitter experimental geometries. (a) Transmission geometry, where the excitation beam is in the direction of the surface normal. The THz is detected in straight-through detection. (b) Quasireflection geometry, where the excitation beam is at 45^{o} angle with respect to the surface normal and THz is detected in specular-reflection direction.

Two different emitter geometries have been used in the THz-TDS system.

(a) Transmission geometry

In this set up, the NIR beam is incident on the emitter crystal in the direction of the surface normal of the emitter. The THz radiation is generated in the front surface and transmitted through the emitter crystal before propagating in the free space towards the detector. Photoconductive antennas are used in this geometry as the current flow for PC emission is in the surface plane and hence maximum signal is expected in the direction of surface normal. Other materials can be used in this geometry to generate THz radiation depending on the material properties and mechanism involved in THz generation.

(b) Quasireflection geometry:

In this set up, the NIR beam is incident on the emitter crystal at a 45^{o} angle with respect to the surface normal and THz is detected in the specular-reflection direction. The transient current emitter produces the dipole in the direction of the surface normal which then radiates THz pulses. Hence, in order to observe this emission mechanism, the emitter needs to be placed in non-normal incidence with quasireflection geometry

being most favourable due to simplicity in detection of THz. Also, the emitters with high THz absorption can be used in this geometry.

Other non-normal incidence angles can also be employed, in particular the Brewster angle of emitter crystal where maximum radiation output is expected[18,115]. The emitter geometry plays an important role in generating THz radiation via particular emission mechanism. Different geometries may lead to different behavior for same THz emitter.

2.3.4 Different emitter properties

A range of semiconductor materials have been tested as potential sources of THz radiation. These include InAs, GaAs, InP, GaBiAs, GaAsSb, InGaAsN, and ZnTe. The experimental results and detailed analysis for these samples are given in following chapters. Different responses for THz emission from these materials are observed due to the involved emission mechanism and material properties such as carrier concentration, doping type, crystal growth temperature, and crystallographic direction. One such parameter, the effect of post-growth annealing of the emitter crystal is presented here.

Post-growth annealing effect for GaAsSb

Low-temperature grown GaAsSb and GaBiAs epilayers deposited on GaAs are able to generate THz radiation under NIR photo-excitation[42,116]. The post growth annealing of GaBiAs on epitaxial layers improves the structural and optical properties of the material[117]. The electrical resistance of LT-GaAsSb and LT-GaAs increases with increasing annealing temperature[118]. The decrease in surface defects due to annealing may be able to improve the THz emission efficiency of the material. In this study, LT-GaAs, GaAsSb, and GaBiAs samples were annealed at temperatures above 500 ^{o}C. The GaAsSb samples used in this study were provided by Prof. Hans Hartnagel from Technical University of Darmstadt, Germany.

An ULVAC-RIKO MILA-5000 vacuum furnace was used to anneal the samples. The annealing of samples was carried out at three different temperatures of 550 ^{o}C, 600 ^{o}C, and 650 ^{o}C. The samples were annealed for 10 minutes under vacuum and then allowed to cool under vacuum to 100 ^{o}C before being exposed to air for cooling to room temperature. The samples were then measured as THz emitters without applying any external bias. The measurements of THz emission, X-ray diffraction

(XRD), and resistivity data were performed[119]. One such result, for effect of annealing the (100) $GaAs_{0.6}Sb_{0.4}$ sample at different temperatures, is shown in Figure 2.6.

As can be seen from the figure, the THz emission improves by a small fraction with annealing the sample at 550 ^{o}C. Further improvement in the signal strength is observed for 600 ^{o}C annealing before it reduces for 650 ^{o}C annealing. The signal observed for 650 ^{o}C annealed sample is even lower than the signal for the as-grown sample. Thus, improved THz emission can be obtained using post-growth annealing up to a critical temperature, after which the emission efficiency reduces. Similarly, an improvement in THz emission efficiency has been observed for GaBiAs with 550 ^{o}C annealing. The variation in THz emission efficiency of these samples may have been caused by change in the defects in the samples while annealing. It is also possible that As loss during the annealing is the reason for change in THz emission properties as the precautions such as annealing in an atmosphere of arsine gas or under a wafer of similar material in order to limit As loss were not taken.

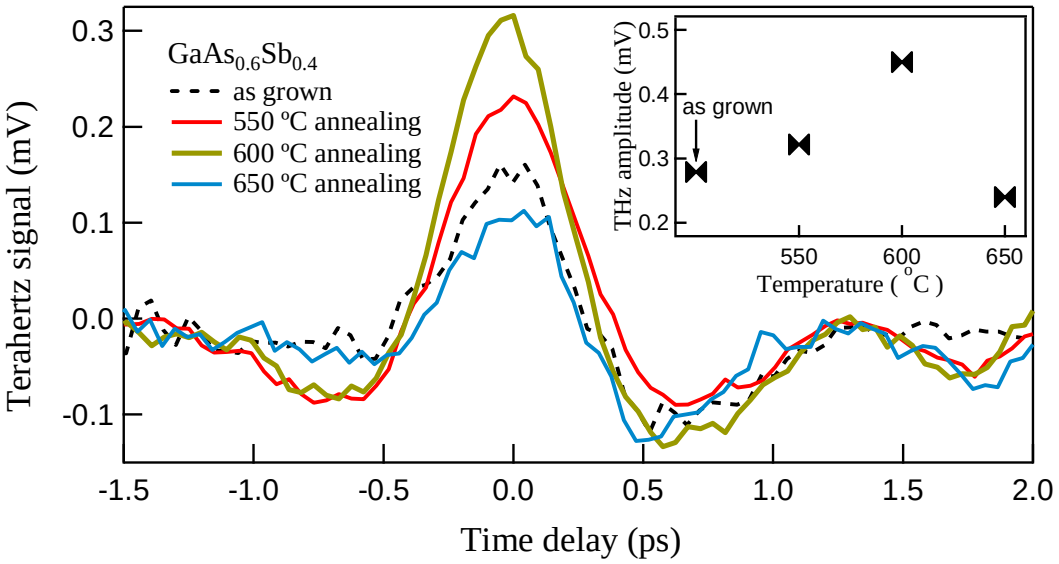

Figure 2.6 THz time-domain signals from $GaAs_{0.6}Sb_{0.4}$ sample with different post-growth annealing temperatures. The signal strength increases with annealing up to 600 ^{o}C, then reduces at 650 ^{o}C. The inset shows change in the THz signal amplitude with annealing temperature.

2.3.5 Effect of bias voltage for photoconductive antenna

For photoconductive emitters, since the generated THz field is proportional to the applied external bias, the THz signal amplitude directly depends on the applied bias voltage. This is illustrated for a commercially available LT-grown GaAs Tera-SED 3 (Serial #1-5C3, GIGAOPTICS GMBH, Germany) emitter in Figure 2.7.

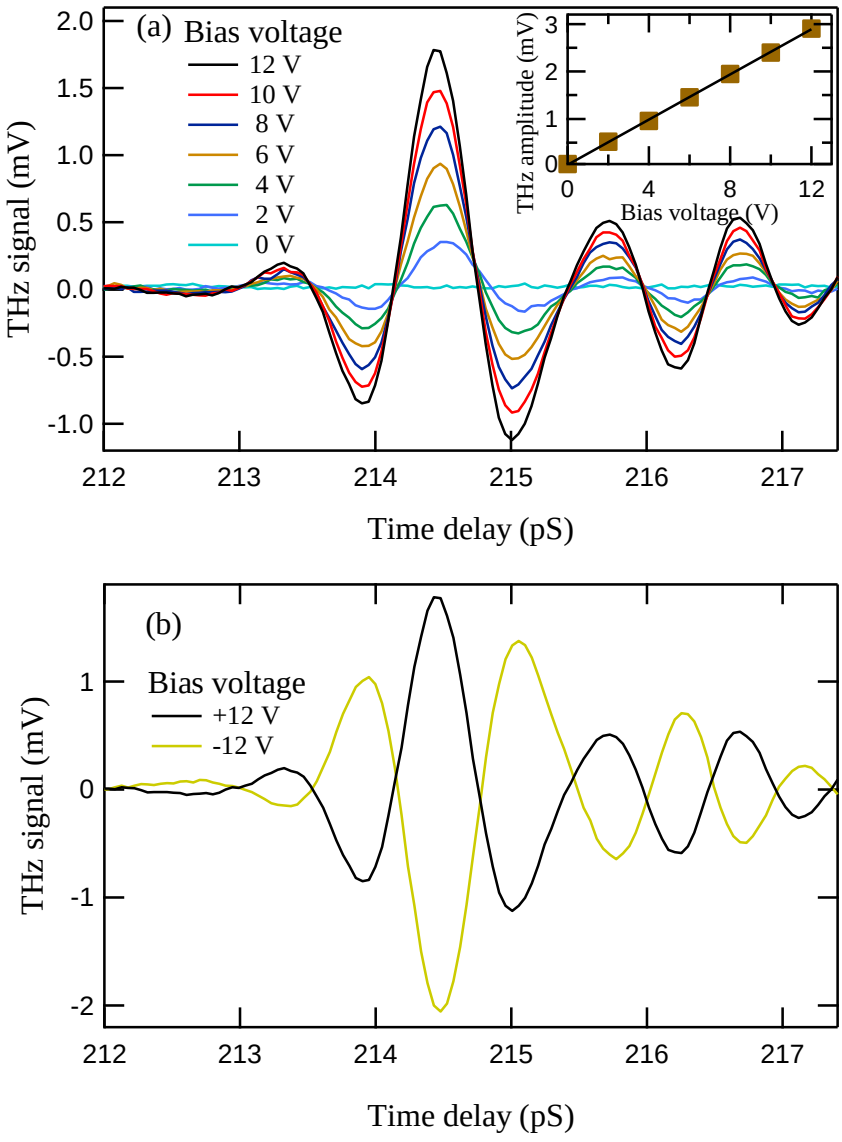

Figure 2.7 (a) Effect of changing external bias voltage in PC THz emission for Tera-SED emitter. The inset shows change in the THz signal amplitude with varying bias voltage. The signal strength increases linearly with increase in the bias. (b) Effect of changing direction of applied voltage. The signal reverses with all features in the signal flipped, including the water vapor oscillations after the main peak.

As shown in the inset in Figure 2.7(a), the THz signal amplitude increases linearly with applied bias voltage. Also, by changing the direction of the bias, the polarity of THz field reverses, as the current flows in opposite direction in this case.

2.3.6 Incident excitation power dependence

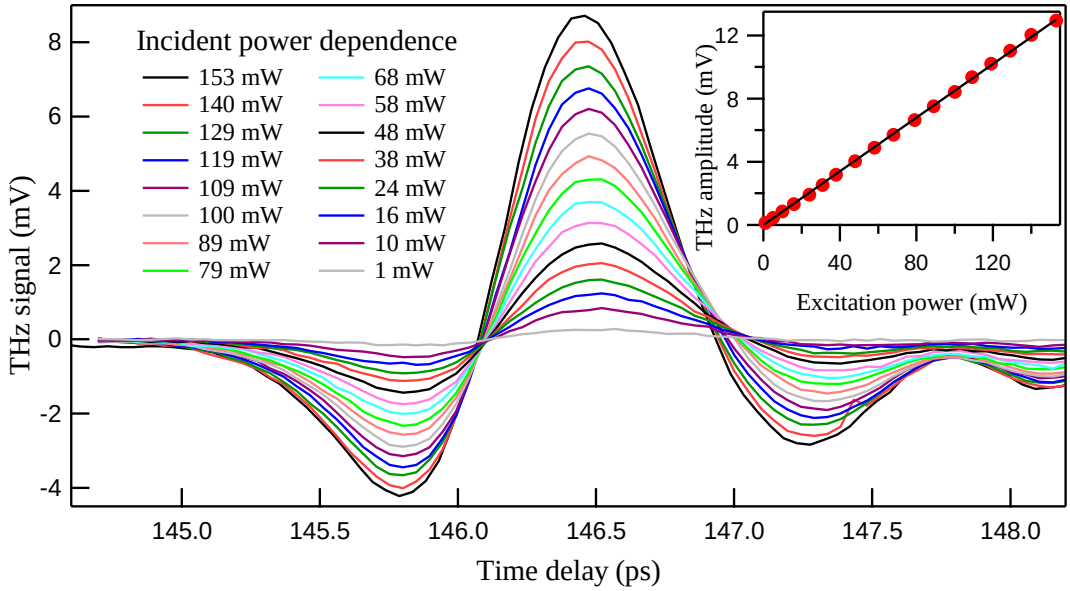

Figure 2.8 Incident excitation fluence dependence for (100) InAs emitter. The inset shows THz signal amplitudes with respect to varying incident excitation power level. The THz signal increases linearly with increasing incident NIR power level.

For all biased and unbiased THz emitters, the incident excitation power level directly affects the THz generation efficiency[120]. In the case of transient current (TC) mechanism, the THz power saturates at high optical fluence, due to screening of the bias field by photocarriers[121]. The change in THz signal with varying incident excitation fluence for a (100) InAs emitter is shown in Figure 2.8. THz signal amplitude increases linearly with excitation fluence, with no evidence of screening. Although, InAs is a TC emitter, the incident excitation might be too small for screening to occur.

During experiments it is often observed that the Femtosource NIR power output deteriorates with time and can be reoptimized by mirror realignments. Hence, the incident power level needs to be considered while making comparison between emitters measured at different point of time. Different behavior can be expected for different THz emitters with changing the incident power levels, on the basis of emission

mechanism. Further study of incident power dependence for other emitter crystals will be discussed in following chapters. Also, other important emitter properties, such as the effect of azimuthal rotation of the emitter crystal and in-plane magnetic field, will be detailed in next chapters.

2.3.7 Sample geometries for THz spectroscopy or imaging

As for the emitter transmission and reflection geometries, so also the sample transmission and reflection geometries are possible, where the THz signal is transmitted through or reflected off the sample. The sample reflection geometry is useful in particular when the sample surface properties need to be investigated, or if the sample under investigation does not transmit THz.

It is possible to calculate number of material parameters using THz time-domain and frequency-domain signal. This includes frequency dependent refractive index, absorption coefficient, complex permittivity, and dielectric constant. As an example, THz spectroscopy of a 1 mm thick b-cut BiB_3O_6 (BiBO) crystal in the sample transmission geometry is presented here. This sample was provided by Prof. Ali Hussain Reshak from the Institute of Physical Biology, South Bohemia University, Czech Republic.

Spectroscopy measurement for BiBO crystal

BiBO is an anisotropic crystal and is a useful material for second harmonic and third harmonic generation applications[122,123]. The THz spectroscopy measurements were performed for different orientations of the BiBO crystal using the THz-TDS system with InAs as the emitter. The time-domain signal is collected for the sample with a particular side being parallel to the THz electric field and compared with the reference scan measured without the sample in place. The sample is then rotated by 90^o and again the time-domain spectrum is collected, with the sample side now being perpendicular to the THz electric field. As we can see in the Figure 2.9, two signals observed for different orientations of BiBO crystal have different signal strength and different time delay with respect to the reference scan. This observed change for two signals reflects the anisotropy of the BiBO crystal. Similar variation is observed with further rotation of the sample.

We can measure the broadband values for refractive index n_b and transmission T_b in the THz range using equations[103]

$$n_b = 1 + \frac{t_d c}{x} \qquad 2.2$$

and

$$T_b(\%) = 100\frac{V_s}{V_R}, \qquad 2.3$$

where, t_d is the time delay between reference scan and sample scan

c is speed of light in vacuum

x is the thickness of the sample

V_s is peak-to-peak voltage of the sample scan

and V_R is peak-to-peak voltage of the reference scan.

Using these equations, the broadband refractive indices for two different sample positions are obtained as 3.61 and 2.63, while the transmission for two orientations are calculated to be 53% and 69%.

More detailed analysis can be carried out by taking Fourier transform of time-domain signals and calculating phase and frequency components for these signals. The frequency dependent refractive index n_f can be calculated using the formula[103]

$$\phi_x - \phi_0 = \frac{2\pi f(n_f - 1)x}{c}, \qquad 2.4$$

where ϕ_x and ϕ_0 are phase values of the signal and reference, respectively.

Figure 2.9(e) represents the frequency-dependent refractive indices for two sample positions. Constant values of 3.6 and 2.6 are obtained for sample position 1 and 2 within range of 0.1 to 1.2 THz, which are consistent with the calculated broadband refractive indices. Thus, it is possible to observe the birefringence property of BiBO crystal in THz range using TDS measurements. Figure 2.9(f) shows the frequency dependent transmission for both sample positions.

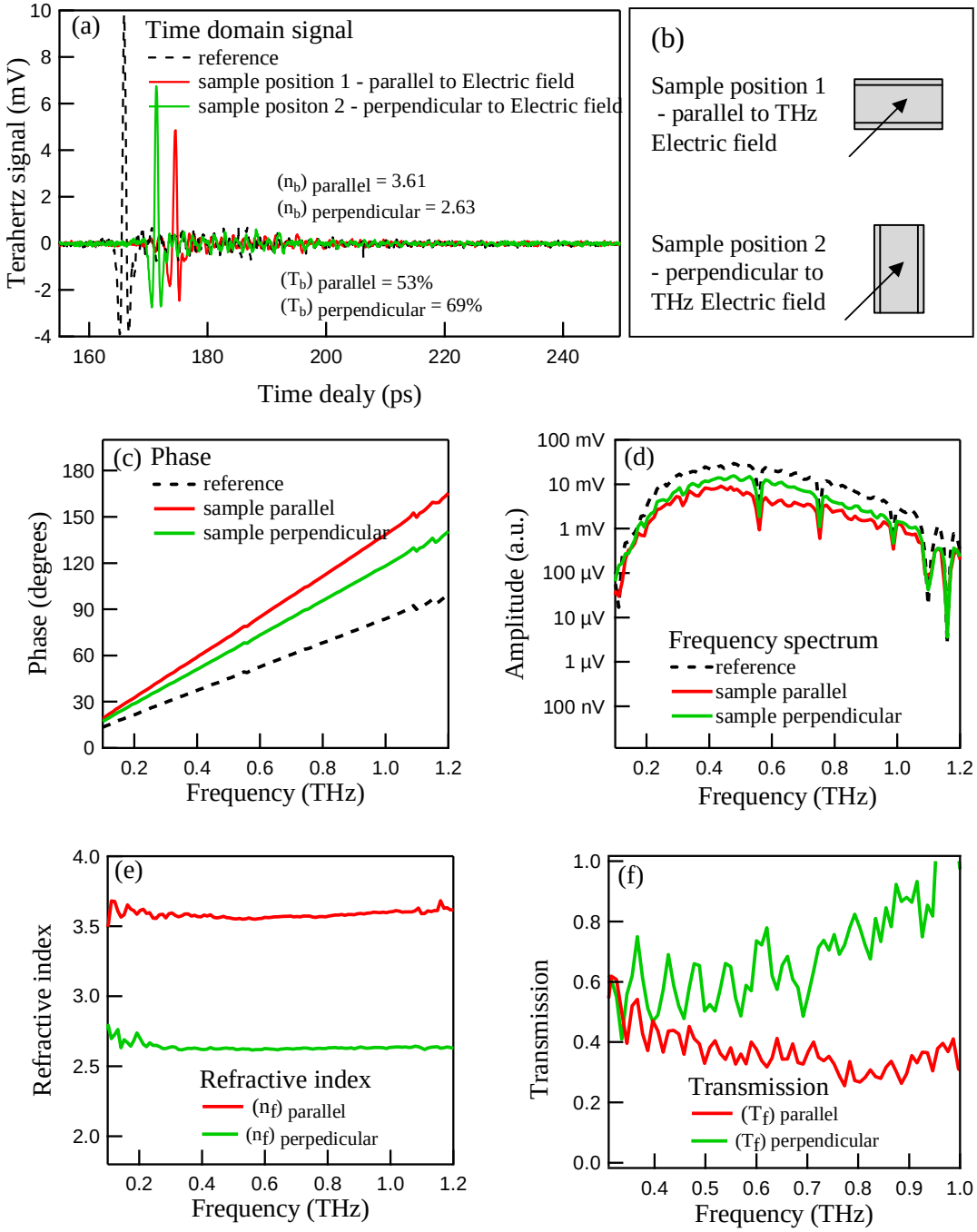

Figure 2.9 Spectroscopy of BiBO sample using THz-TDS system. (a) Time-domain signal with and without BiBO sample. The black dotted line is the reference scan measured without sample. The red line is the time-domain signal with sample in place. The green line is the signal measured by rotating the sample by 90° with respect to the surface normal. n_b and T_b represent the broadband values of refractive index and transmission, respectively. (b) Two different positions of the sample with respect to

incident THz electric field. (c) and (d) represent phase and frequency spectra obtained from Fourier transform of time-domain signals. (e) and (f) represents frequency-dependent refractive indices (n_f) and transmission (T_f) for both sample orientations, respectively.

2.3.8 Detector angular dependence

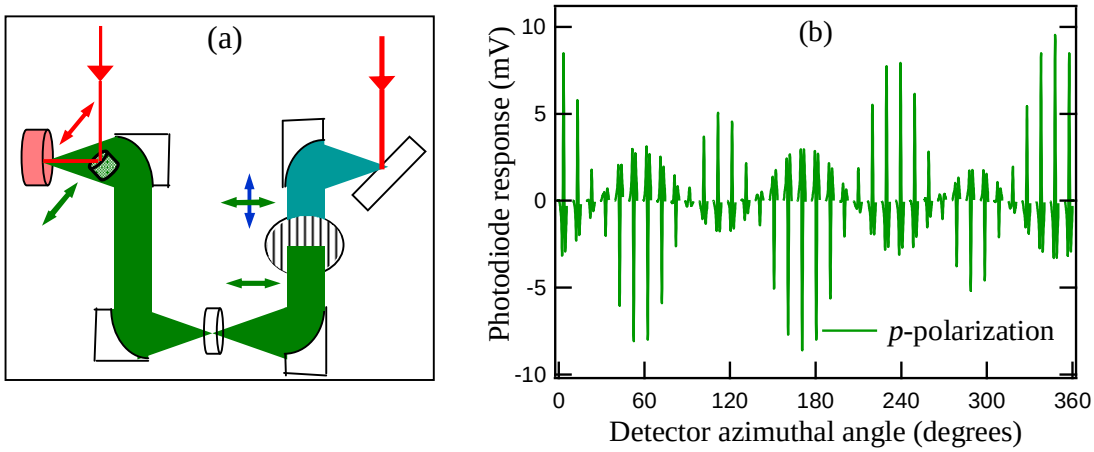

Figure 2.10 (a) Vertical polarizer grid set-up in order to observe horizontally (*p*) polarized THz components only. (b) Detector azimuthal rotation behavior for horizontally (*p*) polarized THz components. Each line represents THz time-domain signal, measured over a period of 3 ps, at particular azimuthal angle of detector crystal.

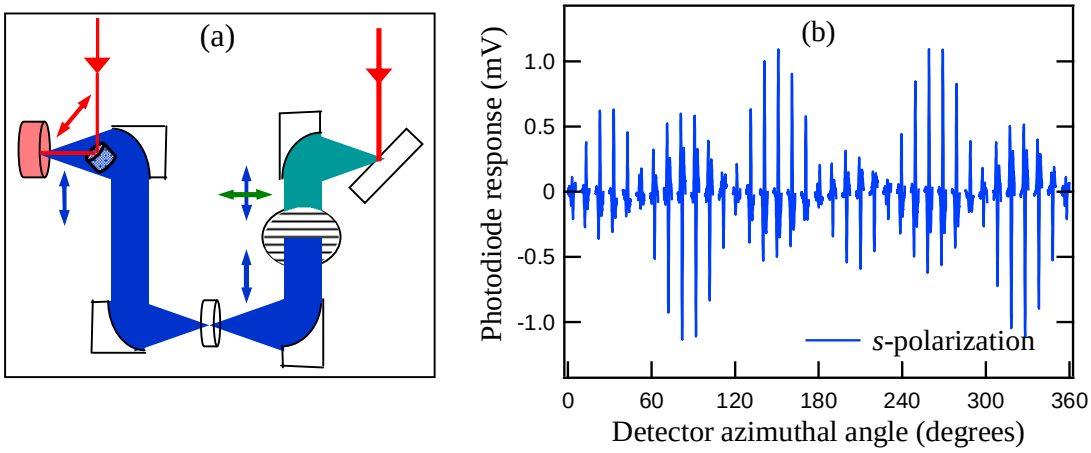

Figure 2.11 (a) Horizontal polarizer grid set-up in order to observe vertically (*s*) polarized THz components only. (b) Detector azimuthal rotation behavior for vertically

(*s*) polarized THz components. Each line represents THz time-domain signal, measured over a period of 3 ps, at particular azimuthal angle of detector crystal.

In the case of electro-optic detection, the THz output is sensitive to detector crystal orientation. The rotation of the crystal leads to change in detected THz signal. Such effect for (110) ZnTe (Cradley Crystals Corporation, Russia) is presented in Figure 2.10 and Figure 2.11.

For horizontally polarized NIR excitation pulses, the THz components parallel (*p*-polarization) and perpendicular (*s*-polarization) to this excitation radiation can be obtained by placing a wire-grid polarizer in the THz beam path with vertical and horizontal alignment of wire-grids, respectively.

Azimuthal rotation of the ZnTe crystal gives a distinctive three cycle dependence for both polarization components. Thus, while measuring the response of *p* and *s*-polarized THz components, it is important to adjust the azimuthal angle of the ZnTe detector in order to observe the maximum possible signal. In normal experimental conditions the detector azimuthal angle is set to detect maximum horizontally (*p*) polarized components of terahertz electric field.

2.3.9 Detector thickness

Another important property of the detector is the thickness of the detector crystal. Phase matching is an important property for electro-optic detection; the thinner crystal may be used in order to reduce the mismatch between the generated THz pulse and the gating NIR pulse, which increases the THz bandwidth. However, thinner crystals suffer from low interaction length and hence produce lower THz power. Hence, there is a trade off between the higher bandwidth and power depending on thickness of the crystals.

Figure 2.12 shows the effect of changing the detector thickness on THz signal generated from InAs emitter. The general trend is that the THz signal strength increases with increasing detector thickness from 0.3 mm to 1 mm. An interesting observation that can be made from the signals is the appearance of secondary peaks and shift of these secondary peaks with increasing thickness. These secondary signals arise due to multiple reflection of the THz beam at surfaces of the detector crystal. This behavior of Fabry-Perot oscillation is shown in Figure 2.12(b).

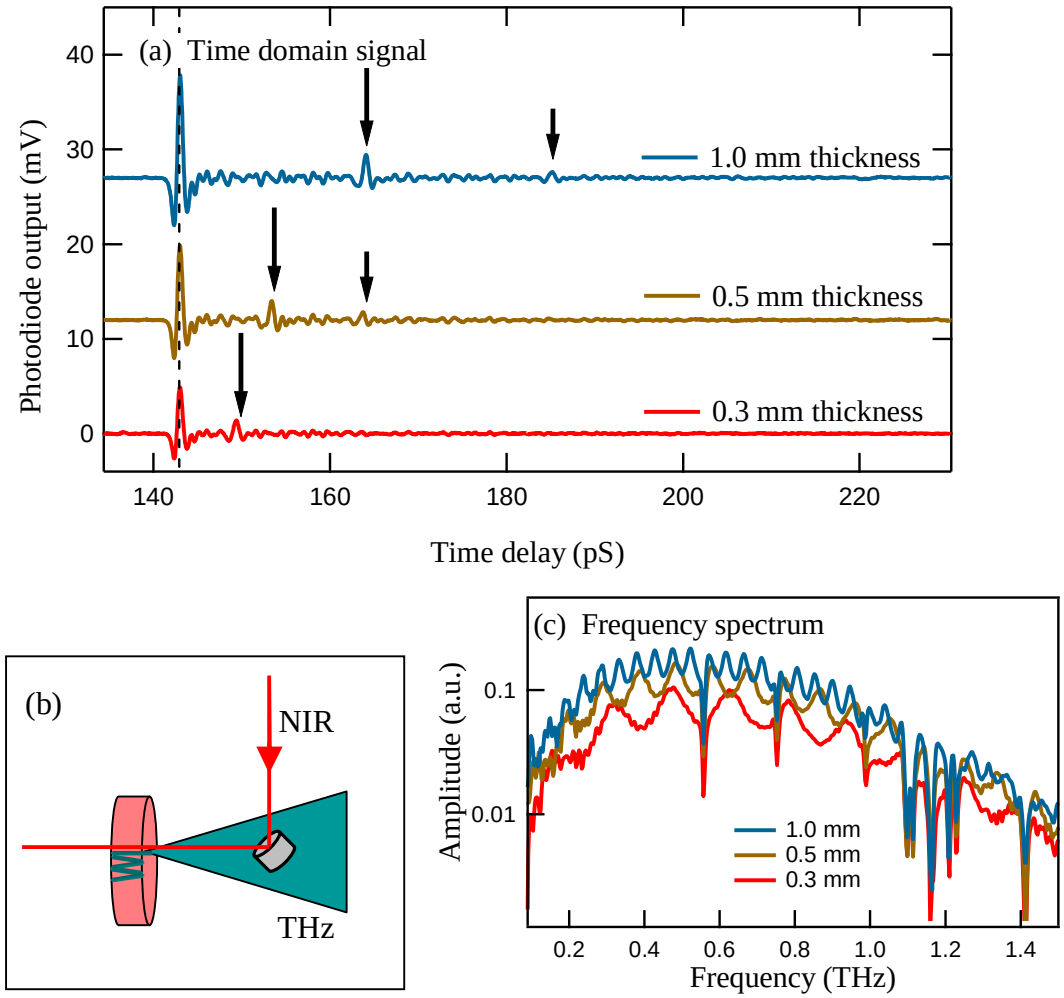

Figure 2.12 (a) Effect of changing detector thickness. The THz signal increases with increasing detector thickness within range of 0.3 to 1.0 mm. The graphs are shifted vertically for clarity. The secondary signals are observed for all measured detectors due to reflection of THz within the detector crystal. The secondary peaks are shown with arrows. (b) Fabry-Perot oscillations in the detector crystal. (c) The frequency spectrum for different thickness ZnTe detectors. The oscillatory behavior in frequency spectra is observed due to multiple peaks present in the signal.

The practical consequence of this effect is that we can use these features for calculating refractive index of the detector crystal in THz frequency range by using information about thickness and time delay between peaks. However, due to these Fabry-Perot oscillations, the frequency spectrum shows oscillatory behavior, which can interfere with the spectroscopic analysis. This unwanted feature can be eliminated by

stopping the scan before the secondary reflection occurrence; but by doing so the frequency resolution reduces. It is also possible to remove this effect by using numerical analysis.

Such oscillatory behavior may be observed for some emitters and spectroscopy samples as well which reflect a considerable amount of THz radiation within the sample.

2.3.10 Photodiode properties

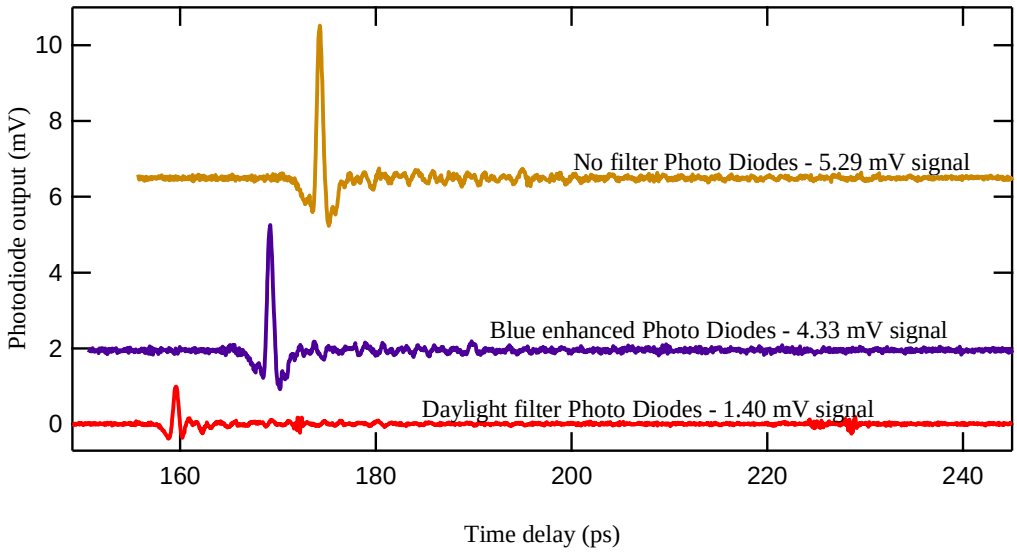

Figure 2.13 Response of different silicon photodiodes. Three Si photodiodes - Daylight filter (BPW 34 F, SIEMENS), blue enhanced (BPW 34 B, OSRAM), and no filter photodiodes (BPW 34, VISHAY) - were used. The data are shifted on both axes for clarity.

The final output for the THz signal is measured from differential voltage across the photodiode pair. Thus the photodiode used for the measurement directly affects the overall system behavior. The response of different photodiodes has been tested for varying spectral sensitivity and different filtering options. One such example of using three different silicon photodiodes with different properties is shown in Figure 2.13.

2.3.11 Optical alignment and focusing

Another important factor is the alignment and focusing of different optical parts used in the system. Since the routine realignment of the system needs to be undertaken

for better NIR excitation output, the THz signal may be affected with variations in these parameters.

Also small fluctuations in the laser power and electrical connections generate noise in the THz signal output which may interfere with the data analysis particularly for less efficient THz emitters. This can be minimized to some extent by using a larger time constant and lower dynamics reserve setting.

2.3.12 Temperature

THz emission efficiency is affected considerably with variation in operating temperature[18,54,115,124-126]. The change may be attributed to material properties or other experimental parameters in the system. While low temperature operation is the fundamental requirement for the thermal detection using bolometer, TDS systems have an advantage of being able to perform equally well at room temperature.

Thus, in normal system performance, there are many factors which need to be taken into account while collecting data and comparing results from different materials. In the following chapters, the focus will be on analyzing semiconductor materials which generate THz emission by all-optical means without using any external bias. In order to make proper comparison among different emitters, experimental parameters such as detector, NIR filter, and photodiodes are kept fixed. Further, (100) InAs and (110) ZnTe crystals are used as reference emitters for emitter reflection and transmission geometry measurements, respectively. Also the measurements were taken at normal atmospheric conditions and fixed temperature (20 ^{o}C).

Chapter 3

3 Optical Rectification and GaAs (11*N*) Crystal Planes in Transmission Geometry

3.1 Introduction

In this chapter, the theory of bulk optical rectification (bulk OR) and surface electric-field-induced optical rectification (surface OR) for zinc-blende $\bar{4}3m$ crystal planes with arbitrary Miller indices (hkl) is presented. The simpler case of emitter transmission geometry for $(11N)$ planes is then discussed and the experimental results for GaAs $(11N)$ planes with $N = 0$, 2, 3, 4, and 5 are compared with theory. The results suggest both bulk OR and surface OR play roles in THz generation from high-index crystal planes. Furthermore, different azimuthal behavior is observed for the two opposing *A* and *B* faces for GaAs samples, where the *A* face is the Ga-rich face and the *B* face is the As-rich face.

Non-linear crystals may be able to produce sum frequency (second harmonic generation) and difference frequency (optical rectification) polarization components by exploiting the excitation beam. Using femtosecond near-infrared optical pulses, the difference frequency components in the THz regime can be obtained, and hence such non-linear crystals are able to generate THz radiation under appropriate conditions. The OR effect is known to depend strongly not only on the angles of incidence and detection but also on the excitation beam polarization, the crystallographic plane on which the surface is cut, and the azimuthal angle of the sample about its surface normal. In order to take all parameters into account, we need to make transformations of the laboratory frame of axes to crystal axes, where the bulk OR and surface OR contributions can be calculated, and then perform inverse transformations to bring this back to the laboratory frame to detect the generated THz. The incidence excitation beam may have any arbitrary polarization with respect to the crystal surface and can strike at any arbitrary angle at the sample. Also, the detector can be at any arbitrary position.

Early experiments on THz generation by OR were made in transmission geometry[45,127-129]. The transmission geometry is useful in order to eliminate the effect of the transient current mechanism (as it cannot be observed in normal incidence of the incident excitation) and hence make it simple to observe the effect of OR components only. Earlier, the theory for second-order bulk OR has been developed and compared

with experimental results for (100), (110), (111), (112) faces[46,47,68,128,130] and for higher indices (113) and (115)[49]. The third-order surface-field-induced OR is also discussed in few works[46,47]. Recently, the effect of elliptically and circularly polarized excitation with energy below bandgap, slightly above bandgap, and far above the bandgap of non-linear crystal have been presented for THz emission from GaAs (100) and (111) crystal planes[131]. With some exceptions, the previous work only dealt with the overall THz field variation with azimuthal rotation of the emitter crystal without paying close attention to other parameters such as the relation of the polarization components at a particular azimuthal angle, the exact in-plane direction of measurement of azimuthal angle and sense of rotation. In this chapter, a complete cohesive study of optical rectification for any arbitrary crystal plane is presented with the general behavior of other important parameters such as the orientation of the incident excitation beam and arbitrary detector position. The theory is then compared with experimental results for GaAs (11*N*) planes with N = 0, 2, 3, 4, 5. High-index crystal planes are particularly interesting as they show interesting electronic properties[132,133]. Further, it will be shown that the information about the intrinsic surface field can be obtained from OR effects for high index planes. Such information is not accessible from low index planes such as (100), (110), and (111).

3.2 General theory of optical rectification

Various transformations are taken from laboratory frame to the crystal frame in order to calculate the polarization within the crystal and then back to the laboratory frame to determine THz emission with respect to the detector crystal orientation.

3.2.1 Excitation radiation in $(\hat{\mathbf{x}}', \hat{\mathbf{y}}', \hat{\mathbf{z}}')$ coordinate system

The excitation radiation may be propagating in any direction in space. First of all we start with single-primed coordinate system specified by unit vectors $\hat{\mathbf{x}}'$, $\hat{\mathbf{y}}'$, and $\hat{\mathbf{z}}'$ in order to represent the directional properties of the excitation radiation. The excitation radiation is assumed to be linearly polarized. We define $\hat{\mathbf{y}}'$ to lie in the direction of the polarization of the excitation radiation, $\hat{\mathbf{x}}'$ to lie in the direction opposite to the propagation of the excitation beam, and $\hat{\mathbf{z}}' = \hat{\mathbf{x}}' \times \hat{\mathbf{y}}'$.

The electric-field vector, with magnitude of the electric field E_0, can be written as,

$$\mathbf{E} = \begin{bmatrix} E_{x'} \\ E_{y'} \\ E_{z'} \end{bmatrix} = \begin{bmatrix} 0 \\ E_0 \\ 0 \end{bmatrix} = \begin{bmatrix} 0 \\ 1 \\ 0 \end{bmatrix} E_0 . \qquad 3.1$$

3.2.2 Angle of Incidence ϕ' and $(\hat{\mathbf{x}}'', \hat{\mathbf{y}}'', \hat{\mathbf{z}}'')$ coordinate system

The excitation radiation strikes the emitter crystal sample at an arbitrary angle of incidence ϕ'. We define a double-primed coordinate system with unit vectors $\hat{\mathbf{x}}''$, $\hat{\mathbf{y}}''$, and $\hat{\mathbf{z}}''$ to represent the coordinate system fixed to the crystal surface. The unit vector $\hat{\mathbf{x}}''$ is in the direction of outward-directed surface normal. The plane in which $\hat{\mathbf{x}}'$ and $\hat{\mathbf{x}}''$ lie defines the plane of reflection for non-normal incidence $(\phi' \neq 0)$ and the unit vector $\hat{\mathbf{z}}''$ is defined to be in the direction perpendicular to this reflection plane in the direction of $\hat{\mathbf{x}}' \times \hat{\mathbf{x}}''$. In the case of normal incidence of the excitation radiation $(\phi' = 0)$, the direction $\hat{\mathbf{z}}'' = \hat{\mathbf{z}}'$. The unit vector $\hat{\mathbf{y}}''$ is defined as $\hat{\mathbf{y}}'' = \hat{\mathbf{z}}'' \times \hat{\mathbf{x}}''$.

Although the angle of incidence of the excitation beam to the sample is ϕ', the angle within the crystal will be different due to refraction. Using Snell's law the resultant refracted angle within the crystal ϕ_{NIR} can be given as

$$n_{\text{air,NIR}} \sin\phi' = n_{\text{crystal,NIR}} \sin\phi_{\text{NIR}} , \qquad 3.2$$

where $n_{\text{air,NIR}}$ and $n_{\text{crystal,NIR}}$ are refractive indices at pump photon frequency of the ambient atmosphere and of the emitter crystal, respectively.

3.2.3 Angle of polarization Φ

In order to represent polarization of the excitation radiation with respect to the emitter crystal, the polarization angle Φ is defined as the angle that the polarization direction of the incident radiation $(\hat{\mathbf{y}}')$ makes with the $\hat{\mathbf{x}}'' - \hat{\mathbf{y}}''$ plane. This plane is perpendicular to the crystal surface and for non-normal incidence $(\phi' \neq 0)$, is the reflection plane. The polarization angle Φ is positive for a clockwise rotation with respect to the direction $\hat{\mathbf{x}}'$ and for $\Phi = 0$, $\hat{\mathbf{z}}'$ is parallel to $\hat{\mathbf{z}}''$.

The two polarization components of the excitation radiation can be written as

$$\begin{bmatrix} E_p \\ E_s \end{bmatrix} = \begin{bmatrix} \cos\Phi \\ \sin\Phi \end{bmatrix} E_0 . \qquad 3.3$$

For normal incidence, $\Phi = 0$, $\hat{\mathbf{x}}'' = \mathbf{x}'$, $\hat{\mathbf{y}}'' = \hat{\mathbf{y}}'$, and $\hat{\mathbf{z}}'' = \hat{\mathbf{z}}'$. Further, for normal incidence, the "reflection plane" is not defined, but the incident beam polarization components will be still written as *p* and *s* components.

The electric field of the excitation radiation $E_0\hat{\mathbf{y}}'$ can be represented in the double-primed coordinate system by taking into account the angle of incidence ϕ' and the angle of polarization Φ as

$$\begin{bmatrix} E_{x''} \\ E_{y''} \\ E_{z''} \end{bmatrix} = \begin{bmatrix} +\cos\phi_{\text{NIR}} & +\sin\phi_{\text{NIR}} & 0 \\ -\sin\phi_{\text{NIR}} & +\cos\phi_{\text{NIR}} & 0 \\ 0 & 0 & 1 \end{bmatrix} \begin{bmatrix} 0 \\ \cos\Phi \\ \sin\Phi \end{bmatrix} E_0 = \begin{bmatrix} \sin\phi_{\text{NIR}}\cos\Phi \\ \cos\phi_{\text{NIR}}\cos\Phi \\ \sin\Phi \end{bmatrix} E_0 . \qquad 3.4$$

3.2.4 Azimuthal angle θ and $(\hat{\mathbf{x}}''', \hat{\mathbf{y}}''', \hat{\mathbf{z}}''')$ coordinate system

The azimuthal angle θ, which represents the rotation of the emitter crystal about its surface normal, is denoted in terms of a triple-primed coordinate system with unit vectors $\hat{\mathbf{x}}'''$, $\hat{\mathbf{y}}'''$, and $\hat{\mathbf{z}}'''$. $\hat{\mathbf{x}}''$ and $\hat{\mathbf{x}}'''$ unit vectors lie perpendicular to the crystal surface, the triple-primed system is defined as the double-primed system being rotated counterclockwise about the $\hat{\mathbf{x}}'' = \hat{\mathbf{x}}'''$ axis through an angle θ.

The transformation matrix for the triple-primed coordinate system in terms of double-primed coordinates can be written as

$$\begin{bmatrix} \hat{\mathbf{x}}''' \\ \hat{\mathbf{y}}''' \\ \hat{\mathbf{z}}''' \end{bmatrix} = \begin{bmatrix} 1 & 0 & 0 \\ 0 & +\cos\theta & -\sin\theta \\ 0 & +\sin\theta & +\cos\theta \end{bmatrix} \begin{bmatrix} \hat{\mathbf{x}}'' \\ \hat{\mathbf{y}}'' \\ \hat{\mathbf{z}}'' \end{bmatrix} . \qquad 3.5$$

Hence the electric field components can be written as

$$\begin{bmatrix} E_{x'''} \\ E_{y'''} \\ E_{z'''} \end{bmatrix} = \begin{bmatrix} 1 & 0 & 0 \\ 0 & +\cos\theta & -\sin\theta \\ 0 & +\sin\theta & +\cos\theta \end{bmatrix} \begin{bmatrix} E_{x''} \\ E_{y''} \\ E_{z''} \end{bmatrix} = \begin{bmatrix} \sin\phi_{\text{NIR}}\cos\Phi \\ \cos\theta\cos\phi_{\text{NIR}}\cos\Phi - \sin\theta\sin\Phi \\ \sin\theta\cos\phi_{\text{NIR}}\cos\Phi + \cos\theta\sin\Phi \end{bmatrix} E_0 . \qquad 3.6$$

Figure 3.1 represents the single-primed, double-primed and triple-primed coordinate axes along with the angles ϕ', Φ, and θ as defined above.

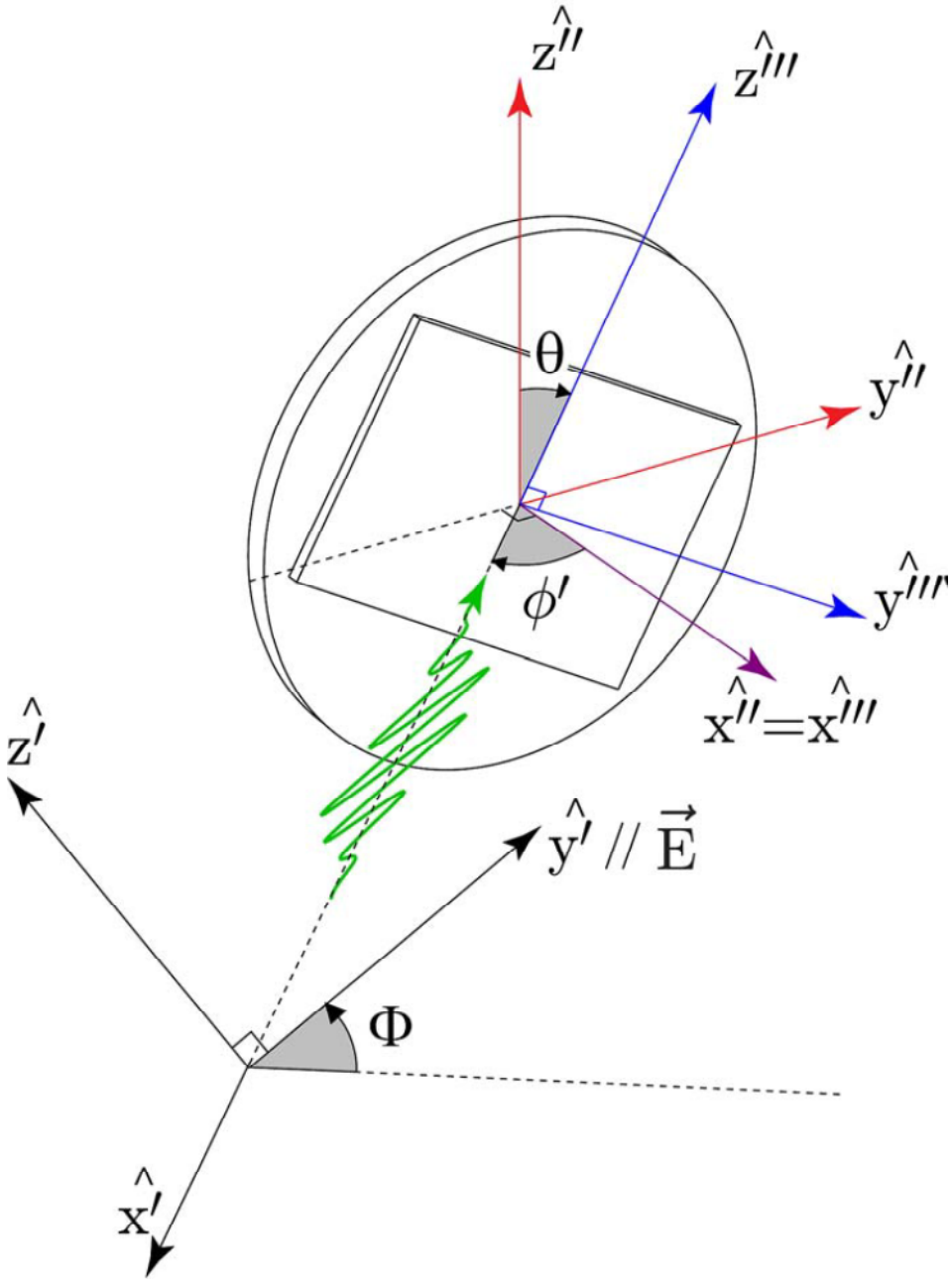

Figure 3.1 The coordinate axes and angles used for determination of optical rectification components. The incident excitation radiation is polarized in the $\hat{\mathbf{y}}'$ direction and propagates in the $-\hat{\mathbf{x}}'$ direction. The angle of incidence of the excitation radiation is ϕ'. $\hat{\mathbf{x}}''$ represents the out-ward pointing surface normal. The triple-primed frame rotates with the crystal about the surface normal by the azimuthal angle θ. The angle of polarization is Φ. (The figure is redrawn from Hargreaves *et al.*[134])

3.2.5 Crystal axes in $(\hat{\mathbf{x}}, \hat{\mathbf{y}}, \hat{\mathbf{z}})$ coordinate system

The crystal axes are defined by the unit vectors $\hat{\mathbf{x}}, \hat{\mathbf{y}}, \text{and } \hat{\mathbf{z}}$ and can be represented in terms of the triple-primed coordinate system. The vector $h\hat{\mathbf{x}} + k\hat{\mathbf{y}} + l\hat{\mathbf{z}}$ is normal to the surface, where $h, k, \text{and } l$ are Miller indices of the crystal. The axis system in this case is chosen in such a way that the vector $\hat{\mathbf{x}}'''$ is perpendicular to the emitter surface along the crystallographic direction $[hkl]$ and $\hat{\mathbf{z}}'''$ lies along the projection of the crystal $\hat{\mathbf{z}}$ axis onto the crystal surface. (This choice is not possible for the (00*l*) crystal plane, where the $\hat{\mathbf{z}}$ axis is normal to the surface. However, these cases can be treated as (*h*00) or (0*k*0) crystals.)

The transformation matrix from triple-primed axes to crystallographic frame can be written as

$$\begin{bmatrix} \hat{\mathbf{x}} \\ \hat{\mathbf{y}} \\ \hat{\mathbf{z}} \end{bmatrix} = \begin{bmatrix} \dfrac{h}{\sqrt{h^2+k^2+l^2}} & \dfrac{-k}{\sqrt{h^2+k^2}} & \dfrac{-hl}{\sqrt{h^2+k^2+l^2}\sqrt{h^2+k^2}} \\ \dfrac{k}{\sqrt{h^2+k^2+l^2}} & \dfrac{h}{\sqrt{h^2+k^2}} & \dfrac{-kl}{\sqrt{h^2+k^2+l^2}\sqrt{h^2+k^2}} \\ \dfrac{l}{\sqrt{h^2+k^2+l^2}} & 0 & \dfrac{h^2+k^2}{\sqrt{h^2+k^2+l^2}\sqrt{h^2+k^2}} \end{bmatrix} \begin{bmatrix} \hat{\mathbf{x}}''' \\ \hat{\mathbf{y}}''' \\ \hat{\mathbf{z}}''' \end{bmatrix}$$

$$= \begin{bmatrix} A_{11} & A_{12} & A_{13} \\ A_{21} & A_{22} & A_{23} \\ A_{31} & 0 & A_{33} \end{bmatrix} \begin{bmatrix} \hat{\mathrm{x}}''' \\ \hat{\mathrm{y}}''' \\ \hat{\mathrm{z}}''' \end{bmatrix} = A \begin{bmatrix} \hat{\mathrm{x}}''' \\ \hat{\mathrm{y}}''' \\ \hat{\mathrm{z}}''' \end{bmatrix}. \qquad 3.7$$

From above equations, it can be seen that the crystallographic directions corresponding to the triple-primed axes $\hat{\mathbf{x}}''', \hat{\mathbf{y}}''', \text{and } \hat{\mathbf{z}}'''$ are $[hkl]$, $[\bar{k}h0]$ and $[-hl, -kl, h^2+k^2]$, respectively.

Now at this point, we would like to extend the theory further in order to incorporate two opposing crystal faces into the general theory of optical rectification. The semiconductor material cut along the (hkl) plane will have two opposing faces in such a way that the surface normal for one face will be along the $[hkl]$ direction, while for the other face the surface normal will be along the $[\bar{h}\bar{k}\bar{l}]$ direction. Let us consider these two faces as *A* face and *B* face respectively.

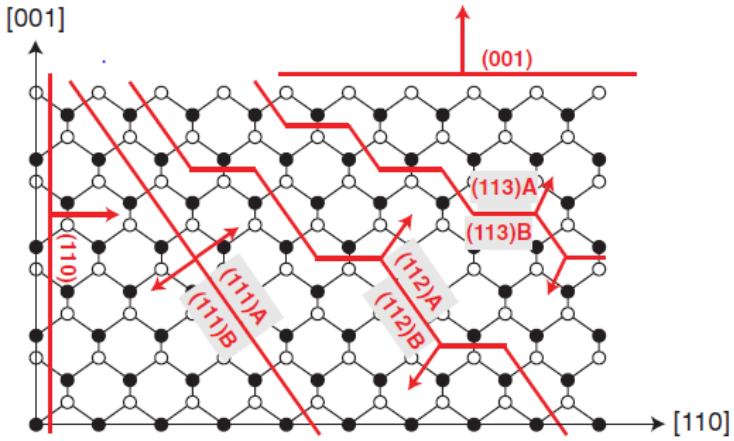

Figure 3.2 GaAs (11*N*) crystal planes with two opposing *A* and *B* faces. Filled circles represent gallium atoms, while empty circles represent arsenic atoms. The distinct feature of opposing faces can be understood as *A* face having more gallium atoms compared to arsenic and *B* face having more arsenic atoms compared to gallium. Further, the surface normal for faces *A* and *B* are along $[11N]$ and $[\bar{1}\,\bar{1}\bar{N}]$ respectively. The planes such as (001) and (110) have higher symmetry and both sides of cuts along these planes are equivalent.

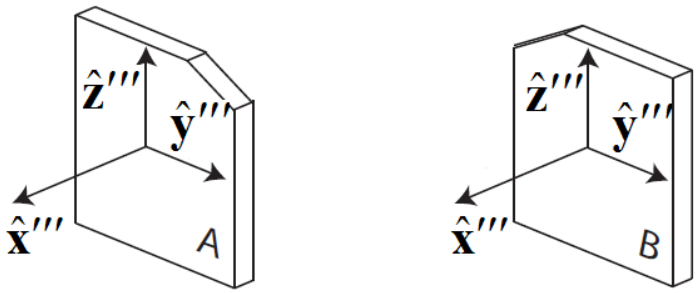

$$\hat{\mathbf{x}}''' \,//\, [hkl] \qquad \hat{\mathbf{x}}''' \,//\, [\bar{h}\bar{k}\bar{l}]$$
$$\hat{\mathbf{y}}''' \,//\, [\bar{k}h0] \qquad \hat{\mathbf{y}}''' \,//\, [k\bar{h}0]$$
$$\hat{\mathbf{z}}''' \,//\, [-hl, -kl, h^2 + k^2]$$

Figure 3.3 The triple-primed coordinate system for two opposing *A* and *B* faces. For the *A* face $\hat{\mathbf{x}}''' \,//\, [hkl]$, $\hat{\mathbf{y}}''' \,//\, [\bar{k}h0]$, and $\hat{\mathbf{z}}''' \,//\, [-hl, -kl, h^2 + k^2]$. For the *B* face $\hat{\mathbf{x}}''' \,//\, [\bar{h}\bar{k}\bar{l}]$, $\hat{\mathbf{y}}''' \,//\, [k\bar{h}0]$, and $\hat{\mathbf{z}}''' \,//\, [-hl, -kl, h^2 + k^2]$. Note the expressions for $\hat{\mathbf{x}}'''$ and $\hat{\mathbf{y}}'''$ are inverted but for $\hat{\mathbf{z}}'''$ remains the same.

The experimental results for GaAs (11*N*) for two opposing faces *A* and *B* will be presented and comparison will be made with the general theory for different experimental conditions. The distinction between these two opposing faces in the case of (11*N*) GaAs crystal planes is shown in Figure 3.2.

As discussed above, if we consider $\hat{\mathbf{x}}'''$ lies along the $[hkl]$ crystallographic direction for the *A* face then it will be along the $[\bar{h}\bar{k}\bar{l}]$ direction for *B* face. Similarly, $\hat{\mathbf{y}}'''$ lies along $[\bar{k}h0]$ and $[k\bar{h}0]$ directions for *A* and *B* faces, respectively, $\hat{\mathbf{z}}'''$ lies along $[-hl,-kl,h^2+k^2]$ direction for both faces. Figure 3.3 illustrates the triple-primed coordinates for opposing *A* and *B* faces. In order to reduce complexity during further transformations, only the components for the *A* face will be shown. We can accommodate the results for *B* face by simply replacing (hkl) values with $(\bar{h}\bar{k}\bar{l})$.

Using the transformation matrix from Equations 3.6 and 3.7, the electric field components in the crystallographic frame can be written as

$$\begin{bmatrix} E_x \\ E_y \\ E_z \end{bmatrix} = \begin{bmatrix} B_{11}+B_{12}\cos\theta+B_{13}\sin\theta \\ B_{21}+B_{22}\cos\theta+B_{23}\sin\theta \\ B_{31}+B_{32}\cos\theta+B_{33}\sin\theta \end{bmatrix} E_0 = \begin{bmatrix} B_{11} & B_{12} & B_{13} \\ B_{21} & B_{22} & B_{23} \\ B_{31} & B_{32} & B_{33} \end{bmatrix} \begin{bmatrix} 1 \\ \cos\theta \\ \sin\theta \end{bmatrix} E_0 . \qquad 3.8$$

Here our emphasis is on the effect of varying azimuthal angle θ. Hence, the electric field components are written in terms of θ and B_{ij}. The quantities B_{ij} depend on number of factors such as Miller indices h, k, l; incidence angle ϕ', and polarization angle Φ. The values of B_{ij} are given in Appendix A.

3.2.6 Bulk optical rectification polarization components

The detailed study for optical rectification in a nonlinear medium has been presented in Boyd[135]. In the case of a nonlinear medium under excitation of very intense light, the induced polarization can be written as

$$P = P^{(1)} + P^{(2)} + P^{(3)} + ... = \chi^{(1)}E + \chi^{(2)}EE + \chi^{(3)}EEE + ... \qquad 3.9$$

The first three terms in the Taylor expansion correspond to the linear, second-order and third-order polarization. Also, $\chi^{(2)}$ and $\chi^{(3)}$ are the second-order and third-order susceptibilities, respectively.

The second-order polarization component can be written in more detail as[46],

$$P_i^{(2)}(\Omega) = \chi_{ijk}^{(2)}(\Omega;\omega_1,\omega_2)E_j(\omega_1)E_k(\omega_2). \qquad 3.10$$

Here $P_i^{(2)}(\Omega)$ is the i^{th} component of the second-order polarization at frequency $\Omega = \omega_1 + \omega_2$, while $E_j(\omega_1)$ and $E_k(\omega_2)$ are the electric field components at frequencies ω_1 and ω_2, respectively. Optical rectification is observed for frequency $\omega_1 = -\omega_2$ (and Ω leads to THz frequency), while $\omega_1 = \omega_2$ generates second-harmonic components.

For zinc-blende $\bar{4}3m$ crystals, there are six nonvanishing elements of $\chi^{(2)}$ and all of them are equal by symmetry[136]. These components are

$$\chi_{xyz} = \chi_{yzx} = \chi_{zxy} = \chi_{xzy} = \chi_{zyx} = \chi_{yxz}. \qquad 3.11$$

Thus the second-order bulk optical rectification polarization components can be written as

$$\begin{bmatrix} P_x^{\text{bulk}} \\ P_y^{\text{bulk}} \\ P_z^{\text{bulk}} \end{bmatrix} = \begin{bmatrix} 0 & 0 & 0 & d_{14} & d_{14} & 0 & 0 & 0 & 0 \\ 0 & 0 & 0 & 0 & 0 & d_{14} & d_{14} & 0 & 0 \\ 0 & 0 & 0 & 0 & 0 & 0 & 0 & d_{14} & d_{14} \end{bmatrix} \begin{bmatrix} E_x^2 \\ E_y^2 \\ E_z^2 \\ E_yE_z \\ E_zE_y \\ E_zE_x \\ E_xE_z \\ E_xE_y \\ E_yE_x \end{bmatrix}, \qquad 3.12$$

where d_{14} is nonlinear optical susceptibility constant.

Again, using symmetry arguments for E_x, E_y, and E_z, the bulk polarization components can be written as

$$\begin{bmatrix} P_x^{\text{bulk}} \\ P_y^{\text{bulk}} \\ P_z^{\text{bulk}} \end{bmatrix} = 2d_{14} \begin{bmatrix} E_yE_z \\ E_zE_x \\ E_xE_y \end{bmatrix}. \qquad 3.13$$

Now as shown in Equation 3.8, the electric field components E_x, E_y, E_z involve $\cos\theta$ and $\sin\theta$ terms. So the terms E_iE_j in Equation 3.13 will involve $\cos\theta$, $\sin\theta$, $\cos\theta\sin\theta$ (which can be represented in terms of $\sin 2\theta$), and $\cos^2\theta$ and $\sin^2\theta$ (which can be expressed in terms of $\cos 2\theta$). So, the bulk polarization may be rewritten as,

$$\begin{bmatrix} P_x^{\text{bulk}} \\ P_y^{\text{bulk}} \\ P_z^{\text{bulk}} \end{bmatrix} = \begin{bmatrix} C_{11} + C_{12}\cos\theta + C_{13}\sin\theta + C_{14}\cos 2\theta + C_{15}\sin 2\theta \\ C_{21} + C_{22}\cos\theta + C_{23}\sin\theta + C_{24}\cos 2\theta + C_{25}\sin 2\theta \\ C_{31} + C_{32}\cos\theta + C_{33}\sin\theta + C_{34}\cos 2\theta + C_{35}\sin 2\theta \end{bmatrix}. \quad 3.14$$

Here the components C_{ij} depend on terms h, k, l, ϕ', Φ, d_{14}, and E_0, and are detailed in Appendix A.

3.2.7 Surface optical rectification polarization components

Along with bulk optical rectification, the third-order nonlinear components may give rise to a polarization in the presence of a surface electric field. Let us consider a constant electric field normal to the crystal surface, $\mathbf{F} = F_0\hat{\mathbf{x}}'''$. The effective second-order susceptibility can be thought of having contributions from both bulk OR and surface OR and can be written as[46]

$$\chi_{ijk}^{(2)\text{eff}} = \chi_{ijk}^{(2)\text{bulk}} + 3\chi_{ijkl}^{(3)}F_l^{\text{surf}}. \quad 3.15$$

The susceptibility tensor for surface OR is represented by $\chi_{ijkl}^{(3)}(\Omega;-\omega,\omega,0)$, where zero term corresponds to the DC surface depletion field. Again for $\bar{4}3m$ crystals, this third-order susceptibility tensor has four unique nonzero elements, which gives the polarization components for surface OR as[46,47,136]

$$\begin{bmatrix} P_x^{\text{surf}} \\ P_y^{\text{surf}} \\ P_z^{\text{surf}} \end{bmatrix} = \begin{bmatrix} \alpha' F_x + \beta' E_x + \gamma' E_x^2 F_x \\ \alpha' F_y + \beta' E_y + \gamma' E_y^2 F_y \\ \alpha' F_z + \beta' E_z + \gamma' E_z^2 F_z \end{bmatrix}, \quad 3.16$$

where $\alpha' = 3\chi_{zxxz}(E_x^2 + E_y^2 + E_z^2)$

$$\beta' = 6\chi_{zzxx}(E_x F_x + E_y F_y + E_z F_z)$$

$$\gamma' = 3(\chi_{zzzz} - \chi_{zxxz} - 2\chi_{zzxx}).$$

The terms involving α' and β' can be written in the double-primed coordinate system as

$$\begin{bmatrix} P_{x''}^{\text{surf}} \\ P_{y''}^{\text{surf}} \\ P_{z''}^{\text{surf}} \end{bmatrix} = \begin{bmatrix} 1 \\ 0 \\ 0 \end{bmatrix} \alpha' F_0 \quad 3.17$$

and

$$\begin{bmatrix} P_{x''}^{\text{surf}} \\ P_{y''}^{\text{surf}} \\ P_{z''}^{\text{surf}} \end{bmatrix} = \begin{bmatrix} \sin\phi_{\text{NIR}} \cos\Phi \\ \cos\phi_{\text{NIR}} \cos\Phi \\ \sin\Phi \end{bmatrix} \beta' E_0 . \qquad 3.18$$

Here the contribution due to α' is normal to the surface and the terms with β' only involve the incidence angle and the polarization angle and do not have any contribution from the azimuthal angle. Hence, these terms can be ignored while considering the effect of azimuthal dependence.

Now let us consider the components involving γ' terms. As can be seen from Equation 3.16, the terms with γ' involve E_i^2, which can be again expanded in terms of $\cos\theta$, $\sin\theta$, $\sin 2\theta$, and $\cos 2\theta$ and can be written in terms of components T_{ij} as

$$\begin{bmatrix} P_x^{\text{surf}} \\ P_y^{\text{surf}} \\ P_z^{\text{surf}} \end{bmatrix} = \begin{bmatrix} T_{11} + T_{12}\cos\theta + T_{13}\sin\theta + T_{14}\cos 2\theta + T_{15}\sin 2\theta \\ T_{21} + T_{22}\cos\theta + T_{23}\sin\theta + T_{24}\cos 2\theta + T_{25}\sin 2\theta \\ T_{31} + T_{32}\cos\theta + T_{33}\sin\theta + T_{34}\cos 2\theta + T_{35}\sin 2\theta \end{bmatrix}. \qquad 3.19$$

Here the T_{ij} components depend on the terms $B_{ij}, \gamma', E_0,$ and F_0 and are detailed in Appendix A.

3.2.8 Transforming back to the laboratory frame from crystal axes

We have calculated bulk and surface OR components in the crystal frame of reference. Now we need to transform the crystal frame to the external frame of reference attached to crystal surface. First, moving from unprimed coordinates to triple-primed coordinates, using Equation 3.7, the polarization components for these two frames of reference are related as

$$\begin{bmatrix} P_{x'''} \\ P_{y'''} \\ P_{z'''} \end{bmatrix} = A^{-1} \begin{bmatrix} P_x \\ P_y \\ P_z \end{bmatrix} = \begin{bmatrix} A_{11} & A_{21} & A_{31} \\ A_{12} & A_{22} & 0 \\ A_{13} & A_{23} & A_{33} \end{bmatrix} \begin{bmatrix} P_x \\ P_y \\ P_z \end{bmatrix}. \qquad 3.20$$

Hence, the bulk and surface optical rectification polarization components can be written as

$$\begin{bmatrix} P_{x'''}^{\text{bulk}} \\ P_{y'''}^{\text{bulk}} \\ P_{z'''}^{\text{bulk}} \end{bmatrix} = \begin{bmatrix} D_{11} + D_{12}\cos\theta + D_{13}\sin\theta + D_{14}\cos 2\theta + D_{15}\sin 2\theta \\ D_{21} + D_{22}\cos\theta + D_{23}\sin\theta + D_{24}\cos 2\theta + D_{25}\sin 2\theta \\ D_{31} + D_{32}\cos\theta + D_{33}\sin\theta + D_{34}\cos 2\theta + D_{35}\sin 2\theta \end{bmatrix} \qquad 3.21$$

and

$$\begin{bmatrix} P_{x'''}^{\text{surf}} \\ P_{y'''}^{\text{surf}} \\ P_{z'''}^{\text{surf}} \end{bmatrix} = \begin{bmatrix} U_{11} + U_{12}\cos\theta + U_{13}\sin\theta + U_{14}\cos 2\theta + U_{15}\sin 2\theta \\ U_{21} + U_{22}\cos\theta + U_{23}\sin\theta + U_{24}\cos 2\theta + U_{25}\sin 2\theta \\ U_{31} + U_{32}\cos\theta + U_{33}\sin\theta + U_{34}\cos 2\theta + U_{35}\sin 2\theta \end{bmatrix}. \quad 3.22$$

Further, in order to transform the triple-primed coordinates back to double-primed coordinates, using Equation 3.5, we can write

$$\begin{bmatrix} P_{x''} \\ P_{y''} \\ P_{z''} \end{bmatrix} = \begin{bmatrix} 1 & 0 & 0 \\ 0 & +\cos\theta & +\sin\theta \\ 0 & -\sin\theta & +\cos\theta \end{bmatrix} \begin{bmatrix} P_{x'''} \\ P_{y'''} \\ P_{z'''} \end{bmatrix}. \quad 3.23$$

So, the bulk and surface OR polarization components in the double-primed coordinates will be

$$\begin{bmatrix} P_{x''}^{\text{bulk}} \\ P_{y''}^{\text{bulk}} \\ P_{z''}^{\text{bulk}} \end{bmatrix} = \begin{bmatrix} G_{11} + G_{12}\cos\theta + G_{13}\sin\theta + G_{14}\cos 2\theta + G_{15}\sin 2\theta + G_{16}\cos 3\theta + G_{17}\sin 3\theta \\ G_{21} + G_{22}\cos\theta + G_{23}\sin\theta + G_{24}\cos 2\theta + G_{25}\sin 2\theta + G_{26}\cos 3\theta + G_{27}\sin 3\theta \\ G_{31} + G_{32}\cos\theta + G_{33}\sin\theta + G_{34}\cos 2\theta + G_{35}\sin 2\theta + G_{36}\cos 3\theta + G_{37}\sin 3\theta \end{bmatrix} \quad 3.24$$

and

$$\begin{bmatrix} P_{x''}^{\text{surf}} \\ P_{y''}^{\text{surf}} \\ P_{z''}^{\text{surf}} \end{bmatrix} = \begin{bmatrix} V_{11} + V_{12}\cos\theta + V_{13}\sin\theta + V_{14}\cos 2\theta + V_{15}\sin 2\theta + V_{16}\cos 3\theta + V_{17}\sin 3\theta \\ V_{21} + V_{22}\cos\theta + V_{23}\sin\theta + V_{24}\cos 2\theta + V_{25}\sin 2\theta + V_{26}\cos 3\theta + V_{27}\sin 3\theta \\ V_{31} + V_{32}\cos\theta + V_{33}\sin\theta + V_{34}\cos 2\theta + V_{35}\sin 2\theta + V_{36}\cos 3\theta + V_{37}\sin 3\theta \end{bmatrix}. \quad 3.25$$

The quantities D_{ij}, U_{ij}, G_{ij}, and V_{ij} are given in detail in Appendix A.

From Equations 3.24 and 3.25, it can be seen that, regardless of crystallographic orientation, the angle of incidence or the angle of polarization, the expressions for both bulk OR and surface OR can be represented in terms of azimuthal angle with terms $\cos n\theta$ and $\sin n\theta$, with n = 3 at most.

3.2.9 Detector axes in $(\hat{\mathbf{x}}''', \hat{\mathbf{y}}''', \hat{\mathbf{z}}''')$ coordinate system and detected terahertz field

In the far-field approximation, the THz field can be assumed to be directly proportional to the polarization field. Hence,

$$\begin{bmatrix} E_{x''}^{\text{THz}} \\ E_{y''}^{\text{THz}} \\ E_{z''}^{\text{THz}} \end{bmatrix} = \begin{bmatrix} P_{x''}^{\text{bulk}} + P_{x''}^{\text{surf}} \\ P_{y''}^{\text{bulk}} + P_{y''}^{\text{surf}} \\ P_{z''}^{\text{bulk}} + P_{z''}^{\text{surf}} \end{bmatrix} Z_0, \quad 3.26$$

where Z_0 is a proportionality factor which depends on experimental parameters such as the distance of the detector from the emitter crystal.

Here we need to consider one more coordinate system which is fixed to detector crystal and defined by the $\hat{\mathbf{x}}''''$, $\hat{\mathbf{y}}''''$, and $\hat{\mathbf{z}}''''$ coordinate system. The unit vector $\hat{\mathbf{x}}''''$ is defined as the direction from the point that the excitation beam strikes the emitter crystal to the detector. The angle ξ is defined as the angle this direction makes with $\hat{\mathbf{z}}''$ axis. The unit vector $\hat{\mathbf{y}}''''$ lies in the $\hat{\mathbf{x}}'' - \hat{\mathbf{y}}''$ plane. Thus, the electric field components in the quadruple-primed coordinate system can be written as

$$\begin{bmatrix} E_{x''''}^{\mathrm{THz}} \\ E_{y''''}^{\mathrm{THz}} \\ E_{z''''}^{\mathrm{THz}} \end{bmatrix} = \begin{bmatrix} +\sin\xi\cos\phi_{\mathrm{THz}} & -\sin\xi\sin\phi_{\mathrm{THz}} & +\cos\xi \\ +\sin\phi_{\mathrm{THz}} & +\cos\phi_{\mathrm{THz}} & 0 \\ -\cos\xi\cos\phi_{\mathrm{THz}} & -\cos\xi\cos\phi_{\mathrm{THz}} & +\sin\xi \end{bmatrix} \begin{bmatrix} E_{x''}^{\mathrm{THz}} \\ E_{y''}^{\mathrm{THz}} \\ E_{z''}^{\mathrm{THz}} \end{bmatrix}. \qquad 3.27$$

Here the angle ϕ_{THz} is the angle of refraction within the emitter crystal and is related to the angle of reflection ϕ'''', which is measured in the same way as the angle of incidence ϕ'. Again using Snell's law, two angles on the detection side are related by the equation

$$n_{\mathrm{air,THz}} \sin\phi'''' = n_{\mathrm{crystal,THz}} \sin\phi_{\mathrm{THz}}, \qquad 3.28$$

where $n_{\mathrm{air,THz}}$ and $n_{\mathrm{crystal,THz}}$ are refractive indices at the THz photon frequency of the ambient atmosphere and of the emitter crystal, respectively.

Since the detector may be placed anywhere, the angle of incidence ϕ' and angle of reflection ϕ'''' do not strictly bear any precise relationship. In typical experimental set ups, the detector is placed in reflection plane (i.e. ξ =90$^{\mathrm{o}}$) and detects the THz signal polarized in the reflection plane, E_p^{THz}, or in the direction perpendicular to the reflection plane, E_s^{THz}. These two orthogonally polarized THz polarization components can be represented in terms of the angle ϕ_{THz} and double-primed coordinate system as

$$\begin{bmatrix} E_p^{\mathrm{THz}} \\ E_s^{\mathrm{THz}} \end{bmatrix} = \begin{bmatrix} E_{y''''}^{\mathrm{THz}} \\ E_{z''''}^{\mathrm{THz}} \end{bmatrix} = \begin{bmatrix} \sin\phi_{\mathrm{THz}} E_{x''}^{\mathrm{THz}} + \cos\phi_{\mathrm{THz}} E_{y''}^{\mathrm{THz}} \\ E_{z''}^{\mathrm{THz}} \end{bmatrix}. \qquad 3.29$$

So from Equations 3.26 and 3.29,

$$\begin{bmatrix} E_p^{\mathrm{THz}} \\ E_s^{\mathrm{THz}} \end{bmatrix} = \begin{bmatrix} \sin\phi_{\mathrm{THz}} (P_{x''}^{\mathrm{bulk}} + P_{x''}^{\mathrm{surf}}) + \cos\phi_{\mathrm{THz}} (P_{y''}^{\mathrm{bulk}} + P_{y''}^{\mathrm{surf}}) \\ P_{z''}^{\mathrm{bulk}} + P_{z''}^{\mathrm{surf}} \end{bmatrix} Z. \qquad 3.30$$

Here Z is a conversion factor and is fixed for particular experimental arrangement.

Let us define, $P_p^{\mathrm{bulk}} = \sin\phi_{\mathrm{THz}} P_{x''}^{\mathrm{bulk}} + \cos\phi_{\mathrm{THz}} P_{y''}^{\mathrm{bulk}}$,

$P_s^{\mathrm{bulk}} = P_{z''}^{\mathrm{bulk}}$,

$$P_p^{\text{surf}} = \sin\phi_{\text{THz}} P_{x''}^{\text{surf}} + \cos\phi_{\text{THz}} P_{y''}^{\text{surf}} ,$$

$$P_s^{\text{surf}} = P_{z''}^{\text{surf}} .$$

Thus, the THz polarization components for horizontal (*p*) polarization and vertical (*s*) polarization can be written as

$$\begin{bmatrix} E_p^{\text{THz}} \\ E_s^{\text{THz}} \end{bmatrix} = \begin{bmatrix} P_p^{\text{bulk}} + P_p^{\text{surf}} \\ P_s^{\text{bulk}} + P_s^{\text{surf}} \end{bmatrix} Z . \qquad 3.31$$

3.3 OR theory for (11*N*) crystal planes in transmission geometry

The general theory for optical rectification for arbitrary crystal faces, arbitrary angles of incidence and reflection, and arbitrary polarization angle of excitation radiation has been discussed above. Now let us consider some cases for particular crystal faces and fixed angles of incidence, reflection, and polarization. We start with choosing the crystal Miller indices as $(hkl) = (11N)$ for transmission geometry where the excitation beam is in the direction of the surface normal $(\phi_{\text{NIR}} = 0)$ and the THz field is detected in the straight-through direction $(\phi_{\text{THz}} = 0)$. For convenience, the angle of polarization Φ is also chosen to be zero. For this experimental set up the terms involving α' and β' will be zero.

From Equation 3.31 and for $\phi_{\text{THz}} = 0$,

$$\begin{bmatrix} E_p^{\text{THz}} \\ E_s^{\text{THz}} \end{bmatrix} = \begin{bmatrix} P_p^{\text{bulk}} + P_p^{\text{surf}} \\ P_s^{\text{bulk}} + P_s^{\text{surf}} \end{bmatrix} Z = \begin{bmatrix} P_{y''}^{\text{bulk}} + P_{y''}^{\text{surf}} \\ P_{z''}^{\text{bulk}} + P_{z''}^{\text{surf}} \end{bmatrix} Z . \qquad 3.32$$

For the *A* face, *p* and *s* polarization components for the bulk and surface OR will be

$$\begin{bmatrix} P_p^{\text{bulk}} \\ P_s^{\text{bulk}} \end{bmatrix} = \frac{d_{14} E_0^2}{\sqrt{2}(N^2+2)^{3/2}} \begin{bmatrix} 3(N^2-1)\sin\theta - 3(N^2+1)\sin 3\theta \\ (N^2-1)\cos\theta - 3(N^2+1)\cos 3\theta \end{bmatrix} \qquad 3.33$$

and

$$\begin{bmatrix} P_p^{\text{surf}} \\ P_s^{\text{surf}} \end{bmatrix} = \frac{\gamma' F_0 E_0^2}{2\sqrt{2}(N^2+2)^2} \begin{bmatrix} -3N(N^2-1)\sin\theta - N(N^2+5)\sin 3\theta \\ -N(N^2-1)\cos\theta - N(N^2+5)\cos 3\theta \end{bmatrix} . \qquad 3.34$$

For the *B* face, the THz polarization components will be

$$\begin{bmatrix} P_p^{\text{bulk}} \\ P_s^{\text{bulk}} \end{bmatrix} = \frac{d_{14}E_0^2}{\sqrt{2}(N^2+2)^{3/2}} \begin{bmatrix} 3(N^2-1)\sin\theta - 3(N^2+1)\sin 3\theta \\ (N^2-1)\cos\theta - 3(N^2+1)\cos 3\theta \end{bmatrix} \quad 3.35$$

and

$$\begin{bmatrix} P_p^{\text{surf}} \\ P_s^{\text{surf}} \end{bmatrix} = \frac{\gamma' F_0 E_0^2}{2\sqrt{2}(N^2+2)^2} \begin{bmatrix} 3N(N^2-1)\sin\theta + N(N^2+5)\sin 3\theta \\ N(N^2-1)\cos\theta + N(N^2+5)\cos 3\theta \end{bmatrix}. \quad 3.36$$

All coefficients from A_{ij} to V_{ij} for (11*N*) crystal planes in transmission geometry are given in Appendix B.

Here *p* and *s* corresponds to the polarization components parallel and perpendicular to the incident excitation radiation polarization, respectively. As we can see from the equations above, both bulk and surface polarization components have θ and 3θ dependence. Further, the bulk polarization is same for both *A* and *B* faces. However, the surface polarization is reversed between the two faces. As a result of that, the overall THz field is enhanced for the *A* face, while it reduces for the *B* face.

It has been observed that (100) crystal planes have no contribution from OR effect in transmission geometry. The particular case of (100) samples will be discussed in later chapters.

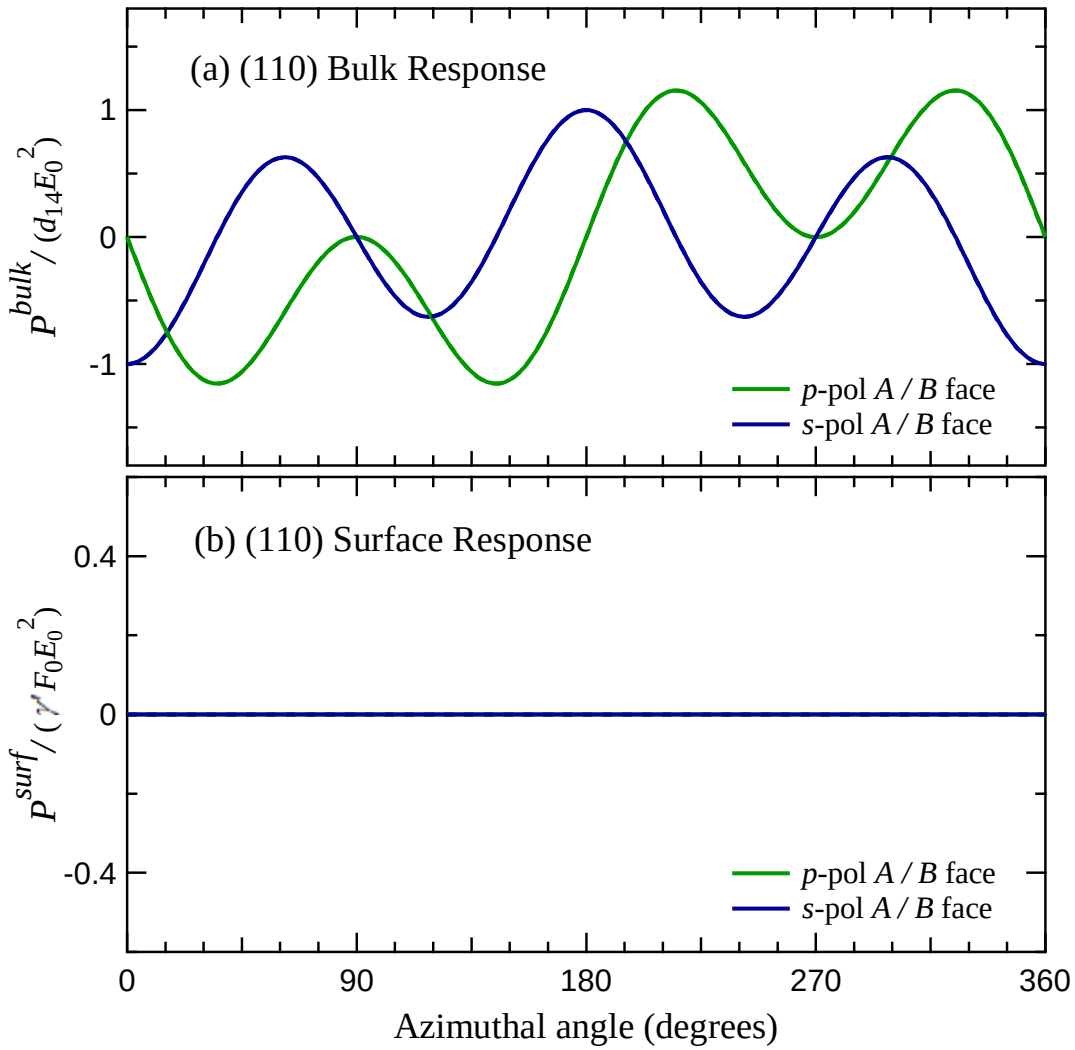

Figure 3.4 (a) Bulk OR and (b) surface OR polarization components for (110)*A* and *B* crystal planes. The surface OR components for both faces are zero. The bulk OR components gives three cycle variation with respect to the azimuthal rotation.

Let us start with the simple case of a GaAs (110) crystal. As shown in Figure 3.4, the bulk OR components exhibit three maxima and three minima due to the 3θ dependence with deviation from symmetrical variation due to the 1θ dependence. The contribution from surface OR is zero for both polarization components. Also for this direction the *A* face and the *B* face are equivalent due to crystal symmetry. Hence the (110)*A* and (110)*B* are actually same crystal faces and should exhibit the same azimuthal dependence.

The polarization components for (111) crystal planes are presented in Figure 3.5. In this case, the contribution of the 1θ term is zero for both bulk and surface OR polarizations and hence the variation is a symmetrical three cycle dependence. The effect of surface OR reverses between the two faces with the same bulk OR components. Hence, the resultant curve show increased and decreased 3θ behavior for *A* and *B* faces, respectively.

Turning now to high-index planes, several observations may be made from theory graphs. The first observation is that all high-index planes have nonzero bulk and surface polarization components with non-symmetrical three cycle dependence due to both 1θ and 3θ dependence. For both bulk and surface OR components, the overall shape is same for all high-index samples, but the signal strength decreases with increasing value of *N*. Also, as *N* approaches infinity, the (11*N*) face approaches a (001) face.

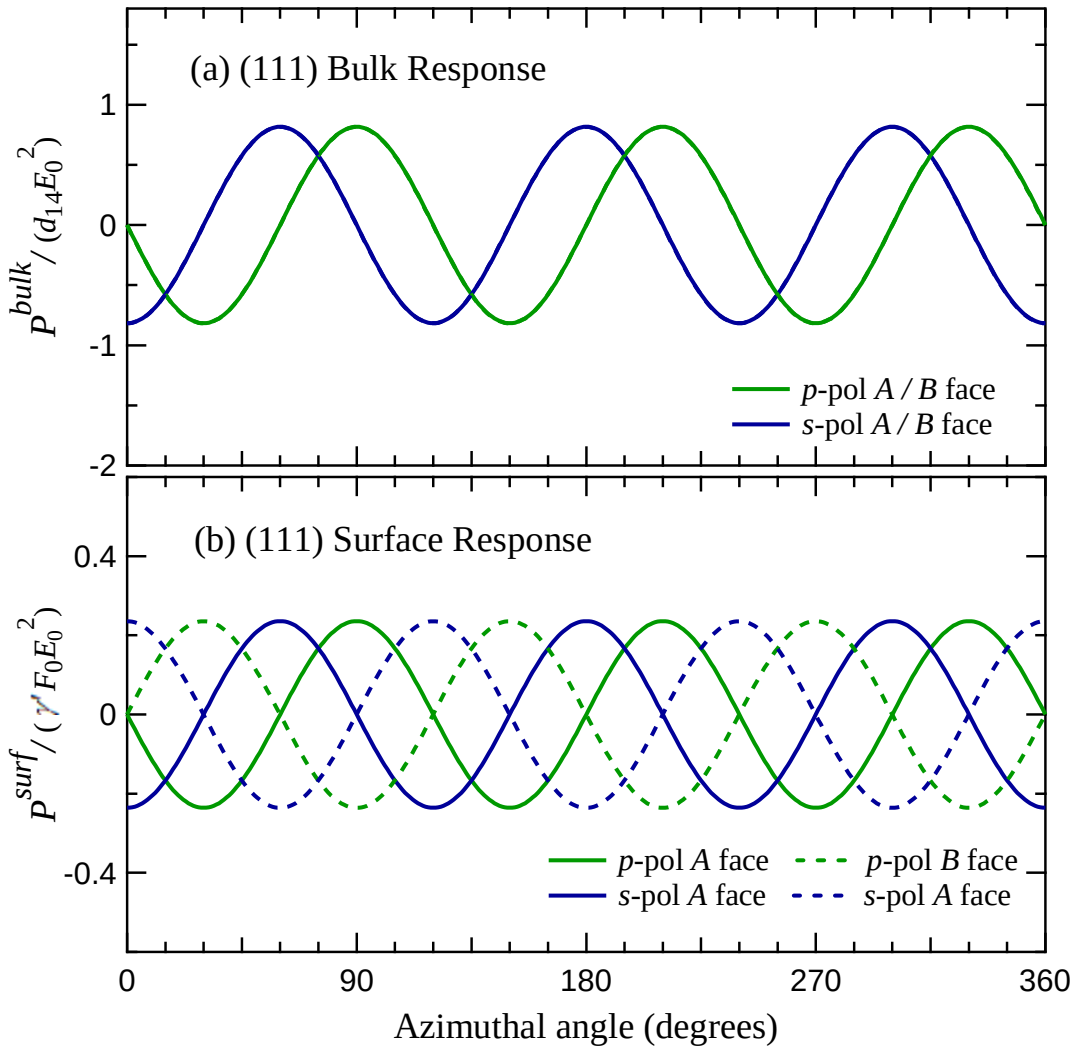

Figure 3.5 (a) Bulk OR and (b) surface OR polarization components for (111)*A* and *B* crystal planes. Due to the threefold rotational symmetry, the polarization components in this case involve only cos3θ and sin3θ terms. The surface polarization components reverse between the *A* and *B* faces.

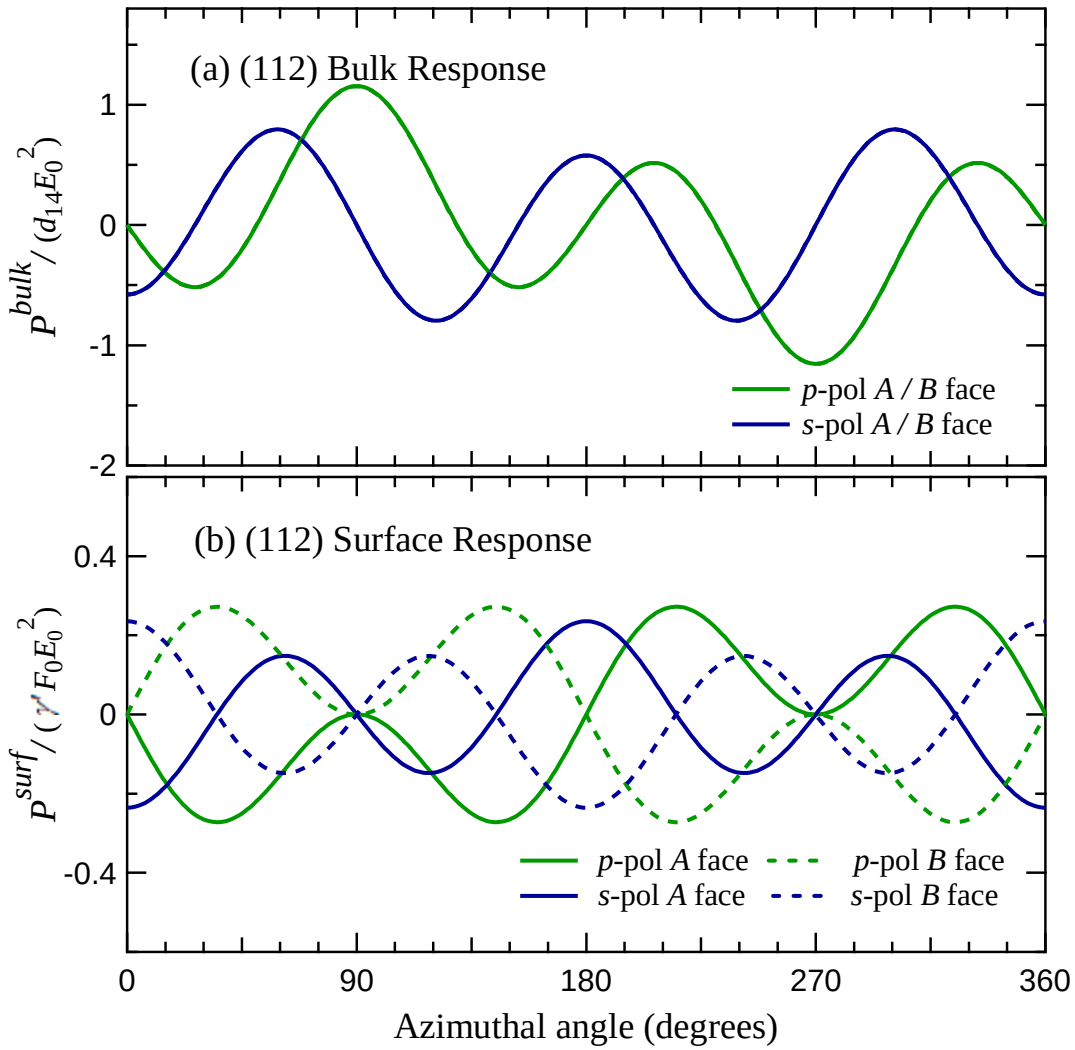

Figure 3.6 (a) Bulk OR and (b) surface OR polarization components for (112)*A* and *B* crystal planes. In this case the observed three cycle dependence is non-symmetrical with surface OR components reversing between the two faces.

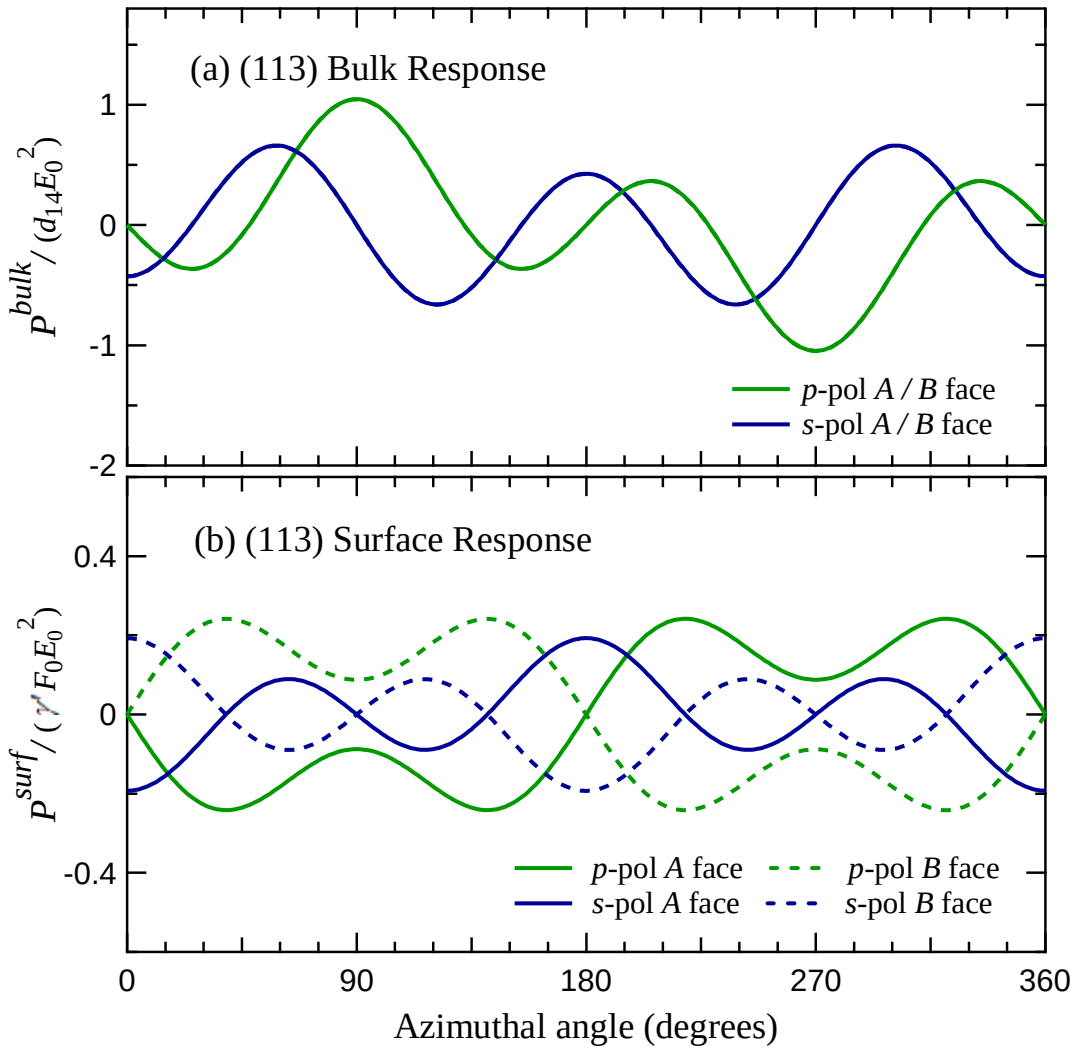

Figure 3.7 (a) Bulk OR and (b) surface OR polarization components for (113)*A* and *B* crystal planes. A similar response as for $N = 2$ with a reduction in the overall polarization signal strength is observed.

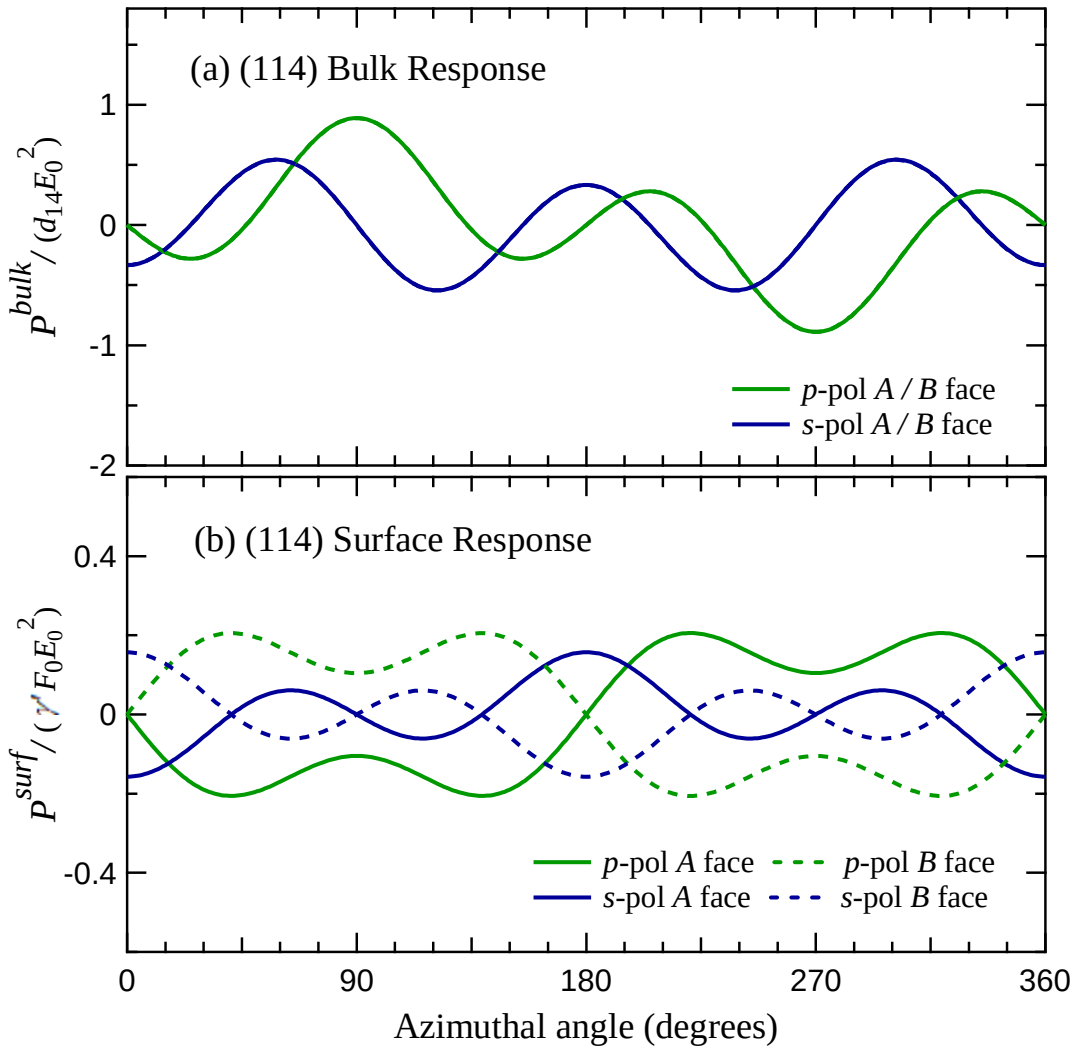

Figure 3.8 (a) Bulk OR and (b) surface OR polarization components for (114)*A* and *B* crystal planes. Both bulk and surface OR components reduce further compared to $N = 2$ and 3.

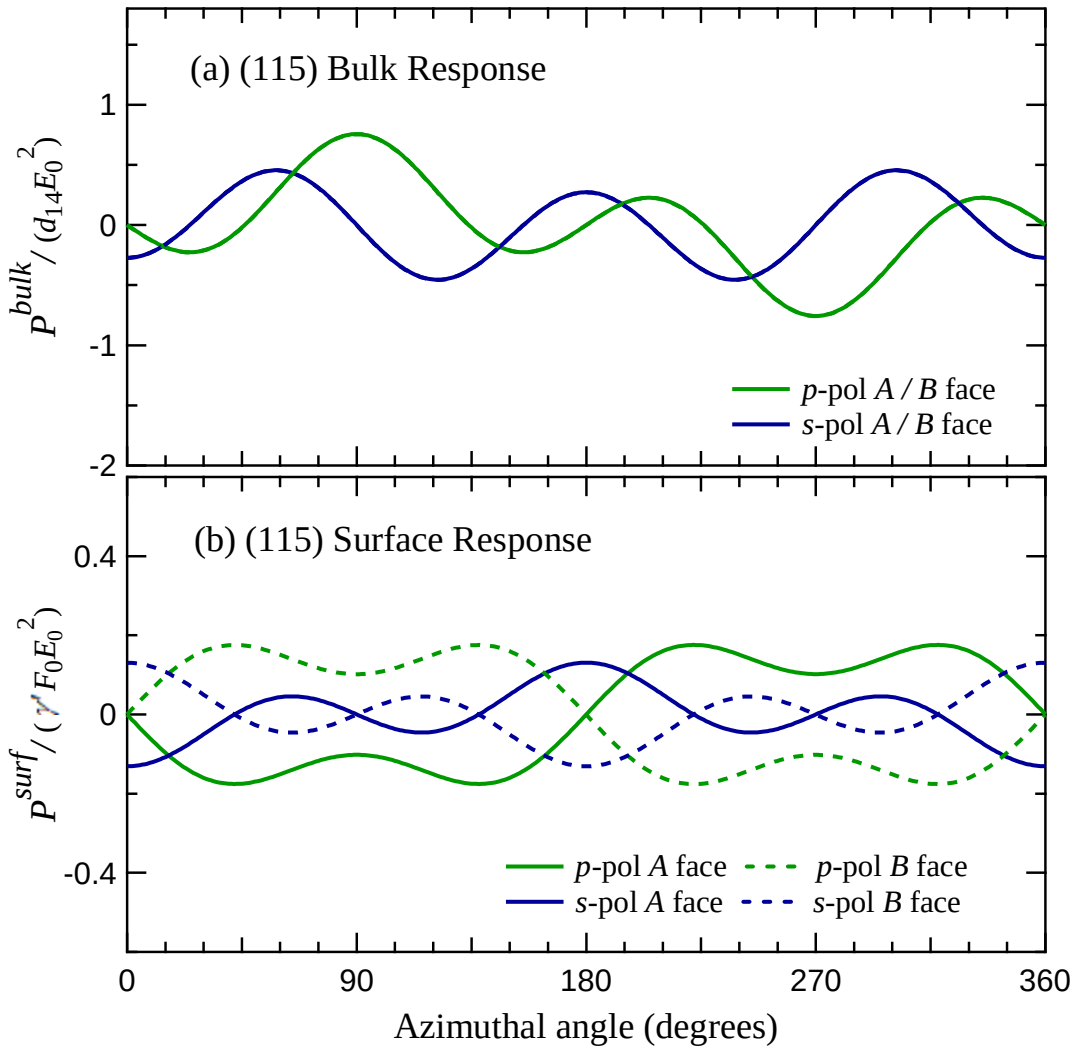

Figure 3.9 (a) Bulk OR and (b) surface OR polarization components for (115)*A* and *B* crystal planes. The signal strength for both bulk and surface OR components is reduced further indicating the further reduction with higher *N* values and the crystal plane approaches towards (001) for very high values of *N* where both OR components are zero.

3.4 Experimental results for GaAs (11*N*) crystal planes

GaAs (11*N*) planes for *N* = 0, 2, 3, 4, and 5 were tested as THz emitters in a conventional TDS set up in transmission geometry. All GaAs samples used in this study and details about crystallographic directions and two opposite *A* and *B* faces were provided by Prof. Mohamed Henini from the University of Nottingham, United Kingdom.

The incident excitation laser was directed horizontally (in the $-\hat{\mathbf{x}}'$ direction) and was polarized horizontally to the right when looking down the beam (in the $\hat{\mathbf{y}}'$ direction). Further, in the transmission geometry, $\hat{\mathbf{y}}'' = \hat{\mathbf{y}}'$ ran horizontally along the crystal surface and $\hat{\mathbf{z}}'' = \hat{\mathbf{z}}'$ ran upwards along the crystal surface. The azimuthal angle θ is measured in the clockwise direction when facing the crystal, with θ =0 corresponds to the $\hat{\mathbf{y}}'''$ direction.

For the *A* face, the crystal directions parallel to the pump electric field with azimuthal rotation can be identified as follows. For θ=0°, the pump electric field is in the direction of $\hat{\mathbf{y}}'''$ axis, or the $\left[\bar{k}h0\right]$ direction. For θ=90°, the pump electric field is in the direction of $\hat{\mathbf{z}}'''$ axis, or the $\left[-hl,-kl,h^2+k^2\right]$ direction; for θ=180°, the $\left[k\bar{h}0\right]$ direction; for θ=270°, the $\left[hl,kl,-(h^2+k^2)\right]$ direction. For the particular case of (11*N*) crystals these directions are $\left[\bar{1}10\right]$, $\left[\bar{N}\bar{N}2\right]$, $\left[1\bar{1}0\right]$, and $\left[NN\bar{2}\right]$, respectively.

For the *B* face these directions will be $\left[1\bar{1}0\right]$, $\left[\bar{N}\bar{N}2\right]$, $\left[\bar{1}10\right]$, and $\left[NN\bar{2}\right]$, respectively.

The signals for both horizontally (*p*) and vertically (*s*) - polarized components of the THz field were measured separately using a wire-grid polarizer for the two opposing *A* and *B* faces in (11*N*) planes. The GaAs crystals were azimuthally rotated and the response of THz electric field was measured as the differential voltage across the balanced photodiode pair.

It is important to note here that, since in this case the transmission geometry is employed, no contribution from the linear transient current mechanism in THz generation is expected, as for transient current effects, the dipole responsible for THz generation is generated normal to the semiconductor surface. For the more complex quasireflection geometry, however, these effects will be detected. The detailed analysis

of the quasireflection geometry measurements for GaAs (11*N*) crystals is given in chapter 4.

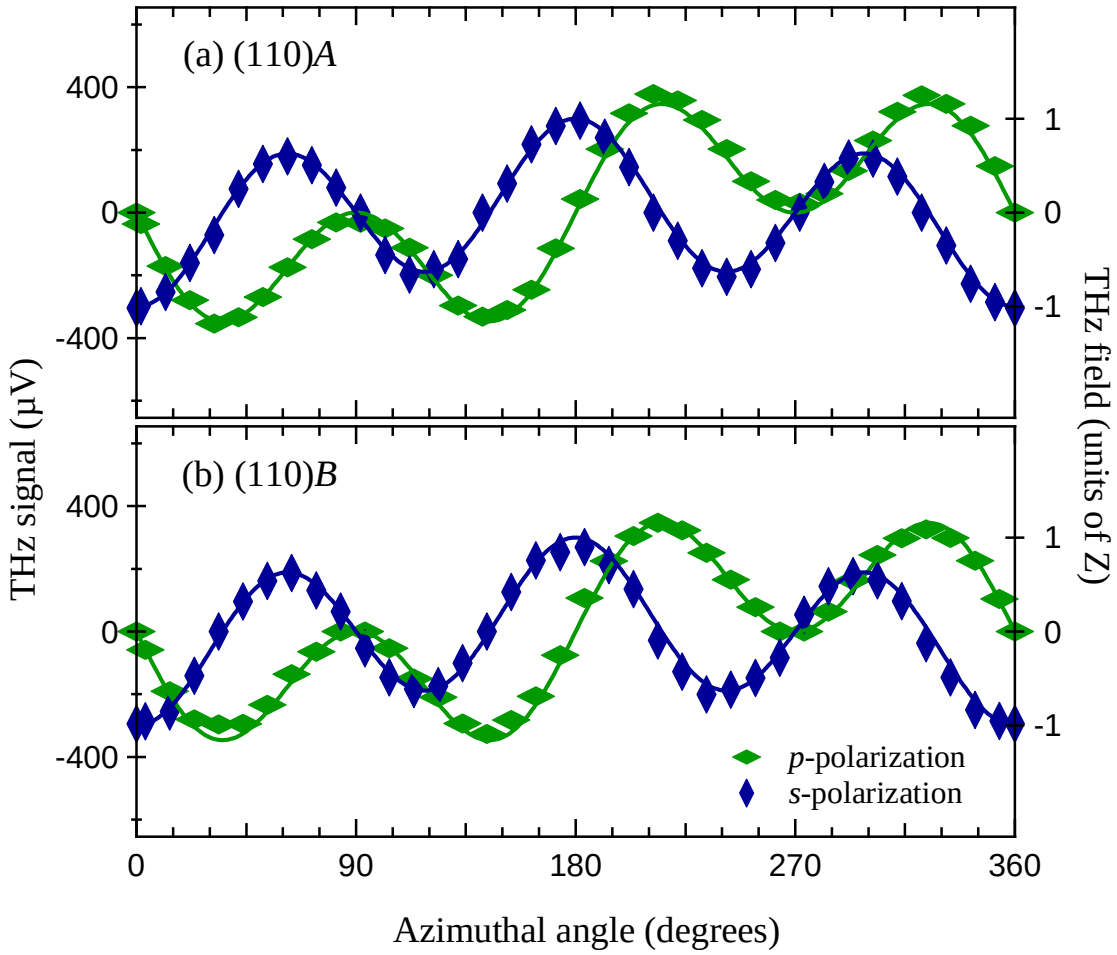

Figure 3.10 GaAs (a) (110)*A* and (b) (110)*B* azimuthal angle dependence. Each mark represents the peak-to-peak THz signal voltage measured at a particular azimuthal angle. The horizontal and vertical diamonds represents the horizontally (*p*) and vertically (*s*) polarized THz components and refer to the left axes. The full lines are the theory results for (110) bulk optical rectification and relate to the right axis. Due to the crystal symmetry of the (110) plane, two faces are theoretically equivalent.

Figure 3.10 represents experimentally observed THz polarization components for (110) crystal planes for both *A* and *B* faces along with appropriate theory fit. The THz response is measured with azimuthal angle rotation in the step size of 10^{o} and peak-to-peak voltage is plotted with respect to the azimuthal angle. All four polarization components (*p* and *s*-polarized THz components for both faces) are plotted on the same THz detector (μV) axis without any scaling. Likewise, the theoretical fit to these results

are plotted on the same axis relative to Z without any scaling. The single fitting parameter needed in order to compare the experimental results with the theory is given by setting Z=1 corresponds to 300 μV. This value has been kept fixed in future comparisons of the azimuthal dependence of all (11*N*) samples.

The (110) crystal plane has a symmetry axis and hence the *A* and *B* faces are theoretically equivalent. The results for the (110) crystal plane for both *A* and *B* faces can be fitted using bulk OR alone, consistent with the theoretical results for this crystal plane; the contribution from surface OR is zero in transmission geometry. Such behavior is also observed for (110) ZnTe crystals.

We next consider the case of GaAs (11*N*)*A* crystal faces with *N* = 2, 3, 4, and 5. The THz field detected as a function of azimuthal angle is given in Figure 3.11. Several observations may be made from the experimental results obtained for these faces. First, the *p*-polarized components are dominated by a negative sin3θ term and the *s*-polarized components are dominated by a negative cos3θ term for all faces, with *p*-polarized components having one major maximum and two minor maxima while *s*-polarized components have two major maxima and one minor maximum. Also, the signal strength for the overall THz reduces with increasing *N* value. These results are consistent with the observations made from the theory curves.

The experimental results for *p*-polarized (green horizontal diamonds) and *s*-polarized (blue vertical diamonds) are fitted with theoretical curves. The same fitting parameter for bulk OR is used as was already found for (110) plane. For bulk OR polarizations, the value of $d_{14}E_0^2$ is set to 1 and the results are shown with dashed line for both polarizations. The theory results for bulk OR broadly reproduces the experimental features, however better agreement can be made by considering both bulk and surface OR effects together. Keeping $d_{14}E_0^2 = 1$ and hence Z = 1 corresponding to 300 μV, the surface parameter $\gamma' F_0 E_0^2$ has varied to get the best match between the theory and experimental results. It has been found that for all *A* faces, the data fits well with the theory for $\gamma' F_0 E_0^2 = (1.9 \pm 0.2) d_{14} E_0^2$ or $\gamma' F_0 = (1.9 \pm 0.2) d_{14}$. The combined bulk and surface response is shown by full lines using this ratio for all (11*N*) faces.

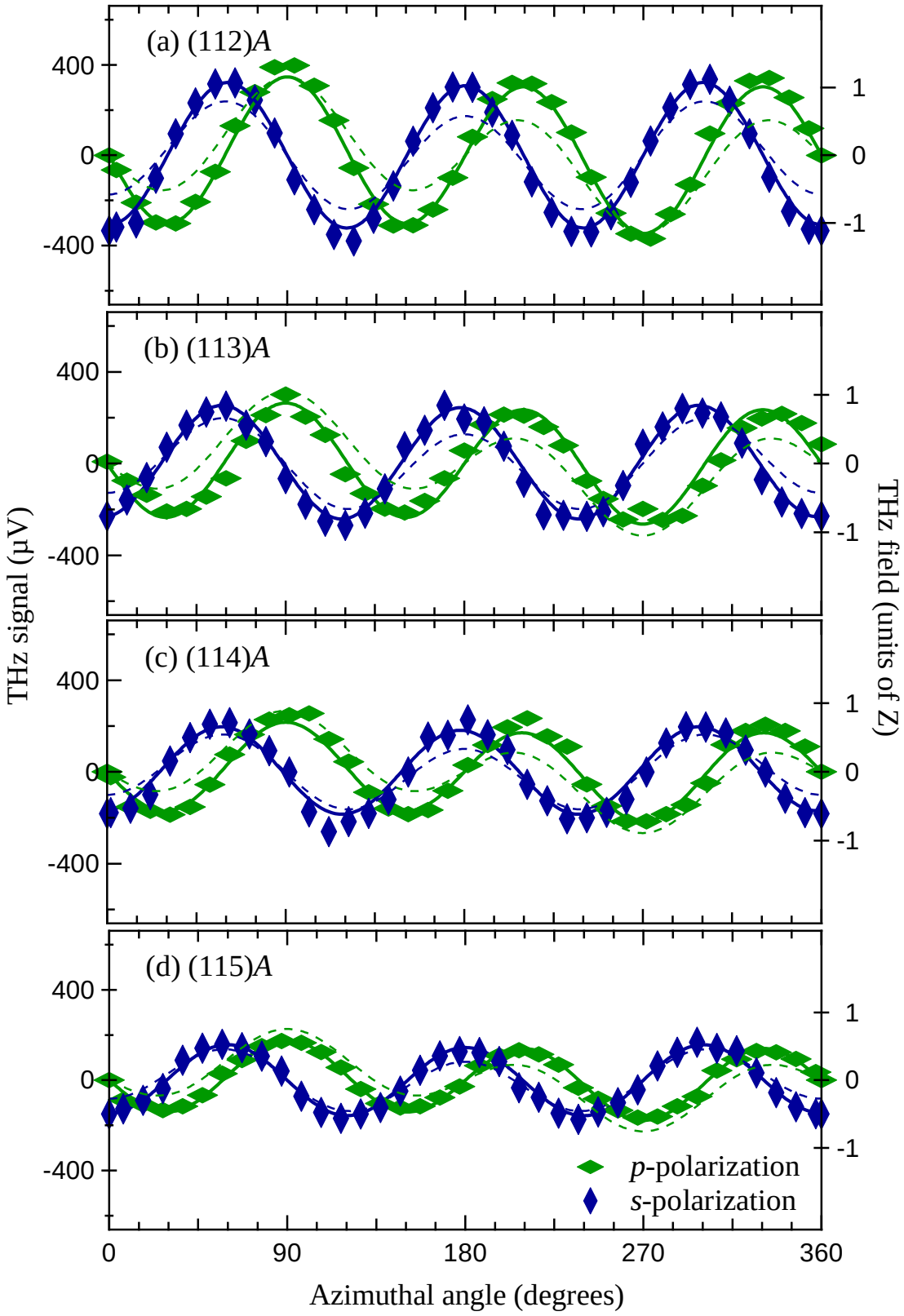

Figure 3.11 GaAs (112)*A* to (115)*A* azimuthal angle dependence. The dashed lines are the theoretical curves for bulk OR with $d_{14}E_0^2=1$. The full lines are the calculation from combined bulk and surface OR with $d_{14}E_0^2=1$ and $\gamma' F_0=(1.9\pm0.2)d_{14}$.

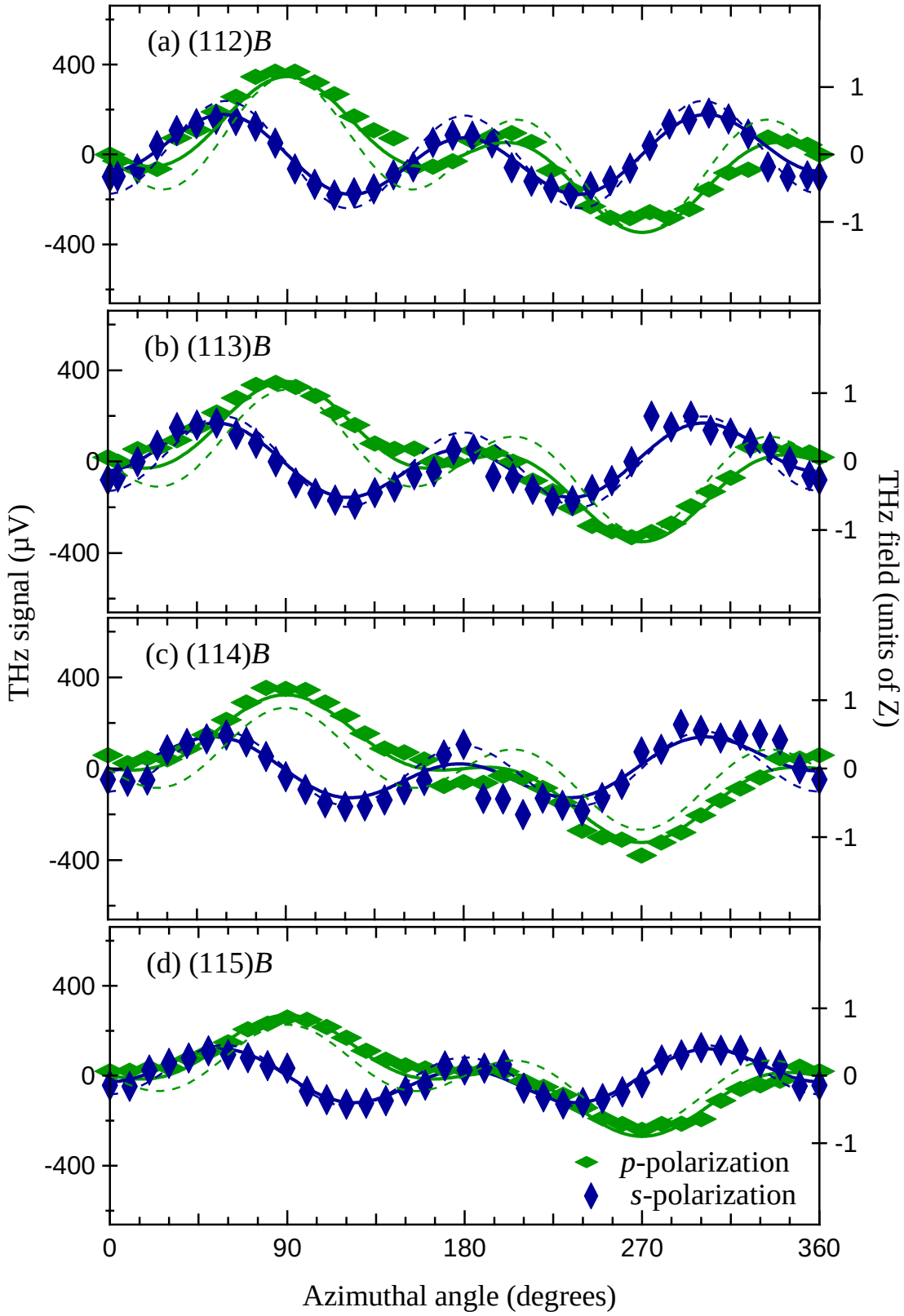

Figure 3.12 GaAs (112)*B* to (115)*B* azimuthal angle dependence. The dashed lines are the theoretical curves for bulk OR with $d_{14}E_0^2$=1. The full lines are the calculation from combined bulk and surface OR with $d_{14}E_0^2$ and $\gamma' F_0 = (1.6 \pm 0.2) d_{14}$.

Figure 3.12 shows azimuthal dependence behavior for GaAs (11*N*)*B* faces. Again the observed data has been fitted with the bulk OR theory as shown with dashed lines, which does not match well with the observations. Hence, the combined bulk-surface OR effects have been tested. Keeping same bulk term used for (110) and (11*N*)*A* faces ($d_{14}E_0^2=1$) and varying the surface term ($\gamma' F_0$), it is found that $\gamma' F_0 = (1.6 \pm 0.2) d_{14}$ fits the data very well, as shown by continuous lines in Figure 3.12. Further, there is no evidence from these data that the term $\gamma' F_0$ varies between the samples.

Thus, by adjusting surface OR parameter, it is possible to get information about surface field F_0 in terms of bulk nonlinear susceptibility coefficient d_{14} and non-linear optical constant γ'. The surface fields for both *A* and *B* faces are positive and of the same strength within experimental error, with the direction being pointing away from the surfaces. By comparing the results for two opposing faces, the general trend for all (11*N*) samples can be seen - the data for azimuthal variation in the *A* face is more symmetrical compared to the *B* face. This can be understood as being due to the fact that the dominant 3θ components are in phase for bulk and surface OR for the *A* face (both being negative), while for *B* face, these components are out of phase (one positive and the other negative). This behavior also affects the overall signal strength such that the *A* face signal amplitude is higher than *B* face for all (11*N*) crystal faces.

[Note: In the paper Hargreaves *et al.*[134], the data for *A* face have been presented as *B* face for all (11*N*) samples. and vice versa. Further, the surface field direction does not reverse between the *A* and *B* faces as presented in the paper. However, the overall results for behaviour of (11*N*) crystal planes and observed magnitude of surface field F_0 do not affected by this.]

It is important to note that using the general theory of optical rectification and from the experimental results for all GaAs samples, the combined contribution from bulk OR and surface OR have been estimated. However, it is not possible to differentiate and find individual contribution from these effects using the theory presented here, unless more than one experimental geometry is used.

3.5 Conclusion

General expressions for bulk and surface electric-field-induced optical rectification for zinc-blende crystals with arbitrary crystallographic orientation, arbitrary polarization of the excitation beam, arbitrary incidence and detection angle have been presented. The bulk and surface OR components for the particular case of (11*N*) crystal faces in transmission geometry has been presented and compared with the experimental results for GaAs (11*N*) samples with $N = 0, 2, 3, 4,$ and 5.

From the theoretical expressions and experimental results, it has been shown that the *A* and *B* face for (110) are the same due to crystal symmetry. Further, no surface OR contribution can be measured for (110) face in transmission geometry and the data can be fitted with the bulk OR alone. Using the same value of bulk parameter obtained from the (110) measurements, it is possible to determine the contribution of the surface-field OR for high-index (11*N*) faces.

For high-index crystal planes, the total THz polarization is the sum of both bulk and surface OR. Within the set (112)*A*, (113)*A*, (114)*A*, and (115)*A*, we find the surface field in terms of bulk nonlinear susceptibility coefficient d_{14} and non-linear optical constant γ' as $(F_0)_A = (1.9 \pm 0.2)\, d_{14}/\gamma'$. Similarly for the set (112)*B*, (113)*B*, (114)*B* and (115)*B*, we find the surface field, $(F_0)_B = (1.6 \pm 0.2)\, d_{14}/\gamma'$. Thus the surface field for both *A* and *B* faces are positive and of the same strength within experimental error, with the direction being pointing away from the surfaces.

Thus, a clear distinction between different crystal planes and between opposing *A* and *B* faces has been observed. Further, by fitting theoretical expressions with experimental results for any crystal face makes it possible to identify the precise crystallographic directions in the crystal. Hence, optical rectification may be used in the analysis of semiconductor surface properties and to identify the precise crystallographic orientation of a sample.

Chapter 4

4 GaAs (11*N*) Crystal Planes in Quasireflection Geometry

4.1 Introduction

In the previous chapter, the general theory for second-order bulk optical rectification (bulk OR) and third-order surface-field-induced optical rectification (surface OR) for zincblende $\bar{4}3m$ crystals with arbitrary Miller indices (*hkl*) along with experimental results for (11*N*) GaAs in transmission geometry were presented. In this chapter, the results for GaAs (11*N*) crystals in quasireflection geometry are presented and a comparison is made with the general theory. The first noticeable difference in the experimental results between the two different geometries is the presence of linear *p*-polarized components for the non-normal incidence of the excitation radiation due to the presence of transient currents along with azimuthally variable optical rectification. The linear azimuthally invariant mechanism can be a photo-Dember effect or a surface-field effect or a combination of both. It has been reported previously that for the wide-bandgap semiconductor material, the mechanism is mainly due to photocarrier acceleration due to surface-depletion fields rather than the photo-Dember effect[54]. The measurements for these high-index crystal planes yield further information about the crystallographic orientation and surface properties of the emitter crystal.

4.2 OR components for (11*N*) crystal planes in quasireflection geometry

For the non-normal incidence of the excitation beam, the angle of incidence ϕ' and angle of reflection ϕ'''' are not zero and hence nonzero terms with ϕ_{NIR} and ϕ_{THz} will represent complex behavior with respect to azimuthal rotation in this experimental set up.

Let us start with rewriting the bulk and surface OR polarization components in terms of the azimuthal angle θ. From Equations 3.24 and 3.25,

$$\begin{bmatrix} P_{x''}^{\mathrm{bulk}} \\ P_{y''}^{\mathrm{bulk}} \\ P_{z''}^{\mathrm{bulk}} \end{bmatrix} = \begin{bmatrix} G_{11} + G_{12}\cos\theta + G_{13}\sin\theta + G_{14}\cos 2\theta + G_{15}\sin 2\theta + G_{16}\cos 3\theta + G_{17}\sin 3\theta \\ G_{21} + G_{22}\cos\theta + G_{23}\sin\theta + G_{24}\cos 2\theta + G_{25}\sin 2\theta + G_{26}\cos 3\theta + G_{27}\sin 3\theta \\ G_{31} + G_{32}\cos\theta + G_{33}\sin\theta + G_{34}\cos 2\theta + G_{35}\sin 2\theta + G_{36}\cos 3\theta + G_{37}\sin 3\theta \end{bmatrix} \tag{4.1}$$

and

$$\begin{bmatrix} P_{x''}^{\text{surf}} \\ P_{y''}^{\text{surf}} \\ P_{z''}^{\text{surf}} \end{bmatrix} = \begin{bmatrix} V_{11} + V_{12}\cos\theta + V_{13}\sin\theta + V_{14}\cos 2\theta + V_{15}\sin 2\theta + V_{16}\cos 3\theta + V_{17}\sin 3\theta \\ V_{21} + V_{22}\cos\theta + V_{23}\sin\theta + V_{24}\cos 2\theta + V_{25}\sin 2\theta + V_{26}\cos 3\theta + V_{27}\sin 3\theta \\ V_{31} + V_{32}\cos\theta + V_{33}\sin\theta + V_{34}\cos 2\theta + V_{35}\sin 2\theta + V_{36}\cos 3\theta + V_{37}\sin 3\theta \end{bmatrix}. \quad 4.2$$

The polarization coefficients G_{ij} and V_{ij} for quasireflection geometry are given in Appendix C.

It is important to note here that Equation 4.2 for surface-field-induced optical rectification is written for the terms involving γ' only, while the terms involving α' and β' surface-field-induced components have not been considered. The components with α' and β' terms are azimuthally invariant but nonzero for quasireflection geometry as opposed to being zero for transmission geometry. However, the estimated linear contribution from these components is very small compared to the transient current effect; hence these terms can be neglected for quasireflection geometry as well.

The final results for bulk polarization components for (11*N*)*A* face can be written in terms of *N*, the refracted angles of incidence ϕ_{NIR} and detection ϕ_{THz}, and the azimuthal angle θ as

$$P_p^{\text{bulk}} = \frac{d_{14}E_0^2}{(N^2+2)^{3/2}} \begin{bmatrix} -\begin{pmatrix} 6N\cos\phi_{\text{NIR}}\sin\phi_{\text{NIR}}\cos\phi_{\text{THz}} \\ +3N(\cos^2\phi_{\text{NIR}} - 2\sin^2\phi_{\text{NIR}})\sin\phi_{\text{THz}} \end{pmatrix} \\ +\begin{pmatrix} \frac{(N^2-1)}{\sqrt{2}}(3\cos^2\phi_{\text{NIR}} - 4\sin^2\phi_{\text{NIR}})\cos\phi_{\text{THz}} \\ -4\sqrt{2}(N^2-1)\cos\phi_{\text{NIR}}\sin\phi_{\text{NIR}}\sin\phi_{\text{THz}} \end{pmatrix}\sin\theta \\ -\begin{pmatrix} 2N(N^2-1)\cos\phi_{\text{NIR}}\sin\phi_{\text{NIR}}\cos\phi_{\text{THz}} \\ +N(N^2-1)\cos^2\phi_{\text{NIR}}\sin\phi_{\text{THz}} \end{pmatrix}\cos 2\theta \\ -\frac{3(N^2+1)}{\sqrt{2}}\cos^2\phi_{\text{NIR}}\cos\phi_{\text{THz}}\sin 3\theta \end{bmatrix} \quad 4.3$$

and

$$P_s^{\text{bulk}} = \frac{d_{14}E_0^2}{(N^2+2)^{3/2}} \begin{bmatrix} \frac{(N^2-1)}{\sqrt{2}}(\cos^2\phi_{\text{NIR}} - 4\sin^2\phi_{\text{NIR}})\cos\theta \\ +2N(N^2-1)\cos\phi_{\text{NIR}}\sin\phi_{\text{NIR}}\sin 2\theta \\ -\frac{3(N^2+1)}{\sqrt{2}}\cos^2\phi_{\text{NIR}}\cos 3\theta \end{bmatrix}. \quad 4.4$$

Similarly, the bulk polarization components for the *B* face will be

$$P_p^{\text{bulk}} = \frac{d_{14}E_0^2}{(N^2+2)^{3/2}} \begin{bmatrix} \begin{pmatrix} 6N\cos\phi_{\text{NIR}}\sin\phi_{\text{NIR}}\cos\phi_{\text{THz}} \\ +3N(\cos^2\phi_{\text{NIR}} - 2\sin^2\phi_{\text{NIR}})\sin\phi_{\text{THz}} \end{pmatrix} \\ + \begin{pmatrix} \frac{(N^2-1)}{\sqrt{2}}(3\cos^2\phi_{\text{NIR}} - 4\sin^2\phi_{\text{NIR}})\cos\phi_{\text{THz}} \\ -4\sqrt{2}(N^2-1)\cos\phi_{\text{NIR}}\sin\phi_{\text{NIR}}\sin\phi_{\text{THz}} \end{pmatrix}\sin\theta \\ + \begin{pmatrix} 2N(N^2-1)\cos\phi_{\text{NIR}}\sin\phi_{\text{NIR}}\cos\phi_{\text{THz}} \\ N(N^2-1)\cos^2\phi_{\text{NIR}}\sin\phi_{\text{THz}} \end{pmatrix}\cos 2\theta \\ -\frac{3(N^2+1)}{\sqrt{2}}\cos^2\phi_{\text{NIR}}\cos\phi_{\text{THz}}\sin 3\theta \end{bmatrix} \qquad 4.5$$

and

$$P_s^{\text{bulk}} = \frac{d_{14}E_0^2}{(N^2+2)^{3/2}} \begin{bmatrix} \frac{(N^2-1)}{\sqrt{2}}(\cos^2\phi_{\text{NIR}} - 4\sin^2\phi_{\text{NIR}})\cos\theta \\ -2N(N^2-1)\cos\phi_{\text{NIR}}\sin\phi_{\text{NIR}}\sin 2\theta \\ -\frac{3(N^2+1)}{\sqrt{2}}\cos^2\phi_{\text{NIR}}\cos 3\theta \end{bmatrix}. \qquad 4.6$$

From the above equations, it can be seen that the bulk OR components in quasireflection geometry include 1θ, 2θ, and 3θ azimuthal angle dependences along with an offset in the horizontal (*p*) polarization components, as opposed to only 1θ and 3θ dependence for transmission geometry. Further, the bulk polarization components are no longer the same for the *A* and *B* faces. The signal offset in the *p*-polarized signal and the components with 2θ dependence are reversed for the *A* and *B* faces.

Turning now to the third order OR effect, the surface polarization components for the (11*N*)*A* face will be

$$P_p^{\text{surf}} = \frac{\gamma' F_0 E_0^2}{(N^2+2)^2}\begin{bmatrix} \begin{pmatrix} 2(2N^2+1)\cos\phi_{\text{NIR}}\sin\phi_{\text{NIR}}\cos\phi_{\text{THz}} \\ +(2N^2+1)\cos^2\phi_{\text{NIR}}\sin\phi_{\text{THz}} + (N^4+2)\sin^2\phi_{\text{NIR}}\sin\phi_{\text{THz}} \end{pmatrix} \\ -\begin{pmatrix} \frac{N(N^2-1)}{2\sqrt{2}}(3\cos^2\phi_{\text{NIR}} - 4\sin^2\phi_{\text{NIR}})\cos\phi_{\text{THz}} \\ -2\sqrt{2}N(N^2-1)\cos\phi_{\text{NIR}}\sin\phi_{\text{NIR}}\sin\phi_{\text{THz}} \end{pmatrix}\sin\theta \\ -\begin{pmatrix} 2(N^2-1)\cos\phi_{\text{NIR}}\sin\phi_{\text{NIR}}\cos\phi_{\text{THz}} \\ +(N^2-1)\cos^2\phi_{\text{NIR}}\sin\phi_{\text{THz}} \end{pmatrix}\cos 2\theta \\ -\frac{N(N^2+5)}{2\sqrt{2}}\cos^2\phi_{\text{NIR}}\cos\phi_{\text{THz}}\sin 3\theta \end{bmatrix} \quad 4.7$$

$$P_s^{\text{surf}} = \frac{\gamma' F_0 E_0^2}{(N^2+2)^2}\begin{bmatrix} -\frac{N(N^2-1)}{2\sqrt{2}}(\cos^2\phi_{\text{NIR}} - 4\sin^2\phi_{\text{NIR}})\cos\theta \\ +2(N^2-1)\cos\phi_{\text{NIR}}\sin\phi_{\text{NIR}}\sin 2\theta \\ -\frac{N(N^2+5)}{2\sqrt{2}}\cos^2\phi_{\text{NIR}}\cos 3\theta \end{bmatrix}. \quad 4.8$$

For the *B* face,

$$P_p^{\text{surf}} = \frac{\gamma' F_0 E_0^2}{(N^2+2)^2}\begin{bmatrix} \begin{pmatrix} 2(2N^2+1)\cos\phi_{\text{NIR}}\sin\phi_{\text{NIR}}\cos\phi_{\text{THz}} \\ +(2N^2+1)\cos^2\phi_{\text{NIR}}\sin\phi_{\text{THz}} + (N^4+2)\sin^2\phi_{\text{NIR}}\sin\phi_{\text{THz}} \end{pmatrix} \\ +\begin{pmatrix} \frac{N(N^2-1)}{2\sqrt{2}}(3\cos^2\phi_{\text{NIR}} - 4\sin^2\phi_{\text{NIR}})\cos\phi_{\text{THz}} \\ -2\sqrt{2}N(N^2-1)\cos\phi_{\text{NIR}}\sin\phi_{\text{NIR}}\sin\phi_{\text{THz}} \end{pmatrix}\sin\theta \\ -\begin{pmatrix} 2(N^2-1)\cos\phi_{\text{NIR}}\sin\phi_{\text{NIR}}\cos\phi_{\text{THz}} \\ +(N^2-1)\cos^2\phi_{\text{NIR}}\sin\phi_{\text{THz}} \end{pmatrix}\cos 2\theta \\ +\frac{N(N^2+5)}{2\sqrt{2}}\cos^2\phi_{\text{NIR}}\cos\phi_{\text{THz}}\sin 3\theta \end{bmatrix} \quad 4.9$$

$$P_s^{\text{surf}} = \frac{\gamma' F_0 E_0^2}{(N^2+2)^2}\begin{bmatrix} \frac{N(N^2-1)}{2\sqrt{2}}(\cos^2\phi_{\text{NIR}} - 4\sin^2\phi_{\text{NIR}})\cos\theta \\ +2(N^2-1)\cos\phi_{\text{NIR}}\sin\phi_{\text{NIR}}\sin 2\theta \\ +\frac{N(N^2+5)}{2\sqrt{2}}\cos^2\phi_{\text{NIR}}\cos 3\theta \end{bmatrix}. \quad 4.10$$

Again a dependence on 1θ, 2θ, and 3θ is observed with the signal offset in the *p*-polarization components. For these polarization components, the terms with 1θ and 3θ

components are reversed between the two faces for both polarizations, while the *p*-polarization offset and terms with 2θ dependence remains the same.

4.3 Theory curves for (11*N*) crystal planes in quasireflection geometry

For quasireflection geometry, the angles of incidence and detection are 45°. For GaAs, the refractive index at 790 nm is 3.67[137] ($n_{\text{crystal,NIR}}$ =3.67) and at THz frequency is 3.58[137] ($n_{\text{crystal,THz}}$ =3.58). Hence, using Snell's law from Equations 3.2 and 3.28, the refracted angles of incidence and detection will be $\phi_{\text{NIR}} = 11.1^{\text{o}}$ and $\phi_{\text{THz}} = 11.4^{\text{o}}$.

As stated earlier in regard to the transmission measurements, for (110) crystal planes the faces *A* and *B* are equivalent. This can be observed from the equations for bulk and surface OR in quasireflection geometry as well. From those equations, it can be seen that for the (110) crystal face, the non-vanishing terms for bulk polarizations are terms involving 1θ and 3θ. These terms are the same for both faces. Hence, the signal exhibits three maxima and three minima. Similarly, for surface polarizations, the non-vanishing terms will be the terms involving 2θ and the offset for the *p*-polarized component, which are again the same for both faces. Here, since only a 2θ azimuthal angle is involved, the signal exhibits two maxima and two minima.

Due to the threefold rotational symmetry of the (111) face, the azimuthal angle dependence contains only $\sin 3\theta$ and $\cos 3\theta$ terms. Hence, the variation in the bulk and surface OR polarization with respect to azimuthal angle is a symmetrical three cycle dependence. These results are in line with the results for (111) in transmission geometry.

In the case of (111) crystal plane, the *s*-polarized components in the bulk polarization are the same while the *p*-polarized components are shifted for the two opposing faces. This result can be understood from Equations 4.3 to 4.6. By replacing *N* = 1, the terms involving azimuthal angle 1θ and 2θ dependence becomes zero, while terms involving 3θ dependence and offsets are nonzero. Since these 3θ terms have the same sign, the overall signal is similar for both faces, while the offsets observed for *p*-polarization have opposite sign for the two faces. Hence, the overall signal shifts downwards and upwards for the *A* and *B* faces, respectively.

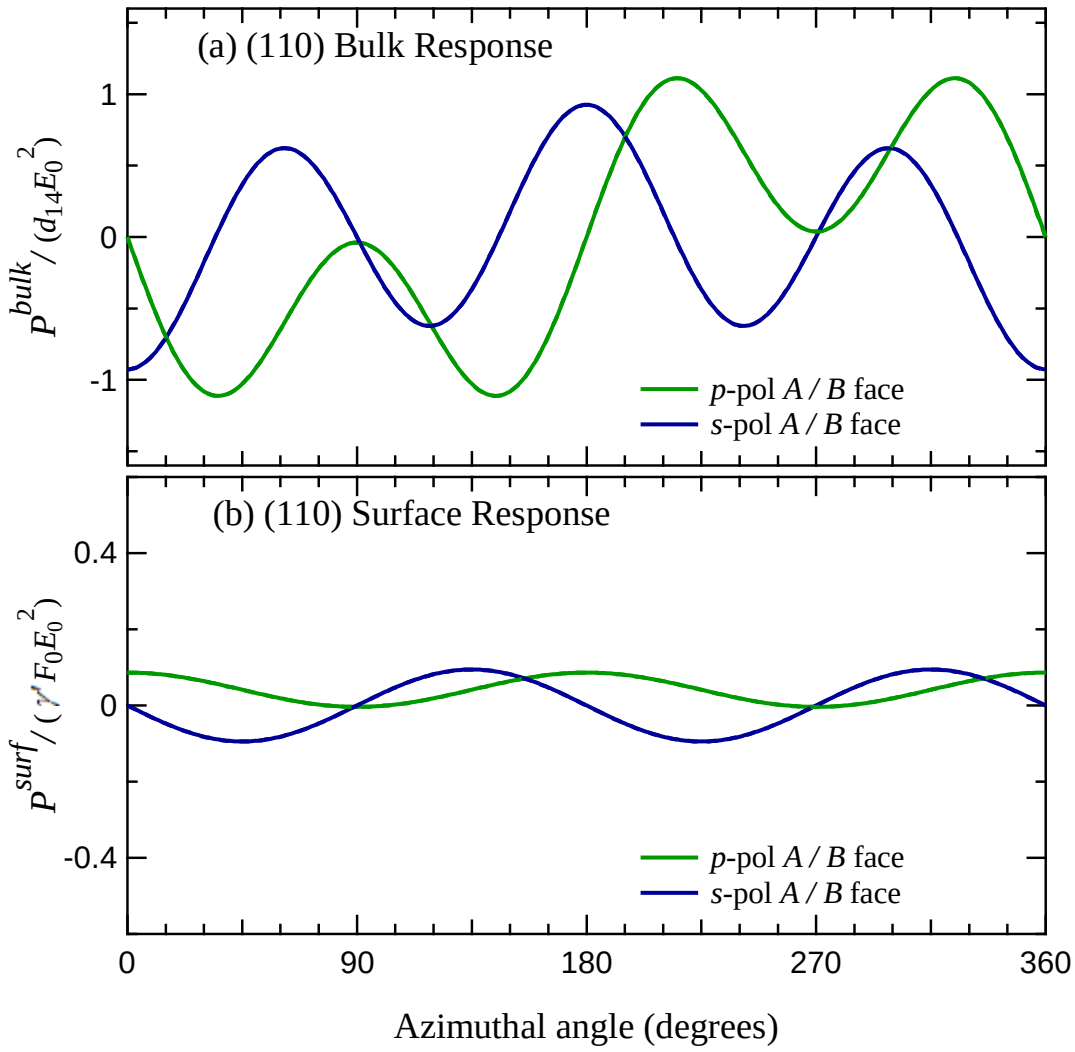

Figure 4.1 (a) Bulk and (b) surface OR polarization components for (110)*A* and *B* crystal planes. Bulk OR shows three maxima and three minima, while surface OR shows two maxima and two minima. For the (110) plane, the crystal symmetry of the *A* and *B* faces results in the same components for bulk and surface OR.

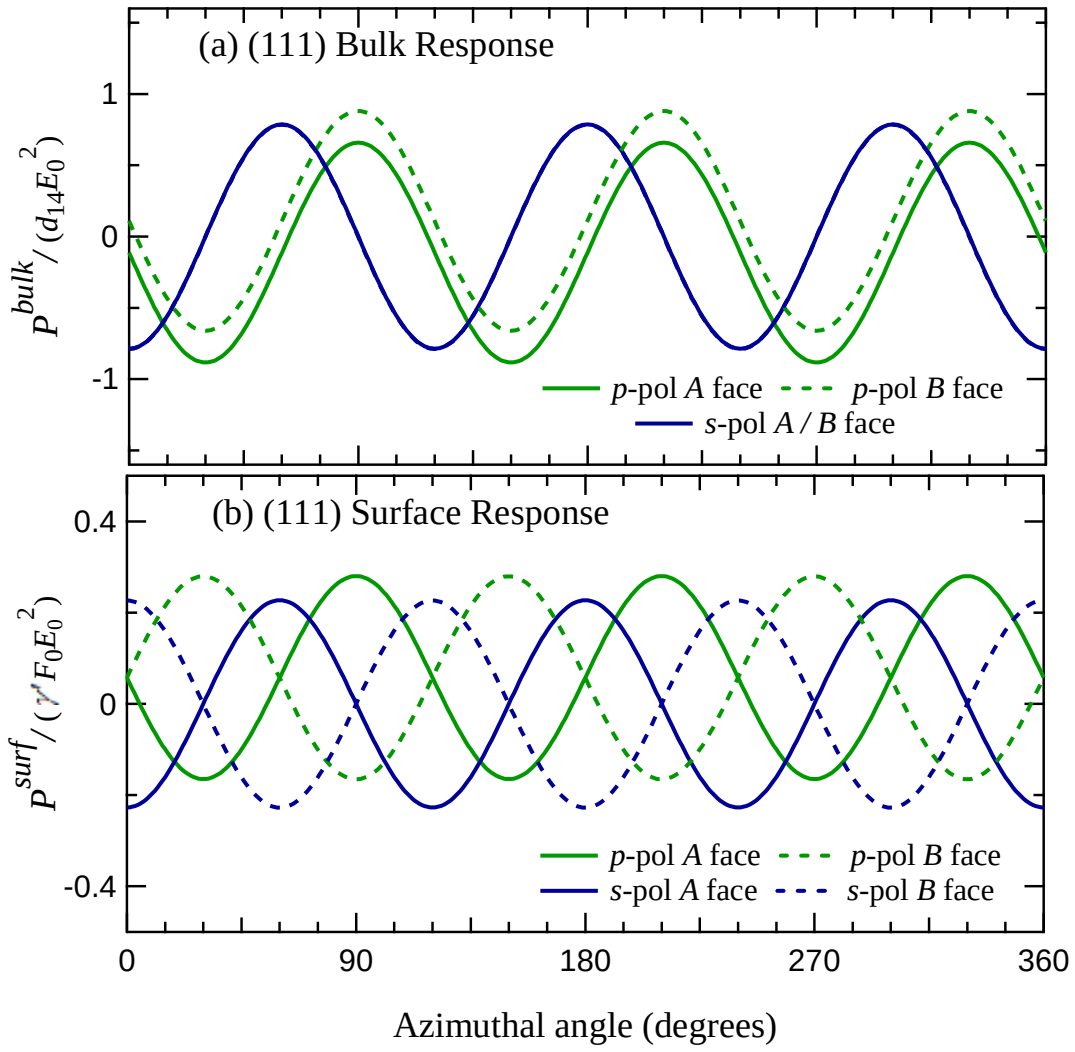

Figure 4.2 (a) Bulk and (b) surface OR polarization components for (111)*A* and *B* crystal planes. The *s*-polarized components for bulk OR are same for both faces, while *p*-polarized components for bulk OR are shifted along vertical axis. The surface polarization components for both *p* and *s* polarization are reversed between two faces.

In the case of surface OR components, the sign for the nonzero 3θ terms changes between the two faces with no 1θ and 2θ dependence. Hence, the signal is inverted for face *B* compared to face *A*. However, in this case the nonzero offset in *p*-polarization has equal sign for two opposite faces, which again shifts the data for the surface OR *p*-polarization vertically.

In the case of a (112) crystal face, all terms involving 1θ, 2θ, 3θ, and the offset for the *p*-polarized components are nonzero for both bulk and surface OR. The term in 2θ and the signal offset reverses between the two faces for the bulk effect. On the other hand, a reversal of the dominant 1θ and 3θ terms between the two faces is evident for the surface-field induced effect. Thus, the behavior of all *p* and *s* polarization curves for both bulk and surface OR are different for the two opposing *A* and *B* faces. Such features are observed for all high-index crystals.

The behavior for higher *N* values are same as for $N = 2$, with the bulk and surface OR depending on 1θ, 2θ, 3θ, for both polarizations, along with the offset for the horizontally polarized signal. The overall signal strength reduces with increasing *N* value which can be seen from the results for (112), (113), (114), and (115) crystal planes, consistent with the observation made from transmission geometry curves.

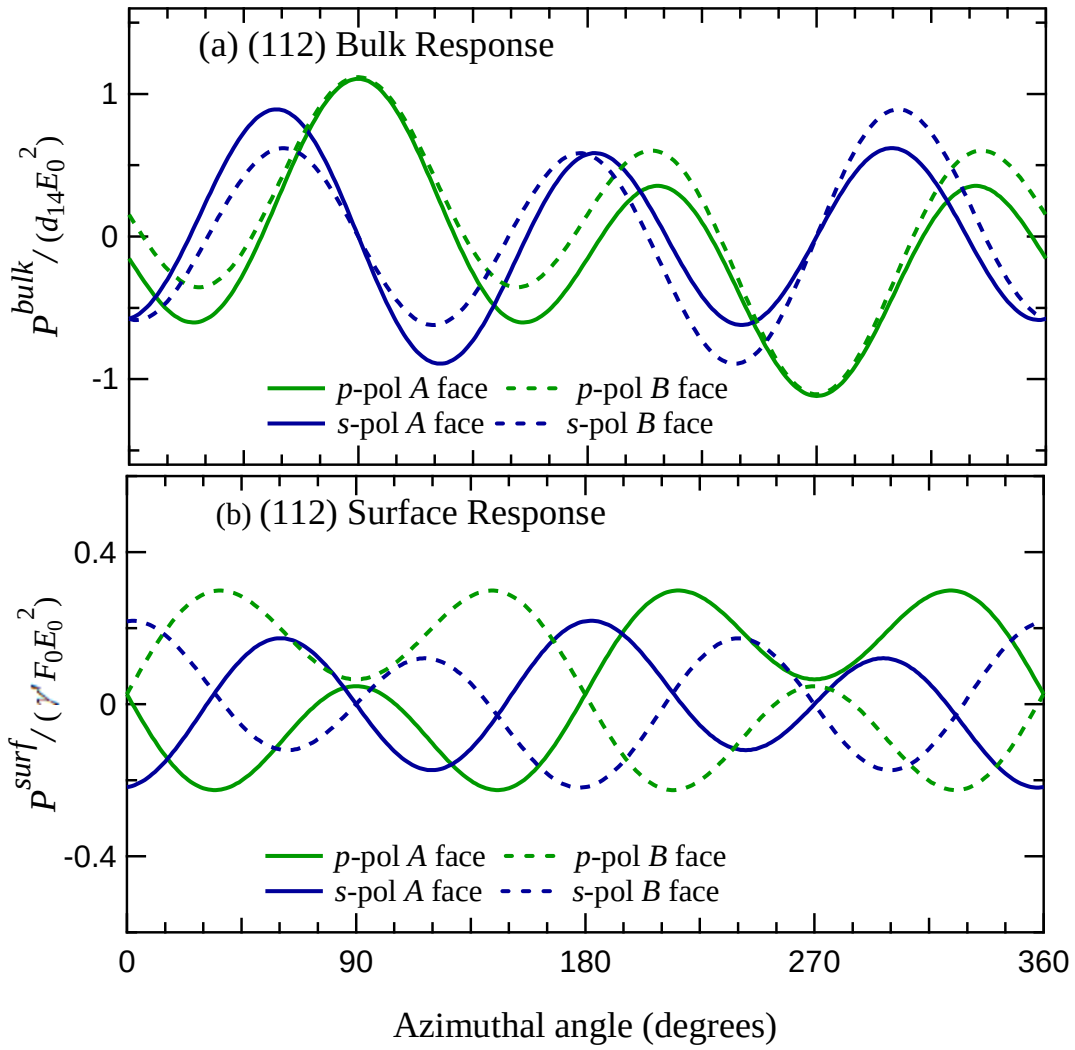

Figure 4.3 (a) Bulk and (b) surface OR polarization components for (112)*A* and *B* crystal planes.

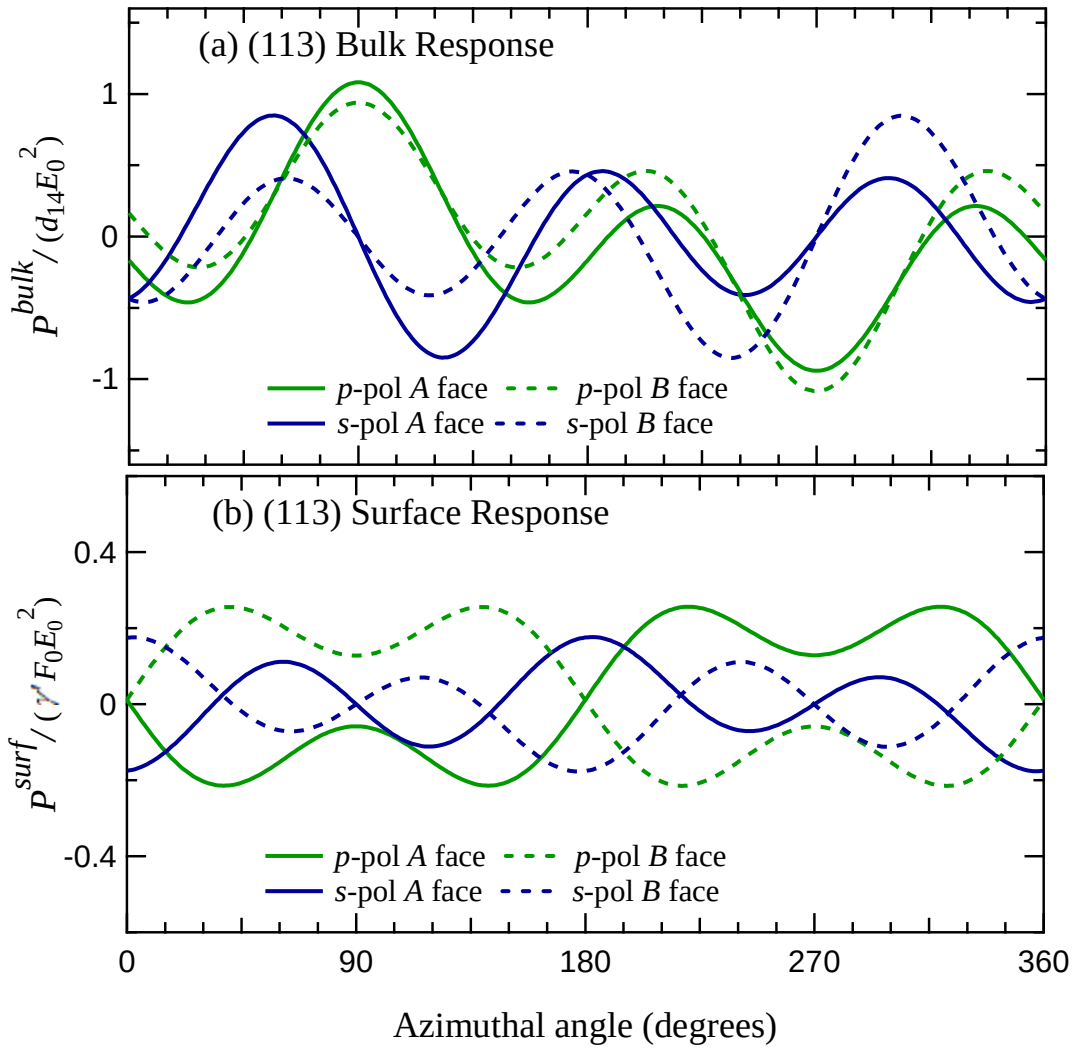

Figure 4.4 (a) Bulk and (b) surface OR polarization components for (113)*A* and *B* crystal planes.

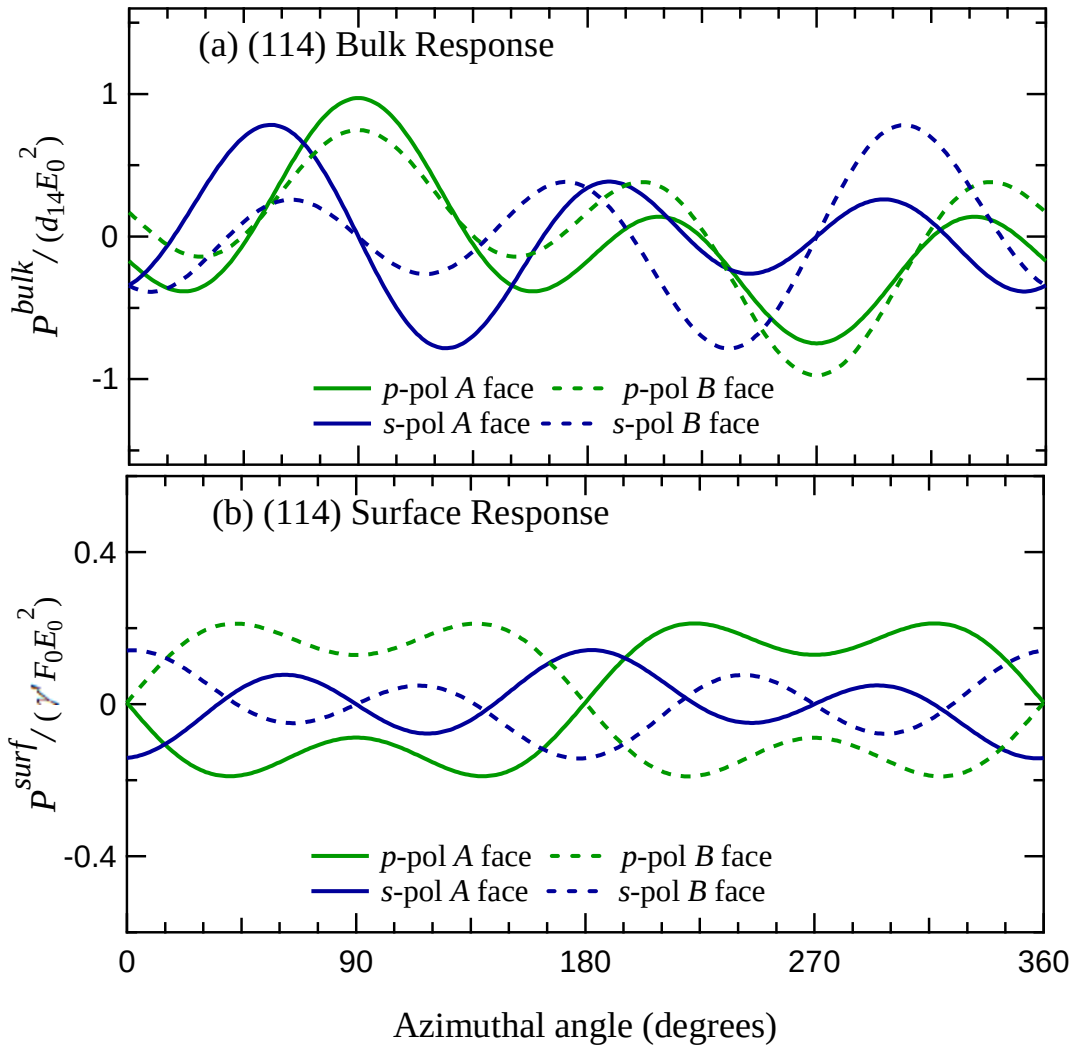

Figure 4.5 (a) Bulk and (b) surface OR polarization components for (114)*A* and *B* crystal planes.

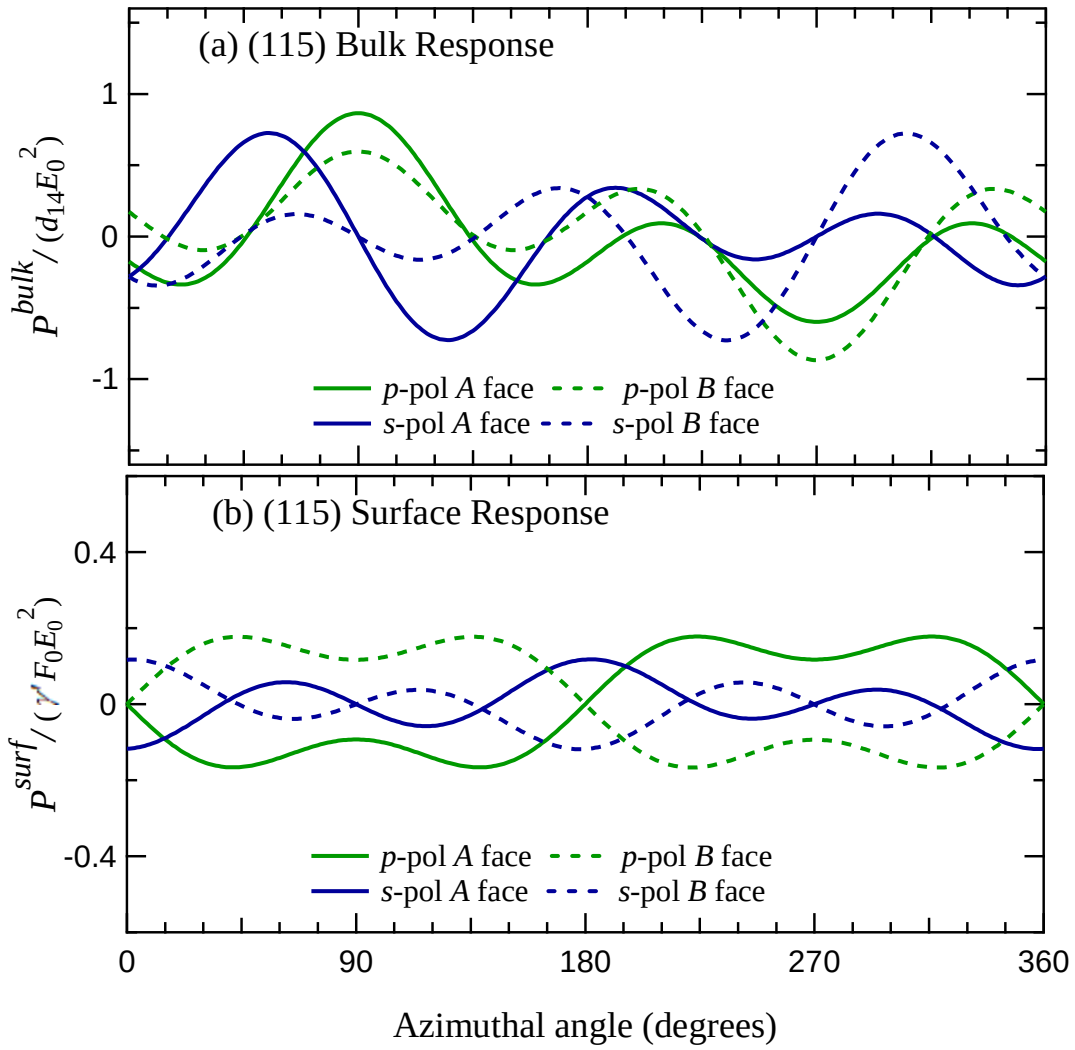

Figure 4.6 (a) Bulk and (b) surface OR polarization components for (115)*A* and *B* crystal planes.

4.4 Experimental results for GaAs (11*N*) crystal planes

GaAs (11*N*) planes for N = 0, 1, 2, 3, 4, and 5 were tested as THz emitters in the conventional TDS set up in quasireflection geometry with the angles of incidence and detection each of 45°. All GaAs samples used in this study and details about crystallographic directions and two opposite *A* and *B* faces were provided by Prof. Mohamed Henini from the University of Nottingham, United Kingdom.

The signals for both horizontally and vertically polarized components of the THz radiation were measured separately using a wire-grid polarizer for the two opposing *A* and *B* faces in (11*N*) planes. In the quasireflection geometry set up, the horizontal polarization corresponds to *p*-polarization and vertical polarization corresponds to *s*-polarization. The GaAs crystals are azimuthally rotated and the response of THz electric field was measured as the differential voltage across balanced photodiode pair, which is directly proportional to the THz field in the ZnTe detector.

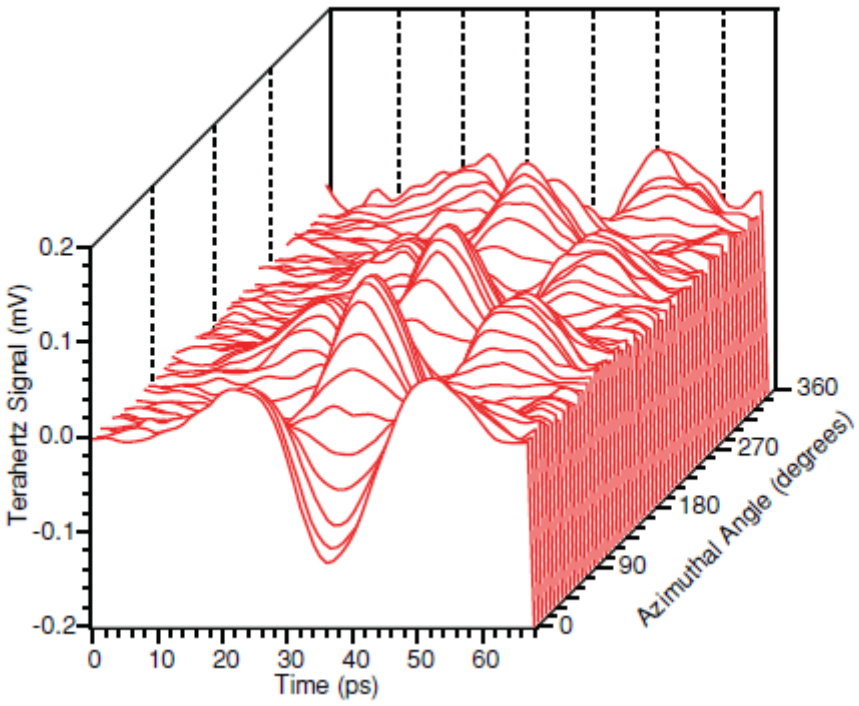

Figure 4.7 A waterfall plot of the *s*-polarized THz signal generated from (112)*A* GaAs with azimuthal rotation. Each line represents the THz temporal profile detected at particular azimuthal angle. The signal phase swaps between positive and negative THz

signal with three maxima and three minima indicating OR being the generation mechanism.

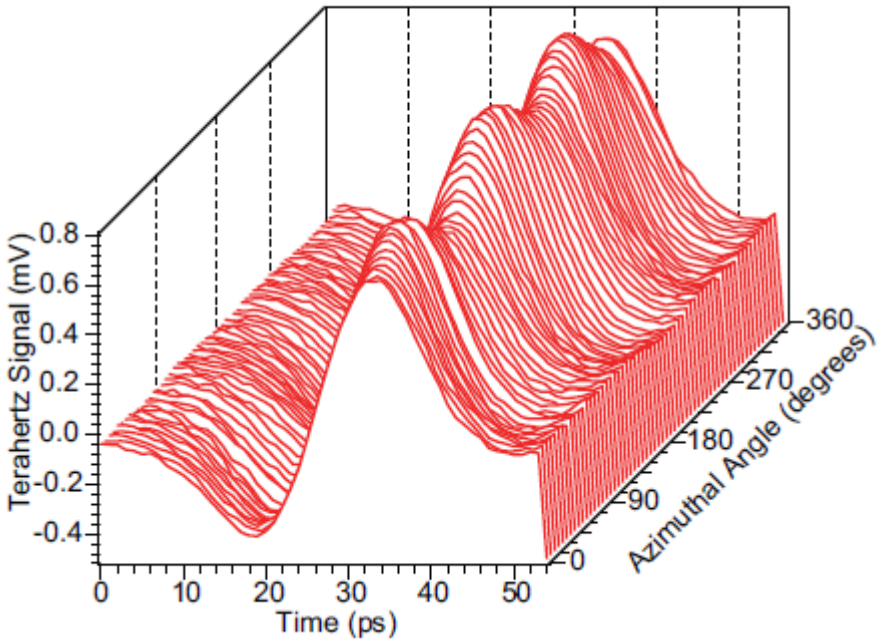

Figure 4.8 A waterfall plot of the *p*-polarized THz signal generated from (112)*A* GaAs with azimuthal rotation. Each line represents the THz temporal profile detected at particular azimuthal angle. For this case, the surface field effect is dominant which is invariant with the azimuthal rotation of the crystal and hence produces a large positive offset. A small variation in the signal with azimuthal variation indicates the contribution of a small optical rectification along with a comparatively large surface field effect.

Since the absorption length of observed samples is sufficiently short relative to the depletion width, the surface depletion field can be considered constant over the absorption length, and the effective surface field component $\gamma' F_0 / d_{14}$ may be determined by comparing the bulk and surface contribution to the signal.

In principle, for non-normal incidence of the excitation beam, both OR and TC effects may be observed. By using waterfall plots, the three dimensional representations for *s*-polarized and *p*-polarized THz time-domain signals measured with respect to different azimuthal angles for (112)*A* GaAs are shown in Figure 4.7 and Figure 4.8, respectively. It can be seen that *p*-polarized and *s*-polarized signals are distinct. The *s*-polarized signals look similar to the results obtained for transmission geometry for

(11*N*) faces, with alternating positive and negative signals being observed with azimuthal rotation of the crystal. However, the *p*-polarized signal is quite different. The *p*-polarized signal is stronger, with a large positive offset due to the contribution from the acceleration of charge carriers (transient current effect) which is invariant with angular rotation of the crystal. The comparatively small variation with angular rotation indicates the smaller contribution from optical rectification along with the large surface field effect. Since the dipole generated from surface field effect is in horizontal plane, the *s*-polarized signal does not have contribution from it and hence the signal for *s*-polarization shows greater temporal symmetry compared to the *p*-polarized signal.

Let us represent the azimuthal dependence data in the conventional two dimensional approach by showing the peak-to-peak signal observed at different azimuthal angles. The azimuthal orientation of the samples was not known beforehand, but it could be obtained from the best fit between the theoretical curves and experimental data, which in turn allow us to identify the crystallographic directions in the surface plane. Figure 4.9 represents the azimuthal angle dependence of the (110) *A* and *B* faces. Due to symmetry, the bulk structure of these two faces is equivalent hence both faces show same azimuthal behavior. Such an observation is also made from the theory curves shown in Figure 4.1. The experimental results show a large *p*-polarized offset, due to the presence of an azimuthally invariant transient current. The offset for *A* face, 1.61 ± 0.02 mV, is slightly stronger compared to 1.21 ± 0.02 mV for *B* face. The difference may have been caused by difference in the surface of the two sides of the sample. Although there was significant noise in the *p*-polarized (110)*B* azimuthal dependence data, the *s*-polarized response for both faces and the *p*-polarized signal for the (110)*A* face show a good fit to the theory with the fitting parameters of $Z = (170 \pm 30)$ mV and bulk and surface contribution ratio of $\gamma' F_0 = (1.5 \pm 0.8) d_{14}$.

By retaining the same fitting parameters as used for the (110) face, the experimental results for (111)*A* and *B* faces are compared with theory. As can be seen from Figure 4.10, the experimental data fits very well with the theory using these parameters. Since the (111) face possesses threefold rotational symmetry, the azimuthal dependence contains terms involving 3θ only, along with offsets for the *p*-polarized signal. Also, the overall signal strength is larger for the *A* face compared to the *B* face for both polarizations, due to bulk and surface polarizations being in phase and out of

phase for these two faces, respectively. The offsets due to the transient current effect are slightly smaller than for the (110) faces, at 1.15 ± 0.02 mV and 0.79 ± 0.02 mV for the *A* and *B* faces, respectively.

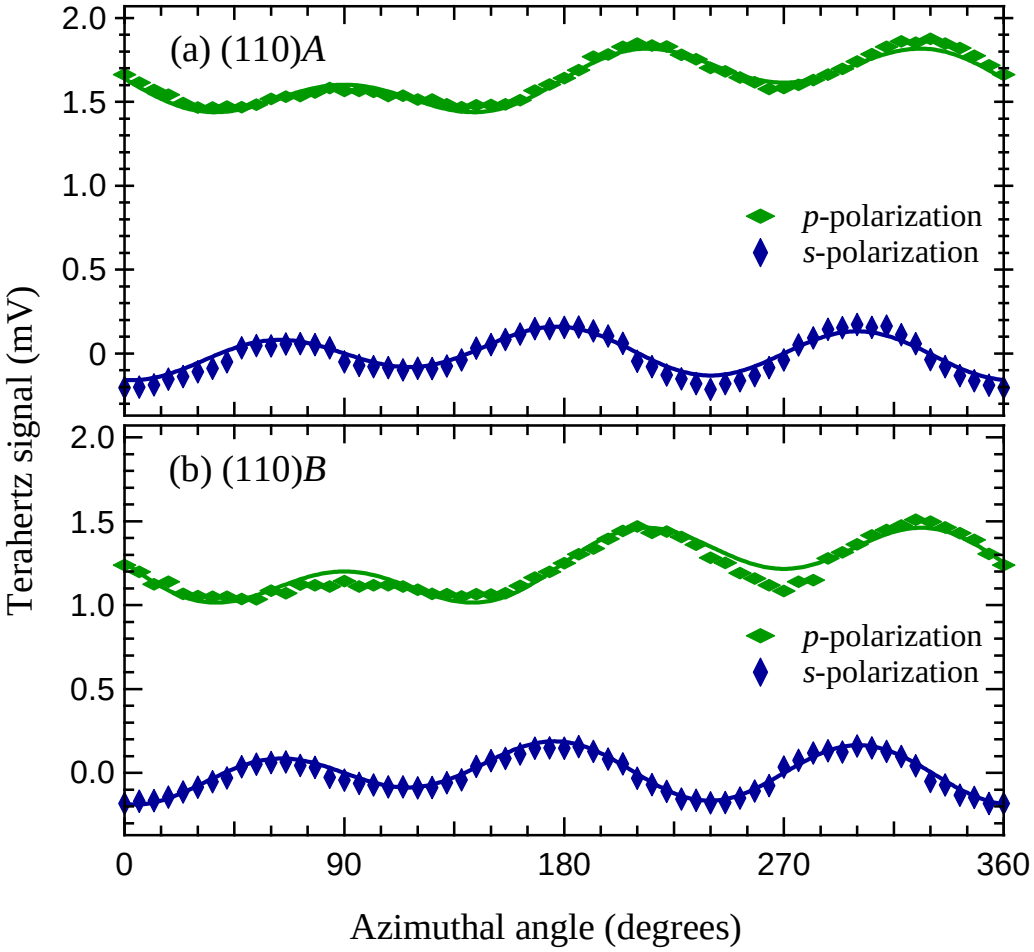

Figure 4.9 Measured terahertz signal amplitude in GaAs (a) (110)*A* and (b) (110)*B* as a function of the azimuthal angle of the sample. Diamonds represent experimental data by calculating the peak-to-peak voltage. The lines are theoretical fits using the parameters $Z = (170 \pm 30)$ mV and $\gamma' F_0 = (1.5 \pm 0.8) d_{14}$. An offset is observed for the *p*-polarized signal for both faces. Due to symmetry of the (110) plane, the two faces are theoretically equivalent.

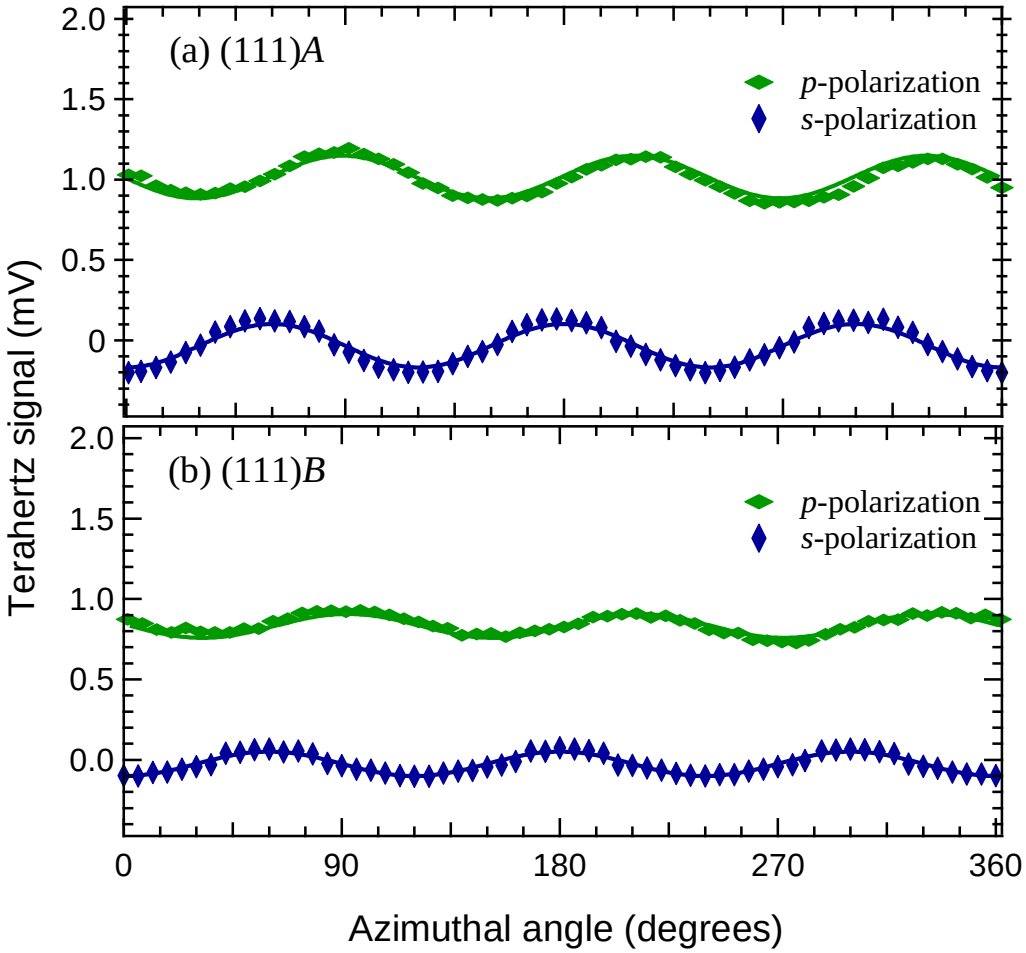

Figure 4.10 Measured terahertz signal amplitude in (a) (111)*A* and (b) (111)*B* GaAs as a function of the azimuthal angle of the sample. The symbols are experimental data and the lines are theory fits obtained by adding both bulk and surface polarization components, along with an offset due to the transient current effect in *p*-polarization.

Results for *s* and *p* polarized THz components for high-index (112), (113), (114), and (115) samples are shown in Figure 4.11 and 4.12, respectively. The theoretical fits are made using same fitting parameters used for the (110) and (111) samples.

The *s*-polarized THz components for the *A* face are stronger compared to the *B* face, as predicted by the theory. The experimental results for *p*-polarized signals also represent the general features predicted by the theory, with distinguished behavior between two opposing faces is quite evident. The transient current offsets for the (112) sample for both faces were comparable to the (110) sample, at 1.37 ± 0.02 mV and 1.67 ± 0.02 mV for the *A* and *B* faces, respectively. The offsets observed for higher-index samples (113), (114), and (115) were in the range of 0.57 to 0.68 mV.

The results obtained for surface-field-induced optical rectification and transient current (surface-field) components from these (11*N*) crystal planes indicate a surface field pointing outward from the surface, consistent with the surface depletion field for the n-type GaAs samples. The transient current components vary among different planes as well as for the two opposite face of same plane. Such behavior is likely to be due to small variations in the surface properties such as carrier concentration. The values of offsets for all (11*N*)*A* and *B* samples are listed in Table 4.1.

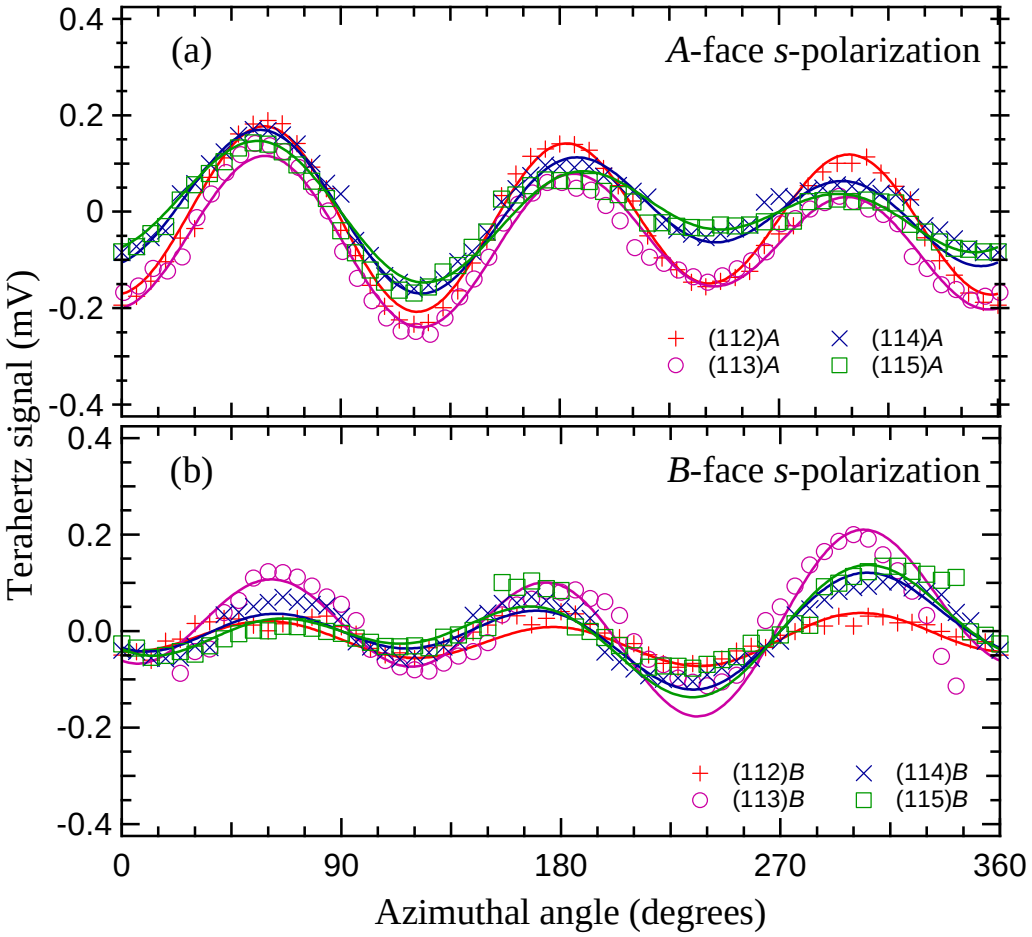

Figure 4.11 Measured *s*-polarized terahertz signal amplitude in (112), (113), (114) and (115) GaAs for both (a) *A* and (b) *B* faces as a function of azimuthal angle. The experimental results (shown with marks) compared with theoretical results (shown with lines) for combined effect of bulk and surface OR.

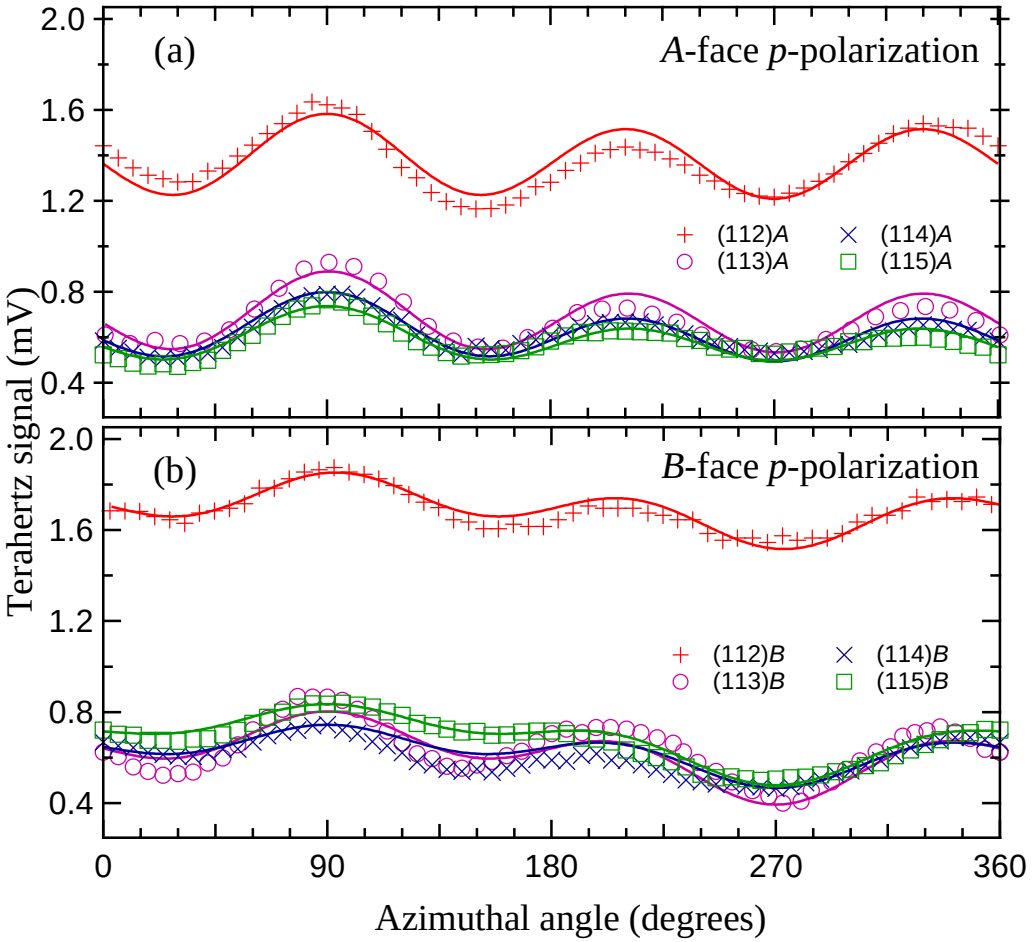

Figure 4.12 Measured *p*-polarized terahertz signal amplitude in (112), (113), (114) and (115) GaAs for both (a) *A* and (b) *B* faces as a function of azimuthal angle. The experimental results (shown with marks) compared with theoretical results (shown with lines) for combined effect of bulk and surface OR, along with offsets due to the presence of transient current effect.

Table 4.1 The *p*-polarized THz signal offsets observed for (11*N*) *A* and *B* faces. The offset is the property of the transient current mechanism involved in THz generation from these faces. The values correspond to the peak-to-peak voltage measured at the photodiode pair.

Surface plane	*A* offset (mV)	*B* offset (mV)
(110)	1.61 ± 0.02	1.21 ± 0.02
(111)	1.15 ± 0.02	0.79 ± 0.02
(112)	1.37 ± 0.02	1.67 ± 0.02
(113)	0.68 ± 0.02	0.57 ± 0.02
(114)	0.62 ± 0.02	0.60 ± 0.02
(115)	0.59 ± 0.02	0.67 ± 0.02

Both the surface-field-induced optical rectification and the surface-field effect are the property of the surface-depletion field present at the semiconductor surface; hence a correlation between these two effects is expected. However, due to uncertainties in the surface-field-induced components, such a correlation could not be conclusively identified.

Part of the uncertainty in finding a correlation arises from the difficulty of separating the optical rectification and transient current components observed together for *p*-polarized THz signals. The total peak-to-peak signal may not correspond to the sum of the peak-to-peak signal for optical rectification and transient current. The effect of comparatively higher noise level present in the system also has a profound effect on the results. Further, it is also possible that the experimental results have been guided by an additional unidentified azimuthally variable mechanism. Such discrepancy of results has been reported previously for (100) InP samples[138].

4.5 Conclusion

In this chapter, the optical rectification components for (11*N*) GaAs crystal planes for quasireflection geometry have been presented. The experimental results for GaAs (11*N*) *A* and *B* planes with $N = 0$ to 5 in this geometry have been presented and compared with the theory.

The results for *A* and *B* faces are quite different for all measured samples, except for (110) due to crystal symmetry along this direction. The general trend observed from the results suggests presence of bulk optical rectification, surface-field-induced optical rectification as well as transient current effect evident from angular dependence of the THz signal along with a large offset observed for the *p*-polarized THz field components. Information about the relative contribution from surface OR and TC effects has been obtained. The surface field for GaAs (11*N*) samples in terms of bulk nonlinear susceptibility coefficient d_{14} and non-linear optical constant γ' has been deduced to be $F_0 = (1.5 \pm 0.8) d_{14} / \gamma'$, which is, within experimental error, consistent with the results obtained from transmission geometry measurements. Thus optical rectification may be used in the analysis of semiconductor surface properties in quasireflection geometry as well as transmission geometry.

Chapter 5

5 Transient Current Effect and (100) InAs Emitter

5.1 (100) InAs: TC and OR contribution

As discussed in chapter 1, the emission of THz radiation from semiconductor surfaces may be due to ultra-fast screening of the depletion field by photoexcited charge carriers (surface-field effect) or due to different diffusion rates of electrons and holes (photo-Dember effect).

InAs has been found to have the highest THz emission efficiency among all unbiased terahertz emitters under similar experimental conditions[48,70]. Many works have been presented for InAs as a THz emitter for different crystal planes such as (100)[54,139], (110), and (111)[54,68]. It has been observed that InAs is capable of generating THz radiation through both optical rectification (OR) and transient current (TC) mechanisms with the latter being the principal mechanism. The surface-field effects may be less pronounced for InAs due to its small bandgap. The THz fields generated in n and p doped InAs samples are not flipped[54], indicating the photo-Dember effect is the responsible mechanism for most of the radiation from this semiconductor. In addition to the OR and TC effects, the effect of coherent phonons and plasma oscillations may also give rise to THz generation[22,140]. It has been demonstrated that the emitted THz radiation may be produced by cold plasma oscillations activated by the photo-Dember effect[130] or by coupled cyclotron-plasma charge oscillations[141] or by coupled plasmon-phonon modes[142].

In general, the THz electric field due to combined effect of TC and OR mechanisms can be represented as[143]

$$E^{\mathrm{THz}} \propto \int_0^{\infty} \left(\frac{\partial J}{\partial t} + \frac{\partial^2 P}{\partial t^2} \right) d\mathrm{x}, \qquad 5.1$$

where J and P represent transient currents and nonlinear polarization components in the direction of THz wave polarization, respectively and x is the direction of the surface normal pointing into the emitter crystal.

For the (100) crystal plane, the bulk and surface polarization components in terms of azimuthal angle θ can be calculated using the general theory of optical rectification presented in chapter 3. In this case most of the G_{ij} and V_{ij} components in Equations 3.24 and 3.25 will be zero. Details about these components can be found in

Appendix D. Further, the two opposite faces of (100) are the same due to crystal symmetry. Hence, by considering the results for the *A* face (i.e. the direction $\hat{\mathbf{x}}'''$ lies along surface normal or along the (100) crystallographic direction), the bulk OR components can be written as

$$\begin{bmatrix} P_p^{\text{bulk}} \\ P_s^{\text{bulk}} \end{bmatrix} = d_{14} E_0^2 \begin{bmatrix} (\cos^2\phi_{\text{NIR}} \sin\phi_{\text{THz}} + 2\cos\phi_{\text{NIR}} \sin\phi_{\text{NIR}} \cos\phi_{\text{THz}}) \sin 2\theta \\ 2\cos\phi_{\text{NIR}} \sin\phi_{\text{NIR}} \cos 2\theta \end{bmatrix}. \qquad 5.2$$

Thus, bulk OR components exhibit 2θ dependence with respect to azimuthal rotation of the crystal.

On the other hand, the γ' terms in the surface OR polarization components will be

$$\begin{bmatrix} P_p^{\text{surf}} \\ P_s^{\text{surf}} \end{bmatrix} = \gamma' F_0 E_0^2 \begin{bmatrix} \sin^2\phi_{\text{NIR}} \sin\phi_{\text{THz}} \\ 0 \end{bmatrix}, \qquad 5.3$$

which shows the surface OR components are invariant with respect to azimuthal rotation.

Further, the above equations suggests no contribution from bulk or surface OR components for (100) crystal planes in transmission geometry ($\phi_{\text{NIR}} = \phi_{\text{THz}} = 0$), agreeing well with the observations made in previous works.

The azimuthal angle dependence for p-type Zn-doped InAs (100) crystal emitter (MTI corporation, USA) in quasireflection set up is presented in Figure 5.1, along with the theory fit using bulk OR obtained from Equation 5.2. As expected, two cycle azimuthal dependence due to bulk OR along with an offset due to surface OR and TC effects is observed. The results obtained here are consistent with the previously published works[46,54].

A large offset of 13.3 mV magnitude was observed for the horizontally-polarized components on azimuthal rotation. The ratio between TC + surface OR and bulk OR contributions can be estimated to be 90:10, agreeing well with previous works, where the effective contribution from OR was obtained as 6% of the total signal[54].

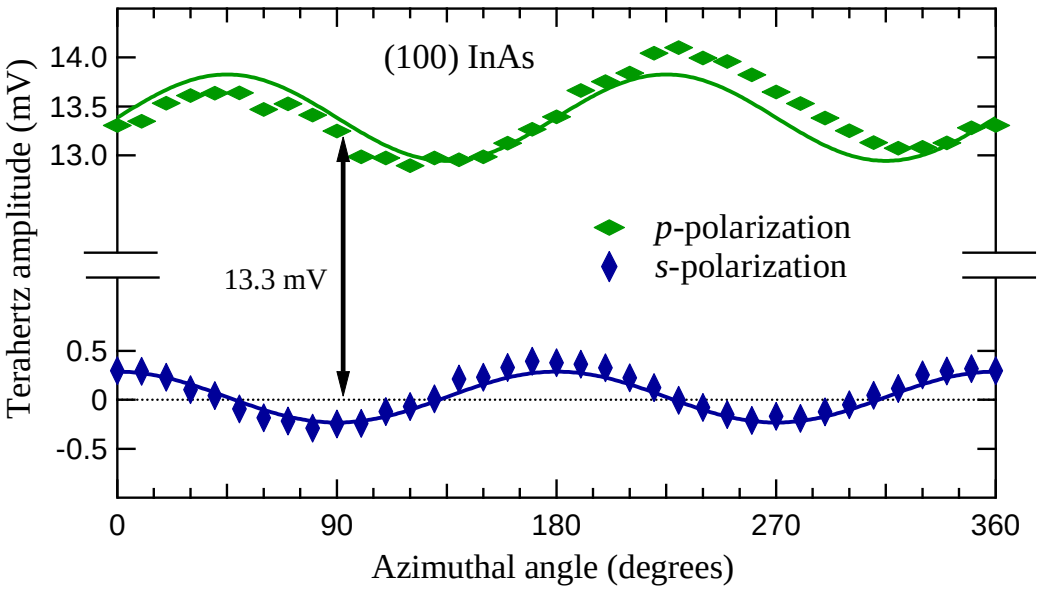

Figure 5.1 Measured THz field amplitude in (100) InAs as a function of the azimuthal angle of the sample for (a) horizontal - *p* polarization and (b) vertical - *s* polarization. The diamonds are the experimental results and lines are theory fit with bulk OR effect along with an offset. A large offset of 13.3 mV magnitude is observed which can be attributed to surface OR and transient current effects.

5.2 Effect of in-plane magnetic field for TC emitters

5.2.1 Introduction

Many groups have investigated the effect of an external magnetic field on the generated THz from different semiconductors. It has been observed that the THz emission is enhanced many fold by the application of an external magnetic field for transient current emitters. Various studies have been presented of the effect of magnetic field on InAs and GaAs semiconductors[18,120,141,144-151]. Few works have been presented for other semiconductors such as InP, GaAs, InSb[147,149,152]. Work as early as in 1993 by X. –C. Zhang *et al.*[153] of the effect of magnetic field on THz emission from InAs has been reported. Initially it was thought that the magnetic field enhanced the generated THz by accelerating charge carriers into the sample, which improves overall THz emission efficiency. However, later it has been confirmed that it is actually the rotation of the dipole due to current flow towards the surface plane that causes the enhancement in THz radiation efficiency, which would have otherwise flowed perpendicular to the

surface[149,152]. The main focus of the previous work was the effect of increasing magnetic field strength[120,124,141,145,150,151] and increasing incident optical fluence with the magnetic field applied in particular direction. Different theoretical models such as the drift-diffusion equation[70] and Drude-Lorentz model[152] have been presented in order to understand the physical origin of the phenomenon. Also Monte Carlo simulation[154,155] have been used in order to differentiate the magnetic field enhancement in a GaAs SF emitter and InAs PD emitter[156].

To date the effect of the magnetic field has been observed for the magnetic field in a particular direction (**+B**) and opposite direction to that (**-B**)[153]. The acceleration components under the influence of the Lorentz force have been measured to determine the generated THz field. The response of different levels of excitation fluence of incident radiation and varying magnetic field strength have been investigated. The generated THz signal increased linearly up to certain magnetic field strength. Results for different magnet positions and geometries indicate an optimum THz radiation emission for magnetic field direction parallel to the semiconductor surface and the angle of incidence of the excitation beam at the Brewster angle[146]. However, no work has included the rotation of the magnetic field, except for (100) InP[138]. In this study, the effect of rotation of B-field with respect to surface normal of the emitter crystal at low excitation level using Drude-Lorentz model is presented.

5.2.2 Theory for magnetic field effect

The contribution from magnetic field on the nonlinear optical susceptibility is expected to be very small. Hence, the OR components can be considered to be invariant with application of magnetic field. In order to avoid any interaction from OR mechanism, let us consider that this effect does not play any role in THz generation. Figure 5.2(a) represents the general THz emission representation in non-normal incidence in terms of $(\hat{\mathbf{x}}, \hat{\mathbf{y}}, \hat{\mathbf{z}})$ coordinate system. The horizontally-polarized NIR excitation beam is incident at the emitter surface at an angle ϕ' with respect to the surface normal in the $\hat{\mathbf{x}}$ direction. Figure 5.2(b) shows the magnet position on the back of the emitter holder.

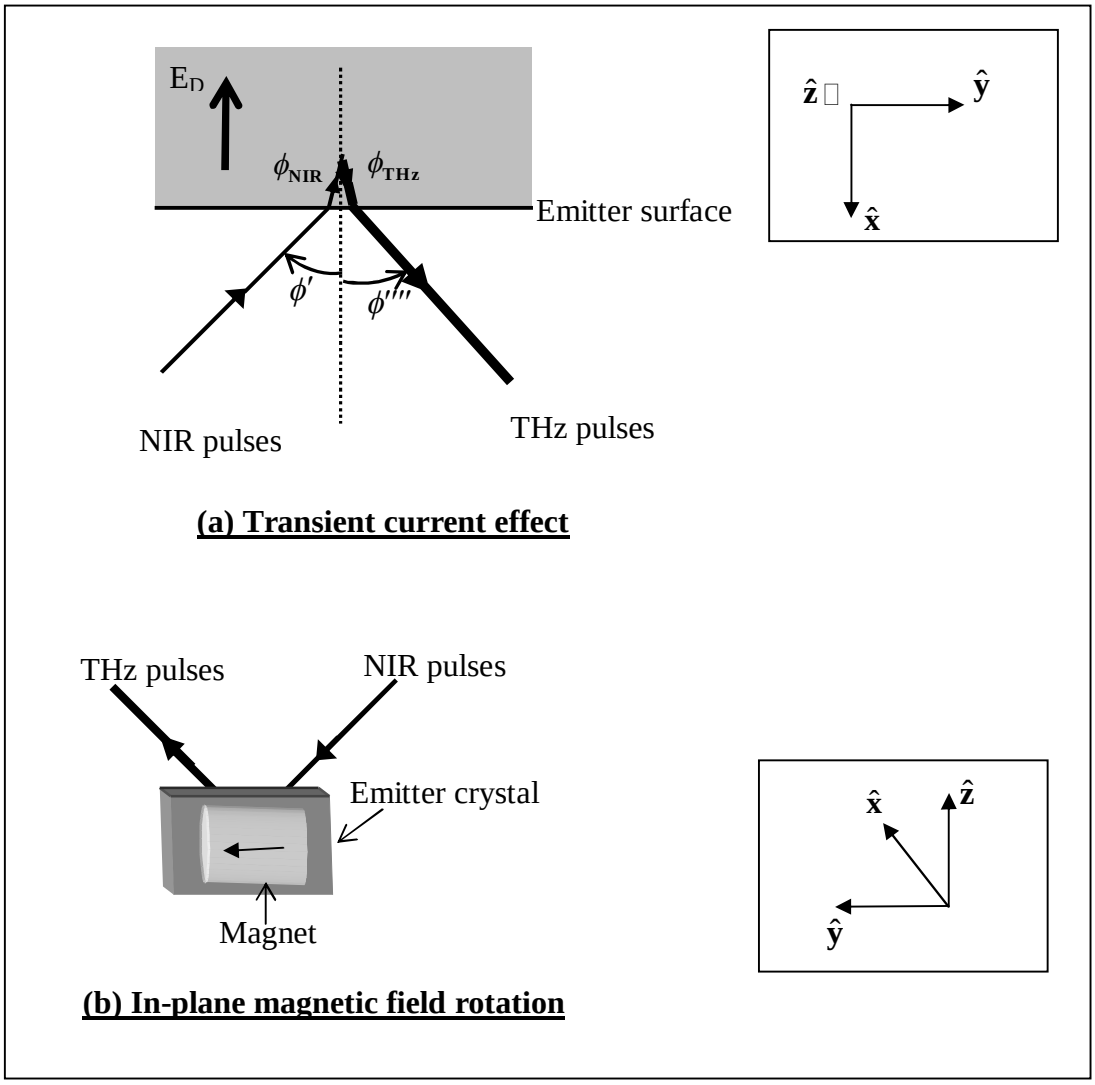

Figure 5.2 (a) General representation of the transient current effect. ϕ' and ϕ'''' are the angles of incidence of the NIR beam onto the emitter and angle of reflection of the THz beam out of the emitter, respectively. The quasireflection geometry is used. E_D represents the surface depletion field in the direction of surface normal and points away from the surface. The inset shows the $(\hat{\mathbf{x}}, \hat{\mathbf{y}}, \hat{\mathbf{z}})$ coordinate system to describe the emission phenomenon. (b) The direction of the in-plane magnetic field. A permanent magnet ($B_0 = 0.15\text{T}$) is rotated at an angle θ with respect to the surface normal. The arrowhead on the magnet represents the north pole of the magnet.

In the case of the transient current mechanism, the incident radiation causes electron-hole pairs to be generated in the emitter crystal. The generated dipole causes the THz transient due to diffusion or drift of these photocarriers. In this case, the plasma oscillations and damping effect[157] also need to be taken into account.

The surface-depletion field is considered to be away from the surface in the $-\hat{\mathbf{x}}$ direction. In the case of photo-Dember effect, THz generation does not rely on intrinsic surface field. However, for simplicity we assume an effective field is present (in the $-\hat{\mathbf{x}}$ direction) which can be thought of as being responsible for photo-Dember emission. Such an assumption does not affect the overall results obtained for various transient current emitters measured for change in THz emission with magnet rotation.

The in-plane magnetic field is provided by a permanent magnet attached to the back of the emitter holder. The magnet is rotated counterclockwise around the excitation beam direction starting from the incident-reflection plane.

For the angle of incidence of the incident excitation beam ϕ'**,** and corresponding internal refracted angle ϕ_{NIR}, the polarization components for the incident NIR beam can be written in terms of $(\hat{\mathbf{x}}, \hat{\mathbf{y}}, \hat{\mathbf{z}})$ coordinate system as

$$\begin{bmatrix} E_x \\ E_y \\ E_z \end{bmatrix} = \begin{bmatrix} \sin\phi_{\mathrm{NIR}} \cos\Phi \\ \cos\phi_{\mathrm{NIR}} \cos\Phi \\ \sin\Phi \end{bmatrix} E_0 , \qquad 5.4$$

where Φ is the polarization angle of the excitation beam, which is taken to be zero.

The THz electric field components for horizontal and vertical polarization with respect to the incident linear excitation polarization can be written as

$$\begin{bmatrix} E_p^{\mathrm{THz}} \\ E_s^{\mathrm{THz}} \end{bmatrix} = \begin{bmatrix} \sin\phi_{\mathrm{THz}} E_x^{\mathrm{THz}} + \cos\phi_{\mathrm{THz}} E_y^{\mathrm{THz}} \\ E_z^{\mathrm{THz}} \end{bmatrix}, \qquad 5.5$$

where ϕ_{THz} is the angle of refraction in the emitter crystal and is related to the angle of reflection ϕ'''' by

$$n_{\mathrm{air,THz}} \sin\phi'''' = n_{\mathrm{crystal,THz}} \sin\phi_{THz} ; \qquad 5.6$$

$n_{\mathrm{air,THz}}$ and $n_{\mathrm{crystal,THz}}$ are refractive indices at the THz photon frequency of the ambient atmosphere and of the emitter crystal, respectively.

Here we consider the Drude-Lorentz model to describe the effect of the magnetic field. The acceleration components, considering the Lorentz force, plasma oscillations and scattering effect, can be written as

$$\frac{d\mathbf{v}}{dt}+\gamma\mathbf{v}+\omega_p^2\mathbf{r}=\frac{e}{m}\left[\mathbf{E}+(\mathbf{v}\times\mathbf{B})\right], \tag{5.7}$$

where γ is the scattering rate of generated charge carriers and ω_p is the plasma frequency.

The surface depletion field is

$$\mathbf{E}=-E_x\hat{\mathbf{x}} \tag{5.8}$$

and the in-plane magnetic is

$$\mathbf{B}=0\hat{\mathbf{x}}+B_0\cos\theta\hat{\mathbf{y}}+B_0\sin\theta\hat{\mathbf{z}}\ , \tag{5.9}$$

with $B_0=0.15$ T and θ is the angle of magnet rotation in the surface plane.

From the above equations, the acceleration components can be written as

$$\frac{dv_x}{dt}=-\frac{eE_x}{m}e^{-\gamma t}\cos\omega_p t\cos\omega_c t\ , \tag{5.10}$$

$$\frac{dv_y}{dt}=\frac{eE_x}{m}e^{-\gamma t}\cos\omega_p t\sin\omega_c t\sin\theta\ , \tag{5.11}$$

$$\frac{dv_z}{dt}=-\frac{eE_x}{m}e^{-\gamma t}\cos\omega_p t\sin\omega_c t\cos\theta\ , \tag{5.12}$$

where $\omega_c=\dfrac{eB_0}{m}$ = cyclotron frequency.

For the geometry presented in Figure 5.2, the Fresnel transmission components for horizontal (*p*) and vertical (*s*) polarization can be written as[12]

$$t_{\square}=\frac{2n_{crys}\cos\phi_{THz}}{n_{crys}\cos\phi''''+\cos\phi_{THz}}\ \text{and}\ t_{\perp}=\frac{2n_{crys}\cos\phi_{THz}}{n_{crys}\cos\phi_{THz}+\cos\phi''''}\ , \tag{5.13}$$

where we have considered $n_{air,THz}=1$ and $n_{crytal,THZ}=n_{crys}$.

The THz field components for *p* and *s* polarized components can be written as

$$\begin{bmatrix}E_p^{\mathrm{THz}}\\E_s^{\mathrm{THz}}\end{bmatrix}\propto\begin{bmatrix}\dfrac{2n_{crys}\cos\phi_{\mathrm{THz}}}{n_{crys}\cos\phi''''+\cos\phi_{\mathrm{THz}}}\left(\sin\phi_{\mathrm{THz}}\dfrac{\partial J_x}{\partial t}+\cos\phi_{\mathrm{THz}}\dfrac{\partial J_y}{\partial t}\right)\\ \dfrac{2n_{crys}\cos\phi_{\mathrm{THz}}}{n_{crys}\cos\phi_{\mathrm{THz}}+\cos\phi''''}\dfrac{\partial J_z}{\partial t}\end{bmatrix}. \tag{5.14}$$

Further, in the simplified approximation with laser-pulse duration << carrier scattering << carrier lifetime[152],

$$\frac{\partial \mathbf{J}(t)}{\partial t} \propto \mathbf{a}(t)\,. \qquad 5.15$$

Hence,

$$\begin{bmatrix} E_p^{\mathrm{THz}} \\ E_s^{\mathrm{THz}} \end{bmatrix} \propto \begin{bmatrix} \dfrac{2n_{crys}\cos\phi_{\mathrm{THz}}}{n_{crys}\cos\phi'''' + \cos\phi_{\mathrm{THz}}}(-\sin\phi_{\mathrm{THz}}\cos\omega_c t + \cos\phi_{\mathrm{THz}}\sin\omega_c t\sin\theta) \\ \dfrac{2n_{crys}\cos\phi_{\mathrm{THz}}}{n_{crys}\cos\phi_{\mathrm{THz}} + \cos\phi''''}(-\sin\omega_c t\cos\theta) \end{bmatrix} \frac{eE_x}{m} e^{-\gamma t}\cos\omega_p t. \qquad 5.16$$

Equation 5.16 represents the THz polarization components in terms of the angle of internal refraction ϕ_{THz}, cyclotron frequency ω_c, magnet angle θ, surface field E_x, scattering rate γ, plasma frequency ω_p, along with other parameters such as distance from the emitter to detector and beam diameter, which are rolled into the proportionality constant.

InAs as the emitter

Let us consider a special case of InAs as the emitter. For quasireflection geometry, $\phi' = \phi'''' = 45^0$. Using $(n_{\mathrm{crys}})_{\mathrm{InAs}} = 3.821$, we find $(\phi_{\mathrm{THz}})_{\mathrm{InAs}} = 10.66^\circ$. Hence, the THz polarization components in terms of ω_c, γ, ω_p and the proportionality constant *A* will become

$$\begin{bmatrix} E_p^{\mathrm{THz}} \\ E_s^{\mathrm{THz}} \end{bmatrix} = A\begin{bmatrix} 0.3773\cos\omega_c t + 2.003\sin\omega_c t\sin\theta \\ -1.6831\sin\omega_c t\cos\theta \end{bmatrix} e^{-\gamma t}\cos\omega_p t\ . \qquad 5.17$$

Let us consider different magnetic field directions.

(a) We start with the situation when no magnetic field is applied. In this case, the THz polarization components can be described in terms of the scattering rate and plasma frequency as

$$\begin{bmatrix} E_p^{\mathrm{THz}} \\ E_s^{\mathrm{THz}} \end{bmatrix} = A\begin{bmatrix} 0.3773 \\ 0 \end{bmatrix} e^{-\gamma t}\cos\omega_p t\,. \qquad 5.18$$

Thus in the absence of an external magnetic field, the *s*-polarized THz component due to the TC effect will be zero. This is due to the fact that in the absence

of magnetic field the current will be in the surface normal direction ($\hat{\mathbf{x}}$ - axis) only, which causes a THz signal for *p*-polarization while no current flows in the $\hat{\mathbf{y}}$ direction and hence the *s*-polarized signal is zero.

(b) For magnet angle $\theta = 0^0$, $\mathbf{B} = B_0\hat{\mathbf{y}}$

In this situation, acceleration of the carriers can be given as

$$\mathbf{a}(t) = \frac{eE_x}{m} e^{-\gamma t} \cos\omega_p t(-\cos\omega_c t\hat{\mathbf{x}} - \sin\omega_c t\hat{\mathbf{z}}). \qquad 5.19$$

The equation for acceleration suggests that the dipole is bent away from the surface normal towards $\bar{\mathbf{x}}\,\bar{\mathbf{z}}$ - plane.

The THz field components will be

$$\begin{bmatrix} E_p^{\mathrm{THz}} \\ E_s^{\mathrm{THz}} \end{bmatrix} = A\begin{bmatrix} 0.3773\cos\omega_c t \\ -1.6831\sin\omega_c t \end{bmatrix} e^{-\gamma t}\cos\omega_p t\,. \qquad 5.20$$

Thus the magnetic field in the $\hat{\mathbf{y}}$ direction causes a very small change in the electric field of the *p*-polarization; however, the *s*-polarized THz component is introduced due to the current flow in $-\hat{\mathbf{z}}$ direction.

(c) For $\theta = 90^0$, $\mathbf{B} = B_0\hat{\mathbf{z}}$

In this situation, the acceleration of the carriers will be

$$\mathbf{a}(t) = \frac{eE_x}{m} e^{-\gamma t} \cos\omega_p t(-\cos\omega_c t\hat{\mathbf{x}} + \sin\omega_c t\hat{\mathbf{y}}). \qquad 5.21$$

Thus the dipole is bent towards the $\bar{\mathbf{x}}\,\mathbf{y}$ - plane.

The THz field components will be

$$\begin{bmatrix} E_p^{\mathrm{THz}} \\ E_s^{\mathrm{THz}} \end{bmatrix} = A\begin{bmatrix} 0.3773\cos\omega_c t + 2.003\sin\omega_c t \\ 0 \end{bmatrix} e^{-\gamma t}\cos\omega_p t\,. \qquad 5.22$$

The magnetic field in the $\hat{\mathbf{z}}$ direction causes an increase in the *p*-polarized THz signal while the *s*-polarized signal will be zero as no current is flowing in the $\hat{\mathbf{z}}$ direction.

(d) For $\theta = 180^0$, $\mathbf{B} = -B_0\hat{\mathbf{y}}$

In this situation acceleration of the carriers can be represented as

$$\mathbf{a}(t) = \frac{eE_x}{m} e^{-\gamma t} \cos\omega_p t(-\cos\omega_c t\hat{\mathbf{x}} + \sin\omega_c t\hat{\mathbf{z}}) . \qquad 5.23$$

Thus the dipole will be bent towards the $\bar{\mathbf{x}}\,\mathbf{z}$- plane in the opposite direction compared to $\theta = 0^o$ case.

For this magnet position, the THz field components will be

$$\begin{bmatrix} E_p^{\mathrm{THz}} \\ E_s^{\mathrm{THz}} \end{bmatrix} = A \begin{bmatrix} 0.3773\cos\omega_c t \\ 1.6831\sin\omega_c t \end{bmatrix} e^{-\gamma t} \cos\omega_p t . \qquad 5.24$$

Compared to the angle $\theta = 0^0$, the magnetic field in the $-\hat{\mathbf{y}}$ direction will have same *p*-polarized component however the *s*-polarized component will be reversed due to the current flow in the $\hat{\mathbf{z}}$ direction.

(e) For $\theta = 270^0$, $\mathbf{B} = -B_0\hat{\mathbf{z}}$

In this situation, the acceleration of the carriers will be

$$\mathbf{a}(t) = \frac{eE_x}{m} e^{-\gamma t} \cos\omega_p t(-\cos\omega_c t\hat{\mathbf{x}} - \sin\omega_c t\hat{\mathbf{y}}) . \qquad 5.25$$

The dipole is bent towards the $\bar{\mathbf{x}}\,\bar{\mathbf{y}}$ plane and the THz field components will be,

$$\begin{bmatrix} E_p^{\mathrm{THz}} \\ E_s^{\mathrm{THz}} \end{bmatrix} = A \begin{bmatrix} 0.3773\cos\omega_c t - 2.003\sin\omega_c t \\ 0 \end{bmatrix} e^{-\gamma t} \cos\omega_p t . \qquad 5.26$$

The magnetic field in the $-\hat{\mathbf{z}}$ direction causes the *p*-polarized THz signal to be reduced, while the *s*-polarized signal will be zero.

(f) For $\theta = 360^0$, $\mathbf{B} = B_0\hat{\mathbf{y}}$

In this situation, the magnet is back to its initial orientation and the acceleration and the THz components will be same as given in (b).

5.2.3 Experimental results and discussion

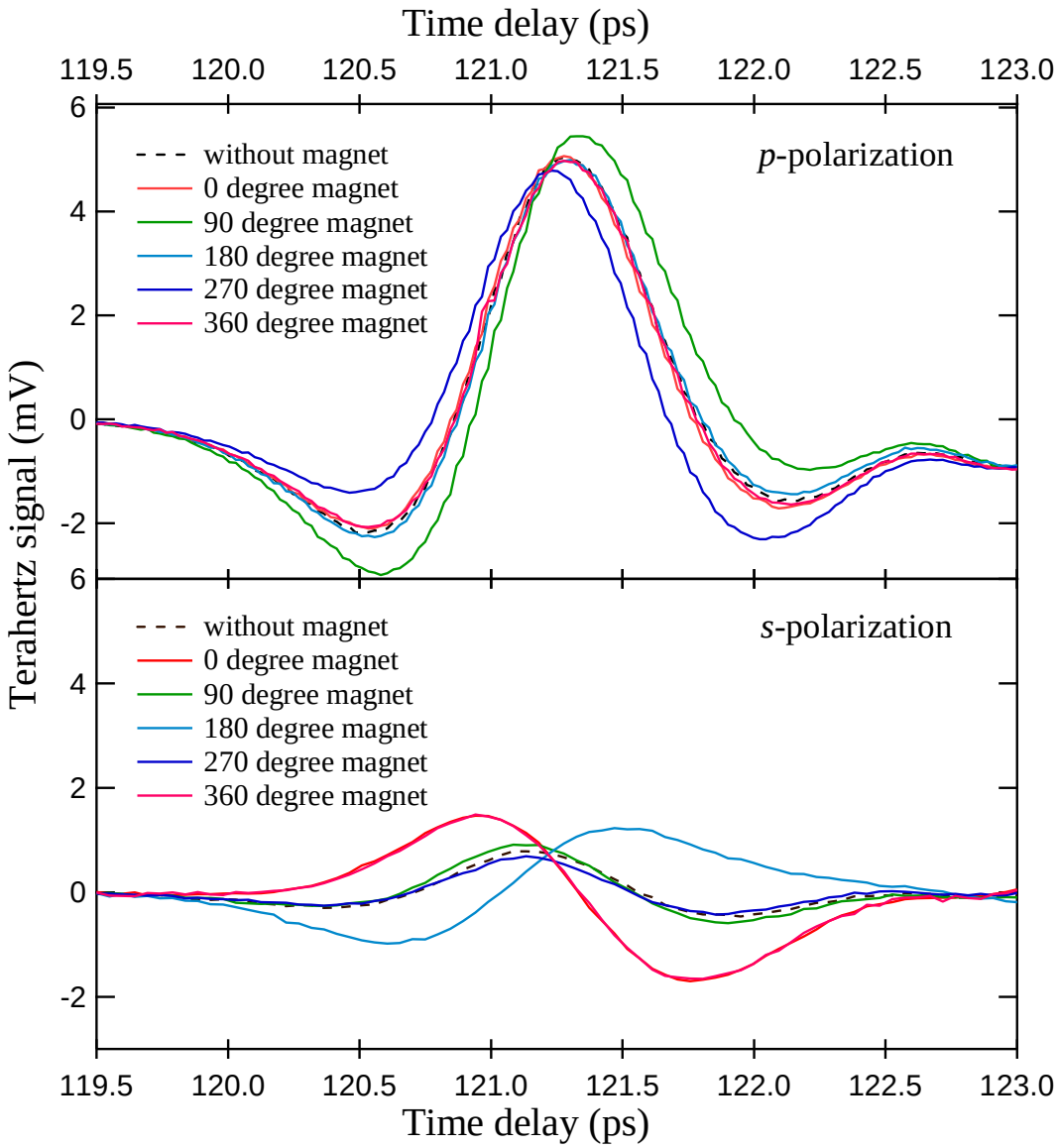

Figure 5.3 (100) InAs *p* and *s*-polarized THz components for various magnet positions. The *p*-polarized signal changes by a small amount in the signal strength. The peak for the signal with 90 degree magnet position appears later on a picosecond timescale with respect to signal without magnet, while the peak for the signal for 270 degree magnet position appears earlier on a picosecond timescale. The *s*-polarized signal is smaller in magnitude compared to the *p*-polarized signal. However, the change in the signal due to magnetic field is larger than for the *p*-polarization.

The above cases indicate a net dipole rotation in **y z** plane with rotation of magnetic field and corresponding increased and decreased THz output for both polarization components. These findings agree with the experimental results for (100) InAs measured in quasireflection set up. A wire-grid polarizer was used in order to separately measure the horizontal and vertical THz polarization components.

Figure 5.3 displays experimental results for *p* and *s*-polarized THz components for (100) InAs for all six cases discussed above. The peak-to-peak amplitude for *p*-polarized signal without the magnet is 7.2 mV, which is increased to 7.5 mV for the 90^o magnet position, while the signal at the 270^o magnet position is reduced to 7.0 mV. The signals for 0^o and 180^o magnet positions are almost the same as for the signal without the magnet. An interesting observation that can be made from these signals is that the peaks for 0^o magnet and 180^o magnet positions coincided with signal without magnet at 121.28 ps, while peaks for 90^o and 270^o occur at 121.35 ps and 121.23 ps, respectively.

The *s*-polarized components have lower signal strength compared to the *p*-polarized signal. However, the percentage change in the signal strength is larger. Figure 5.4 gives the three dimensional representation for *p* and *s* polarized components for 360^o rotation of the magnet. The magnet is rotated in the steps of 15^o and *p* and *s*-polarized THz signals are measured for each magnet position.

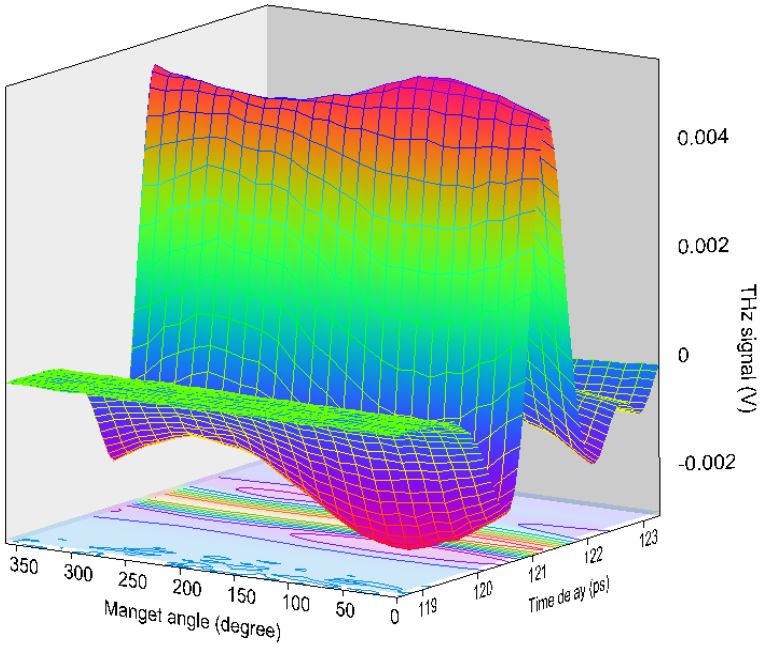

(a) *p*-polarization

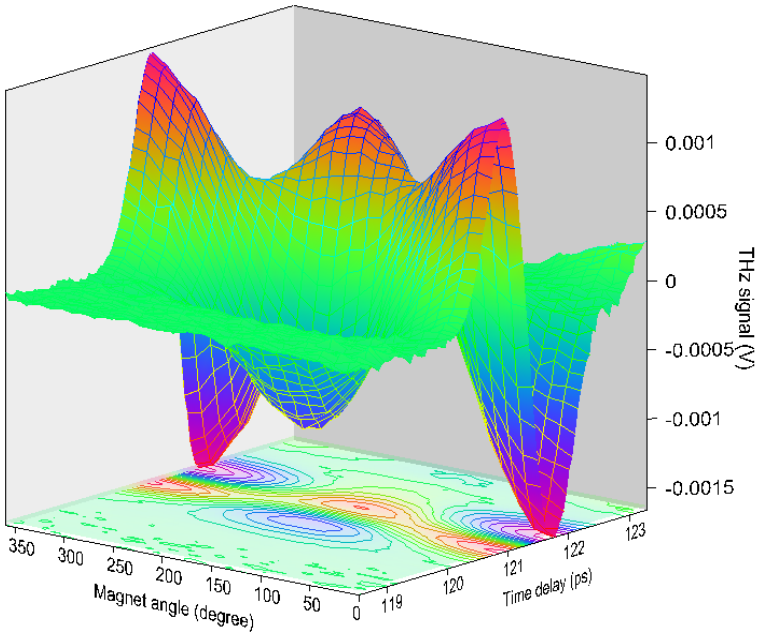

(b) *s*-polarization

Figure 5.4 Three-dimensional representation of *p* and *s*-polarized THz signals from (100) InAs with rotation of the magnet.

Equation 5.17 suggests that in the absence of magnetic field, the *s*-polarized component should be zero. However, from Figure 5.3, it can be seen that there is an *s*-polarized signal even in the absence of magnetic field. This is due to the fact that we have considered in the theory that the THz emission from material is due to transient current mechanism alone. However, as discussed in section 5.1, (100) InAs generates THz signal due to both optical rectification and transient current mechanisms. Thus, the nonzero signal present in the absence of magnetic field in the *s*-polarization can be thought of appearing due to presence of OR. Similar OR components are present in the *p*-polarized signals also. However, for *p*-polarization, the contribution from optical rectification is very small compared to the large transient current effect.

The net change in the THz polarization components due to application of magnetic field can be obtained by subtracting the signal without magnet from the signals with magnet, which also eliminate OR components from the THz signals. From Equations 5.17 and 5.18, the net magnetic field components can be written as

$$\begin{bmatrix} E_p^{\mathrm{THz}} \\ E_s^{\mathrm{THz}} \end{bmatrix} = A \begin{bmatrix} 0.3773(\cos\omega_c t - 1) + 2.003\sin\theta\sin\omega_c t \\ -1.6831\cos\theta\sin\omega_c t \end{bmatrix} e^{-\gamma t}\cos\omega_p t\,. \qquad 5.27$$

In above equation for *p*-polarized component, the first term $(\cos\omega_c t - 1)$ will be very small compared to the second term $\sin\theta\sin\omega_c t$. So the signal will be driven by the second term with $\sin\omega_c t$ dependence as opposed to $\cos\omega_c t$ for the signal with the magnet. On the other hand, the *s*-polarized components will be also driven by $\sin\omega_c t$. Further, the overall change in the *p* and *s* polarized components will be nearly equal. These features can be seen from the graphs shown in Figure 5.5. Three-dimensional representations of magnet rotation for *p* and *s* polarization are given in Figure 5.6.

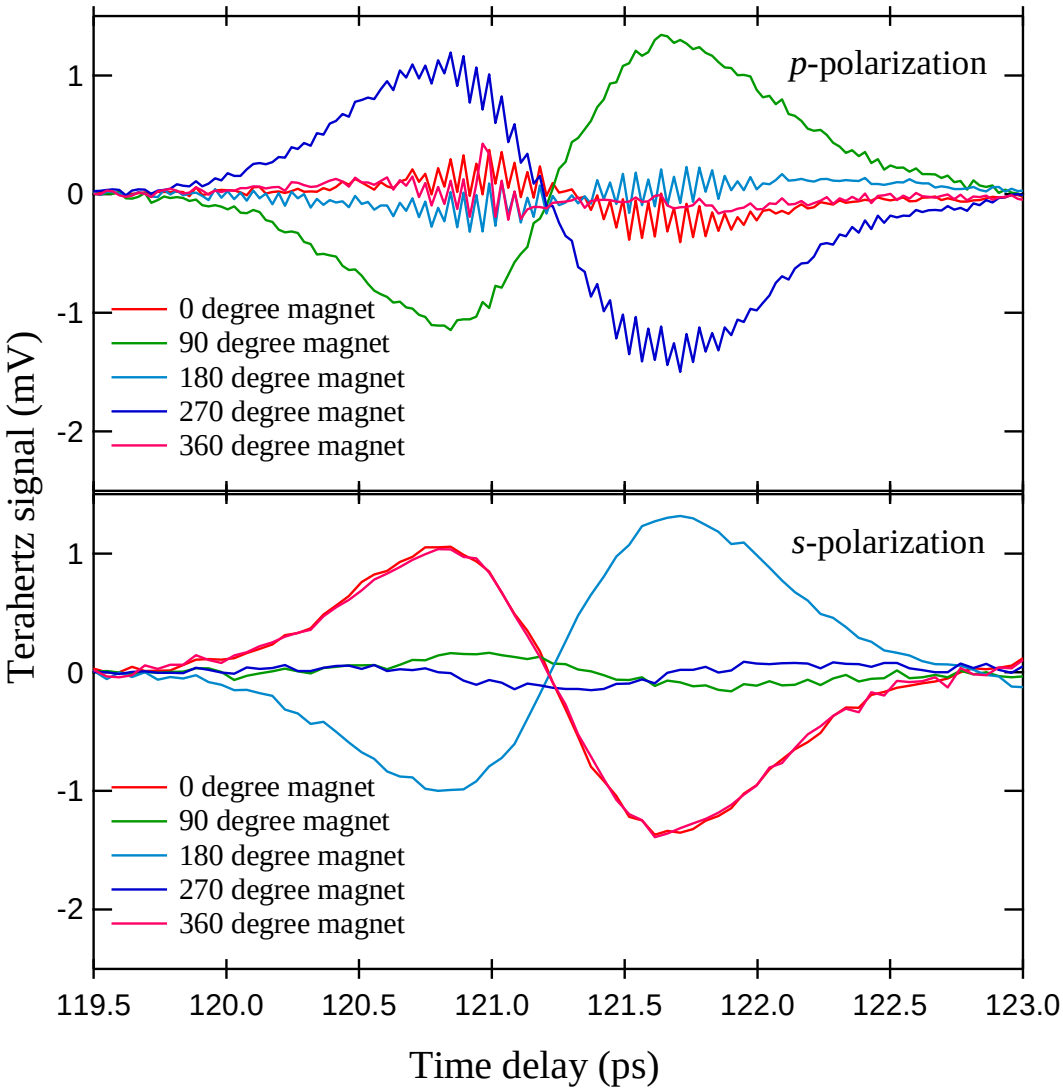

Figure 5.5 Net effect of magnetic field for *p* and *s*-polarized THz components generated from (100) InAs emitter. Both polarization components change as $\sin\omega_c t$ with nearly equal signal strength for varying magnet positions.

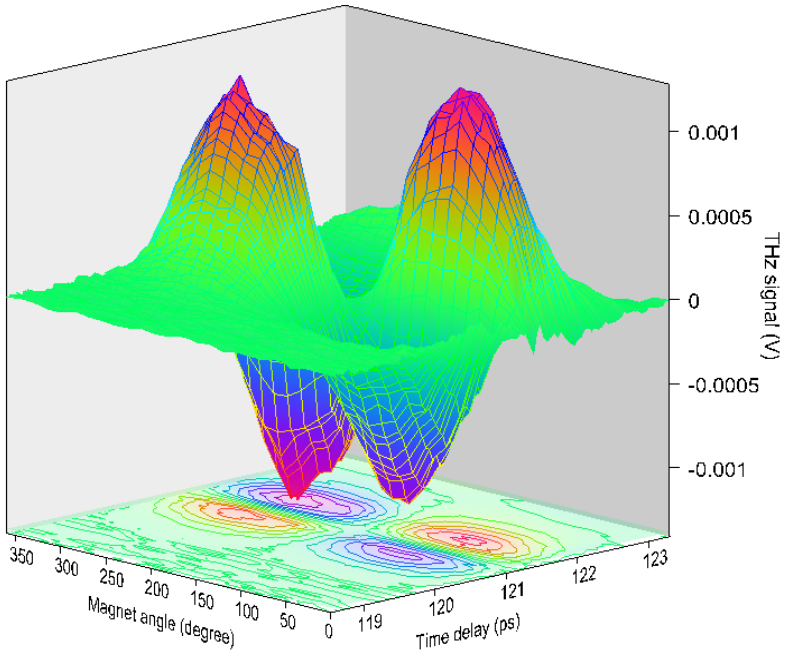

(a) *p*-polarization

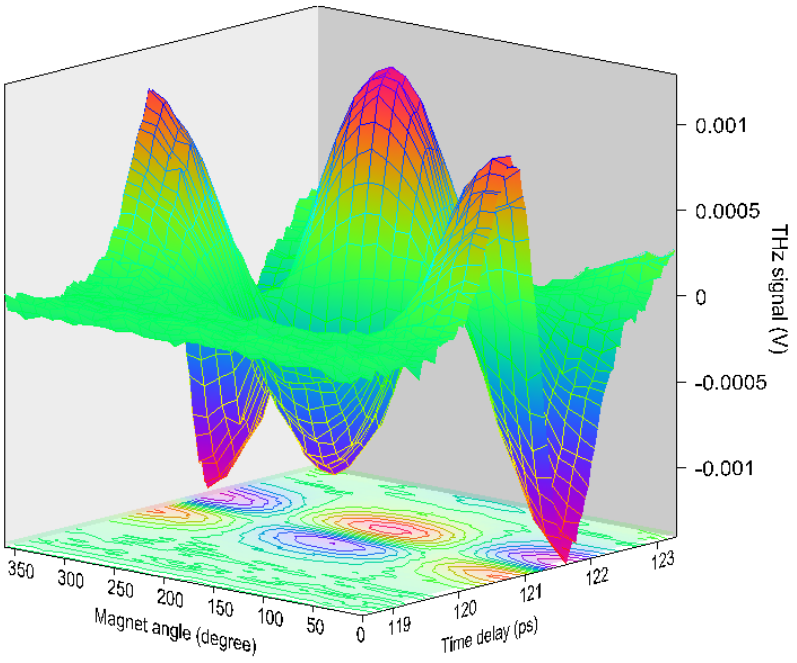

(b) *s*-polarization

Figure 5.6 Three-dimensional representation of net magnetic field effect for *p* and *s*-polarized THz components from (100) InAs with rotation of the magnet.

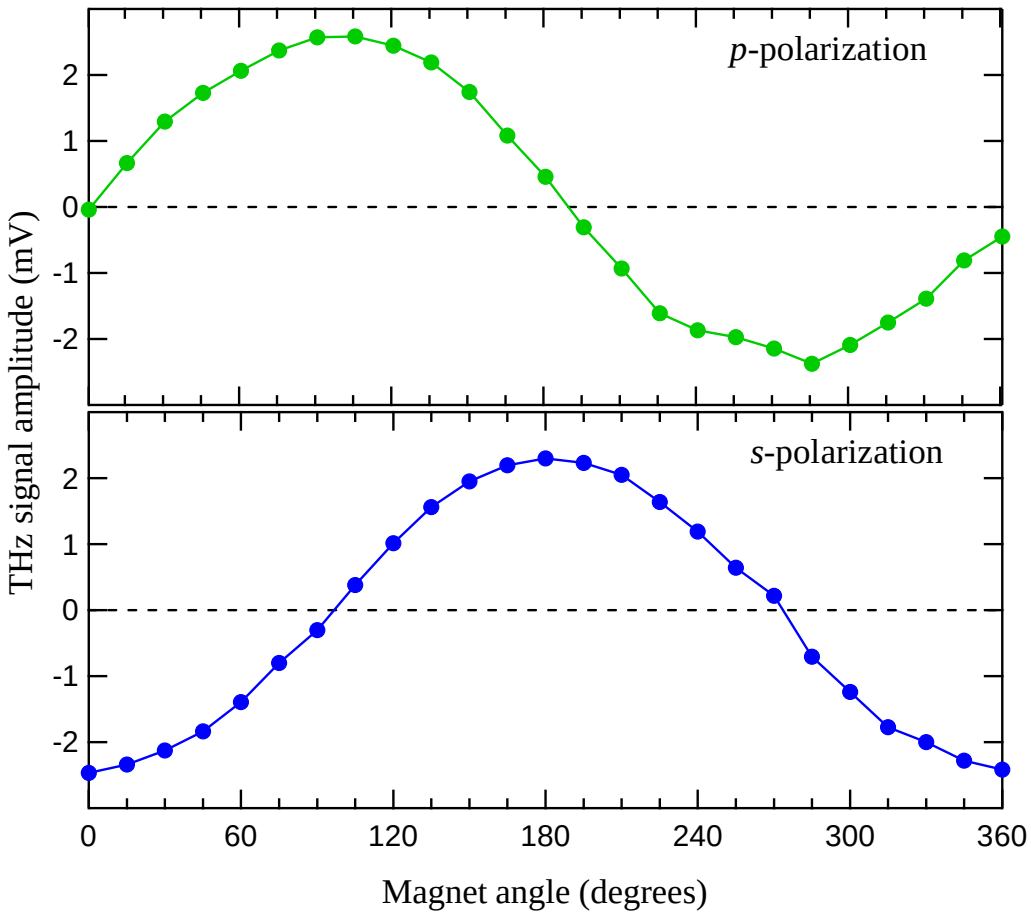

Figure 5.7 InAs *p* and *s*-polarized THz signal amplitude with rotation of the magnet for net magnetic field effect. Each filled circle represents the THz peak-to-peak signal measured at that magnet angle. Both polarization signal amplitudes follow a single cycle dependence for magnetic field with *p*-polarization having sinθ dependence and *s*-polarization having cosθ dependence.

Figure 5.7 represents the peak-to-peak voltage for net effect from magnet rotation for both *p* and *s* polarized THz field components. Such one cycle dependence with magnetic field rotation has been observed for number of other THz emitters such as GaAs, InP, and CdTe. Thus, effectively the enhancement in the THz field in the presence of magnetic field may be attributed to rotation of the dipole due to current flow away from surface normal, which reduces the effect of total internal reflection which is quite pronounced in the materials with large refractive index mismatch[154].

Further, it is not necessary to use a magnet in order to get the rotation of the dipole. It has been shown that same sort of enhancement in THz generation may be observed by modifying the dipole orientation using a prism or lens or by changing the refractive index of the sample[156]. A nearly 20-fold increase in THz power has been observed with such set up[158]. Also, the special structure of nanowires or nanorods have been fabricated on surface of different semiconductors in order to reduce the total internal reflection of generated THz. InAs nanowires on GaAs substrate increases the THz power efficiency by 15 times[159], while an InN nanorod sample shows threefold increase in THz field amplitude in comparison to InN thin film[160]. Similar improvement has been observed for GaAs nanowires[161].

As stated earlier, the optical rectification components are not influenced by magnetic field. Hence, the magnetic field dependence can be used as an effective way to differentiate TC and OR mechanism responsible for THz generation from any material.

5.3 Lateral photo-Dember effect

The THz generated in dielectric materials may be affected by total internal reflection, which limits emission efficiency of these materials. Recently a new mechanism for THz generation from semiconductor materials has been proposed which is called lateral photo-Dember (LPD) effect. The basic principle of this mechanism is same as the photo-Dember effect, where the THz generation relies on dipole generation due to photoexcited carriers. However, in lateral photo-Dember effect the dipole is generated in the sample surface plane as opposed to in the surface normal direction for photo-Dember effect. Thus, improved THz efficiency may be obtained due to the favorable reorientation of the dipole. This mechanism can be observed at the interface of the metal-semiconductor structure by partially shadowing the excitation area[71,162,163]. A large improvement in THz emission has been observed using multiplexed LPD emitter with gold wedged strips on InGaAs and GaAs substrates[71]. The THz output improves due to multiple LPD effects observed at each metal-semiconductor edge. Also simulation work suggests a similar effect may be observed by fabricating a material with repeating masks using electron-beam lithography[164]. Two different models have been proposed in order to understand the origin of this mechanism. One model relies on the faster diffusion of electrons under the metal and formation of the net polarization in the surface plane[71], while other suggest suppression of radiation under the metal due to

destructive interference between reflected and non-reflected radiation at the metal-semiconductor edge[162]. The pictorial representation for PD effect and LPD effect using diffusion model is presented in Figure 5.8.

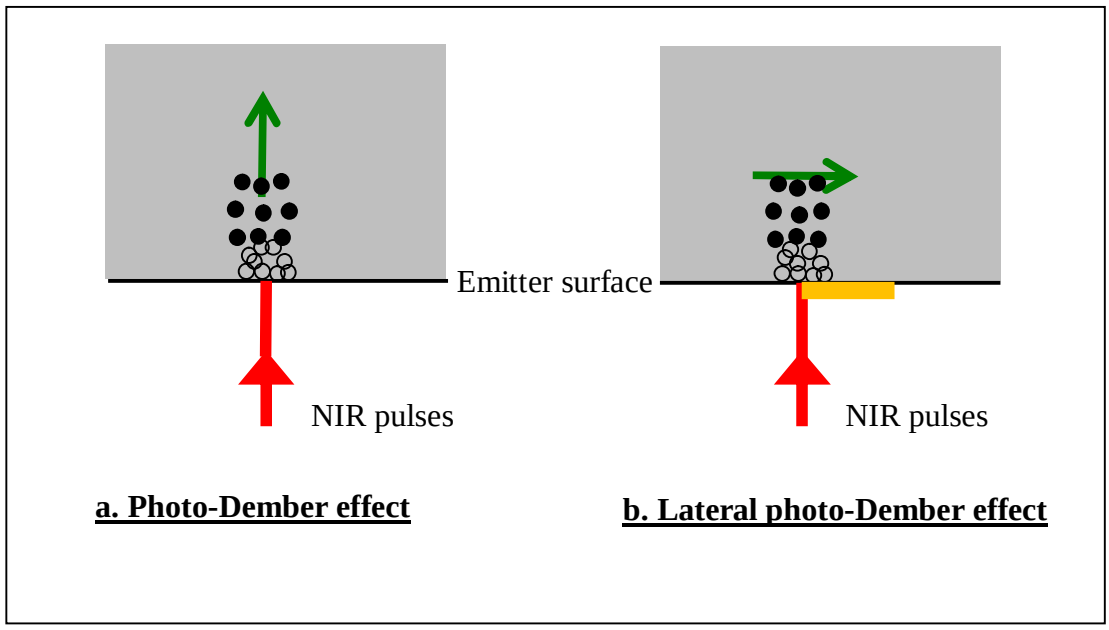

Figure 5.8 The dipole generation in (a) photo-Dember effect and (b) lateral photo-Dember effect. Photoexcited electrons and holes are shown with filled circles and empty circles, respectively. In the photo-Dember effect, the electron-hole pairs are diffused in surface normal direction and the effective dipole is generated perpendicular to the surface plane. In lateral photo-Dember effect, a metal structure is deposited on semiconductor surface and the excitation beam excites the sample at the edge of metal-semiconductor. Diffusion of electrons under the metal causes dipole to be formed in the direction of the surface plane.

The results from both diffusion and interference models indicate THz field amplitude from LPD effect is comparable to PC antenna. An attempt has been made to observe this phenomenon by fabricating silver and gold strips on InAs, GaAs and InGaAs samples. Being the best PD emitter, InAs can be thought of generating THz radiation through this mechanism. In order to check this effect and confirm the emission principle, a metal structure using silver/gold strip was deposited on this sample. The sample was then mounted for transmission geometry measurement.

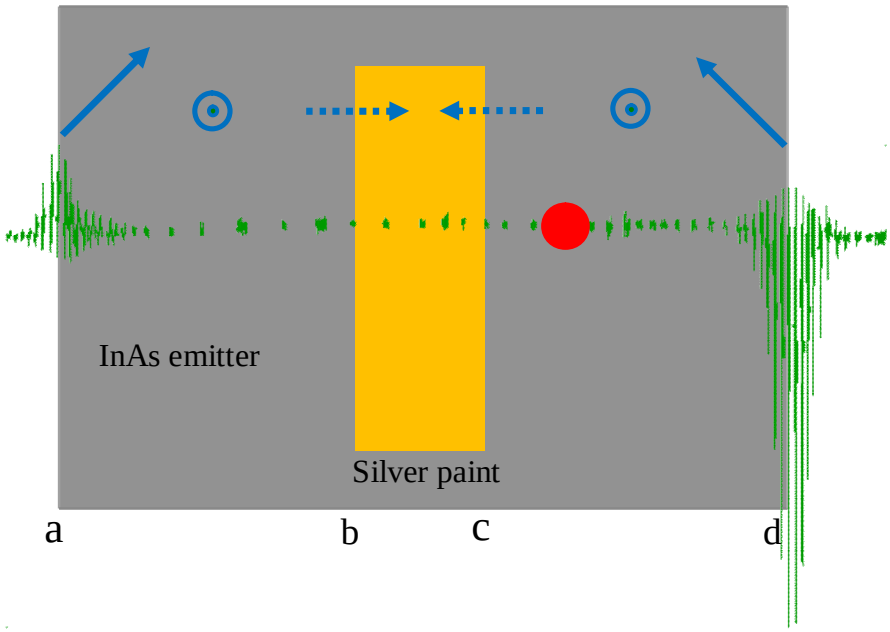

Figure 5.9 Photo Dember and Lateral photo-Dember measurements for (100) InAs emitter in transmission geometry with silver metal structure on the sample surface. Each green line shows the THz signal obtained by focusing the NIR beam at particular point on the sample. The red circle is the estimated diameter of incident NIR beam. The blue lines and circles indicate estimated dipole direction for normal incidence of the NIR beam. The THz is detected at the left and right edge of the semiconductor due to PD effect (point a and d) with the signal being inverted at two edges. No signal is observed on the semiconductor or on the silver paint as predicted due to normal incidence of the excitation beam. The expected THz signals on metal-semiconductor interfaces (at point b and c) due to LPD effect were also not observed.

Figure 5.9 shows the experimental results obtained for InAs emitter. The sample was scanned with respect to the NIR beam and THz signals were measured at different place on the emitter. The red circle indicates the estimated diameter of the excitation NIR beam. Green vertical lines represent the THz signal measured across whole sample by scanning the sample with respect to the excitation beam.

Since, the emitter is placed in the transmission geometry set up, no THz was expected from the sample in the regions between ‘a’ and ‘b’ and ‘c’ and ‘d’. This is due to the fact that the THz detection is in the direction of the dipole generated across the

surface normal and hence no THz electric field observed in this case. The generated dipole in this case will be pointing into the page as shown in the figure.

At the edges of semiconductor at points ‘a’ and ‘d’, the THz signal is observed due to the dipole creation in the diagonal direction owing to the PD effect. The generated dipoles are shown with blue lines. The signal observed due to this ‘sideways’ PD effect flipped on both sides as expected from the dipole directions. The unevenness on the edge of the sample may have caused the signal strength being different on both ends. At point ‘b’ and ‘c’, i.e. at the interface of metal-semiconductor, the THz signal was expected due to lateral orientation of the dipole. However, no THz signal was observed at interfaces on both sides.

Similarly GaAs and InGaAs samples have been tested for LPD effect but none of them showed any THz due to this mechanism. The failure in observing the LPD may have many sources. This includes requirement of special structure of the semiconductor/metal, smaller beam diameter, high excitation power, or some other parameter. Also, the THz absorption in these samples may have blocked any THz to be detected.

5.4 Conclusion

THz emission from (100) InAs has been discussed. The measurement on azimuthal angle dependence for this sample indicate less than 10% contribution from non-linear bulk OR mechanism. The effect of in-plane magnetic field for transient current emitters has been discussed and the results for (100) InAs have been compared with theory. Both horizontal and vertical THz polarization components show increased and decreased signal with rotation of the magnet as predicted. Further, the peak observed for horizontally polarized components occurs at different time delay between excitation beam and THz beam indicating an effective refractive index change within emitter crystal. The lateral photo-Dember measurement for InAs crystal has been presented with forming metal structure on emitter crystal. The expected result of THz generation due to lateral dipole formation along the metal semiconductor surface could not be observed, but a ‘sideways’ photo-Dember effect, due to geometrical factors, was observed.

Chapter 6

6 Kr and Xe Irradiated InP Nanoporous Honeycomb Membranes

6.1 Introduction

In this chapter, the effect of heavy noble gas Kr and Xe irradiation on THz emission efficiency of (100) and (111) InP bulk materials and nanoporous honeycomb membranes is presented. THz emission from bulk InP depends on the doping type and doping level, with transient current being the principal mechanism for THz generation from these semiconductor materials[138]. Porous membranes on (100) InP surfaces give an enhanced nonlinear optical (NLO) response for both second-harmonic and terahertz generation, which is related to optical rectification rather than to transient current effects. The enhanced nonlinear response may be attributed to strong local fields in the porous network[165]. Similar enhancement in the terahertz emission from porous (111) InP samples has been observed[166]. For porous InP samples, upward band bending at the pore surfaces produces a lower density and lower mobility of charge carriers with much longer recombination lifetime compared to bulk InP[167]. Here we extend the study of bulk and porous InP structures with modification of the base material by the creation of radiation defects through Kr and Xe heavy gas ion irradiation. It has been observed from studies on GaN and ZnO that nanostructuring the surface improves radiation hardness[168,169]. Terahertz emission efficiency is also improved for GaAs by As implantation[170].

The samples presented in this study and details about pore growth and ion irradiation are provided by L. Sirbu from Institute of Electronics Engineering and Nanotechnologies, Moldova and I. M. Tiginyanu from National Center for Materials Study and Testing, Moldova.

6.2 Sample specifications

(100) and (111)-oriented n-InP substrates with 500 μm thickness were used as base materials with free electron concentrations of 5×10^{18} cm^{-3}. In order to grow pore structures, the samples were chemically etched at room temperature in a 5% HCl aqueous solution in the potentiostatic regime using an electrochemical double cell[171]. The sample, of exposed area 1 cm^2, was mounted between the cells. The electrolyte was continuously pumped through both cells. Four Pt electrodes were used; a reference

electrode in the electrolyte, a sense electrode on the sample, a counter electrode, and a working electrode. The top nucleation layer was removed by isotropic wet etching.

The (100) and (111) bulk and nanoporous samples were irradiated at room temperature by 85 MeV Kr^{+15} ions at doses of 10^{12} and 10^{13} cm^{-2} and by 130 MeV Xe^{+23} ions at doses of 5×10^{11} and 5×10^{12} cm^{-2}, at the IC-100 cyclotron of the joint Institute for Nuclear Research, Dubna, Russia.

A VEGA TESCAN TS 5130MM scanning electron microscope with an Oxford Instruments energy-dispersive x-ray (EDX) system was used to analyze the morphology and chemical composition of the samples. The EDX microanalysis confirmed the stoichiometric composition of the InP nanoporous skeleton both before and after irradiation.

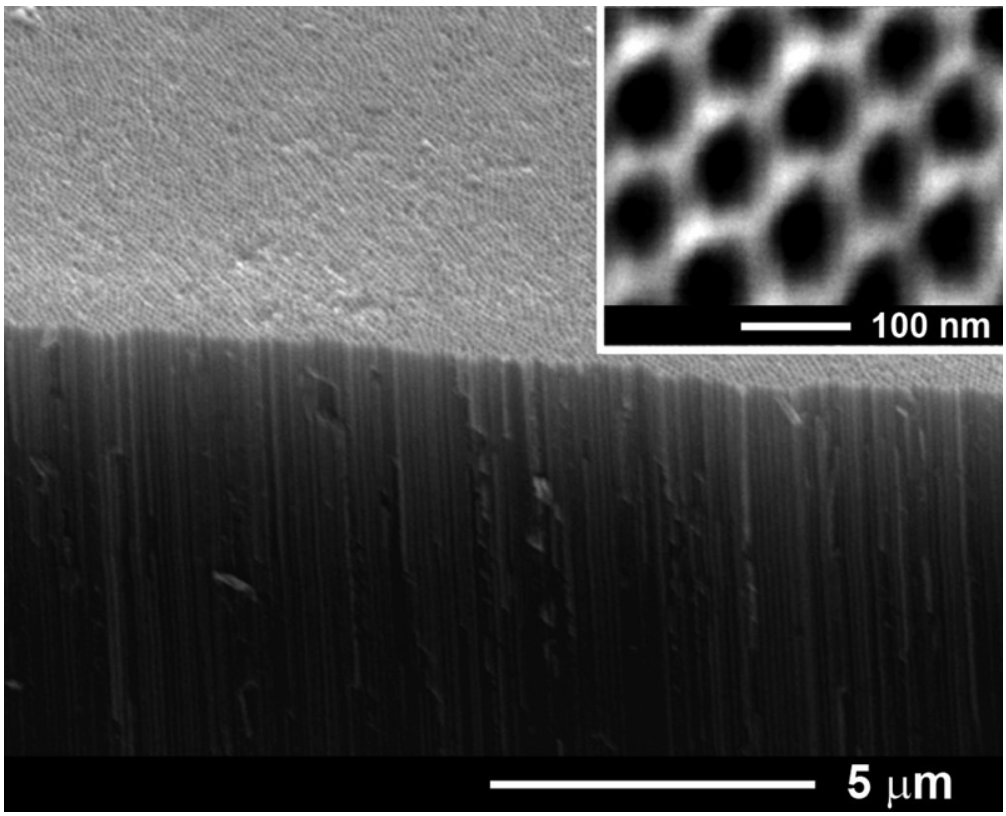

Figure 6.1 Scanning electron micrograph of a nanoporous InP (111) membrane. The inset shows the hexagonal arrangement of the pores from a top view.

Figure 6.1 represents micrograph of a typical nanoporous structure for (111) InP. The mean diameter of the hexagonal pores is 60 nm with interpore spacing of 100

nm. The total thickness of the nanoporous membrane is ~30 μm. Similarly for the (100) InP nanoporous structure, the mean diameter of 100 nm is observed.

6.3 Experimental results and discussion

The response of bulk and nanoporous InP samples irradiated with Kr and Xe at two different irradiation levels (10^{12} cm^{-2} and $10^{13}cm^{-2}$ for Kr and 5×10^{11} cm^{-2} and 5×10^{12} cm^{-2} for Xe) have been investigated for THz emission from these samples. The results for both (100) and (111) crystallographic directions are presented. Also, the results for unirradiated bulk InP crystal are shown for comparison. In total 18 samples have been measured.

The conventional THz TDS set up is used to measure the response of InP samples for THz emission. None of the observed InP samples transmit any THz through them. Hence, it is not possible to measure their response in the emitter transmission geometry. The results here presented are obtained in quasireflection geometry.

Figure 6.2 gives the response of (111) InP bulk and nanoporous samples as terahertz emitters. The THz output is shown in mV range with the Kr 10^{13} cm^{-2} irradiated sample generating the maximum THz output of 0.66 mV peak-to-peak voltage. Also, the picosecond time scale for the horizontal axis is shown by an arrow. The numerical comparison of THz amplitude for these samples is given in Table 6.1.

As can be seen from Figure 6.2, the unirradiated sample generates negligible THz radiation. Variation in the scan indicates the electrical and/or thermal noise level in the system. For both bulk and nanoporous samples, the terahertz emission increases with increasing ion dose. This holds for both Xe and Kr irradiations. Further, the Xe ion irradiation is more effective than Kr ion irradiation in enhancing THz emission. The nanoporous structures yield more terahertz radiation compared to bulk samples. Overall, the best emitters in this series are the nanoporous Kr 10^{13} cm^{-2} and Xe 5×10^{12} cm^{-2} irradiated samples.

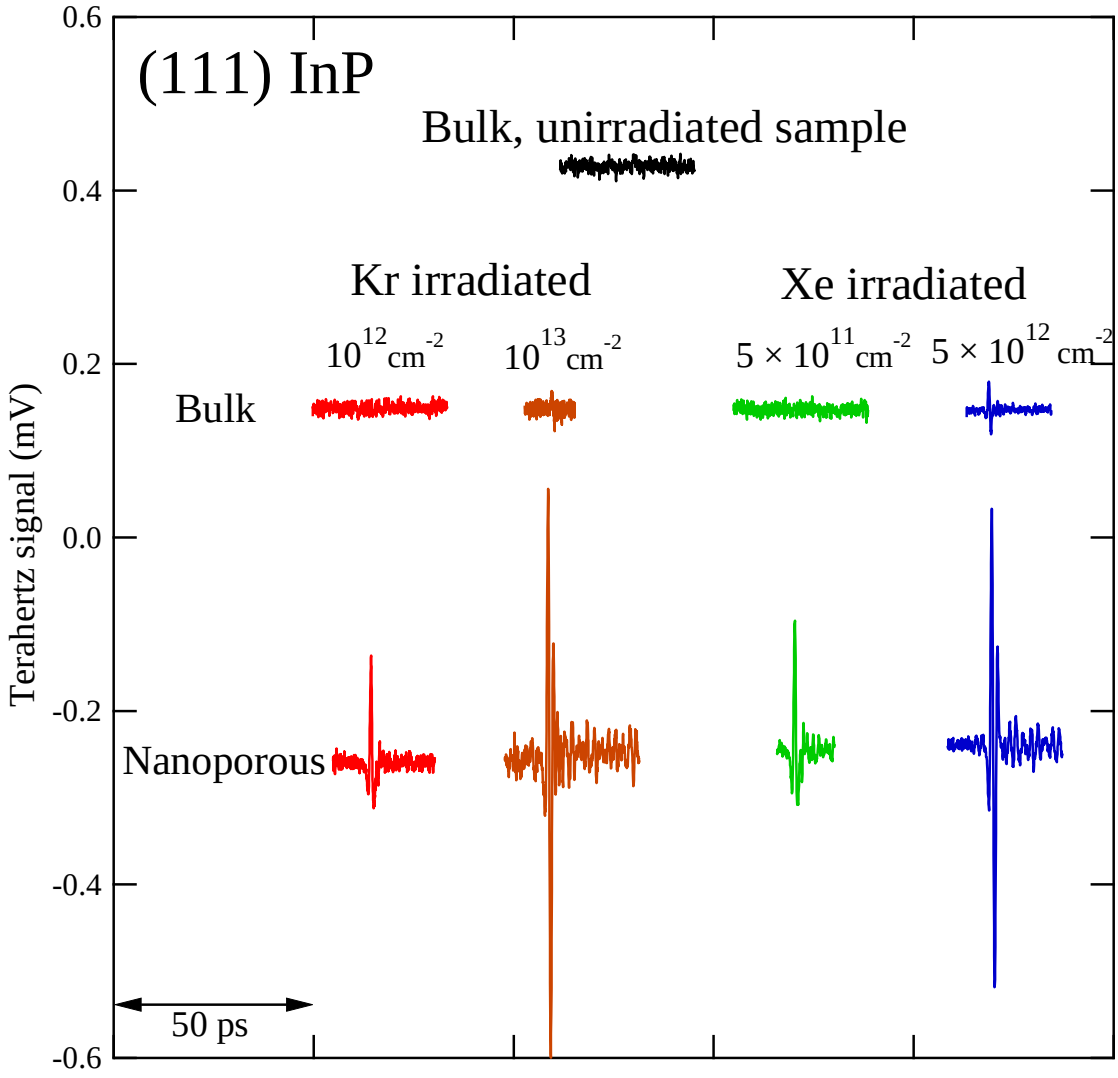

Figure 6.2 Measured terahertz signals for (111) Kr and Xe irradiated InP bulk and nanoporous samples. The signal for an unirradiated bulk sample is also shown. In total nine different InP (111) samples are compared. The signals are shifted on both axes for clarity.

Table 6.1 Relative terahertz electric field amplitude from different InP (111) samples shown in Figure 6.2

	Bulk, unirradiated sample: THz emission ~0			
	Kr irradiated		Xe irradiated	
	10^{12} cm^{-2}	10^{13} cm^{-2}	5×10^{11} cm^{-2}	5×10^{12} cm^{-2}
Bulk	~0	1	~0	1
Nanoporous	4	14	5	12

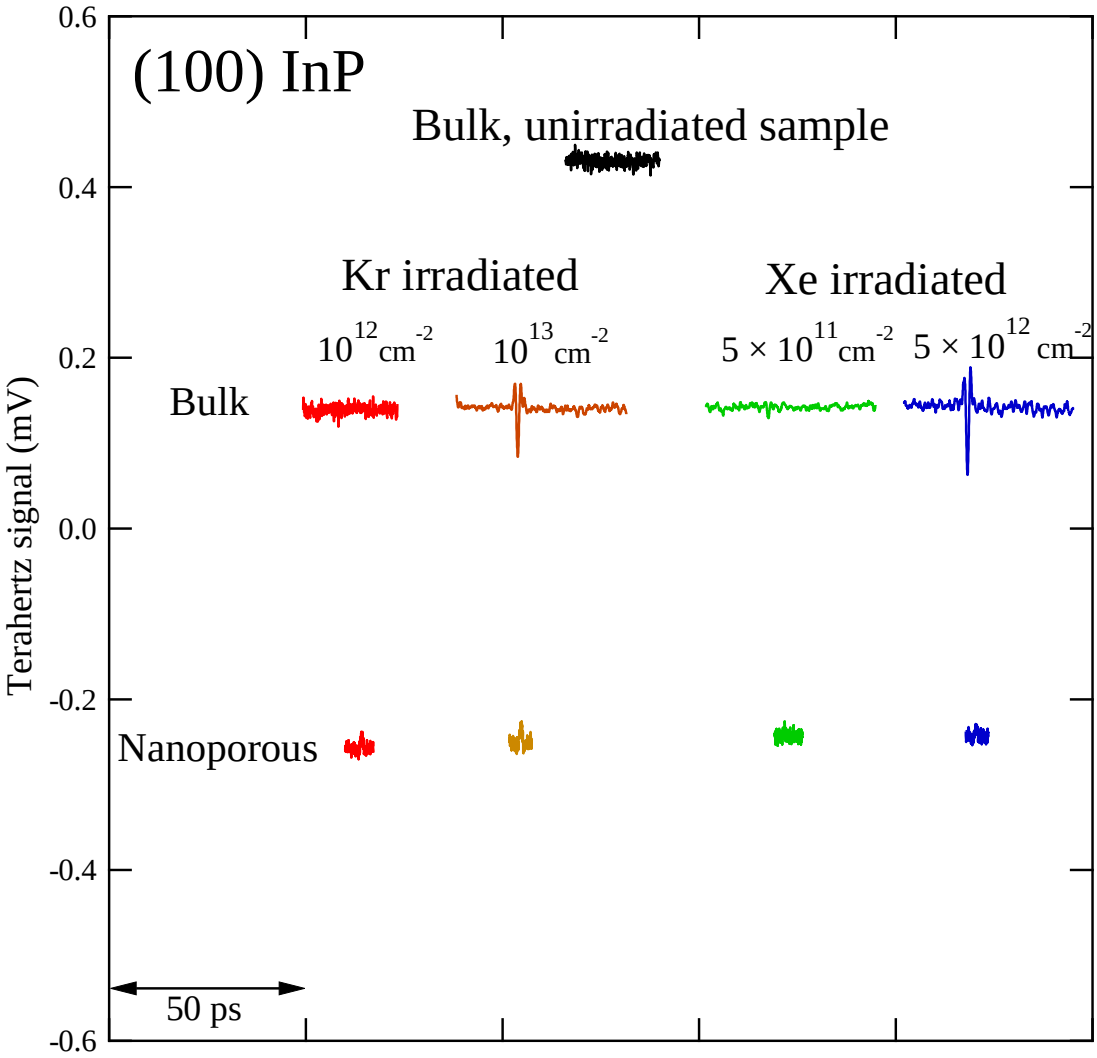

Figure 6.3 Measured terahertz signals for (100) Kr and Xe irradiated InP bulk and nanoporous samples. The signal for an unirradiated bulk sample is also shown. In total nine different InP (100) samples are compared. The same scaling factors are used as for InP (111) samples to permit direct comparison of all 18 samples. The signals are shifted on both axes for clarity.

Table 6.2 Relative terahertz electric field amplitude from different InP (100) samples shown in Figure 6.3

	Bulk, unirradiated sample: THz emission ~0			
	Kr irradiated		Xe irradiated	
	10^{12} cm^{-2}	10^{13} cm^{-2}	5×10^{11} cm^{-2}	5×10^{12} cm^{-2}
Bulk	~0	2	~0	3
Nanoporous	1	1	~0	1

As shown in Figure 6.3, the bulk unirradiated (100) sample generates negligible THz radiation. Also, with increase in ion irradiation, THz signal amplitude increases for both Xe and Kr irradiation as evident from the results for bulk (100) samples. Further, the Xe ion irradiation is more effective than Kr ion irradiation in generating THz signals. These results are consistent with the results obtained from the (111) InP samples.

However, in the case of (100) samples, the nanoporous structures generate *less* THz signal for both Xe and Kr irradiation. This is opposite to what we have observed for (111) samples, where nanoporous samples emit more THz signal than bulk samples.

Put another way, we can say that (100) bulk samples emit better THz radiation than (111) bulk samples for both Xe and Kr irradiation, while the (111) nanoporous samples generates better THz output compared to (100) nanoporous samples. Among all 18 samples measured, the best THz emitters are (111) nanoporous samples with the highest levels of Kr and Xe ion irradiation. The improvement in THz emission from ion irradiated samples can be thought of due to change in the electronic structure caused by irradiation which may have led to reduction in the carrier lifetime and hence gave better THz response[170].

Further analysis of these samples can be performed by knowing the mechanism responsible for generation of THz radiation from these samples. For samples in quasireflection geometry, both transient current (TC) and optical rectification (OR) can play a role in THz emission. For precise knowledge of the mechanism involved, the effects of changing a few experimental parameters were investigated. In particular, the results for (111) InP samples are given here, as the THz radiation observed from (100) samples was very small.

We start with the effect of in-plane magnetic field. As discussed in the previous chapter, for TC emission mechanism, a single-cycle variation with rotation of the magnet can be observed. On the other hand, for OR effect, the signal is invariant with rotation of magnet.

Figure 6.4 shows the effect of an in-plane magnetic field on the terahertz emission. Only samples identified having a strong THz emission were investigated for this response. The InP samples do not show a strong angular dependence on the magnetic field direction, in contrast to the work on InP from other sources[138]. Also the data from (111) InP sample with carrier concentration of $0.8\sim2.0 \times10^{15}$ cm^{-3} (MTI

Corporation, USA) as shown in Figure 6.4(a) exhibits single cycle behavior with magnet rotation. The non-varying behavior of THz signal for nanoporous samples indicate that no role is played by TC mechanism in THz generation from these samples.

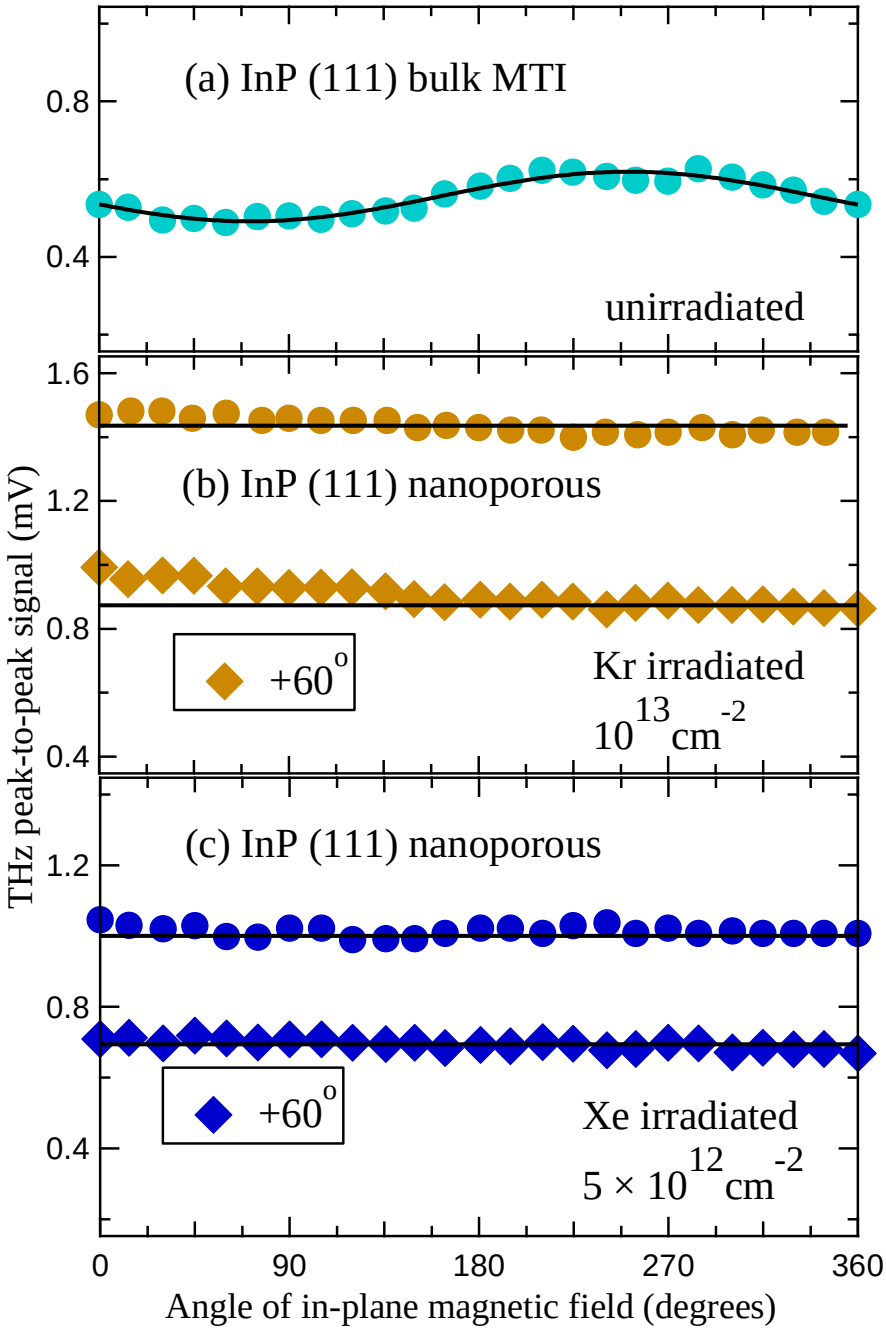

Figure 6.4 Effect of rotation of the in-plane magnetic field on the terahertz field emitted from (a) bulk InP (111) sample without ion irradiation, (b) nanoporous InP (111) sample with Kr ion irradiation at a level of 10^{13} cm^{-2} (circles) and the same sample, now rotated through an azimuthal angle of 60^{o} (diamonds). (c) nanoporous InP (111) sample with Xe ion irradiation at a level of 5×10^{12} cm^{-2} (circles) and the same sample being

rotated through an azimuthal angle of 60^{o} (diamonds). The data shows that the transient current effects are present in the bulk sample but not in the irradiated nanoporous material.

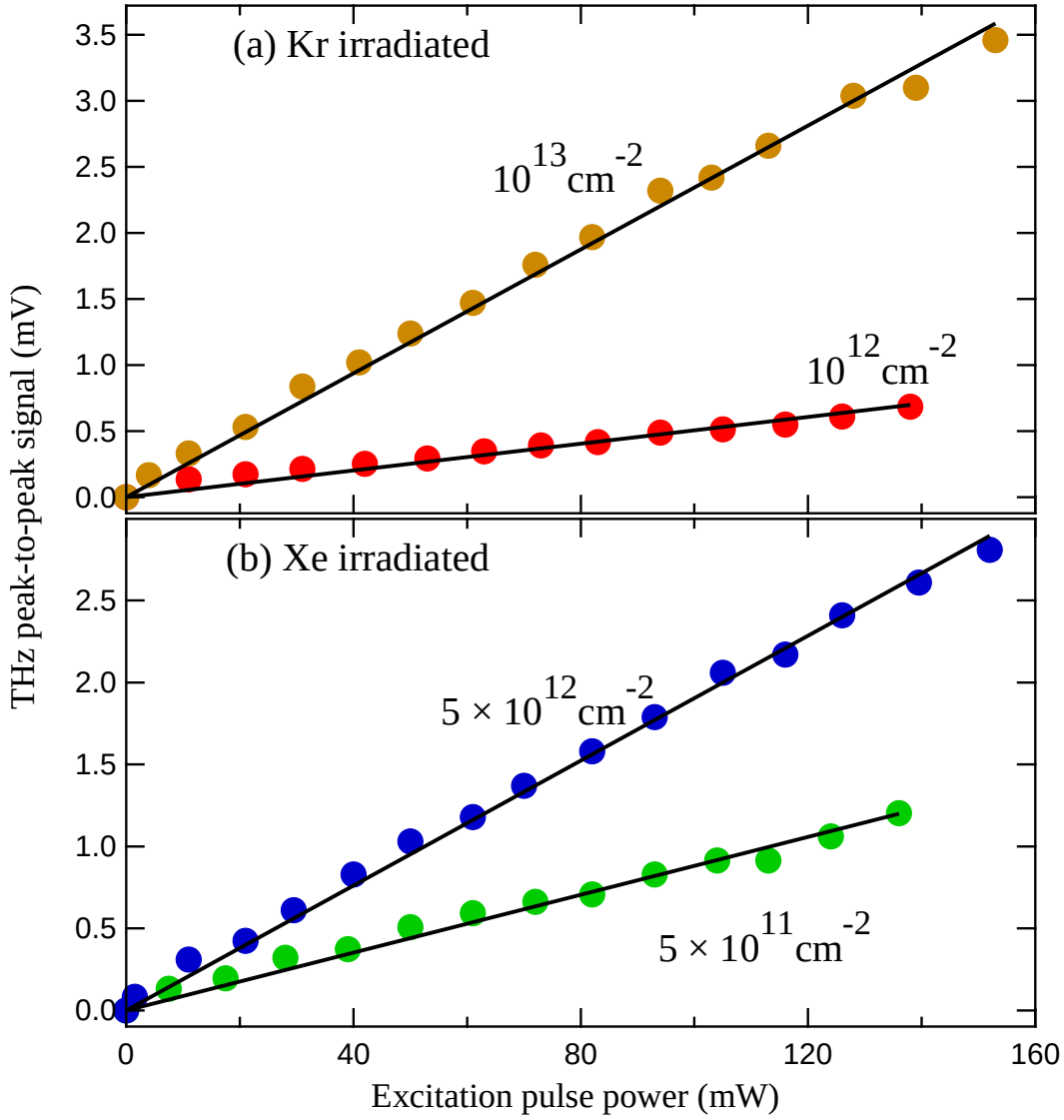

Figure 6.5 Effect of varying the incident excitation fluence on THz emission from nanoporous (111) InP with (a) Kr ion irradiation and (b) Xe ion irradiation. The THz emissions in all four samples vary linearly with excitation power level. There is no evidence of saturation in the signal with increasing excitation fluence.

One of the important property of the TC mechanism is the saturation of the THz emission at relatively low excitation fluences (<0.20 μJ/cm^2)[172]. The saturation at high excitation fluence can be attributed to the large amount of electron-hole pairs which

increases the carrier-carrier scattering rate, which causes less efficient THz emission[150]. On the other hand, the OR effect does not saturate with increase in excitation fluence, making it useful for high power applications.

Figure 6.5 shows the effect of the excitation pump fluence on the terahertz emission. The data for all (111) nanoporous ion irradiated samples are shown. For all four samples, the detected THz signal varies linearly with the pump fluence. There is no evidence of saturation, which suggest negligible or no contribution from TC effects. It is possible that the fluence is too small for saturation effect to be observed but the present data give no support to a TC mechanism for THz emission detected in these samples.

Figure 6.6 shows horizontal (*p*) and vertical (*s*) polarization components for InP (111) nanoporous Kr 10^{13} cm^{-2} irradiated sample with respect to the azimuthal angle rotation. The observed signal is symmetric about zero with very small offset observed in the signal. This result confirms very small or no contribution from TC effect in THz generation from this sample. The data can be fitted with the general theory of optical rectification.

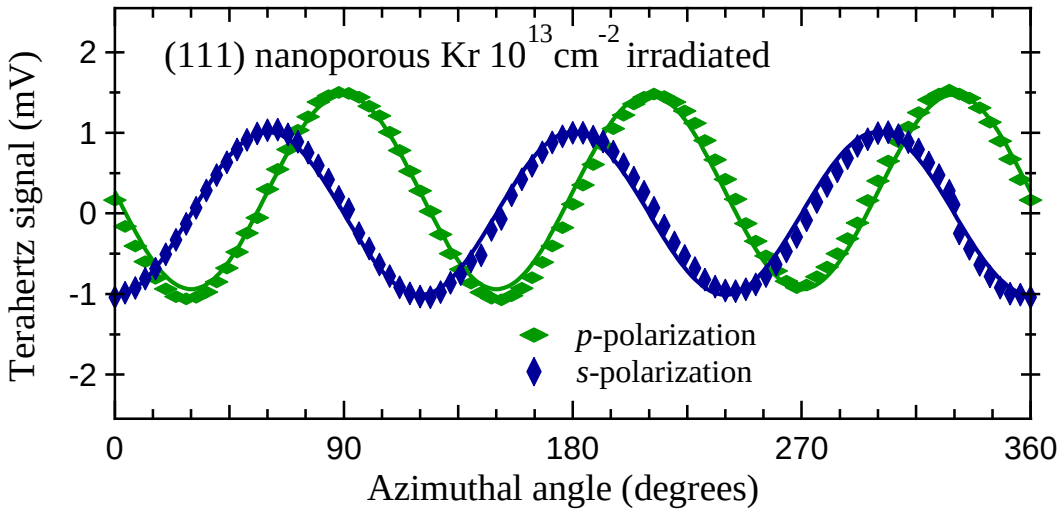

Figure 6.6 Azimuthal angle dependence for Kr 10^{13} cm^{-2} irradiated nanoporous InP (111) membrane. Both horizontally (*p*) polarized and vertically (*s*) polarized components of THz emission are presented. Three cycle symmetrical behavior along with very small offset from zero is observed for both polarization components.

The symmetrical three cycle dependence results are consistent with the theory results for bulk and surface OR. However, it is difficult to determine whether the mechanism involved in THz generation is bulk OR alone or the combined effects of

bulk and surface OR, as such information is only accessible for high-index planes using the OR theory presented earlier.

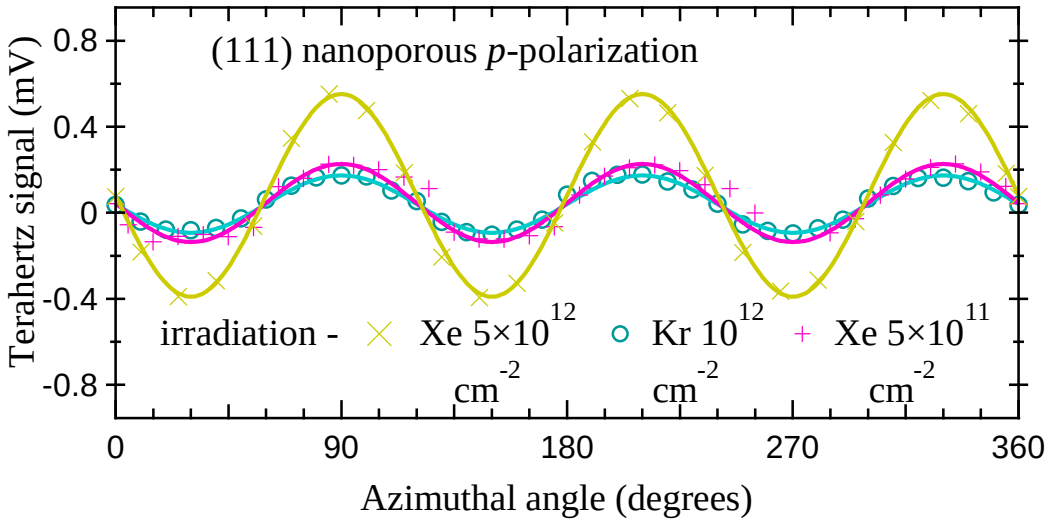

Figure 6.7 Azimuthal angle dependence for *p*-polarized THz components from Xe 5 × 10^{12} cm^{-2}, Kr 10^{12} cm^{-2}, and Xe 5 × 10^{11} cm^{-2} irradiated nanoporous InP (111) samples.

Figure 6.7 shows the azimuthal angle dependence for *p*-polarized THz components generated from Xe 5 × 10^{12} cm^{-2}, Kr 10^{12} cm^{-12} and Xe 5 × 10^{11} cm^{-2} irradiated (111) InP samples. The features observed for these samples are same as shown in Figure 6.6 except for the reduction in overall signal strength.

6.4 Conclusion

It has been demonstrated that irradiating nanoporous membranes of (111) InP with heavy noble-gas ions Kr and Xe enhances the terahertz emission. The effect of ion irradiation for (100) InP samples reduces the terahertz emission efficiency of these samples. Systematic investigation of the generated THz signal by varying in-plane magnetic field, excitation pump power, and azimuthal angle indicate that the principal generation mechanism for nanoporous (111) samples is an OR rather than TC effect.

Chapter 7

7 GaBiAs Epitaxial Layers on GaAs Substrates

7.1 Introduction

In chapter 3 and 4 the response of bulk GaAs (11*N*) samples as THz emitters in transmission and quasireflection geometries was presented. In this chapter, the change in THz emission efficiency by growth of epitaxial layers of $GaBi_yAs_{1-y}$ using molecular beam epitaxy on GaAs substrates will be discussed.

GaAs has been used extensively as a source of terahertz radiation[141,173,174]. Changes in the optical and structural properties caused by substitutional atoms and dopants alter the efficiency of THz generation from the material. Different effects on THz generation have been observed for substitution of atoms in GaAs such as GaAsSb[42], GaAs:Be[175], and GaInAsN[176].

The substitution of Bi for As in GaAs[177-181] results in a dramatic decrease in the bandgap, 90 meV per percent of Bi. Hence, GaBiAs is attracting attention for long wavelength (>1 μm) photonics applications including terahertz optoelectronics. Using time-resolved terahertz spectroscopy measurements, it is found that the electron mobility μ_e does not reduce significantly with incorporation of Bi up to level of 1.4%[182]. Other studies[183,184] show a double exponential decay on picosecond timescales corresponding to electron trapping and trap emptying. Photoconductive antenna structures on GaBiAs can be used as effective THz detectors with a spectral width >4 THz[185,186]. Also an all-GaBiAs terahertz TDS system has been developed by using GaBiAs photoconductive structures[116].

Earlier work on GaBiAs as a THz emitter has been restricted to the photoconductivity mechanism. However, GaBiAs is capable of generating THz radiation by all-optical means via transient current (TC) and optical rectification (OR) mechanisms.

7.2 Sample specifications

The epitaxial layers of nominal 1 μm thickness were grown by molecular beam epitaxy (MBE) on GaAs (100) and (113)*B* crystal planes. These samples were provided by Prof. Mohamed Henini from the University of Nottingham, United Kingdom. Details about the MBE growth, high resolution X-ray diffraction, transmission electron

microscopy, Z-contrast imaging, and optical transmission spectroscopy of these samples have been given previously[187]. For both (100) and (113)*B* orientations, four $GaBi_yAs_{1-y}$ layers corresponding to four different As fluxes during growth (Figure 2 in ref 187) as well as a control epilayer with y=0 and semi-insulating (SI) substrate were examined as THz emitters; a total of 12 samples in all.

The samples were tested as emitters in the THz-TDS system in both transmission and quasireflection geometry. Since the absorption coefficient of GaAs at the excitation radiation of 790 nm wavelength (photon energy 1.57 eV) is $\alpha_{NIR} = 1.2 \times 10^4 \, cm^{-1}$, most of the interaction is with the epilayer, not the substrate. It is also possible that some THz is generated at the interface between the epilayer and the substrate. Before examining these samples as THz emitters, all GaBiAs samples in the series were measured for terahertz transmission in the TDS system. All the samples found to transmit THz radiation with little attenuation. These measurements indicate that the charge-carrier concentration is not large in both epilayers and substrates and confirm that terahertz radiation generated in the layers on the front of the sample may travel with little loss through to the back of the sample.

7.3 Experimental results and discussion

Figure 7.1 shows the terahertz time-domain signals generated from (113)*B* GaBiAs samples along with (113)*B* GaAs SI substrate and the control (y=0) sample measured in transmission geometry. All (113)*B* GaBiAs samples were found to generate THz radiation, with $GaBi_{0.035}As_{0.965}$ being best emitter in the series. The details about peak-to-peak voltage observed for all samples are listed in Table 7.1.

In the case of the (100) GaBiAs sample series, except for one sample ($GaBi_{0.026}As_{0.974}$), none of the samples generated a noticeable signal in the transmission geometry arrangement. Also, the signal strength for the only observed (100) THz emitter is very small compared to the (113)*B* GaBiAs samples. This striking contrast between two orientations immediately suggests that the THz emission observed from these samples is related to the orientation of the pump beam polarization relative to the principal crystal axes, which is the property of the OR mechanism.

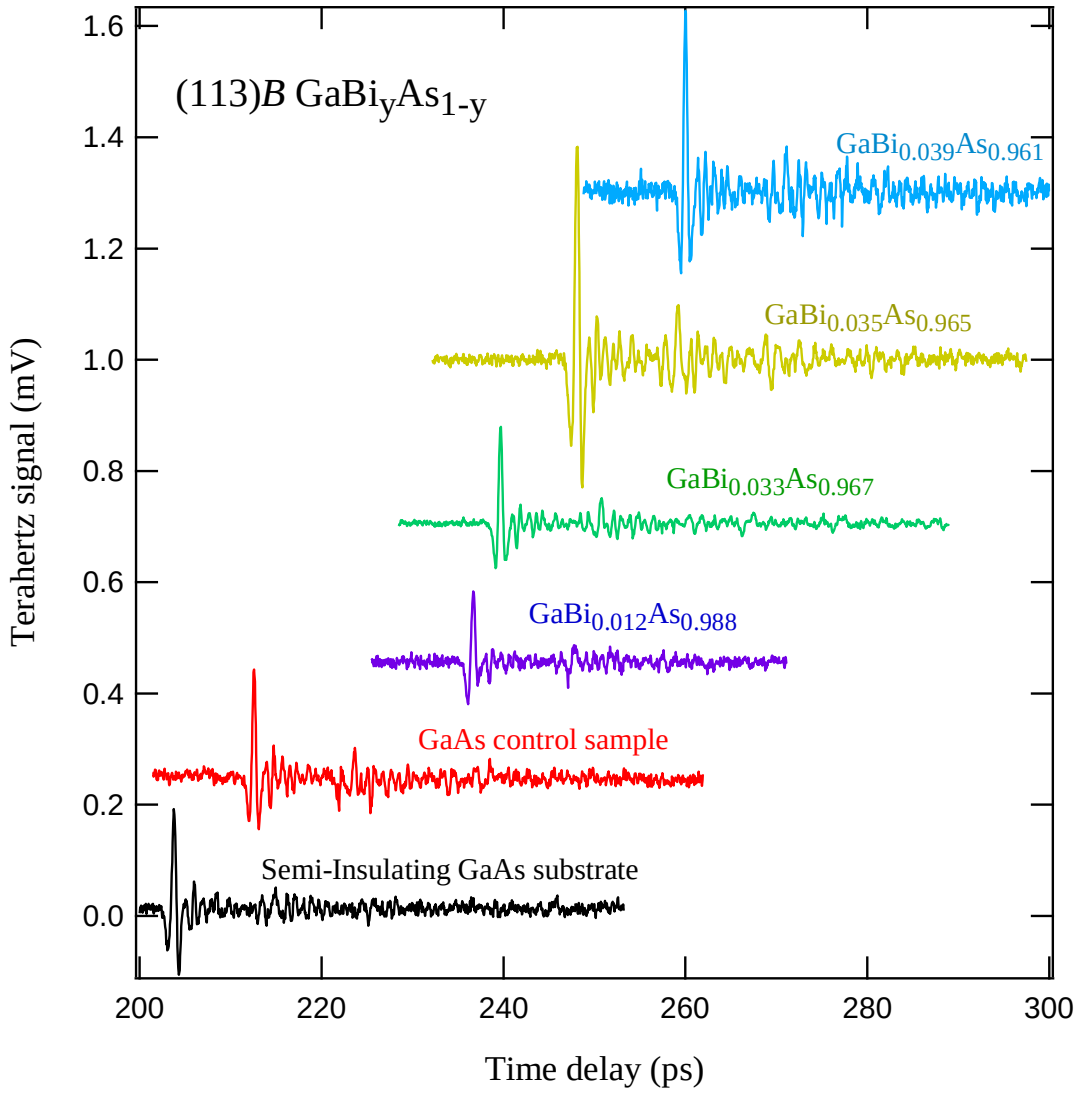

Figure 7.1 Response of GaBiAs samples with different Bi content as terahertz emitters. Terahertz signal generated from (113)*B* GaBiAs samples along with (113)*B* SI GaAs substrate and (113)*B* GaAs control sample were measured in TDS transmission geometry set up. The signals are shifted along both axes for clarity.

As we have discussed earlier, the OR components for the (100) direction in transmission geometry are zero. Further, the transient current may not be able to play any role in the THz generation as the dipole is generated at the surface normal, which does not emit any radiation in the direction of detection for this geometry. Hence, no signal is expected from (100) samples in transmission geometry. The signal observed from one (100) sample may have appeared due to sample misalignment or some other factor.

Now let us focus on the (113)*B* GaBiAs samples to further investigate the variation in THz emission with bismuth content and the mechanism behind THz emission from these crystals. The details about Bi content, As flux and THz amplitude observed for all (113) GaBiAs samples are given in Table 7.1.

Figure 7.2 (a) shows THz amplitude with respect to the Bi content in order to compare the dependence of Bi content on the THz emission efficiency. No specific relationship can be made between the two from the results obtained for these samples. Figure 7.2(b) represents the THz amplitude with respect to the As flux at which different GaBiAs epilayers were grown. It can be seen from the graph that the THz signal amplitude increases linearly with As flux, within experimental error, for GaBiAs samples.

Table 7.1 Comparison of THz signal amplitude with respect to Bi content and As flux for all (113)*B* GaBiAs samples including GaAs substrate and control sample.

	Bi content	As flux (Torr)	THz amplitude (mV)
Substrate	-	-	0.298
Control sample	0	12×10^{-6}	0.287
	0.012	6×10^{-6}	0.203
	0.033	8×10^{-6}	0.254
	0.035	12×10^{-6}	0.612
	0.039	10×10^{-6}	0.472

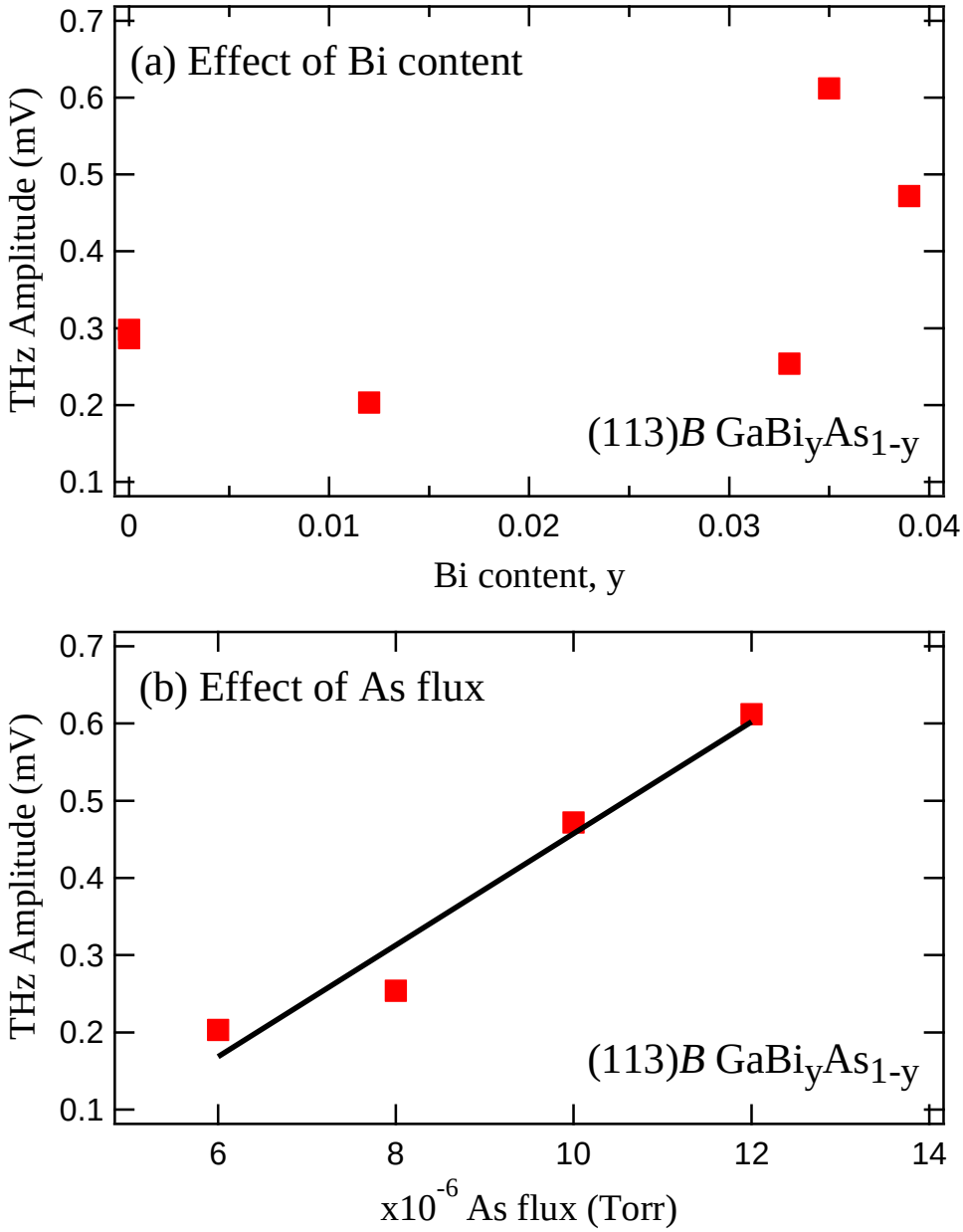

Figure 7.2 Variation in terahertz field amplitude in GaBiAs samples with change in (a) Bi content and (b) As flux. A linear relationship is observed between THz amplitude and As flux for GaBiAs samples.

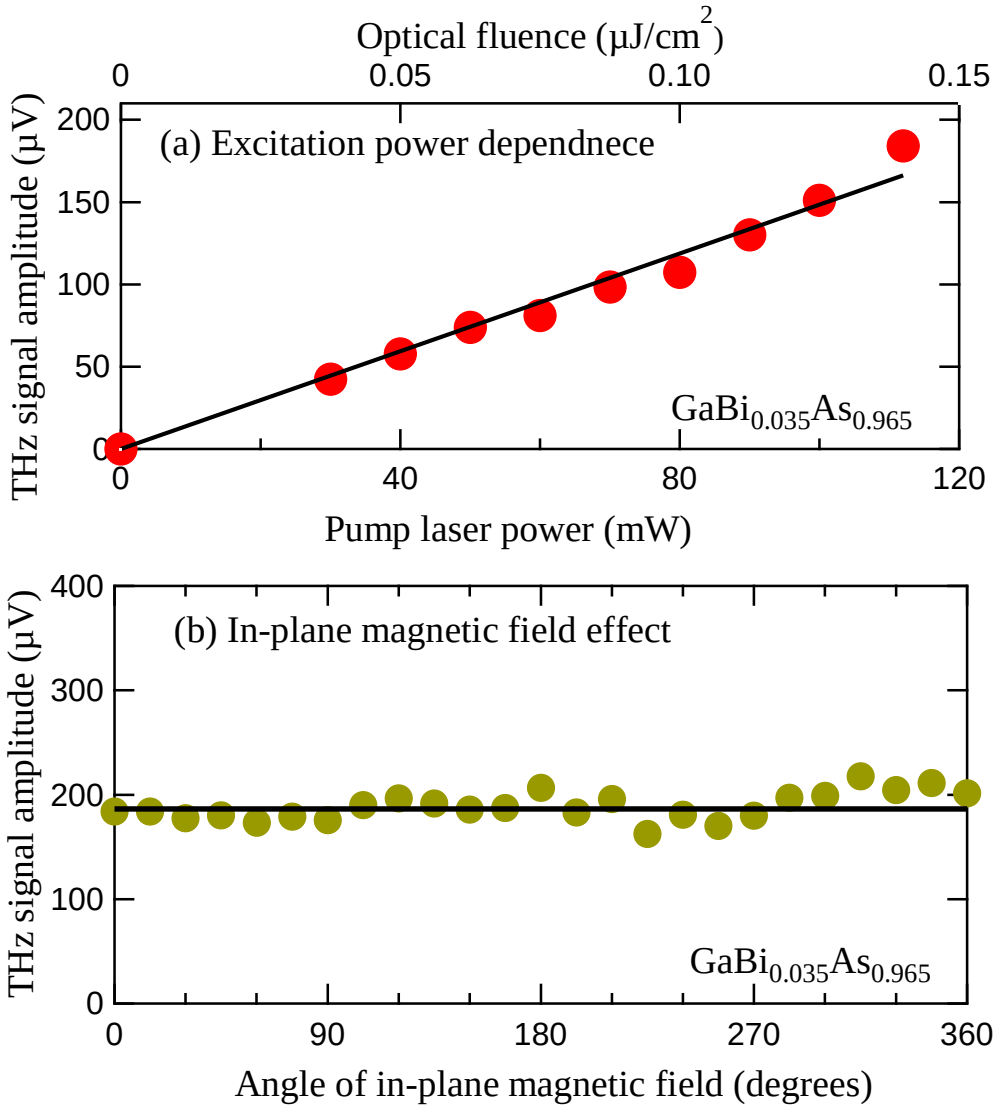

Figure 7.3 Effect of (a) varying optical fluence of the pump beam and (b) rotation of the in-plane magnetic field on THz field generated from the $GaBi_{0.035}As_{0.965}$ sample. Each circle represents the peak-to-peak THz signal with the lines showing fit to the data. The measurements are performed in quasireflection geometry.

In order to explicate the mechanism responsible for terahertz emission, the dependence of the terahertz field on excitation fluence was investigated using a variable power attenuator. The result for $GaBi_{0.035}As_{0.965}$, measured in quasireflection geometry, is shown in Figure 7.3(a). The peak THz electric field is seen to increase linearly with excitation power. At low optical fluence, this is expected behavior for both TC and OR mechanisms. However, at high fluences, the TC effect is expected to saturate due to the screening of charge carriers. For this sample, there is no sign of saturation and hence

there is no evidence of presence of TC effects. However, the fluences employed here may be too small for surface-field screening to be observed.

Figure 7.3(b) shows the effect of rotation of the in-plane magnetic field on THz field generated from $GaBi_{0.035}As_{0.965}$ in the quasireflection geometry. As we have discussed before, the TC effects are influenced by in-plane magnetic field due to rotation of the radiating dipole which causes an increase or decrease in the radiated THz field. In rotating the magnetic field through 360^{o}, one maximum and one minimum in the THz signal is expected[138]. In order to investigate this behavior a permanent magnet of 0.15 T magnitude was rotated behind the emitter crystal and the THz signal is measured in the step size of 15^{o} magnet rotation. Within experimental error, there is no evidence of variation in the radiated THz field with rotation of the magnet. The fluctuations in the measured peak-to-peak signals are caused by higher noise level present in the system. This result further confirms the negligible role of TC effects in THz emission from these samples.

Having discovered the principal mechanism for THz generation from (113)*B* GaBiAs samples, the variation of the THz field amplitude with respect to the azimuthal rotation of the emitter crystal in transmission geometry was investigated. The observed response can be compared with OR theory presented in chapter 3, which may be able to give more insight about contribution from bulk and surface OR effects.

Figure 7.4(a) shows the horizontally (*p*)-polarized and vertically (*s*)- polarized THz components with respect to the azimuthal rotation of the (113)*A* GaAs SI substrate sample. Both polarizations give three cycle dependence with respect to azimuthal dependence behavior, consistent with the theory and results presented in chapter 3. Thus, the OR effect is quite evident for this sample. Figure 7.4(b) shows the azimuthal dependence for (113)*B* GaAs SI substrate sample. The data for (113)*A* and (113)*B* can be fitted with same surface electric-field-induced OR contribution with respect to the bulk OR contribution with surface field being $F_0 = (1.7 \pm 0.3)\, d_{14}/\gamma'$, where d_{14} is susceptibility tensor component and γ' is non-linear optical constant. Hence, it can be said that both bulk and surface OR effects are present in the generation of THz from GaAs (113) SI sample.

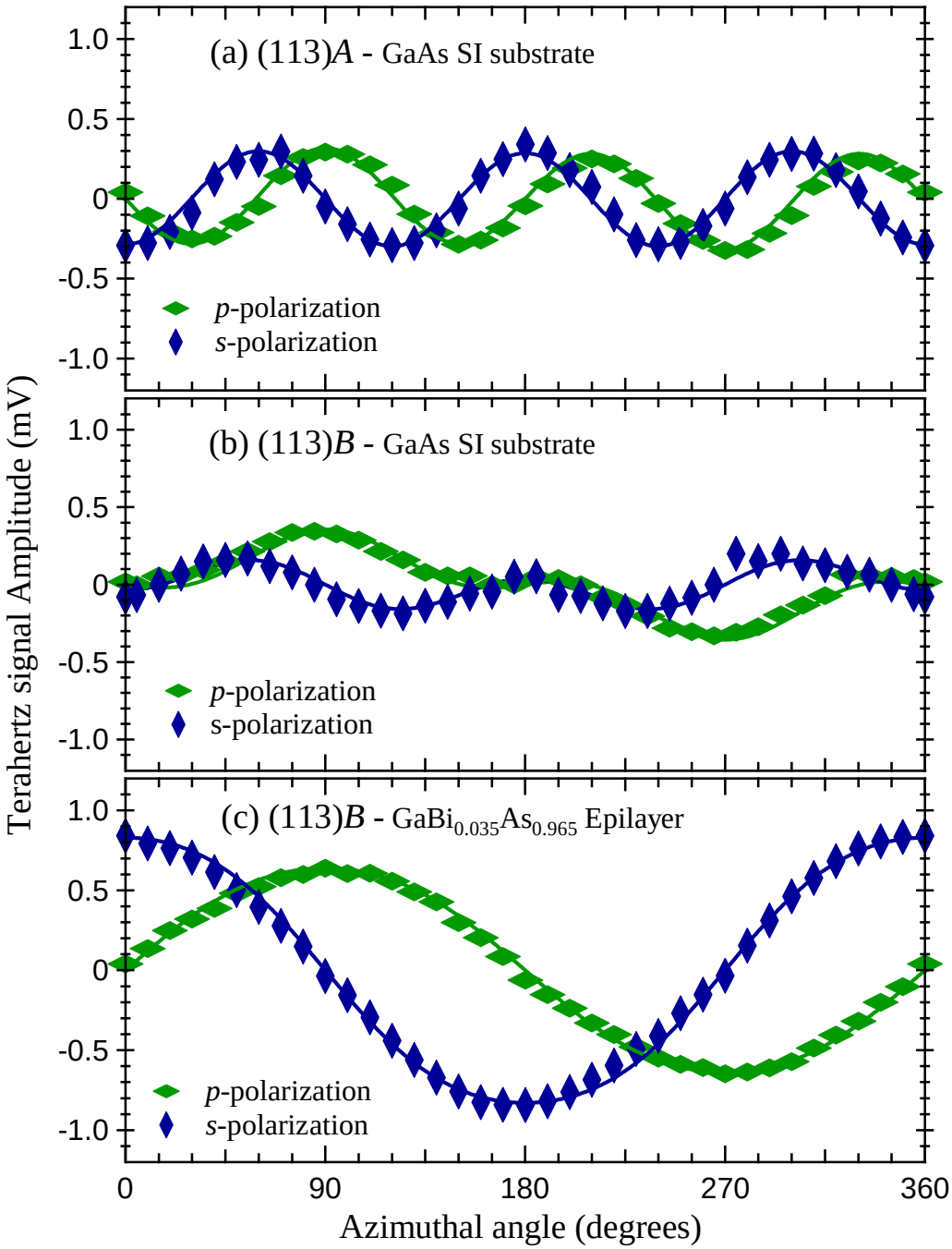

Figure 7.4 Measured THz signal amplitude for *p* and *s* polarized components with respect to the azimuthal rotation of the sample for (a) GaAs SI substrate - (113)*A* face, (b) GaAs SI substrate - (113)*B* face, and (b) $GaBi_{0.035}As_{0.965}$ epilayer - (113)*B* face. The measurements are performed in transmission geometry. Diamonds are the experimental data and lines are theoretical fits. The data fits well with theory for surface field contribution of $\gamma' F_0 = (1.7 \pm 0.3) d_{14}$ and $\gamma' F_0 = (4.8 \pm 0.1) d_{14}$ for GaAs and GaBiAs samples, respectively.

Now, let us discuss the effect of OR mechanism for epilayer samples. Figure 7.4(c) represents the *p* and *s* polarized THz components observed for (113)*B* $GaBi_{0.035}As_{0.965}$ sample with respect to the azimuthal angle. For this sample, the behavior observed is different from (113) GaAs SI samples. Instead of having three maxima and three minima, the polarization components exhibit one maximum and one minimum with rotation of the crystal about its surface normal. The general trend is still same with offset being zero for both polarized components indicating a zero or very small contribution from TC effects.

In the case of (113)*B* $GaBi_{0.035}As_{0.965}$ epilayer sample, by varying the contribution of surface OR components with respect to bulk components, it has been found that the close fit between theory and experiment can be obtained by setting the ratio $\gamma' F_0 = (4.8 \pm 0.1) d_{14}$. This is applicable to both *p* and *s* polarization components. This result indicates enhanced surface-field OR contribution in GaBiAs epilayer structure compared to GaAs substrate. Also, the overall signal strength for GaBiAs sample increases threefold in comparison to GaAs substrate. The improvement in THz signal strength for GaBiAs sample compared to GaAs substrate may have been caused by different electric fields or strain for these samples.

[Note: In the paper Radhanpura *et al.*[188], the results for azimuthal dependence of GaAs (113)*A* face have been presented as (113)*B*. However, the final outcome of GaBiAs having threefold increase in THz signal strength and surface field contribution being three times compared to GaAs is equally applicable to both *A* and *B* faces.]

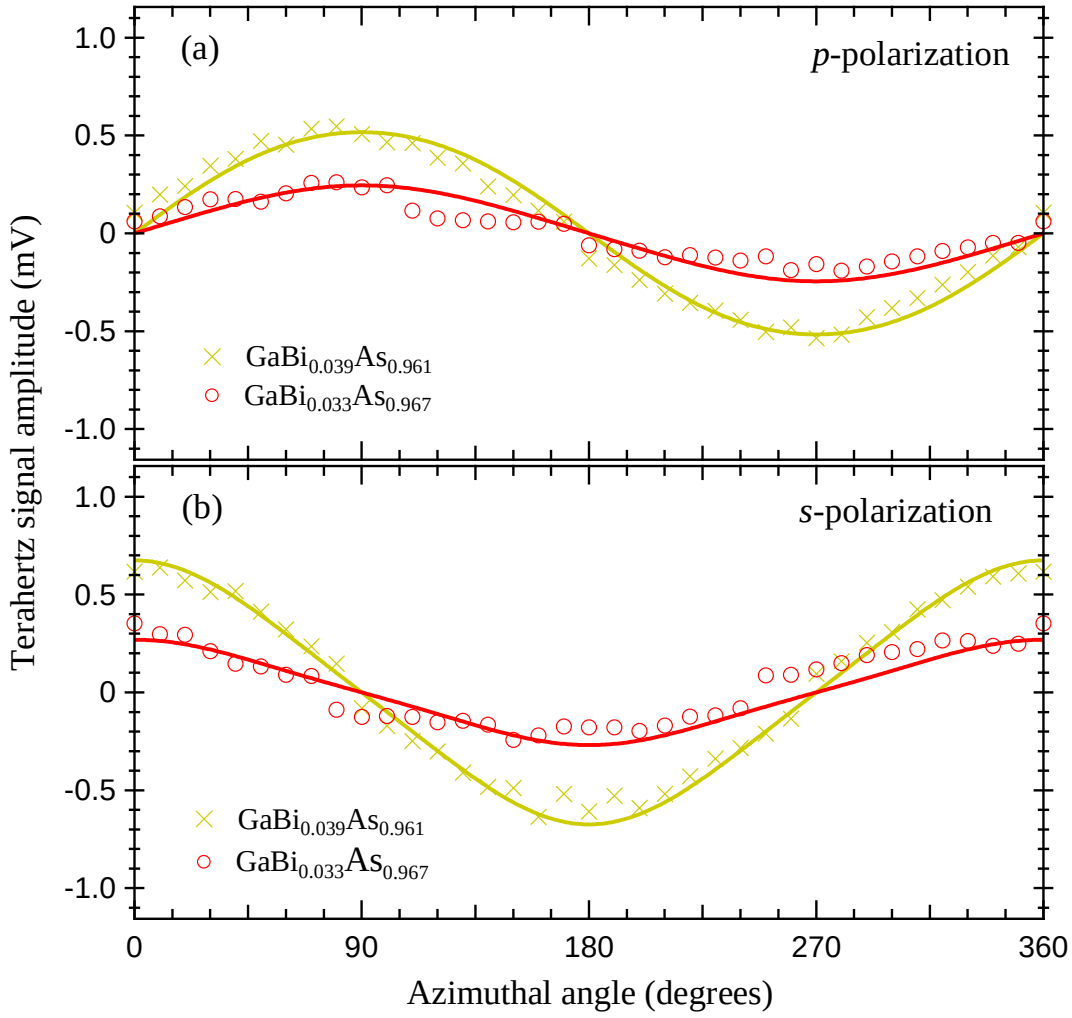

Figure 7.5 Measured THz signal amplitude with respect to azimuthal angle rotation for $GaBi_{0.039}As_{0.961}$ and $GaBi_{0.033}As_{0.967}$ for (a) *p*-polarization and (b) *s*-polarization. Both GaBiAs samples exhibit a single cycle azimuthal dependence for both *p* and *s* polarization components. Each mark represents the THz signal amplitude at a particular azimuthal angle. The lines show theory fits for these data. The surface polarization contribution is calculated to be $\gamma' F_0 = (4.7 \pm 0.5) d_{14}$.

Figure 7.5 shows the azimuthal angle dependence for other (113) epilayer samples. Both samples $GaBi_{0.039}As_{0.961}$ and $GaBi_{0.033}As_{0.967}$ exhibit one maximum and one minimum with 360° rotation of the sample azimuthally. Comparing experimental results for these samples with OR theory, the surface field contribution is calculated to be $\gamma' F_0 = (4.7 \pm 0.5) d_{14}$, which is consistent with the results for $GaBi_{0.035}As_{0.965}$ sample.

Hence, it can be said that the surface-field OR contribution in the generation of THz radiation increases in a GaBiAs epilayer structure on GaAs substrate.

7.4 Conclusion

Molecular beam epitaxial grown GaBiAs epilayers on GaAs substrates with different Bi content have been investigated for terahertz emission properties. For transmission geometry measurements, it was found that, except one, none of the (100) GaBiAs samples emit any THz radiation. All (113)*B* GaBiAs samples emit THz radiation with $GaBi_{0.035}As_{0.965}$ generating maximum terahertz output. Also, it has been shown that the THz efficiency of GaBiAs samples increases with increasing As flux used during the growth of the epilayers.

The results for varying incident optical fluence and in-plane magnetic field rotation indicate TC mechanism playing a negligible role in the THz emission and OR being the principal mechanism for generation of THz radiation in GaBiAs epilayer samples. Further, the azimuthal dependence measurements indicate an enhanced surface field OR contribution with the surface field being $F_0 = (4.7 \pm 0.5) d_{14}/\gamma'$ for (113)*B* GaBiAs epilayers as opposed to $F_0 = (1.7 \pm 0.3) d_{14}/\gamma'$ observed for (113)*A*/*B* GaAs substrate. Hence, it can be said that the effective surface-field OR contribution, as well as the surface field strength, increases in GaBiAs epilayers on GaAs substrates.

Chapter 8

8 GaAsN Epitaxial Layers on GaAs Substrates

8.1 Introduction

In the previous chapter, the effect of bismuth doping on THz emission efficiency of GaAs (113) and (100) crystal planes was discussed. In this chapter, the effect of nitrogen doping in GaAs (100) samples will be presented.

The substitution of nitrogen on the arsenic site causes a decrease in the bandgap of GaAs by 100 meV per percent of nitrogen[189]. Hence, it is possible to adjust the emission wavelength in the near-infrared range. It is found that the optical and structural quality of dilute nitrides degrades with increasing N content[190,191]. Using Deep Level Transient Spectroscopy (DLTS), a number of shallow and deep traps have been detected for GaAsN samples for different N contents[189]. These non-radiative recombination traps significantly modify the material's optical properties. They also reduce the life time of the charge carriers[176,192] and affect charge transport properties, which in turn may be expected to affect the THz generation efficiency of these materials. In this chapter, the change in terahertz generation efficiency caused by different N substitutions in GaAs over the range of N = 0% to 3% is presented.

8.2 Sample specifications

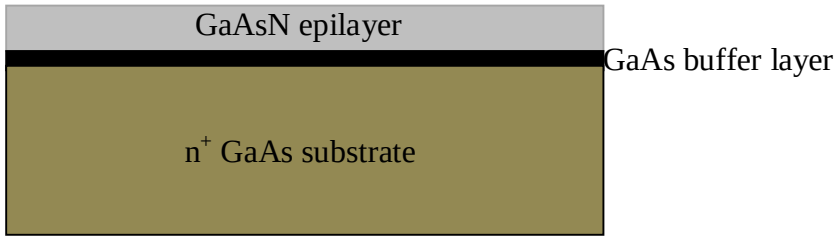

Figure 8.1 Structure of GaAsN epitaxial layer of 1 μm thickness grown by MBE on n^+ GaAs substrates. A highly doped 0.1 μm thick GaAs layer is used as buffer layer between the epilayer and the substrate.

The samples reported on here are 1 μm thick epitaxial layers of GaAsN grown by Molecular Beam Epitaxy (MBE) on n+ GaAs substrates with (100) crystallographic orientation. The growth temperature was 500 ^oC. A heavily Si-doped GaAs layer of 0.1 μm thickness was used as a buffer layer between the epitaxial layer and substrate. In

total seven samples were investigated as THz emitters: Vn1256 - control sample (N=0%), Vn667 (N=0.2%), Vn666 (N=0.4%), Vn669 (N=0.8%), Vn668 (N=1.2%), Vn670 (N=2.5%), and InGaAsN Vn671 (N=3%) with In=8% substituted for Ga. These samples were provided by Prof. Mohamed Henini from the University of Nottingham, United Kingdom. The details of the MBE growth and DLTS results have been reported previously[189,193].

8.3 Experimental results and discussion

All $GaAs_{1-x}N_x$samples were tested for transmission of THz radiation through them. None of the sample in the series, including control sample, transmitted any THz. This is due to the fact that all these samples were grown on n^+ substrate. Hence, it is not possible to measure the response of these samples as emitters in the transmission geometry. The data presented here are taken in quasireflection geometry with angle of incidence and detection being 45^o with the surface normal. Further, it can be said that for these GaAsN epilayer structures, most of the interaction with the NIR pulses is within the epilayer or at the interface between epilayer and substrate.

THz spectra were observed from all GaAsN samples and are shown in Figure 8.2. The vertical axis is the THz signal measured as differential voltage across the photo-diode pair and the horizontal axis is the time delay between the excitation pump beam and the probe beam. A systematic decrease is observed with increasing nitrogen content. The peak-to-peak signals for different N content are given in Table 8.1.

The general trend is that the THz signal decreases with increasing N content, except for the N = 0.4% GaAsN sample. The GaAs (Vn1256) control sample generates the maximum signal. InGaAsN with N = 3% shows a small improvement in the signal strength compared to GaAsN with N = 2.5%.

The small increase in InGaAsN THz emission may be due to the incorporation of indium. The variation in THz field amplitude with nitrogen content is shown in Figure 8.3 for N = 0.2% to N = 2.5%. An exponential decay in THz field amplitude is observed with increase in N content as shown by the fit. (excluding the N = 0.4% sample)

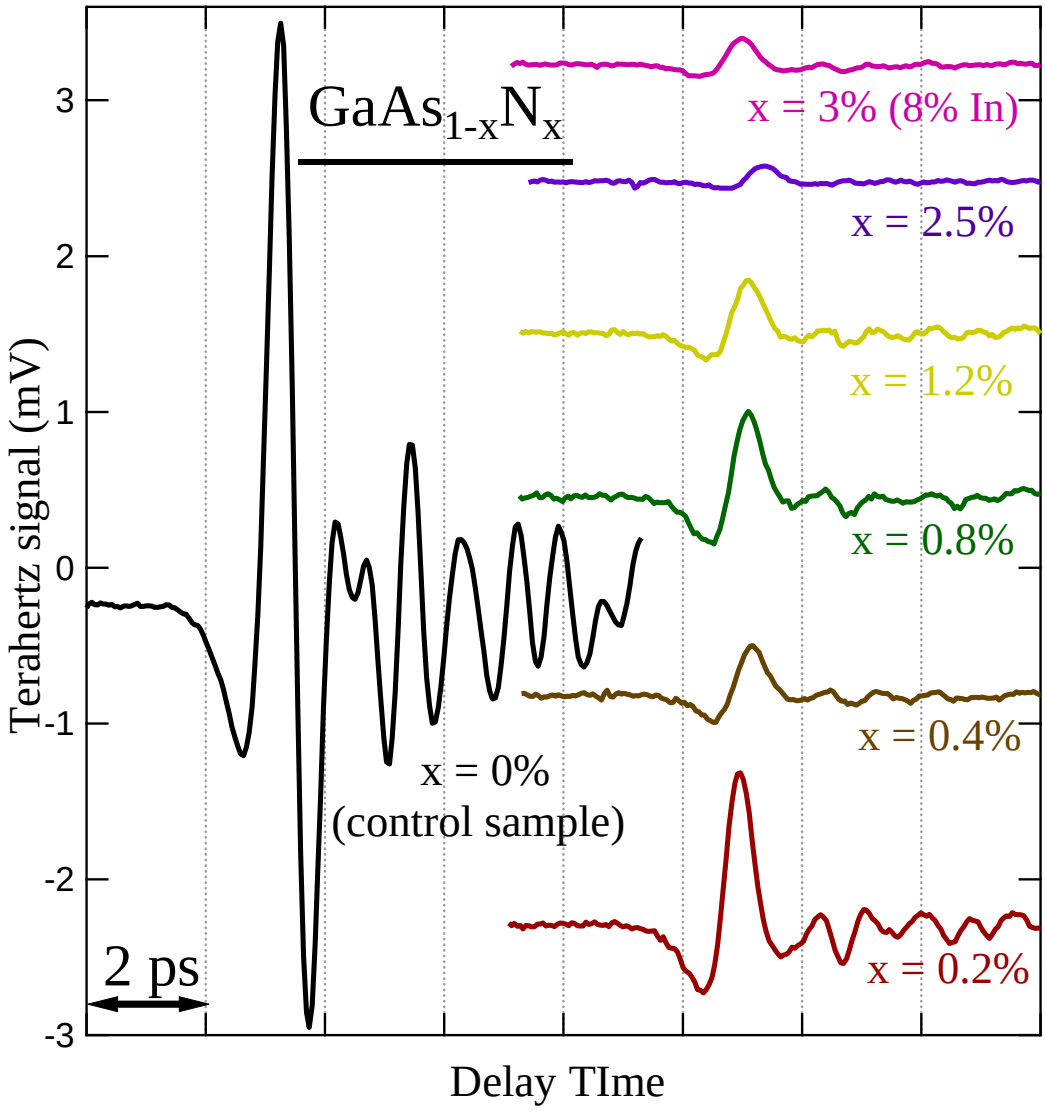

Figure 8.2 Response of GaAsN samples as terahertz emitters in quasireflection geometry with different N contents. The THz electric field is measured as the differential voltage across the photodiode pair. The horizontal axis is the pump-probe delay time on a ps time scale. The signals are shifted on both axes for clarity. As can be seen from the figure, the GaAs control sample generates maximum THz signal. Incorporation of nitrogen quenches THz generation.

Table 8.1 Response of GaAsN samples measured as THz emitters. Vn671 is a InGaAsN sample with 3% nitrogen and 8% indium. Substitution of indium with gallium causes a small improvement in THz output as compared to the GaAsN sample with 2.5% N

Sample	N (%)	THz signal amplitude (mV)
Vn1256 (control sample)	0	6.45
Vn667	0.2	1.42
Vn666	0.4	0.49
Vn669	0.8	0.85
Vn668	1.2	0.51
Vn670	2.5	0.14
Vn671	3.0 (with 8% In)	0.24

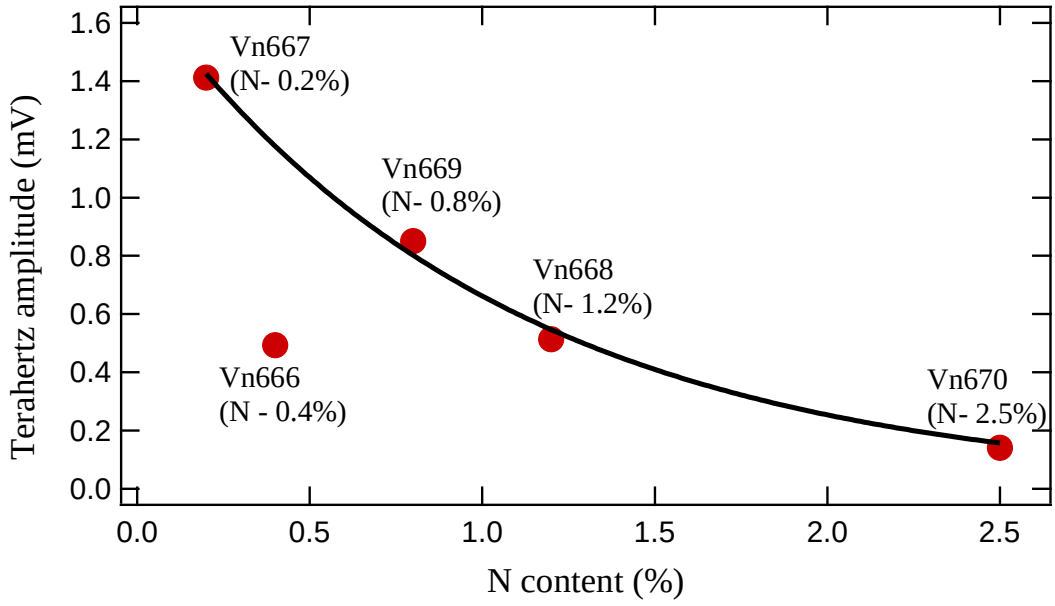

Figure 8.3 Variation in terahertz field amplitude with N content for $GaAs_{1-x}N_x$ samples for x=0.2% to 2.5%. Each dot represents the peak-to-peak THz amplitude. The general trend is that as N concentration increases, the THz signal decreases exponentially (except for N = 0.4% Vn666 sample). Fitting the data ignoring N = 0.4% (Vn666) gives the fit $A = A_0 \exp(-N / N_0)$ with $A_0 = 1.7$ and $N_0 = 1.1$.

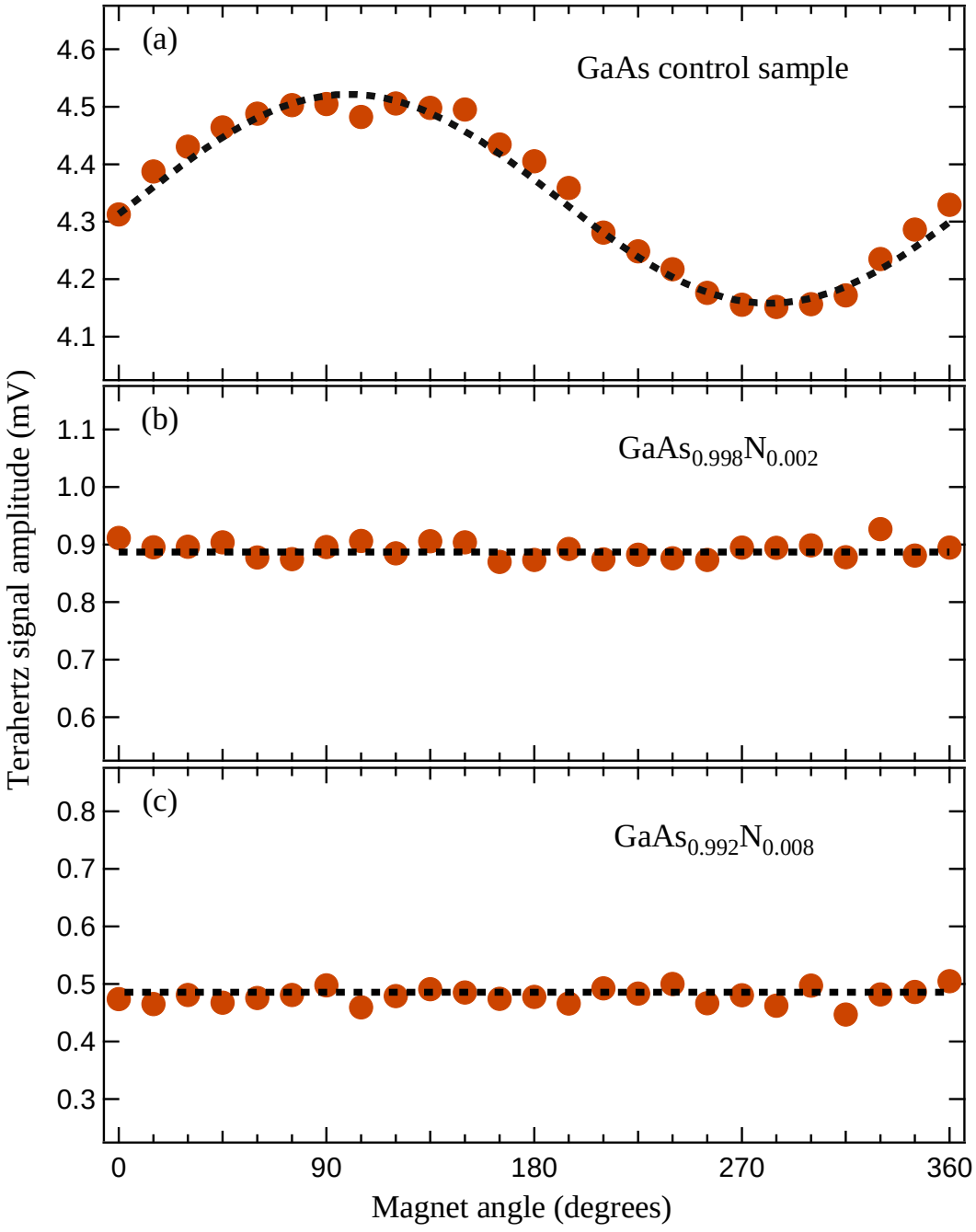

Figure 8.4 Effect of rotation of in-plane magnetic field for GaAsN samples. Each dot represents the THz peak-to-peak signal measured at different magnet angles and the dashed line is the appropriate sinusoidal or straight line fit to the signal variation. For the GaAs control sample, a systematic increased and decreased THz signal is observed with the magnet rotation in the sample surface plane. On the other hand, for the $GaAs_{0.998}N_{0.002}$ and $GaAs_{0.992}N_{0.008}$ samples, the THz signal does not vary with magnet rotation within experimental error. A similar non-varying response with magnet rotation has been observed for all the GaAsN samples.

In order to determine explicitly the mechanism behind THz generation from these set of samples, the effect of an in-plane magnetic field on the generated THz was measured. Figure 8.4 shows the in-plane magnetic field dependence for GaAs, $GaAs_{0.98}N_{0.02}$, and $GaAs_{0.92}N_{0.08}$ using a 0.15-T magnet. A symmetrical change with magnet rotation is observed for GaAs, indicative of a contribution of transient current (TC) to THz generation. On the other hand, for the GaAsN samples, no change is observed with magnet rotation. This result confirms that there is no or very little contribution of TC effects in THz generated from the GaAsN samples. Such non-varying response with magnet rotation is observed for all GaAsN samples. Hence, it can be said that the effect of transient currents reduces by incorporation of nitrogen in GaAs crystals.

As we have observed in previous chapters, the azimuthal rotation of the crystal can reveal contribution from non-linear emission mechanism conclusively. Such azimuthal angle dependence for *p*-polarized THz components from GaAs control sample, $GaAs_{0.988}N_{0.012}$, and $In_{0.08}Ga_{0.92}As_{0.97}N_{0.03}$ epilayers samples are given in Figure 8.5. All three samples show a single cycle azimuthal variation in the THz amplitude with rotation of the sample azimuthally. This confirms the presence of optical rectification (OR) in generation of THz radiation from these samples. A similar single cycle dependence has been observed for all other GaAsN samples.

The offsets from zero of this single cycle behavior give an indication of the contribution of transient currents in the THz generation. For (100) orientation, bulk OR causes systematic change for emitter rotation, while no variation is observed for surface OR[46]. Thus, in Figure 8.5, the azimuthal change observed for (100) GaAsN samples is purely due to the bulk OR, while the offset observed represents the combined effect of TC and surface OR components. Further, it has been observed that the principal mechanism for linear effects in GaAs is the surface field effect rather than the photo-Dember effect[18]. Thus, the linear components observed for GaAsN samples are the property of surface field present at the sample surface. The GaAs control sample has a large offset of 5.40 mV, while the offsets for the GaAsN and InGaAsN samples are 0.31 mV and 0.19 mV, respectively, which immediately suggests substantial change in surface properties of the latter two materials which causes a reduction in the overall THz signal.

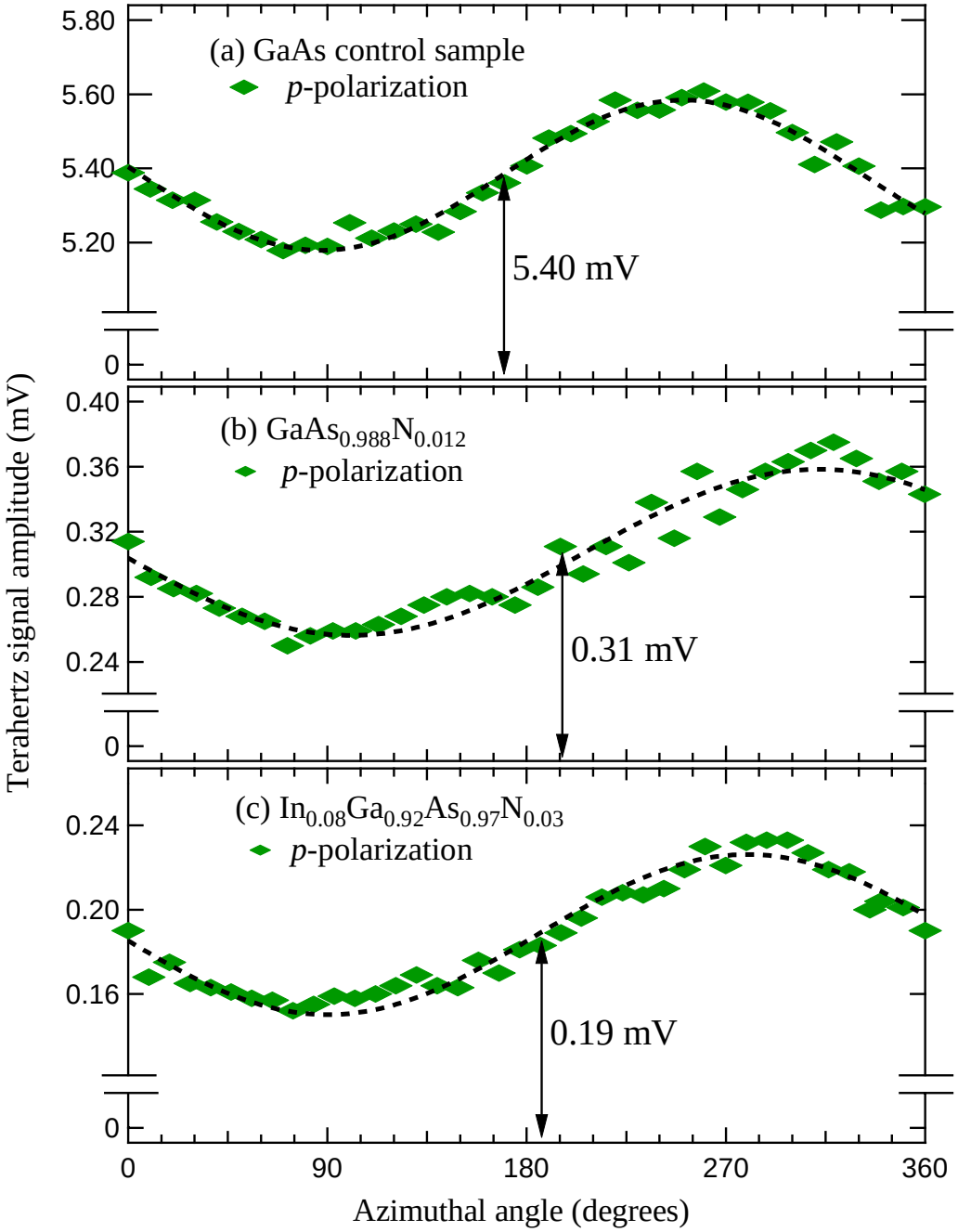

Figure 8.5 Azimuthal angle dependence for *p*-polarized THz field components generated from (a) GaAs, (b) $GaAs_{0.988}N_{0.012}$, and (c) $In_{0.08}Ga_{0.92}As_{0.97}N_{0.03}$ samples. Each data point represents the peak-to-peak voltage measured at particular azimuthal angle of emitter and the dashed line is the appropriate sinusoidal fit. A single cycle dependence is observed with the rotation of emitter through 360 degrees, which is the characteristic of THz emission by optical rectification. Similar behavior is observed for all the other GaAsN samples.

These findings for GaAsN samples are opposite to what have been observed for GaBiAs samples as presented in chapter 7, where it was observed that the Bi substitution in GaAs improved the surface field contribution in THz generation and led to enhanced THz emission from GaBiAs samples.

The cause of the drastic change in THz emission efficiency of GaAsN samples is attributed to degradation of the surface and electron traps produced in these materials. The DLTS measurements show only a single deep trap level in the GaAs control sample with activation energy of 0.76 eV. In contrast, in GaAsN samples several electron traps are detected, including both shallow and deep traps[189,193]. These traps alter the charge transport properties of the material significantly and hence directly affect the amount of THz generated through surface emission.

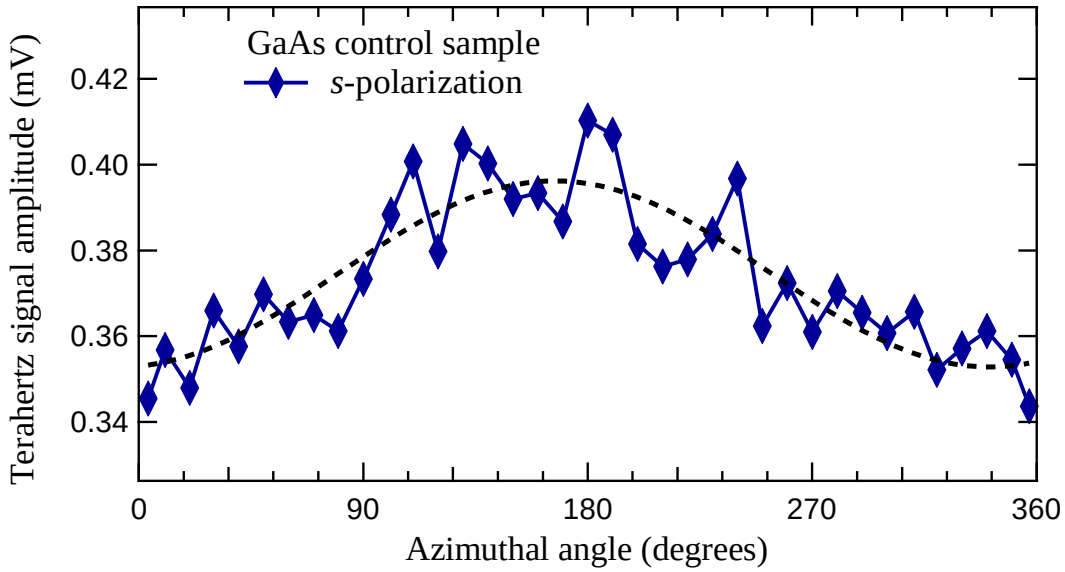

Figure 8.6 Azimuthal angle dependence for *s*-polarized THz field components generated in the GaAs control sample. Each data point represents peak-to-peak voltage measured at particular azimuthal angle of emitter and dashed line is the appropriate fit.

Figure 8.6 shows *s*-polarized THz field components with respect to azimuthal variation for GaAs control sample. Although the noise level was very high, the data can be broadly fitted to one cycle dependence consistent with the results observed for *p*-polarized components. The results for azimuthal variation obtained from these samples can be compared with general theory of optical rectification. As discussed in chapter 5, the THz polarization components for bulk and surface OR effects for (100) crystal plane exhibit two cycle dependence due to bulk OR along with an offset due to surface OR

and transient current effects. The behavior for (100) InAs sample match well with the theory (Figure 5.1). However, the observed results for (100) GaAsN samples give one cycle azimuthal dependence instead of expected two cycle change.

The 1θ dependence for (100) GaAsN samples suggest that it is quite possible that there is some unknown azimuthally varying mechanism also involved in generation of THz radiation from these crystal planes. Such one cycle dependence behavior was earlier observed for (100) InP samples[138] which was thought to be due to crystal twinning. Also, a quite distinct feature of four-cycle azimuthal angle dependence have been observed for (100) InAs[172] and a-plane InN[194] samples.

8.4 Conclusion

MBE grown GaAsN epilayer samples with different nitrogen concentration have been studied as source of THz radiation. A significant reduction is observed in THz emission efficiency as the nitrogen concentration increases. The GaAs control sample generates THz through both optical rectification and transient current mechanisms, while in the GaAsN epilayers the THz is generated mainly through bulk optical rectification and the transient current effect is negligible. This behavior is attributed to the change in surface properties caused by presence of multiple electron traps. Further, from the azimuthal behavior of these samples, it can be seen that there is a possible presence of other mechanism along with conventional OR and TC mechanisms.

Chapter 9

9 Conclusion

Various semiconductor materials have been investigated as sources of THz emission in the absence of any external bias. A time-domain terahertz spectroscopy system was used with electro-optic detection and different experimental geometries for characterization of materials with respect to the different mechanisms involved in THz generation. The measurements in turn provide information about important properties of the material examined as emitters.

In chapter 3, the general theory of optical rectification (OR) for zinc-blende structure with any arbitrary crystallographic direction was presented. The theory was then fitted with the experimental results for (11*N*) GaAs crystal planes for normal incidence of excitation radiation. The comparison of results with theory indicates a contribution from both bulk and surface OR effects for THz emission from these planes. Further analyses gave information about the surface-depletion field present at the semiconductor surface. The OR measurements also make it possible to obtain the precise crystal direction.

In chapter 4, the theory for OR was presented for non-normal incidence of the excitation radiation and the experimental results for (11*N*) GaAs crystal planes in quasireflection geometry were compared with theory. It is possible to obtain additional information using this set up; in particular, about the surface field effect. The results show presence of both bulk OR and surface OR, along with an azimuthally invariant transient current mechanism.

In chapter 5, the experimental results for azimuthal angle variation for the transient current emitter (100) InAs were presented. The effective contribution from linear and non-linear effects was estimated. Further, the general theory for in-plane magnetic field rotation on THz field for TC emitters was presented, along with the experimental results for the InAs emitter. The external magnetic field may be able to enhance the THz field strength due to rotation of the dipole responsible for generating THz transient. Also, the lateral photo-Dember effect was discussed.

In chapter 6, the effect of heavy noble gas Xe and Kr irradiation on (100) and (111) InP was presented for bulk and nanoporous honeycomb structures. With ion irradiation, the THz emission efficiency of (111) samples increases. On the other hand, the signal strength for (100) InP does not improve with ion irradiation. Xe irradiation is more effective than Kr irradiation. Further, the effect of in-plane magnet rotation, varying optical fluence, and azimuthal angle dependence confirms that the principal mechanism for THz emission from these samples is optical rectification rather than a transient current.

In chapter 7, the investigation of epilayer structures of GaBiAs on GaAs samples as THz emitter with different bismuth content was presented. Two different planes, (100) and (113)*B*, were used for epilayer growth. The general trend is that the THz signal strength increases with increase in the As flux used during epilayer growth. The measurements of (113)*B* GaBiAs samples with optical fluence variation and magnetic field rotation confirms optical rectification being the principal mechanism involved in THz generation from these semiconductors. The results for azimuthal angle dependence for (113)*B* GaBiAs with Bi = 3.5% shows a threefold increase in the signal strength with respect to the GaAs substrate. Further, a single cycle azimuthal dependence indicates a higher proportion of surface OR components in comparison to the GaAs substrate.

In chapter 8, the study of epilayer structures of GaAsN on GaAs substrate as THz emitters have been presented with varying nitrogen percentage. The THz field amplitude decreases exponentially with increasing nitrogen concentration. Azimuthal angle dependence and magnetic field dependence results indicate a large reduction in the surface field contribution in THz generation. The quenching of THz emission efficiency is attributed to the change in surface properties caused by presence of multiple electron traps in GaAsN samples.

Thus, it has been shown that THz emission from semiconductor materials can be improved significantly by modification of base materials in a variety of ways. Further study on changing the sample properties and experimental conditions may lead to find even better THz sources.

Appendices

Appendix A – Optical Rectification Coefficients: General Case

Optical rectification coefficients for (*hkl*) crystal planes as they appear in chapter 3.

$$m = \sqrt{h^2 + k^2 + l^2}, \quad \text{A. 1}$$

$$n = \sqrt{h^2 + k^2}, \quad \text{A. 2}$$

$$s = \sin\phi_{\text{NIR}} \cos\Phi, \quad \text{A. 3}$$

$$c = \cos\phi_{\text{NIR}} \cos\Phi, \quad \text{A. 4}$$

$$t = \sin\Phi, \quad \text{A. 5}$$

$$d = d_{14} E_0^2, \quad \text{A. 6}$$

$$g = \gamma F_0 E_0^2, \quad \text{A. 7}$$

$$(A_{11})_{\frac{A}{B}} = \pm\frac{h}{m}, \quad \text{A. 8}$$

$$(A_{12})_{\frac{A}{B}} = \mp\frac{k}{n}, \quad \text{A. 9}$$

$$(A_{13})_{\frac{A}{B}} = -\frac{hl}{mn}, \quad \text{A. 10}$$

$$(A_{21})_{\frac{A}{B}} = \pm\frac{k}{m}, \quad \text{A. 11}$$

$$(A_{22})_{\frac{A}{B}} = \pm\frac{h}{n}, \quad \text{A. 12}$$

$$(A_{23})_{\frac{A}{B}} = -\frac{kl}{mn}, \quad \text{A. 13}$$

$$(A_{31})_{\frac{A}{B}} = \pm\frac{l}{m}, \quad \text{A. 14}$$

$$(A_{32})_{\frac{A}{B}} = 0, \quad \text{A. 15}$$

$$(A_{33})_{\frac{A}{B}} = \frac{n}{m}, \quad \text{A. 16}$$

$$(B_{11})_{\frac{A}{B}} = \pm\frac{hs}{m}, \qquad \text{A. 17}$$

$$(B_{12})_{\frac{A}{B}} = \mp\frac{kc}{n} - \frac{hlt}{mn}, \qquad \text{A. 18}$$

$$(B_{13})_{\frac{A}{B}} = -\frac{hlc}{mn} \pm \frac{kt}{n}, \qquad \text{A. 19}$$

$$(B_{21})_{\frac{A}{B}} = \pm\frac{ks}{m}, \qquad \text{A. 20}$$

$$(B_{22})_{\frac{A}{B}} = \pm\frac{hc}{n} - \frac{klt}{mn}, \qquad \text{A. 21}$$

$$(B_{23})_{\frac{A}{B}} = -\frac{klc}{mn} \mp \frac{ht}{n}, \qquad \text{A. 22}$$

$$(B_{31})_{\frac{A}{B}} = \pm\frac{ls}{m}, \qquad \text{A. 23}$$

$$(B_{32})_{\frac{A}{B}} = \frac{nt}{m}, \qquad \text{A. 24}$$

$$(B_{33})_{\frac{A}{B}} = \frac{nc}{m}, \qquad \text{A. 25}$$

$$(C_{11}/d)_{\frac{A}{B}} = \frac{kl}{m^2}(2s^2 - c^2 - t^2), \qquad \text{A. 26}$$

$$(C_{12}/d)_{\frac{A}{B}} = \frac{2hl}{mn}sc \pm \frac{2k(h^2 + k^2 - l^2)}{m^2 n}st, \qquad \text{A. 27}$$

$$(C_{13}/d)_{\frac{A}{B}} = \pm\frac{2k(h^2 + k^2 - l^2)}{m^2 n}sc - \frac{2hl}{mn}st, \qquad \text{A. 28}$$

$$(C_{14}/d)_{\frac{A}{B}} = \frac{kl}{m^2}(c^2 - t^2) \pm \frac{2h}{m}ct, \qquad \text{A. 29}$$

$$(C_{15}/d)_{\frac{A}{B}} = \pm\frac{h}{m}(c^2 - t^2) - \frac{2kl}{m^2}ct, \qquad \text{A. 30}$$

$$(C_{21}/d)_{\frac{A}{B}} = \frac{hl}{m^2}(2s^2 - c^2 - t^2), \quad \text{A. 31}$$

$$(C_{22}/d)_{\frac{A}{B}} = -\frac{2kl}{mn}sc \pm \frac{2h(h^2+k^2-l^2)}{m^2n}st, \quad \text{A. 32}$$

$$(C_{23}/d)_{\frac{A}{B}} = \pm\frac{2h(h^2+k^2-l^2)}{m^2n}sc + \frac{2kl}{mn}st, \quad \text{A. 33}$$

$$(C_{24}/d)_{\frac{A}{B}} = \frac{hl}{m^2}(c^2 - t^2) \mp \frac{2k}{m}ct, \quad \text{A. 34}$$

$$(C_{25}/d)_{\frac{A}{B}} = \mp\frac{k}{m}(c^2 - t^2) - \frac{2hl}{m^2}ct, \quad \text{A. 35}$$

$$(C_{31}/d)_{\frac{A}{B}} = \frac{hk}{m^2}(2s^2 - c^2 - t^2), \quad \text{A. 36}$$

$$(C_{32}/d)_{\frac{A}{B}} = \frac{2(h^2-k^2)}{mn}sc \mp \frac{4hkl}{m^2n}st, \quad \text{A. 37}$$

$$(C_{33}/d)_{\frac{A}{B}} = \mp\frac{4hkl}{m^2n}sc - \frac{2(h^2-k^2)}{mn}st, \quad \text{A. 38}$$

$$(C_{34}/d)_{\frac{A}{B}} = -\frac{hk(h^2+k^2+2l^2)}{m^2n^2}(c^2 - t^2) \mp \frac{2l(h^2-k^2)}{mn^2}ct, \quad \text{A. 39}$$

$$(C_{35}/d)_{\frac{A}{B}} = \mp\frac{l(h^2-k^2)}{mn^2}(c^2 - t^2) + \frac{2hk(h^2+k^2+2l^2)}{m^2n^2}ct, \quad \text{A. 40}$$

$$(D_{11}/d)_{\frac{A}{B}} = \pm\frac{3hkl}{m^3}(2s^2 - c^2 - t^2), \quad \text{A. 41}$$

$$(D_{12}/d)_{\frac{A}{B}} = \pm\frac{4l(h^2-k^2)}{m^2n}sc + \frac{4hk(h^2+k^2-2l^2)}{m^3n}st, \quad \text{A. 42}$$

$$(D_{13}/d)_{\frac{A}{B}} = \frac{4hk(h^2+k^2-2l^2)}{m^3n}sc \mp \frac{4l(h^2-k^2)}{m^2n}st, \quad \text{A. 43}$$

$$(D_{14}/d)_{\frac{A}{B}} = \pm\frac{hkl(h^2+k^2-2l^2)}{m^3n^2}(c^2 - t^2) + \frac{2(h^2-k^2)(h^2+k^2-l^2)}{m^2n^2}ct, \quad \text{A. 44}$$

$$(D_{15}/d)_{\frac{A}{B}} = \frac{(h^2-k^2)(h^2+k^2-l^2)}{m^2n^2}(c^2 - t^2) \mp \frac{2hkl(h^2+k^2-2l^2)}{m^3n^2}ct, \quad \text{A. 45}$$

$$(D_{21}/d)_{\frac{A}{B}} = \pm\frac{l(h^2-k^2)}{m^2n}(2s^2-c^2-t^2), \quad \text{A. 46}$$

$$(D_{22}/d)_{\frac{A}{B}} = \mp\frac{4hkl}{mn^2}sc + \frac{2(h^2-k^2)(h^2+k^2-l^2)}{m^2n^2}st, \quad \text{A. 47}$$

$$(D_{23}/d)_{\frac{A}{B}} = \frac{2(h^2-k^2)(h^2+k^2-l^2)}{m^2n^2}sc \pm \frac{4hkl}{mn^2}st, \quad \text{A. 48}$$

$$(D_{24}/d)_{\frac{A}{B}} = \pm\frac{l(h^2-k^2)}{m^2n}(c^2-t^2) - \frac{4hk}{mn}ct, \quad \text{A. 49}$$

$$(D_{25}/d)_{\frac{A}{B}} = -\frac{2hk}{mn}(c^2-t^2) \mp \frac{2l(h^2-k^2)}{m^2n}ct, \quad \text{A. 50}$$

$$(D_{31}/d)_{\frac{A}{B}} = \frac{hk(h^2+k^2-2l^2)}{m^3n}(2s^2-c^2-t^2), \quad \text{A. 51}$$

$$(D_{32}/d)_{\frac{A}{B}} = \frac{2(h^2-k^2)(h^2+k^2-l^2)}{m^2n^2}sc \mp \frac{4hkl(2h^2+2k^2-l^2)}{m^3n^2}st, \quad \text{A. 52}$$

$$(D_{33}/d)_{\frac{A}{B}} = \mp\frac{4hkl(2h^2+2k^2-l^2)}{m^3n^2}sc - \frac{2(h^2-k^2)(h^2+k^2-l^2)}{m^2n^2}st, \quad \text{A. 53}$$

$$(D_{34}/d)_{\frac{A}{B}} = -\frac{hk(h^2+k^2+4l^2)}{m^3n}(c^2-t^2) \mp \frac{4l(h^2-k^2)}{m^2n}ct, \quad \text{A. 54}$$

$$(D_{35}/d)_{\frac{A}{B}} = \mp\frac{2l(h^2-k^2)}{m^2n}(c^2-t^2) + \frac{2hk(h^2+k^2+4l^2)}{m^3n}ct, \quad \text{A. 55}$$

$$(G_{11}/d)_{\frac{A}{B}} = \pm\frac{3hkl}{m^3}(2s^2-c^2-t^2), \quad \text{A. 56}$$

$$(G_{12}/d)_{\frac{A}{B}} = \pm\frac{4l(h^2-k^2)}{m^2n}sc + \frac{4hk(h^2+k^2-2l^2)}{m^3n}st, \quad \text{A. 57}$$

$$(G_{13}/d)_{\frac{A}{B}} = \frac{4hk(h^2+k^2-2l^2)}{m^3n}sc \mp \frac{4l(h^2-k^2)}{m^2n}st, \quad \text{A. 58}$$

$$(G_{14}/d)_{\frac{A}{B}} = \pm\frac{hkl(h^2+k^2-2l^2)}{m^3n^2}(c^2-t^2) + \frac{2(h^2-k^2)(h^2+k^2-l^2)}{m^2n^2}ct, \quad \text{A. 59}$$

$$(G_{15}/d)_{\frac{A}{B}} = \frac{(h^2-k^2)(h^2+k^2-l^2)}{m^2n^2}(c^2-t^2) \mp \frac{2hkl(h^2+k^2-2l^2)}{m^3n^2}ct, \quad \text{A. 60}$$

$$(G_{16}/d)_{\frac{A}{B}} = 0, \qquad \text{A. 61}$$

$$(G_{17}/d)_{\frac{A}{B}} = 0, \qquad \text{A. 62}$$

$$(G_{21}/d)_{\frac{A}{B}} = \mp\frac{6hkl}{m^3}sc, \qquad \text{A. 63}$$

$$(G_{22}/d)_{\frac{A}{B}} = \pm\frac{l(h^2-k^2)}{2m^2n}(4s^2-3c^2-t^2) - \frac{hk(h^2+k^2-2l^2)}{m^3n}ct, \qquad \text{A. 64}$$

$$(G_{23}/d)_{\frac{A}{B}} = \frac{hk(h^2+k^2-2l^2)}{2m^3n}(4s^2-3c^2-t^2) \pm \frac{l(h^2-k^2)}{m^2n}ct, \qquad \text{A. 65}$$

$$(G_{24}/d)_{\frac{A}{B}} = \pm\frac{2hkl(h^2+k^2-2l^2)}{m^3n^2}sc + \frac{2(h^2-k^2)(h^2+k^2-l^2)}{m^2n^2}st, \qquad \text{A. 66}$$

$$(G_{25}/d)_{\frac{A}{B}} = \frac{2(h^2-k^2)(h^2+k^2-l^2)}{m^2n^2}sc \mp \frac{2hkl(h^2+k^2-2l^2)}{m^3n^2}st, \qquad \text{A. 67}$$

$$(G_{26}/d)_{\frac{A}{B}} = \pm\frac{3l(h^2-k^2)}{2m^2n}(c^2-t^2) - \frac{3hk(h^2+k^2+2l^2)}{m^3n}ct, \qquad \text{A. 68}$$

$$(G_{27}/d)_{\frac{A}{B}} = -\frac{3hk(h^2+k^2+2l^2)}{2m^3n}(c^2-t^2) \mp \frac{3l(h^2-k^2)}{m^2n}ct, \qquad \text{A. 69}$$

$$(G_{31}/d)_{\frac{A}{B}} = \mp\frac{6hkl}{m^3}st, \qquad \text{A. 70}$$

$$(G_{32}/d)_{\frac{A}{B}} = \frac{hk(h^2+k^2-2l^2)}{2m^3n}(4s^2-c^2-3t^2) \mp \frac{l(h^2-k^2)}{m^2n}ct, \qquad \text{A. 71}$$

$$(G_{33}/d)_{\frac{A}{B}} = \mp\frac{l(h^2-k^2)}{2m^2n}(4s^2-c^2-3t^2) - \frac{hk(h^2+k^2-2l^2)}{m^3n}ct, \qquad \text{A. 72}$$

$$(G_{34}/d)_{\frac{A}{B}} = \frac{2(h^2-k^2)(h^2+k^2-l^2)}{m^2n^2}sc \mp \frac{2hkl(h^2+k^2-2l^2)}{m^3n^2}st, \qquad \text{A. 73}$$

$$(G_{35}/d)_{\frac{A}{B}} = \mp\frac{2hkl(h^2+k^2-2l^2)}{m^3n^2}sc - \frac{2(h^2-k^2)(h^2+k^2-l^2)}{m^2n^2}st, \qquad \text{A. 74}$$

$$(G_{36}/d)_{\frac{A}{B}} = -\frac{3hk(h^2+k^2+2l^2)}{2m^3n}(c^2-t^2) \mp \frac{3l(h^2-k^2)}{m^2n}ct, \qquad \text{A. 75}$$

$$(G_{37}/d)_{\frac{A}{B}} = \mp\frac{3l(h^2-k^2)}{2m^2n}(c^2-t^2)+\frac{3hk(h^2+k^2+2l^2)}{m^3n}ct, \quad \text{A. 76}$$

$$(T_{11}/g)_{\frac{A}{B}} = \pm\frac{h^3}{m^3}s^2 \pm \frac{h(k^2+l^2)}{2m^3}(c^2+t^2), \quad \text{A. 77}$$

$$(T_{12}/g)_{\frac{A}{B}} = \mp\frac{2h^2k}{m^2n}sc-\frac{2h^3l}{m^3n}st, \quad \text{A. 78}$$

$$(T_{13}/g)_{\frac{A}{B}} = -\frac{2h^3l}{m^3n}sc \pm \frac{2h^2k}{m^2n}st, \quad \text{A. 79}$$

$$(T_{14}/g)_{\frac{A}{B}} = \pm\frac{h(h^2k^2+k^4+k^2l^2-h^2l^2)}{2m^3n^2}(c^2-t^2)+\frac{2h^2kl}{m^2n^2}ct, \quad \text{A. 80}$$

$$(T_{15}/g)_{\frac{A}{B}} = \frac{h^2kl}{m^2n^2}(c^2-t^2)\mp\frac{h(h^2k^2+k^4+k^2l^2-h^2l^2)}{m^3n^2}ct, \quad \text{A. 81}$$

$$(T_{21}/g)_{\frac{A}{B}} = \pm\frac{k^3}{m^3}s^2 \pm \frac{k(h^2+l^2)}{2m^3}(c^2+t^2), \quad \text{A. 82}$$

$$(T_{22}/g)_{\frac{A}{B}} = \pm\frac{2hk^2}{m^2n}sc-\frac{2k^3l}{m^3n}st, \quad \text{A. 83}$$

$$(T_{23}/g)_{\frac{A}{B}} = -\frac{2k^3l}{m^3n}sc\mp\frac{2hk^2}{m^2n}st, \quad \text{A. 84}$$

$$(T_{24}/g)_{\frac{A}{B}} = \pm\frac{k(h^4+h^2k^2+h^2l^2-k^2l^2)}{2m^3n^2}(c^2-t^2)-\frac{2hk^2l}{m^2n^2}ct, \quad \text{A. 85}$$

$$(T_{25}/g)_{\frac{A}{B}} = -\frac{hk^2l}{m^2n^2}(c^2-t^2)\mp\frac{k(h^4+h^2k^2+h^2l^2-k^2l^2)}{m^3n^2}ct, \quad \text{A. 86}$$

$$(T_{31}/g)_{\frac{A}{B}} = \pm\frac{l^3}{m^3}s^2 \pm \frac{l(h^2+k^2)}{2m^3}(c^2+t^2), \quad \text{A. 87}$$

$$(T_{32}/g)_{\frac{A}{B}} = \frac{2l^2n}{m^3}st, \quad \text{A. 88}$$

$$(T_{33}/g)_{\frac{A}{B}} = \frac{2l^2n}{m^3}sc, \quad \text{A. 89}$$

$$(T_{34}/g)_{\frac{A}{B}} = \mp\frac{(h^2+k^2)l}{2m^3}(c^2-t^2), \qquad \text{A. 90}$$

$$(T_{35}/g)_{\frac{A}{B}} = \pm\frac{(h^2+k^2)l}{m^3}ct, \qquad \text{A. 91}$$

$$(U_{11}/g)_{\frac{A}{B}} = \frac{(h^4+k^4+l^4)}{m^4}s^2 + \frac{(h^2k^2+h^2l^2+k^2l^2)}{m^4}(c^2+t^2), \qquad \text{A. 92}$$

$$(U_{12}/g)_{\frac{A}{B}} = -\frac{2hk(h^2-k^2)}{m^3n}sc \pm \frac{2l(h^2l^2+k^2l^2-h^4-k^4)}{m^4n}st, \qquad \text{A. 93}$$

$$(U_{13}/g)_{\frac{A}{B}} = \pm\frac{2l(h^2l^2+k^2l^2-h^4-k^4)}{m^4n}sc + \frac{2hk(h^2-k^2)}{m^3n}st, \qquad \text{A. 94}$$

$$(U_{14}/g)_{\frac{A}{B}} = \frac{(h^4k^2+h^2k^4-h^4l^2-k^4l^2)}{m^4n^2}(c^2-t^2) \pm \frac{2hkl(h^2-k^2)}{m^3n^2}ct, \qquad \text{A. 95}$$

$$(U_{15}/g)_{\frac{A}{B}} = \pm\frac{hkl(h^2-k^2)}{m^3n^2}(c^2-t^2) - \frac{2(h^4k^2+h^2k^4-h^4l^2-k^4l^2)}{m^4n^2}ct, \qquad \text{A. 96}$$

$$(U_{21}/g)_{\frac{A}{B}} = -\frac{hk(h^2-k^2)}{2m^3n}(2s^2-c^2-t^2), \qquad \text{A. 97}$$

$$(U_{22}/g)_{\frac{A}{B}} = \frac{4h^2k^2}{m^2n^2}sc \pm \frac{2hkl(h^2-k^2)}{m^3n^2}st, \qquad \text{A. 98}$$

$$(U_{23}/g)_{\frac{A}{B}} = \pm\frac{2hkl(h^2-k^2)}{m^3n^2}sc - \frac{4h^2k^2}{m^2n^2}st, \qquad \text{A. 99}$$

$$(U_{24}/g)_{\frac{A}{B}} = \frac{hk(h^2-k^2)(h^2+k^2+2l^2)}{2m^3n^3}(c^2-t^2) \mp \frac{4h^2k^2l}{m^2n^3}ct, \qquad \text{A. 100}$$

$$(U_{25}/g)_{\frac{A}{B}} = \mp\frac{2h^2k^2l}{m^2n^3}(c^2-t^2) - \frac{hk(h^2-k^2)(h^2+k^2+2l^2)}{m^3n^3}ct, \qquad \text{A. 101}$$

$$(U_{31}/g)_{\frac{A}{B}} = \pm\frac{l(h^2l^2+k^2l^2-h^4-k^4)}{2m^4n}(2s^2-c^2-t^2), \qquad \text{A. 102}$$

$$(U_{32}/g)_{\frac{A}{B}} = \pm\frac{2hkl(h^2-k^2)}{m^3n^2}sc + \frac{4l^2(h^4+h^2k^2+k^4)}{m^4n^2}st, \qquad \text{A. 103}$$

$$(U_{33}/g)_{\frac{A}{B}} = \frac{4l^2(h^4+h^2k^2+k^4)}{m^4n^2}sc \mp \frac{2hkl(h^2-k^2)}{m^3n^2}st, \qquad \text{A. 104}$$

$$(U_{34}/g)_{\frac{A}{B}} = \pm\frac{l(h^4l^2+k^4l^2-5h^4k^2-5h^2k^4-2h^2k^2l^2-h^6-k^6)}{2m^4n^3}(c^2-t^2) - \frac{2hkl^2(h^2-k^2)}{m^3n^3}ct, \qquad \text{A. 105}$$

$$(U_{35}/g)_{\frac{A}{B}} = -\frac{hkl^2(h^2-k^2)}{m^3n^3}(c^2-t^2) \mp \frac{l(h^4l^2+k^4l^2-5h^4k^2-5h^2k^4-2h^2k^2l^2-h^6-k^6)}{m^4n^3}ct, \qquad \text{A. 106}$$

$$(V_{11}/g)_{\frac{A}{B}} = \frac{(h^4+k^4+l^4)}{m^4}s^2 + \frac{(h^2k^2+h^2l^2+k^2l^2)}{m^4}(c^2+t^2), \qquad \text{A. 107}$$

$$(V_{12}/g)_{\frac{A}{B}} = -\frac{2hk(h^2-k^2)}{m^3n}sc \pm \frac{2l(h^2l^2+k^2l^2-h^4-k^4)}{m^4n}st, \qquad \text{A. 108}$$

$$(V_{13}/g)_{\frac{A}{B}} = \pm\frac{2l(h^2l^2+k^2l^2-h^4-k^4)}{m^4n}sc + \frac{2hk(h^2-k^2)}{m^3n}st, \qquad \text{A. 109}$$

$$(V_{14}/g)_{\frac{A}{B}} = \frac{(h^4k^2+h^2k^4-h^4l^2-k^4l^2)}{m^4n^2}(c^2-t^2) \pm \frac{2hkl(h^2-k^2)}{m^3n^2}ct, \qquad \text{A. 110}$$

$$(V_{15}/g)_{\frac{A}{B}} = \pm\frac{hkl(h^2-k^2)}{m^3n^2}(c^2-t^2) - \frac{2(h^4k^2+h^2k^4-h^4l^2-k^4l^2)}{m^4n^2}ct, \qquad \text{A. 111}$$

$$(V_{16}/g)_{\frac{A}{B}} = 0, \qquad \text{A. 112}$$

$$(V_{17}/g)_{\frac{A}{B}} = 0, \qquad \text{A. 113}$$

$$(V_{21}/g)_{\frac{A}{B}} = \frac{2(h^2k^2+h^2l^2+k^2l^2)}{m^4}sc, \qquad \text{A. 114}$$

$$(V_{22}/g)_{\frac{A}{B}} = -\frac{hk(h^2-k^2)}{4m^3n}(4s^2-3c^2-t^2) \mp \frac{l(h^2l^2+k^2l^2-h^4-k^4)}{2m^4n}ct, \qquad \text{A. 115}$$

$$(V_{23}/g)_{\frac{A}{B}} = \pm\frac{l(h^2l^2+k^2l^2-h^4-k^4)}{4m^4n}(4s^2-3c^2-t^2) - \frac{hk(h^2-k^2)}{2m^3n}ct, \qquad \text{A. 116}$$

$$(V_{24}/g)_{\frac{A}{B}} = \frac{2(h^4k^2+h^2k^4-h^4l^2-k^4l^2)}{m^4n^2}sc \pm \frac{2hkl(h^2-k^2)}{m^3n^2}st, \qquad \text{A. 117}$$

$$(V_{25}/g)_{\frac{A}{B}} = \pm\frac{2hkl(h^2-k^2)}{m^3n^2}sc - \frac{2(h^4k^2+h^2k^4-h^4l^2-k^4l^2)}{m^4n^2}st, \qquad \text{A. 118}$$

$$(V_{26}/g)_{\frac{A}{B}} = \frac{hk(h^2-k^2)(h^2+k^2+4l^2)}{4m^3n^3}(c^2-t^2)$$

$$\pm\frac{l(-9h^4k^2+h^4l^2-9h^2k^4+k^4l^2-6h^2k^2l^2-h^6-k^6)}{2m^4n^3}ct, \qquad \text{A. 119}$$

$$(V_{27}/g)_{\frac{A}{B}} = \pm\frac{l(-9h^4k^2+h^4l^2-9h^2k^4+k^4l^2-6h^2k^2l^2-h^6-k^6)}{4m^4n^3}(c^2-t^2)$$

$$-\frac{hk(h^2-k^2)(h^2+k^2+4l^2)}{2m^3n^3}ct, \qquad \text{A. 120}$$

$$(V_{31}/g)_{\frac{A}{B}} = \frac{2(h^2k^2+h^2l^2+k^2l^2)}{m^4}st, \qquad \text{A. 121}$$

$$(V_{32}/g)_{\frac{A}{B}} = \pm\frac{l(h^2l^2+k^2l^2-h^4-k^4)}{4m^4n}(4s^2-c^2-3t^2)+\frac{hk(h^2-k^2)}{2m^3n}ct, \qquad \text{A. 122}$$

$$(V_{33}/g)_{\frac{A}{B}} = \frac{hk(h^2-k^2)}{4m^3n}(4s^2-c^2-3t^2)\mp\frac{l(h^2l^2+k^2l^2-h^4-k^4)}{2m^4n}ct, \qquad \text{A. 123}$$

$$(V_{34}/g)_{\frac{A}{B}} = \pm\frac{2hkl(h^2-k^2)}{m^3n^2}sc - \frac{2(h^4k^2+h^2k^4-h^4l^2-k^4l^2)}{m^4n^2}st, \qquad \text{A. 124}$$

$$(V_{35}/g)_{\frac{A}{B}} = -\frac{2(h^4k^2+h^2k^4-h^4l^2-k^4l^2)}{m^4n^2}sc\mp\frac{2hkl(h^2-k^2)}{m^3n^2}st, \qquad \text{A. 125}$$

$$(V_{36}/g)_{\frac{A}{B}} = \pm\frac{l(-9h^4k^2+h^4l^2-9h^2k^4+k^4l^2-6h^2k^2l^2-h^6-k^6)}{4m^4n^3}(c^2-t^2)$$

$$-\frac{hk(h^2-k^2)(h^2+k^2+4l^2)}{2m^3n^3}ct, \qquad \text{A. 126}$$

$$(V_{37}/g)_{\frac{A}{B}} = -\frac{hk(h^2-k^2)(h^2+k^2+4l^2)}{4m^3n^3}(c^2-t^2)$$

$$\mp\frac{l(-9h^4k^2+h^4l^2-9h^2k^4+k^4l^2-6h^2k^2l^2-h^6-k^6)}{2m^4n^3}ct\,. \qquad \text{A. 127}$$

Appendix B – Optical Rectification Coefficients: Transmission Geometry and (11*N*) Crystal Planes

Optical rectification coefficients for (11*N*) crystal planes in transmission geometry experimental set up are presented as they appear in chapter 3. Equations for both *A* and *B* faces are given.

In this case, $h = k = 1, l = N$. Also $\phi_{\mathrm{NIR}} = \Phi = 0$.

$$m = \sqrt{N^2 + 2}, \quad \text{B. 1}$$

$$n = \sqrt{2}, \quad \text{B. 2}$$

$$s = 0, \quad \text{B. 3}$$

$$c = 1, \quad \text{B. 4}$$

$$t = 0, \quad \text{B. 5}$$

$$d = d_{14} E_0^2, \quad \text{B. 6}$$

$$g = \gamma F_0 E_0^2, \quad \text{B. 7}$$

$$(A_{11})_{\frac{A}{B}} = \pm \frac{1}{\sqrt{N^2 + 2}}, \quad \text{B. 8}$$

$$(A_{12})_{\frac{A}{B}} = \mp \frac{1}{\sqrt{2}}, \quad \text{B. 9}$$

$$(A_{13})_{\frac{A}{B}} = -\frac{N}{\sqrt{2}\sqrt{N^2 + 2}}, \quad \text{B. 10}$$

$$(A_{21})_{\frac{A}{B}} = \pm \frac{1}{\sqrt{N^2 + 2}}, \quad \text{B. 11}$$

$$(A_{22})_{\frac{A}{B}} = \pm \frac{1}{\sqrt{2}}, \quad \text{B. 12}$$

$$(A_{23})_{\frac{A}{B}} = -\frac{N}{\sqrt{2}\sqrt{N^2 + 2}}, \quad \text{B. 13}$$

$$(A_{31})_{\frac{A}{B}} = \pm\frac{N}{\sqrt{N^2+2}}, \quad \text{B. 14}$$

$$(A_{32})_{\frac{A}{B}} = 0, \quad \text{B. 15}$$

$$(A_{33})_{\frac{A}{B}} = \frac{\sqrt{2}}{\sqrt{N^2+2}}, \quad \text{B. 16}$$

$$(B_{11})_{\frac{A}{B}} = 0, \quad \text{B. 17}$$

$$(B_{12})_{\frac{A}{B}} = \mp\frac{1}{\sqrt{2}}, \quad \text{B. 18}$$

$$(B_{13})_{\frac{A}{B}} = -\frac{N}{\sqrt{2}\sqrt{N^2+2}}, \quad \text{B. 19}$$

$$(B_{21})_{\frac{A}{B}} = 0, \quad \text{B. 20}$$

$$(B_{22})_{\frac{A}{B}} = \pm\frac{1}{\sqrt{2}}, \quad \text{B. 21}$$

$$(B_{23})_{\frac{A}{B}} = -\frac{N}{\sqrt{2}\sqrt{N^2+2}}, \quad \text{B. 22}$$

$$(B_{31})_{\frac{A}{B}} = 0, \quad \text{B. 23}$$

$$(B_{32})_{\frac{A}{B}} = 0, \quad \text{B. 24}$$

$$(B_{33})_{\frac{A}{B}} = \frac{\sqrt{2}}{\sqrt{N^2+2}}, \quad \text{B. 25}$$

$$(C_{11}/d)_{\frac{A}{B}} = -\frac{N}{(N^2+2)}, \quad \text{B. 26}$$

$$(C_{12}/d)_{\frac{A}{B}} = 0, \quad \text{B. 27}$$

$$(C_{13}/d)_{\frac{A}{B}} = 0, \quad \text{B. 28}$$

$$(C_{14}/d)_{\frac{A}{B}} = \frac{N}{(N^2+2)}, \quad \text{B. 29}$$

$$(C_{15}/d)_{\frac{A}{B}} = \pm\frac{1}{\sqrt{N^2+2}}, \quad \text{B. 30}$$

$$(C_{21}/d)_{\frac{A}{B}} = -\frac{N}{(N^2+2)}, \quad \text{B. 31}$$

$$(C_{22}/d)_{\frac{A}{B}} = 0, \quad \text{B. 32}$$

$$(C_{23}/d)_{\frac{A}{B}} = 0, \quad \text{B. 33}$$

$$(C_{24}/d)_{\frac{A}{B}} = \frac{N}{(N^2+2)}, \quad \text{B. 34}$$

$$(C_{25}/d)_{\frac{A}{B}} = \mp\frac{1}{\sqrt{N^2+2}}, \quad \text{B. 35}$$

$$(C_{31}/d)_{\frac{A}{B}} = -\frac{1}{(N^2+2)}, \quad \text{B. 36}$$

$$(C_{32}/d)_{\frac{A}{B}} = 0, \quad \text{B. 37}$$

$$(C_{33}/d)_{\frac{A}{B}} = 0, \quad \text{B. 38}$$

$$(C_{34}/d)_{\frac{A}{B}} = -\frac{(N^2+1)}{(N^2+2)}, \quad \text{B. 39}$$

$$(C_{35}/d)_{\frac{A}{B}} = 0, \quad \text{B. 40}$$

$$(D_{11}/d)_{\frac{A}{B}} = \mp\frac{3N}{(N^2+2)^{3/2}}, \quad \text{B. 41}$$

$$(D_{12}/d)_{\frac{A}{B}} = 0, \quad \text{B. 42}$$

$$(D_{13}/d)_{\frac{A}{B}} = 0, \quad \text{B. 43}$$

$$(D_{14}/d)_{\frac{A}{B}} = \mp\frac{N(N^2-1)}{(N^2+2)^{3/2}}, \quad \text{B. 44}$$

$$(D_{15}/d)_{\frac{A}{B}} = 0, \qquad \text{B. 45}$$

$$(D_{21}/d)_{\frac{A}{B}} = 0, \qquad \text{B. 46}$$

$$(D_{22}/d)_{\frac{A}{B}} = 0, \qquad \text{B. 47}$$

$$(D_{23}/d)_{\frac{A}{B}} = 0, \qquad \text{B. 48}$$

$$(D_{24}/d)_{\frac{A}{B}} = 0, \qquad \text{B. 49}$$

$$(D_{25}/d)_{\frac{A}{B}} = -\frac{\sqrt{2}}{\sqrt{N^2+2}}, \qquad \text{B. 50}$$

$$(D_{31}/d)_{\frac{A}{B}} = \frac{\sqrt{2}(N^2-1)}{\left(N^2+2\right)^{3/2}}, \qquad \text{B. 51}$$

$$(D_{32}/d)_{\frac{A}{B}} = 0, \qquad \text{B. 52}$$

$$(D_{33}/d)_{\frac{A}{B}} = 0, \qquad \text{B. 53}$$

$$(D_{34}/d)_{\frac{A}{B}} = -\frac{\sqrt{2}(2N^2+1)}{\left(N^2+2\right)^{3/2}}, \qquad \text{B. 54}$$

$$(D_{35}/d)_{\frac{A}{B}} = 0, \qquad \text{B. 55}$$

$$(G_{11}/d)_{\frac{A}{B}} = \mp\frac{3N}{\left(N^2+2\right)^{3/2}}, \qquad \text{B. 56}$$

$$(G_{12}/d)_{\frac{A}{B}} = 0, \qquad \text{B. 57}$$

$$(G_{13}/d)_{\frac{A}{B}} = 0, \qquad \text{B. 58}$$

$$(G_{14}/d)_{\frac{A}{B}} = \mp\frac{N(N^2-1)}{\left(N^2+2\right)^{3/2}}, \qquad \text{B. 59}$$

$$(G_{15}/d)_{\frac{A}{B}} = 0, \qquad \text{B. 60}$$

$$(G_{16}/d)_{\frac{A}{B}} = 0, \qquad \text{B. 61}$$

$$(G_{17}/d)_{\frac{A}{B}} = 0, \qquad \text{B. 62}$$

$$(G_{21}/d)_{\frac{A}{B}} = 0, \qquad \text{B. 63}$$

$$(G_{22}/d)_{\frac{A}{B}} = 0, \qquad \text{B. 64}$$

$$(G_{23}/d)_{\frac{A}{B}} = \frac{3(N^2-1)}{\sqrt{2}\left(N^2+2\right)^{3/2}}, \qquad \text{B. 65}$$

$$(G_{24}/d)_{\frac{A}{B}} = 0, \qquad \text{B. 66}$$

$$(G_{25}/d)_{\frac{A}{B}} = 0, \qquad \text{B. 67}$$

$$(G_{26}/d)_{\frac{A}{B}} = 0, \qquad \text{B. 68}$$

$$(G_{27}/d)_{\frac{A}{B}} = -\frac{3(N^2+1)}{\sqrt{2}\left(N^2+2\right)^{3/2}}, \qquad \text{B. 69}$$

$$(G_{31}/d)_{\frac{A}{B}} = 0, \qquad \text{B. 70}$$

$$(G_{32}/d)_{\frac{A}{B}} = \frac{(N^2-1)}{\sqrt{2}\left(N^2+2\right)^{3/2}}, \qquad \text{B. 71}$$

$$(G_{33}/d)_{\frac{A}{B}} = 0, \qquad \text{B. 72}$$

$$(G_{34}/d)_{\frac{A}{B}} = 0, \qquad \text{B. 73}$$

$$(G_{35}/d)_{\frac{A}{B}} = 0, \qquad \text{B. 74}$$

$$(G_{36}/d)_{\frac{A}{B}} = -\frac{3(N^2+1)}{\sqrt{2}\left(N^2+2\right)^{3/2}}, \qquad \text{B. 75}$$

$$(G_{37}/d)_{\frac{A}{B}} = 0, \qquad \text{B. 76}$$

$$(T_{11}/g)_{\frac{A}{B}} = \pm\frac{(N^2+1)}{2\left(N^2+2\right)^{3/2}}, \quad \text{B. 77}$$

$$(T_{12}/g)_{\frac{A}{B}} = 0, \quad \text{B. 78}$$

$$(T_{13}/g)_{\frac{A}{B}} = 0, \quad \text{B. 79}$$

$$(T_{14}/g)_{\frac{A}{B}} = \pm\frac{1}{2\left(N^2+2\right)^{3/2}}, \quad \text{B. 80}$$

$$(T_{15}/g)_{\frac{A}{B}} = \frac{N}{2\left(N^2+2\right)}, \quad \text{B. 81}$$

$$(T_{21}/g)_{\frac{A}{B}} = \pm\frac{(N^2+1)}{2\left(N^2+2\right)^{3/2}}, \quad \text{B. 82}$$

$$(T_{22}/g)_{\frac{A}{B}} = 0, \quad \text{B. 83}$$

$$(T_{23}/g)_{\frac{A}{B}} = 0, \quad \text{B. 84}$$

$$(T_{24}/g)_{\frac{A}{B}} = \pm\frac{1}{2\left(N^2+2\right)^{3/2}}, \quad \text{B. 85}$$

$$(T_{25}/g)_{\frac{A}{B}} = -\frac{N}{2\left(N^2+2\right)}, \quad \text{B. 86}$$

$$(T_{31}/g)_{\frac{A}{B}} = \pm\frac{N}{\left(N^2+2\right)^{3/2}}, \quad \text{B. 87}$$

$$(T_{32}/g)_{\frac{A}{B}} = 0, \quad \text{B. 88}$$

$$(T_{33}/g)_{\frac{A}{B}} = 0, \quad \text{B. 89}$$

$$(T_{34}/g)_{\frac{A}{B}} = \mp\frac{N}{\left(N^2+2\right)^{3/2}}, \quad \text{B. 90}$$

$$(T_{35}/g)_{\frac{A}{B}} = 0, \quad \text{B. 91}$$

$$(U_{11}/g)_{\frac{A}{B}} = \frac{(2N^2+1)}{\left(N^2+2\right)^2}, \quad \text{B. 92}$$

$$(U_{12}/g)_{\frac{A}{B}} = 0, \quad \text{B. 93}$$

$$(U_{13}/g)_{\frac{A}{B}} = 0, \quad \text{B. 94}$$

$$(U_{14}/g)_{\frac{A}{B}} = -\frac{(N^2-1)}{\left(N^2+2\right)^2}, \quad \text{B. 95}$$

$$(U_{15}/g)_{\frac{A}{B}} = 0, \quad \text{B. 96}$$

$$(U_{21}/g)_{\frac{A}{B}} = 0, \quad \text{B. 97}$$

$$(U_{22}/g)_{\frac{A}{B}} = 0, \quad \text{B. 98}$$

$$(U_{23}/g)_{\frac{A}{B}} = 0, \quad \text{B. 99}$$

$$(U_{24}/g)_{\frac{A}{B}} = 0, \quad \text{B. 100}$$

$$(U_{25}/g)_{\frac{A}{B}} = \mp\frac{N}{\sqrt{2}\left(N^2+2\right)}, \quad \text{B. 101}$$

$$(U_{31}/g)_{\frac{A}{B}} = \mp\frac{N(N^2-1)}{\sqrt{2}\left(N^2+2\right)^2}, \quad \text{B. 102}$$

$$(U_{32}/g)_{\frac{A}{B}} = 0, \quad \text{B. 103}$$

$$(U_{33}/g)_{\frac{A}{B}} = 0, \quad \text{B. 104}$$

$$(U_{34}/g)_{\frac{A}{B}} = \mp\frac{3N}{\sqrt{2}\left(N^2+2\right)^2}, \quad \text{B. 105}$$

$$(U_{35}/g)_{\frac{A}{B}} = 0, \quad \text{B. 106}$$

$$(V_{11}/g)_{\frac{A}{B}} = \frac{(2N^2+1)}{\left(N^2+2\right)^2}, \quad \text{B. 107}$$

$$(V_{12}/g)_{\frac{A}{B}} = 0, \qquad \text{B. 108}$$

$$(V_{13}/g)_{\frac{A}{B}} = 0, \qquad \text{B. 109}$$

$$(V_{14}/g)_{\frac{A}{B}} = -\frac{(N^2-1)}{\left(N^2+2\right)^2}, \qquad \text{B. 110}$$

$$(V_{15}/g)_{\frac{A}{B}} = 0, \qquad \text{B. 111}$$

$$(V_{16}/g)_{\frac{A}{B}} = 0, \qquad \text{B. 112}$$

$$(V_{17}/g)_{\frac{A}{B}} = 0, \qquad \text{B. 113}$$

$$(V_{21}/g)_{\frac{A}{B}} = 0, \qquad \text{B. 114}$$

$$(V_{22}/g)_{\frac{A}{B}} = 0, \qquad \text{B. 115}$$

$$(V_{23}/g)_{\frac{A}{B}} = \mp\frac{3N(N^2-1)}{2\sqrt{2}\left(N^2+2\right)^2}, \qquad \text{B. 116}$$

$$(V_{24}/g)_{\frac{A}{B}} = 0, \qquad \text{B. 117}$$

$$(V_{25}/g)_{\frac{A}{B}} = 0, \qquad \text{B. 118}$$

$$(V_{26}/g)_{\frac{A}{B}} = 0, \qquad \text{B. 119}$$

$$(V_{27}/g)_{\frac{A}{B}} = \mp\frac{N(N^2+5)}{2\sqrt{2}\left(N^2+2\right)^2}, \qquad \text{B. 120}$$

$$(V_{31}/g)_{\frac{A}{B}} = 0, \qquad \text{B. 121}$$

$$(V_{32}/g)_{\frac{A}{B}} = \mp\frac{N(N^2-1)}{2\sqrt{2}\left(N^2+2\right)^2}, \qquad \text{B. 122}$$

$$(V_{33}/g)_{\frac{A}{B}} = 0, \qquad \text{B. 123}$$

$$(V_{34}/g)_{\frac{A}{B}} = 0, \qquad \text{B. 124}$$

$$(V_{35}/g)_{\frac{A}{B}} = 0, \qquad \text{B. 125}$$

$$(V_{36}/g)_{\frac{A}{B}} = \mp\frac{N(N^2+5)}{2\sqrt{2}\left(N^2+2\right)^2}, \qquad \text{B. 126}$$

$$(V_{37}/g)_{\frac{A}{B}} = 0\,. \qquad \text{B. 127}$$

Appendix C - Optical Rectification Coefficients for Quasireflection Geometry and (11*N*) Crystal Planes

Optical rectification coefficients for (11*N*) crystal planes in quasireflection experimental set up are presented as they appear in chapter 4. Equations for both *A* and *B* faces are given. Only the coefficients in the final equations of bulk and surface OR polarization components are shown here, which are G_{ij} and V_{ij}, respectively.

Here $h = k = 1, l = N$. Also $\Phi = 0$.

$$m = \sqrt{N^2 + 2}, \quad \text{C. 1}$$

$$n = \sqrt{2}, \quad \text{C. 2}$$

$$s = \sin\phi_{\text{NIR}}, \quad \text{C. 3}$$

$$c = \cos\phi_{\text{NIR}}, \quad \text{C. 4}$$

$$t = 0, \quad \text{C. 5}$$

$$d = d_{14}E_0^2, \quad \text{C. 6}$$

$$g = \gamma F_0 E_0^2, \quad \text{C. 7}$$

$$(G_{11}/d)_{\frac{A}{B}} = \mp\frac{3N}{(N^2+2)^{3/2}}(\cos^2\phi_{NIR} - 2\sin^2\phi_{NIR}), \quad \text{C. 8}$$

$$(G_{12}/d)_{\frac{A}{B}} = 0, \quad \text{C. 9}$$

$$(G_{13}/d)_{\frac{A}{B}} = -\frac{4\sqrt{2}(N^2-1)}{(N^2+2)^{3/2}}\sin\phi_{NIR}\cos\phi_{NIR}, \quad \text{C. 10}$$

$$(G_{14}/d)_{\frac{A}{B}} = \mp\frac{N(N^2-1)}{(N^2+2)^{3/2}}\cos^2\phi_{NIR}, \quad \text{C. 11}$$

$$(G_{15}/d)_{\frac{A}{B}} = 0, \quad \text{C. 12}$$

$$(G_{16}/d)_{\frac{A}{B}} = 0, \quad \text{C. 13}$$

$$(G_{17}/d)_{\frac{A}{B}} = 0, \quad \text{C. 14}$$

$$(G_{21}/d)_{\frac{A}{B}} = \mp\frac{6N}{(N^2+2)^{3/2}}\sin\phi_{NIR}\cos\phi_{NIR}, \quad \text{C. 15}$$

$$(G_{22}/d)_{\frac{A}{B}} = 0, \quad \text{C. 16}$$

$$(G_{23}/d)_{\frac{A}{B}} = \frac{(N^2-1)}{\sqrt{2}(N^2+2)^{3/2}}(3\cos^2\phi_{NIR} - 4\sin^2\phi_{NIR}), \quad \text{C. 17}$$

$$(G_{24}/d)_{\frac{A}{B}} = \mp\frac{2N(N^2-1)}{(N^2+2)^{3/2}}\sin\phi_{NIR}\cos\phi_{NIR}, \quad \text{C. 18}$$

$$(G_{25}/d)_{\frac{A}{B}} = 0, \quad \text{C. 19}$$

$$(G_{26}/d)_{\frac{A}{B}} = 0, \quad \text{C. 20}$$

$$(G_{27}/d)_{\frac{A}{B}} = -\frac{3(N^2+1)}{\sqrt{2}(N^2+2)^{3/2}}\cos^2\phi_{NIR}, \quad \text{C. 21}$$

$$(G_{31}/d)_{\frac{A}{B}} = 0, \quad \text{C. 22}$$

$$(G_{32}/d)_{\frac{A}{B}} = \frac{(N^2-1)}{\sqrt{2}(N^2+2)^{3/2}}(\cos^2\phi_{NIR} - 4\sin^2\phi_{NIR}), \quad \text{C. 23}$$

$$(G_{33}/d)_{\frac{A}{B}} = 0, \quad \text{C. 24}$$

$$(G_{34}/d)_{\frac{A}{B}} = 0, \quad \text{C. 25}$$

$$(G_{35}/d)_{\frac{A}{B}} = \pm\frac{2N(N^2-1)}{(N^2+2)^{3/2}}\sin\phi_{NIR}\cos\phi_{NIR}, \quad \text{C. 26}$$

$$(G_{36}/d)_{\frac{A}{B}} = -\frac{3(N^2+1)}{\sqrt{2}(N^2+2)^{3/2}}\cos^2\phi_{NIR}, \quad \text{C. 27}$$

$$(G_{37}/d)_{\frac{A}{B}} = 0, \quad \text{C. 28}$$

$$(V_{11}/g)_{\frac{A}{B}} = \frac{(N^4+2)}{(N^2+2)^2}\sin^2\phi_{NIR} + \frac{(2N^2+1)}{(N^2+2)^2}\cos^2\phi_{NIR}, \quad \text{C. 29}$$

$$(V_{12}/g)_{\frac{A}{B}} = 0, \quad \text{C. 30}$$

$$(V_{13}/g)_{\frac{A}{B}} = \pm\frac{2\sqrt{2}N(N^2-1)}{(N^2+2)^2}\sin\phi_{NIR}\cos\phi_{NIR}, \quad \text{C. 31}$$

$$(V_{14}/g)_{\frac{A}{B}} = -\frac{(N^2-1)}{(N^2+2)^2}\cos^2\phi_{NIR}, \quad \text{C. 32}$$

$$(V_{15}/g)_{\frac{A}{B}} = 0, \quad \text{C. 33}$$

$$(V_{16}/g)_{\frac{A}{B}} = 0, \quad \text{C. 34}$$

$$(V_{17}/g)_{\frac{A}{B}} = 0, \quad \text{C. 35}$$

$$(V_{21}/g)_{\frac{A}{B}} = \frac{2(2N^2+1)}{(N^2+2)^2}\sin\phi_{NIR}\cos\phi_{NIR}, \quad \text{C. 36}$$

$$(V_{22}/g)_{\frac{A}{B}} = 0, \quad \text{C. 37}$$

$$(V_{23}/g)_{\frac{A}{B}} = \mp\frac{N(N^2-1)}{2\sqrt{2}(N^2+2)^2}(3\cos^2\phi_{NIR} - 4\sin^2\phi_{NIR}), \quad \text{C. 38}$$

$$(V_{24}/g)_{\frac{A}{B}} = -\frac{2(N^2-1)}{(N^2+2)^2}\sin\phi_{NIR}\cos\phi_{NIR}, \quad \text{C. 39}$$

$$(V_{25}/g)_{\frac{A}{B}} = 0, \quad \text{C. 40}$$

$$(V_{26}/g)_{\frac{A}{B}} = 0, \quad \text{C. 41}$$

$$(V_{27}/g)_{\frac{A}{B}} = \mp\frac{N(N^2+5)}{2\sqrt{2}(N^2+2)^2}\cos^2\phi_{NIR}, \quad \text{C. 42}$$

$$(V_{31}/g)_{\frac{A}{B}} = 0, \quad \text{C. 43}$$

$$(V_{32}/g)_{\frac{A}{B}} = \mp\frac{N(N^2-1)}{2\sqrt{2}(N^2+2)^2}(\cos^2\phi_{NIR} - 4\sin^2\phi_{NIR}), \quad \text{C. 44}$$

$$(V_{33}/g)_{\frac{A}{B}} = 0, \qquad \text{C. 45}$$

$$(V_{34}/g)_{\frac{A}{B}} = 0, \qquad \text{C. 46}$$

$$(V_{35}/g)_{\frac{A}{B}} = \frac{2(N^2-1)}{(N^2+2)^2}\sin\phi_{NIR}\cos\phi_{NIR}, \qquad \text{C. 47}$$

$$(V_{36}/g)_{\frac{A}{B}} = \mp\frac{N(N^2+5)}{2\sqrt{2}(N^2+2)^2}\cos^2\phi_{NIR}, \qquad \text{C. 48}$$

$$(V_{37}/g)_{\frac{A}{B}} = 0. \qquad \text{C. 49}$$

Appendix D - Optical Rectification Coefficients for (100) Crystal Face

Optical rectification coefficients for (100) crystal planes are presented as they appear in chapter 5. Only the coefficients in the final equations of bulk and surface OR polarization components are shown here, which are G_{ij} and V_{ij}, respectively.

Here $h=1, k=l=0$. Also $\Phi=0$.

$$m=1, \quad \text{D. 1}$$

$$n=1, \quad \text{D. 2}$$

$$s=\sin\phi_{\mathrm{NIR}}, \quad \text{D. 3}$$

$$c=\cos\phi_{\mathrm{NIR}}, \quad \text{D. 4}$$

$$t=0, \quad \text{D. 5}$$

$$d=d_{14}E_0^2, \quad \text{D. 6}$$

$$g=\gamma' F_0 E_0^2, \quad \text{D. 7}$$

$$(G_{11}/d)=0, \quad \text{D. 8}$$

$$(G_{12}/d)=0, \quad \text{D. 9}$$

$$(G_{13}/d)=0, \quad \text{D. 10}$$

$$(G_{14}/d)=0, \quad \text{D. 11}$$

$$(G_{15}/d)=\cos^2\phi_{NIR}, \quad \text{D. 12}$$

$$(G_{16}/d)=0, \quad \text{D. 13}$$

$$(G_{17}/d)=0, \quad \text{D. 14}$$

$$(G_{21}/d)=0, \quad \text{D. 15}$$

$$(G_{22}/d)=0, \quad \text{D. 16}$$

$$(G_{23}/d)=0, \quad \text{D. 17}$$

$$(G_{24}/d)=0, \quad \text{D. 18}$$

$$(G_{25}/d)=2\sin\phi_{NIR}\cos\phi_{NIR}, \quad \text{D. 19}$$

$$(G_{26}/d)=0, \quad \text{D. 20}$$

$$(G_{27} / d) = 0, \quad \text{D. 21}$$

$$(G_{31} / d) = 0, \quad \text{D. 22}$$

$$(G_{32} / d) = 0, \quad \text{D. 23}$$

$$(G_{33} / d) = 0, \quad \text{D. 24}$$

$$(G_{34} / d) = 2 \sin \phi_{NIR} \cos \phi_{NIR}, \quad \text{D. 25}$$

$$(G_{35} / d) = 0, \quad \text{D. 26}$$

$$(G_{36} / d) = 0, \quad \text{D. 27}$$

$$(G_{37} / d) = 0, \quad \text{D. 28}$$

$$(V_{11} / g) = \sin^2 \phi_{NIR}, \quad \text{D. 29}$$

$$(V_{12} / g) = 0, \quad \text{D. 30}$$

$$(V_{13} / g) = 0, \quad \text{D. 31}$$

$$(V_{14} / g) = 0, \quad \text{D. 32}$$

$$(V_{15} / g) = 0, \quad \text{D. 33}$$

$$(V_{16} / g) = 0, \quad \text{D. 34}$$

$$(V_{17} / g) = 0, \quad \text{D. 35}$$

$$(V_{21} / g) = 0, \quad \text{D. 36}$$

$$(V_{22} / g) = 0, \quad \text{D. 37}$$

$$(V_{23} / g) = 0, \quad \text{D. 38}$$

$$(V_{24} / g) = 0, \quad \text{D. 39}$$

$$(V_{25} / g) = 0, \quad \text{D. 40}$$

$$(V_{26} / g) = 0, \quad \text{D. 41}$$

$$(V_{27} / g) = 0, \quad \text{D. 42}$$

$$(V_{31} / g) = 0, \quad \text{D. 43}$$

$$(V_{32} / g) = 0, \quad \text{D. 44}$$

$$(V_{33} / g) = 0, \qquad \text{D. 45}$$

$$(V_{34} / g) = 0, \qquad \text{D. 46}$$

$$(V_{35} / g) = 0, \qquad \text{D. 47}$$

$$(V_{36} / g) = 0, \qquad \text{D. 48}$$

$$(V_{37} / g) = 0\,. \qquad \text{D. 49}$$

References

References

[1] B Ferguson and X-C Zhang. "Materials for terahertz science and technology", *Nature Materials*, **1**, 26-33 (2002).

[2] A G Davies, A D Burnett, W Fan, E H Linfield, and J E Cunningham. "Terahertz spectroscopy of explosives and drugs", *Materials Today*, **11** (3), 18-26 (2008).

[3] A Geižutis, A Krotkus, K Bertulis, G Molis, R Adomavičius, A Urbanowicz, S Balakauskas, and S Valaika. "Terahertz radiation emitters and detectors", *Optical Materials*, **30** (5), 786-788 (2008).

[4] "Terahertz spectroscopy: principles and applications" edited by Susan L. Dexheimer, (CRC Press, 2007)

[5] R Parthasarathy, T Globus, T Khromova, N Swami, and D Woolard. "Dielectric properties of biological molecules in the Terahertz gap", *Applied Physics Letters*, **87** (11), 113901 (2005).

[6] G Zhao, R N Schouten, N V D Valk, W T Wenckebach, and P C M Planken. "A terahertz system using semi-large emitters: noise and performance characteristics", *Physics in Medicine and Biology*, **47**, 3699–3704 (2002).

[7] A Tredicucci, R Köhler, F Beltram, H E Beere, E H Linfield, A G Davies, and D A Ritchie. "Terahertz quantum cascade lasers", *Physica E: Low-dimensional Systems and Nanostructures*, **21** (2-4), 846-851 (2004).

[8] S Fathololoumi, E Dupont, C W I Chan, Z R Wasilewski, S R Laframboise, D Ban, A Mátyás, C Jirauschek, Q Hu, and H C Liu. "Terahertz quantum cascade lasers operating up to ~ 200 K with optimized oscillator strength and improved injection tunneling", *Optics Express*, **20** (4), 3866-3876 (2012).

[9] M S Vitiello, D Coquillat, L Vicarelli, L Viti, L Romeo, D Ercolani, A C Ferrari, G Scalari, J Faist, M Polini, F Beltram, L Sorba, V Pellegrini, W Knap, and A Tredicucci,"Nanowire and graphene architectures for room temperature THz detection", *presented at the 37th International Conference on Infrared, Millimeter and Terahertz Waves*, Wollongong, Australia, (2012).

[10] E Gornik, K Unterrainer, and C Kremser. "Tunable far-infrared solid-state lasers based on hot holes in germanium", *Optical and Quantum Electronics*, **23** (2), 267-286 (1991).

[11] E Bründermann, D R Chamberlin, and E E Haller. "High duty cycle and continuous terahertz emission from germanium", *Applied Physics Letters*, **76** (21), 2991-2993 (2000).

[12] Y-S Lee, "Principles of Terahertz Science and Technology". (Springer Science+Buiness Media, 2008)

[13] E M Telles, R C Viscovini, A Scalabrin, and D Pereira, "Far-infrared laser lines from CH_3 rocking of $^{13}CD_3OD$", *presented at the Millimeter and Submillimeter Waves IV*, Washington, DC, U.S.A., San Diego, CA, U.S.A., (1998).

[14] M Ghoranneviss, M a M Kashani, A Hogabri, A Kohiyan, and A Anvari, "Design and modification of the FIR HCN laser", *presented at the Millimeter and Submillimeter Waves IV*, Washington, DC, U.S.A., San Diego, CA, U.S.A., (1998).

[15] D H Auston, K P Cheung, and P R Smith. "Picosecond photoconducting Hertzian dipoles", *Applied Physics Letters*, **45** (3), 284-286 (1984).

[16] S L Chuang, S Schmitt-Rink, B I Greene, P N Saeta, and A F J Levi. "Optical rectification at semiconductor surfaces", *Physical Review Letters*, **68** (1), 102-105 (1992).

[17] B I Greene, P N Saeta, D R Dykaar, S Schmitt-Rink, and S L Chuang. "Far-Infrared light generation at semiconductor surfaces and its spectroscopic applications", *IEEE Journal of Quantum Electronics*, **28** (10), 2302-2312 (1992).

[18] X-C Zhang and D H Auston. "Optoelectronic measurement of semiconductor surfaces and interfaces with femtosecond optics", *Journal of Applied Physics*, **71** (1), 326-338 (1992).

[19] T Dekorsy, H Auer, C Waschke, H J Bakker, H G Roskos, H Kurz, V Wagner, and P Grosse. "Emission of submillimeter electromagnetic waves by coherent phonons", *Physical Review Letters*, **74** (5), 738-741 (1995).

[20] G A Garrett, T F Albrecht, J F Whitaker, and R Merlin. "Coherent THz Phonons Driven by Light Pulses and the Sb Problem: What is the Mechanism?", *Physical Review Letters*, **77** (17), 3661-3664 (1996).

[21] R Merlin. "Generating coherent THz phonons with light pulses", *Solid State Communications*, **102** (2–3), 207-220 (1997).

[22] R Kersting, K Unterrainer, G Strasser, H F Kauffmann, and E Gornik. "Few-cycle THz emission from cold plasma oscillations", *Physical Review Letters*, **79** (16), 3038-3041 (1997).

[23] R Kersting, J N Heyman, G Strasser, and K Unterrainer. "Coherent plasmons in n-doped GaAs", *Physical Review B*, **58** (8), 4553-4559 (1998).

[24] W Pötz. "Infrared light emission from semiconductor double wells", *Applied Physics Letters*, **68** (18), 2553-2555 (1996).

[25] Y Tominari, T Kiwa, H Murakami, M Tonouchi, H Wald, P Seidel, and H Schneidewind. "Resonant terahertz radiation from $Tl_2Ba_2CaCu_2O_{8+\delta}$ thin films by ultrafast optical pulse excitation", *Applied Physics Letters*, **80** (17), 3147-3149 (2002).

[26] J Dai, X Xie, and X-C Zhang. "Detection of Broadband Terahertz Waves with a Laser-Induced Plasma in Gases", *Physical Review Letters*, **97** (10), 103903 (2006).

[27] H Wang, K Wang, J Liu, H Dai, and Z Yang. "Theoretical research on terahertz air-breakdown coherent detection with the transient photocurrent model", *Optics Express*, **20** (17), 19264-19270 (2012).

[28] J Dai, J Liu, and X-C Zhang. "Terahertz wave air photonics: terahertz wave generation and detection with laser-induced gas plasma", *IEEE Journal of Selected Topics in Quantum Electronics*, **17** (1), 183-190 (2011).

[29] B Clough, J Dai, and X-C Zhang. "Laser air photonics: beyond the terahertz gap", *Materials Today*, **15** (1-2), 50-58 (2012).

[30] J R Middendorf and E R Brown. "THz generation using extrinsic photoconductivity at 1550 nm", *Optics Express*, **20** (15), 16504-16509 (2012).

[31] A Schwagmann, Z-Y Zhao, F Ospald, H Lu, D C Driscoll, M P Hanson, A C Gossard, and J H Smet. "Terahertz emission characteristics of ErAs:InGaAs-based photoconductive antennas excited at 1.55μm", *Applied Physics Letters*, **96** (14), 141108 (2010).

[32] J R Middendorf and E R Brown,"Extrinsic photoconductivity at 1550 nm and 1030 nm for THz Generation", *presented at the 37th International Conference on Infrared, Millimeter and Terahertz Waves*, Wollongong, Australia, (2012).

[33] M Tani, Y Hirota, C T Que, S Tanaka, R Hattori, M Yamaguchi, S Nishizawa, and M Hangyo. "Novel terahertz photoconductive antennas", *International Journal of Infrared and Millimeter Waves*, **27** (4), 531-546 (2006).

[34] S P Mickan and X-C Zhang. "T-ray sensing and imaging", *International Journal of High Speed Electronics and Systems*, **13** (2), 601-676 (2003).

[35] P Lefur and D H Auston. "A kilovolt picosecond optoelectronic switch and Pockel's cell", *Applied Physics Letters*, **28** (1), 21-23 (1976).

[36] Y Cai, I Brener, J Lopata, J Wynn, L Pfeiffer, and J Federici. "Design and performance of singular electric field terahertz photoconducting antennas", *Applied Physics Letters*, **71** (15), 2076-2078 (1997).

[37] D Dragoman and M Dragoman. "Terahertz fields and applications", *Progress in Quantum Electronics*, **28** (1), 1-66 (2004).

[38] Y C Shen, P C Upadhya, E H Linfield, H E Beere, and A G Davies. "Ultrabroadband terahertz radiation from low-temperature-grown GaAs photoconductive emitters", *Applied Physics Letters*, **83** (15), 3117-3119 (2003).

[39] G Zhao, R N Schouten, N Van Der Valk, W T Wenckebach, and P C M Planken. "Design and performance of a THz emission and detection setup based on a semi-insulating GaAs emitter", *Review of Scientific Instruments*, **73**, 1715-1719 (2002).

[40] "Terahertz Optoelectronics" edited by K. Sakai, (Springer-Verlag GmbH, 2005)

[41] F Peter, S Winnerl, H Schneider, M Helm, and K Köhler. "Terahertz emission from a large-area GaInAsN emitter", *Applied Physics Letters*, **93** (10), 101102 (2008).

[42] S Hargreaves, L J Bignell, R A Lewis, D Schoenherr, M Sağlam, and H L Hartnagel. "Investigation of p-GaAsSb as a THz emitter", *Journal of The Electrochemical Society*, **155** (10), H734-H737 (2008).

[43] X-C Zhang, B B Hu, J T Darrow, and D H Auston. "Generation of femtosecond electromagnetic pulses from semiconductor surfaces", *Applied Physics Letters*, **56** (11), 1011-1013 (1990).

[44] X-C Zhang, J T Darrow, B B Hu, D H Auston, M T Schmidt, P Tham, and E S Yang. "Optically induced electromagnetic radiation from semiconductor surfaces", *Applied Physics Letters*, **56** (22), 2228-2230 (1990).

[45] A Rice, Y Jin, X F Ma, X-C Zhang, D Bliss, J Larkin, and M Alexander. "Terahertz optical rectification from 110 zinc-blende crystals", *Applied Physics Letters*, **64** (11), 1324-1326 (1994).

[46] M Reid, I V Cravetchi, and R Fedosejevs. "Terahertz radiation and second-harmonic generation from InAs: Bulk versus surface electric-field-induced contributions", *Physical Review B*, **72** (3), 035201 (2005).

[47] V L Malevich, A Krotkus, A Bičiūnas, and V Pačebutas. "Terahertz emission from femtosecond laser illuminated (112) surfaces of InSb", *Journal of Applied Physics*, **104** (11), 113117 (2008).

[48] R Adomavičius, A Urbanowicz, G Molis, A Krotkus, and E Šatkovskis. "Terahertz emission from p-lnAs due to the instantaneous polarization", *Applied Physics Letters*, **85** (13), 2463-2465 (2004).

[49] A Corchia, C M Ciesla, D D Arnone, E H Linfield, M Y Simmons, and M Pepper. "Crystallographic orientation dependence of bulk optical rectification", *Journal of Modern Optics*, **47** (11), 1837-1845 (2000).

[50] J B Khurgin. "Optical rectification and terahertz emission in semiconductors excited above the band gap", *Journal of the Optical Society of America B*, **11** (12), 2492-2501 (1994).

[51] X Mu, I B Zotova, and Y J Ding. "Power scaling on efficient generation of ultrafast terahertz pulses", *IEEE Journal of Selected Topics in Quantum Electronics*, **14** (2), 315-332 (2008).

[52] Q Wu and X-C Zhang. "Free-space electro-optics sampling of mid-infrared pulses", *Applied Physics Letters*, **71** (10), 1285-1286 (1997).

[53] A Nahata, A S Weling, and T F Heinz. "A wideband coherent terahertz spectroscopy system using optical rectification and electro-optic sampling", *Applied Physics Letters*, **69** (16), 2321-2323 (1996).

[54] P Gu, M Tani, S Kono, K Sakai, and X-C Zhang. "Study of terahertz radiation from InAs and InSb", *Journal of Applied Physics*, **91** (9), 5533-5537 (2002).

[55] R Huber, A Brodschelm, F Tauser, and A Leitenstorfer. "Generation and field-resolved detection of femtosecond electromagnetic pulses tunable up to 41 THz", *Applied Physics Letters*, **76** (22), 3191-3193 (2000).

[56] W Shi, Y J Ding, N Fernelius, and K Vodopyanov. "Efficient, tunable, and coherent 0.18-5.27-THz source based on GaSe crystal", *Optics Letters*, **27** (16), 1454-1456 (2002).

[57] X Xie, J Xu, and X-C Zhang. "Terahertz wave generation and detection from a CdTe crystal characterized by different excitation wavelengths", *Optics Letters*, **31** (7), 978-980 (2006).

[58] K Liu, H-S Kang, T-K Kim, and X-C Zhang. "Study of ZnCdTe crystals as terahertz wave emitters and detectors", *Applied Physics Letters*, **81** (22), 4115-4117 (2002).

[59] K H Yang, P L Richards, and Y R Shen. "Generation of far-infrared radiation by picosecond light pulses in LiNbO3", *Applied Physics Letters*, **19** (9), 320-323 (1971).

[60] X-C Zhang, Y Jin, and X F Ma. "Coherent measurement of THz optical rectification from electro-optic crystals", *Applied Physics Letters*, **61** (23), 2764-2766 (1992).

[61] Y-S Lee, T Meade, V Perlin, H Winful, T B Norris, and A Galvanauskas. "Generation of narrow-band terahertz radiation via optical rectification of femtosecond pulses in periodically poled lithium niobate", *Applied Physics Letters*, **76** (18), 2505-2507 (2000).

[62] B B Hu, X-C Zhang, D H Auston, and P R Smith. "Free-space radiation from electro-optic crystals", *Applied Physics Letters*, **56** (6), 506-508 (1990).

[63] X-C Zhang, X F Ma, Y Jin, T-M Lu, E P Boden, P D Phelps, K R Stewart, and C P Yakymyshyn. "Terahertz optical rectification from a nonlinear organic crystal", *Applied Physics Letters*, **61** (26), 3080-3082 (1992).

[64] C P Hauri, C Ruchert, C Vicario, and F Ardana. "Strong-field single-cycle THz pulses generated in an organic crystal", *Applied Physics Letters*, **99** (16), 161116- (2011).

[65] F Kadlec, P Kuzel, and J-L Coutaz. "Optical rectification at metal surfaces", *Optics Letters*, **29** (22), 2674-2676 (2004).

[66] F Kadlec, P Kuzel, and J-L Coutaz. "Study of terahertz radiation generated by optical rectification on thin gold films", *Optics Letters*, **30** (11), 1402-1404 (2005).

[67] H Takahashi, A Quema, M Goto, S Ono, and N Sarukura. "Terahertz radiation mechanism from femtosecond-laser-irradiated InAs (100) surface", *Japanese Journal of Applied Physics*, **42**, L1259-L1261 (2003).

[68] S Kono, P Gu, M Tani, and K Sakai. "Temperature dependence of terahertz radiation from n-type InSb and n-type InAs surfaces", *Applied Physics B*, **71** (6), 901-904 (2000).

[69] J N Heyman, N Coates, A Reinhardt, and G Strasser. "Diffusion and drift in terahertz emission at GaAs surfaces", *Applied Physics Letters*, **83** (26), 5476-5478 (2003).

[70] K Liu, J Xu, T Yuan, and X-C Zhang. "Terahertz radiation from InAs induced by carrier diffusion and drift", *Physical Review B*, **73** (15), 155330 (2006).

[71] G Klatt, F Hilser, W Qiao, M Beck, R Gebs, A Bartels, K Huska, U Lemmer, G Bastian, M B Johnston, M Fischer, J Faist, and T Dekorsy. "Terahertz emission from lateral photo-Dember currents", *Optics Express*, **18** (5), 4939-4947 (2010).

[72] C Fattinger and D Grischkowsky. "Terahertz beams", *Applied Physics Letters*, **54** (6), 490-492 (1989).

[73] S Kono, M Tani, and K Sakai. "Ultrabroadband photoconductive detection: Comparison with free-space electro-optic sampling", *Applied Physics Letters*, **79** (7), 898-900 (2001).

[74] S Kono, M Tani, P Gu, and K Sakai. "Detection of up to 20 THz with a low-temperature-grown GaAs photoconductive antenna gated with 15 fs light pulses", *Applied Physics Letters*, **77** (25), 4104-4106 (2000).

[75] S Le Boiteux, N Del Fatti, I Manek-Hönninger, and L Sarger. "THz-Time Domain Spectroscopy system for applications to radical detection", *Comptes Rendus de l'Academie des Sciences (Paris)*, **2** (5), 983–988 (2001).

[76] G Gallot, J Zhang, R W Mcgowan, T-I Jeon, and D Grischkowsky. "Measurements of the THz absorption and dispersion of ZnTe and their relevance to the electro-optic detection of THz radiation", *Applied Physics Letters*, **74** (23), 3450-3452 (1999).

[77] Q Wu and X-C Zhang. "7 terahertz broadband GaP electro-optic sensor", *Applied Physics Letters*, **70** (14), 1784-1786 (1997).

[78] M Vossebürger, M Brucherseifer, G C Cho, H G Roskos, and H Kurz. "Propagation effects in electro-optic sampling of terahertz pulses in GaAs", *Applied Optics*, **37** (15), 3368-3371 (1998).

[79] A M Sinyukov and L M Hayden. "Generation and detection of terahertz radiation with multilayered electro-optic polymer films", *Optics Letters*, **27** (1), 55-57 (2002).

[80] H Cao, T F Heinz, and A Nahata. "Electro-optic detection of femtosecond electromagnetic pulses by use of poled polymers", *Optics Letters*, **27** (9), 775-777 (2002).

[81] M Walther, K Jensby, S R Keiding, H Takahashi, and H Ito. "Far-infrared properties of DAST", *Optics Letters*, **25** (12), 911-913 (2000).

[82] A Brodschelm, F Tauser, R Huber, J Y Sohn, and A Leitenstorfer, "Amplitude and phased resolved detection of tunable femtosecond pulses with frequency components beyond 100 THz", *presented at the Ultrafast Phenomena XII*, Springer, Berlin,Heidelberg, (2000).

[83] K Kawase, Y Ogawa, Y Watanabe, and H Inoue. "Non-destructive terahertz imaging of illicit drugs using spectral fingerprints", *Optics Express*, **11** (20), 2549-2554 (2003).

[84] W R Tribe, D A Newnham, P F Taday, and M C Kemp, "Hidden object detection: security applications of terahertz technology", *presented at the Proceedings of SPIE*, SPIE, Bellingham, WA, 2004, (2004).

[85] M C Kemp, P F Taday, B E Cole, J A Cluff, A J Fitzgerald, and W R Tribe, "Security applications of terahertz technology", *presented at the Proceedings of SPIE*, (2003).

[86] C J Strachan, T Rades, D A Newnham, K C Gordon, M Pepper, and P F Taday. "Using terahertz pulsed spectroscopy to study crystallinity of pharmaceutical materials", *Chemical Physics Letters*, **390** (1-3), 20-24 (2004).

[87] V P Wallace, P F Taday, A J Fitzgerald, R M Woodward, J Cluff, R J Pye, and D D Arnone. "Terahertz pulsed imaging and spectroscopy for biomedical and pharmaceutical applications", *Faraday Disscusions* **126**, 255-263 (2004).

[88] Z Yan, Y Ying, H Zhang, and H Yu. "Research progress of terahertz wave technology in food inspection", *Proceedings of SPIE*, **6373**, 63730R (2006).

[89] G M Png, J W Choi, B W-H Ng, S P Mickan, D Abbott, and X-C Zhang. "The impact of hydration changes in fresh bio-tissue on THz spectroscopic measurements", *Physics in Medicine and Biology*, **53** (13), 3501-3517 (2008).

[90] D M Mittleman, R H Jacobsen, and M C Nuss. "T-ray imaging", *IEEE Journal of Selected Topics in Quantum Electronics*, **2** (3), 679-692 (1996).

[91] D M Mittleman, M Gupta, R Neelamani, R G Baraniuk, J V Rudd, and M Koch. "Recent advances in terahertz imaging", *Applied Physics B*, **68**, 1085-1094 (1999).

[92] D A Crawley, C Longbottom, B E Cole, C M Ciesla, D Arnone, V P Wallace, and M Pepper. "Terahertz pulse imaging: a pilot study of potential applications in dentistry", *Caries Research*, **37** (5), 352-359 (2003).

[93] T Löffler, T Bauer, K Siebert, H Roskos, A Fitzgerald, and S Czasch. "Terahertz dark-field imaging of biomedical tissue", *Optics Express*, **9** (12), 616-621 (2001).

[94] R M Woodward, B E Cole, V P Wallace, R J Pye, D D Arnone, E H Linfield, and M Pepper. "Terahertz pulse imaging in reflection geometry of human skin cancer and skin tissue", *Physics in Medicine and Biology*, **47** (21), 3853-3863 (2002).

[95] J-H Son. "Terahertz electromagnetic interactions with biological matter and their applications", *Journal of Applied Physics*, **105** (10), 102033- (2009).

[96] A G Markelz, A Roitberg, and E J Heilweil. "Pulsed terahertz spectroscopy of DNA, bovine serum albumin and collagen between 0.1 and 2.0 THz", *Chemical Physics Letters*, **320**, 42-48 (2000).

[97] K Fukunaga and I Hosako. "Innovative non-invasive analysis techniques for cultural heritage using terahertz technology", *Comptes Rendus Physique*, **11** (7-8), 519-526 (2010).

[98] J-M Manceau, A Nevin, C Fotakis, and S Tzortzakis. "Terahertz time domain spectroscopy for the analysis of cultural heritage related materials", *Applied Physics B*, **90** (3-4), 365-368 (2008).

[99] B Ferguson, S Wang, D Gray, D Abbot, and X-C Zhang. "T-ray computed tomography", *Optics Letters*, **27** (15), 1312-1314 (2002).

[100] W Withayachumnankul, G M Png, X Yin, S Atakaramians, I Jones, H Lin, B S Yu Ung, J Balakrishnan, B W-H Ng, B Ferguson, S P Mickan, B M Fischer, and

D Abbott. "T-Ray sensing and imaging", *Proceedings of the IEEE*, **95** (8), 1528-1558 (2007).

[101] P Parkinson, J Lloyd-Hughes, Q Gao, H H Tan, C Jagadish, M B Johnston, and L M Herz. "Transient Terahertz Conductivity of GaAs Nanowires", *Nano Letters*, **7** (7), 2162-2165 (2007).

[102] J Lloyd-Hughes, S K E Merchant, L Fu, H H Tan, C Jagadish, E Castro-Camus, and M B Johnston. "Influence of surface passivation on ultrafast carrier dynamics and terahertz radiation generation in GaAs", *Applied Physics Letters*, **89** (23), 232102 (2006).

[103] M R Stringer, D N Lund, A P Foulds, A Uddin, E Berry, R E Miles, and A G Davies. "The analysis of human cortical bone by terahertz time-domain spectroscopy", *Physics in Medicine and Biology*, **50** (14), 3211-3219 (2005).

[104] B B Hu and M C Nuss. "Imaging with terahertz waves", *Opt. Lett.*, **20** (16), 1716-1718 (1995).

[105] Z Zhang, Y Zhang, G Zhao, and C Zhang. "Terahertz time-domain spectroscopy for explosive imaging", *Optik - International Journal for Light and Electron Optics*, **118** (7), 325-329 (2007).

[106] S Hargreaves and R A Lewis. "Terahertz imaging: materials and methods", *Journal of Materials Science: Materials in Electronics*, **18** (S1), 299-303 (2007).

[107] J B Baxter and C A Schmuttenmaer. "Conductivity of ZnO nanowires, nanoparticles, and thin films using time-resolved terahertz spectroscopy", *Journal of Physical Chemistry B*, **110**, 25229-25239 (2006).

[108] M C Beard, G M Turner, and C A Schmuttenmaer. "Size-dependent photoconductivity in CdSe nanoparticles as measured by time-resolved terahertz spectroscopy", *Nano Letters*, **2** (9), 983-987 (2002).

[109] E Hendry, M Koeberg, B O'regan, and M Bonn. "Local field effects on electron transport in nanostructured TiO_2 revealed by terahertz spectroscopy", *Nano Letters*, **6** (4), 755-759 (2006).

[110] X L Xu, P Parkinson, K-C Chuang, M B Johnston, R J Nicholas, and L M Herz. "Dynamic terahertz polarization in single-walled carbon nanotubes", *Physical Review B*, **82** (8), 085441 (2010).

[111] M C Beard, G M Turner, J E Murphy, O I Micic, M C Hanna, A J Nozik, and C A Schmuttenmaer. "Electronic coupling in InP nanoparticle arrays", *Nano Letters*, **3** (12), 1695-1699 (2003).

[112] Z Jiang, M Li, and X-C Zhang. "Dielectric constant measurement of thin films by differential time-domain spectroscopy", *Applied Physics Letters*, **76** (22), 3221-3223 (2000).

[113] S P Mickan, D Abbott, J Munch, and X-C Zhang. "Noise reduction in terahertz thin film measurements using a double modulated differential technique", *Fluctuation and Noise Letters*, **2** (1), R13-R18 (2002).

[114] W Withayachumnankul, B M Fischer, and D Abbott. "Numerical removal of water vapour effects from terahertz time-domain spectroscopy measurements", *Proceedings of the Royal Society A: Mathematical, Physical and Engineering Sciences*, **464** (2097), 2435-2456 (2008).

[115] R Mendis, M L Smith, L J Bignell, R E M Vickers, and R A Lewis. "Strong terahertz emission from (100) p-type InAs", *Journal of Applied Physics*, **98** (12), 126104 (2005).

[116] K Bertulis, A Krotkus, G Aleksejenko, V Pačebutas, R Adomavičius, G Molis, and S Marcinkevičius. "GaBiAs: A material for optoelectronic terahertz devices", *Applied Physics Letters*, **88** (20), 201112 (2006).

[117] J F Rodrigo, D L Sales, M Shafi, M Henini, L Turyanska, S Novikov, and S I Molina. "Effect of annealing on the structural and optical properties of (311)B GaAsBi layers", *Applied Surface Science*, **256** (18), 5688-5690 (2010).

[118] J Sigmund and H L Hartnagel. "Low-temperature growth and post-growth annealing of GaAsSb", *Journal of Crystal Growth*, **278** (1-4), 209-213 (2005).

[119] J C Knott, K Radhanpura, and R A Lewis, "Annealing of Sb-doped GaAs to optimize for terahertz emission", *presented at the Proceedings of the 19th Australian Institute of Physics Congress*, Melbourne, Australia, (2010).

[120] N Sarukura, H Ohtake, S Izumida, and Z Liu. "High average-power THz radiation from femtosecond laser-irradiated InAs in a magnetic field and its elliptical polarization characteristics", *Journal of Applied Physics*, **84** (1), 654-656 (1998).

[121] J T Darrow, X-C Zhang, D H Auston, and J D Morse. "Saturation properties of large-aperture photoconducting antennas", *IEEE Journal of Quantum Electronics*, **28** (6), 1607-1616 (1992).

[122] A H Reshak, S Auluck, and I V Kityk. "Experimental and theoretical investigations of the first and second order optical susceptibilities of BiB_3O_6 single crystal", *Applied Physics A*, **91** (3), 451-457 (2008).

[123] A H Reshak, S Auluck, A Majchrowski, and I Kityk. "Comparison of the Density of States Obtained from the X-ray Photoelectron Spectra with the Electronic Structure Calculations for α-BiB_3O_6", *Japanese Journal of Applied Physics*, **48** (1), 011601 (2009).

[124] R Mclaughlin, Q Chen, A Corchia, C M Ciesla, D D Arnone, X-C Zhang, G A C Jones, E H Linfield, and M Pepper. "Enhanced coherent terahertz emission from indium arsenide", *Journal of Modern Optics*, **47** (11), 1847-1856 (2000).

[125] M Nakajima, M Takahashi, and M Hangyo. "Reversal of subpicosecond carrier transport direction with temperature observed in semi-insulating InP using THz radiation", *Physica B* **314**, 176-179 (2002).

[126] G Molis, R Adomavičius, and A Krotkus. "Temperature-dependent terahertz radiation from the surfaces of narrow-gap semiconductors illuminated by femtosecond laser pulses", *Physica B: Condensed Matter*, **403** (19-20), 3786-3788 (2008).

[127] D You, R R Jones, P H Bucksbaum, and D R Dykaar. "Coherent generation of far-infrared radiation from InP", *Journal of the Optical Society of America B*, **11** (3), 486-491 (1994).

[128] Y H Jin and X-C Zhang. "Terahertz Optical Rectification", *Journal of Nonlinear Optical Physics & Materials*, **4** (2), 459 (1995).

[129] Q Chen, M Tani, Z Jiang, and X-C Zhang. "Electro-optic transceivers for terahertz-wave applications", *Journal of the Optical Society of America B*, **18** (6), 823-831 (2001).

[130] A Urbanowicz, A Krotkus, R Adomavičius, and V L Malevich. "Terahertz emission from femtosecond laser excited Ge surfaces due to the electrical field-induced optical rectification", *Physica B: Condensed Matter*, **398** (1), 98-101 (2007).

[131] J M Schleicher, S M Harrel, and C A Schmuttenmaer. "Effect of spin-polarized electrons on terahertz emission from photoexcited GaAs", *Journal of Applied Physics*, **105**, 113116 (2009).

[132] W I Wang, E E Mendez, T S Kuan, and L Esaki. "Crystal orientation dependence of silicon doping in molecular beam epitaxial AlGaAs/GaAs heterostructures", *Applied Physics Letters*, **47** (8), 826-828 (1985).

[133] S S Bose, B Lee, M H Kim, G E Stillman, and W I Wang. "Influence of the substrate orientation on Si incorporation in molecular-beam epitaxial GaAs", *Journal of Applied Physics*, **63** (3), 743-748 (1988).

[134] S Hargreaves, K Radhanpura, and R A Lewis. "Generation of terahertz radiation by bulk and surface optical rectification from crystal planes of arbitrary orientation", *Physical Review B*, **80** (19), 195323 (2009).

[135] R W Boyd, "Nonlinear Optics", 2nd ed. (Academic Press, San Diego,, 2002)

[136] T A Germer, K W Kołasin-Acuteski, J C Stephenson, and L J Richter. "Depletion-electric-field-induced second-harmonic generation near oxidized GaAs (001) surfaces", *Physical Review B*, **55** (16), 10694-10706 (1997).

[137] J S Blakemore. "Semiconducting and other major properties of gallium arsenide", *Journal of Applied Physics*, **53** (10), R123-R181 (1982).

[138] S Hargreaves and R A Lewis. "Single-cycle azimuthal angle dependence of terahertz radiation from (100) n-type InP", *Applied Physics Letters*, **93** (24), 242101 (2008).

[139] R A Lewis, M L Smith, R Mendis, and R E M Vickers. "THz generation in InAs", *Physica B: Condensed Matter*, **376-377**, 618-621 (2006).

[140] T Dekorsy, H Auer, H J Bakker, H G Roskos, and H Kurz. "THz electromagnetic emission by coherent infrared-active phonons", *Physical Review B*, **53** (7), 4005-4014 (1996).

[141] J N Heyman, P Neocleous, D Hebert, P A Crowell, T Müller, and K Unterrainer. "Terahertz emission from GaAs and InAs in a magnetic field", *Physical Review B*, **64** (8), 085202 (2001).

[142] M P Hasselbeck, D Stalnaker, L A Schlie, T J Rotter, A Stintz, and M Sheik-Bahae. "Emission of terahertz radiation from coupled plasmon-phonon modes in InAs", *Physical Review B*, **65** (23), 233203 (2002).

[143] V L Malevich, R Adomavičius, and A Krotkus. "THz emission from semiconductor surfaces", *Comptes Rendus Physique*, **9** (2), 130-141 (2008).

[144] S Izumida, S Ono, Z Liu, H Ohtake, and N Sarukura. "Spectrum control of THz radiation from InAs in a magnetic field by duration and frequency chirp of the excitation pulses", *Applied Physics Letters*, **75** (4), 451-453 (1999).

[145] R Mclaughlin, A Corchia, M B Johnston, Q Chen, C M Ciesla, D D Arnone, G a C Jones, E H Linfield, A G Davies, and M Pepper. "Enhanced coherent terahertz emission from indium arsenide in the presence of a magnetic field", *Applied Physics Letters*, **76** (15), 2038-2040 (2000).

[146] H Ohtake, S Ono, M Sakai, Z Liu, H Murakami, and N Sarukura,"Femtosecond-laser-irradiated, magnetic-field enhanced, InAs THz-radiation emitter and its saturation effect in high magnetic field", *presented at the Nonlinear Optics: Materials, Fundamentals and Applications (NLO)*, Kaua'i-Lihue, Hawaii, (2000).

[147] C Weiss, R Wallenstein, and R Beigang. "Magnetic-field-enhanced generation of terahertz radiation in semiconductor surfaces", *Applied Physics Letters*, **77** (25), 4160-4162 (2000).

[148] M Migita and M Hangyo. "Pump-power dependence of THz radiation from InAs surfaces under magnetic fields excited by ultrashort laser pulses", *Applied Physics Letters*, **79** (21), 3437-3439 (2001).

[149] M B Johnston, A Corchia, A Dowd, E H Linfield, A G Daviesa, R Mclaughlin, D D Arnone, and M Pepper. "Magnetic-field-induced enhancement of terahertz emission from III–V semiconductor surfaces", *Physica E*, **13**, 896-899 (2002).

[150] H Takahashi, A Quema, R Yoshioka, S Ono, and N Sarukura. "Excitation fluence dependence of terahertz radiation mechanism from femtosecond-laser-irradiated InAs under magnetic field", *Applied Physics Letters*, **83** (6), 1068-1070 (2003).

[151] H Takahashi, M Sakai, A Quema, S Ono, N Sarukura, G Nishijima, and K Watanabe. "Terahertz radiation from InAs with various surface orientations under magnetic field irradiated with femtosecond optical pulses at different wavelengths", *Journal of Applied Physics*, **95** (9), 4545-4550 (2004).

[152] J Shan, C Weiss, R Wallenstein, R Beigang, and T F Heinz. "Origin of magnetic field enhancement in the generation of terahertz radiation from semiconductor surfaces", *Optical Letters*, **26** (11), 849-851 (2001).

[153] X-C Zhang, Y Jin, T D Hewitt, T Sangsiri, L E Kingsley, and M Weiner. "Magnetic switching of THz beams", *Applied Physics Letters*, **62** (17), 2003-2005 (1993).

[154] M B Johnston, D M Whittaker, A Corchia, A G. Davies, and E H Linfield. "Theory of magnetic-field enhancement of surface-field terahertz emission", *Journal of Applied Physics*, **91** (4), 2104-2106 (2002).

[155] V L Malevich. "Monte Carlo simulation of Dember effect in n-InAs under subpicosecond laser pulse excitation", *Acta Physica Polonica A*, **107** (1), 169-173 (2005).

[156] M B Johnston, D M Whittaker, A Corchia, A G Davies, and E H Linfield. "Simulation of terahertz generation at semiconductor surfaces", *Physical Review B*, **65** (16), 165301 (2002).

[157] G Meinert, L Bányai, P Gartner, and H Haug. "Theory of THz emission from optically excited semiconductors in crossed electric and magnetic fields", *Physical Review B*, **62** (8), 5003-5009 (2000).

[158] M B Johnston, D M Whittaker, A Dowd, A G Davies, E H Linfield, X Li, and D A Ritchie. "Generation of high-power terahertz pulses in a prism", *Optics Letters*, **27** (21), 1935-1937 (2002).

[159] D V Seletskiy, M P Hasselbeck, J G Cederberg, A Katzenmeyer, M E Toimil-Molares, F Léonard, A A Talin, and M Sheik-Bahae. "Efficient terahertz emission from InAs nanowires", *Physical Review B*, **84** (11), 115421 (2011).

[160] H Ahn, Y-P Ku, Y-C Wang, C-H Chuang, S Gwo, and C-L Pan. "Terahertz emission from vertically aligned InN nanorod arrays", *Applied Physics Letters*, **91** (13), 132108 (2007).

[161] V N Trukhina, A S Buyskiha, A D Buravleva, G E Cirlina, D P Horkova, L L Samoilova, and Y B Samsonenkoa,"Terahertz generation by GaAs nanowires", *presented at the 37th International Conference on Infrared, Millimeter and Terahertz Waves*, Wollongong, Australia, (2012).

[162] M E Barnes, D Mcbryde, G J Daniell, G Whitworth, A L Chung, A H Quarterman, K G Wilcox, A Brewer, H E Beere, D A Ritchie, and V

Apostolopoulos. "Terahertz emission by diffusion of carriers and metal-mask dipole inhibition of radiation", *Optics Express*, **20** (8), 8898-8906 (2011).

[163] G Klatt, B Surrer, D Stephan, O Schubert, M Fischer, J Faist, A Leitenstorfer, R Huber, and T Dekorsy. "Photo-Dember terahertz emitter excited with an Er:fiber laser", *Applied Physics Letters*, **98** (2), 021114 (2011).

[164] D Mcbryde, M E Barnes, G J Daniell, A L Chung, Z Mihoubi, A H Quarterman, K G Wilcox, A C Tropper, and V Apostolopoulos,"Simulation of metallic nanostructures for emission of THz radiation using the lateral photo-Dember effect", *presented at the 36th International Conference on Infrared, Millimeter and Terahertz Waves* (2011).

[165] M Reid, I Cravetchi, R Fedosejevs, I M Tiginyanu, L Sirbu, and R W Boyd. "Enhanced nonlinear optical response of InP(100) membranes", *Physical Review B*, **71** (8), 081306 (2005).

[166] M Reid, I V Cravetchi, R Fedosejevs, I M Tiginyanu, and L Sirbu. "Enhanced terahertz emission from porous InP (111) membranes", *Applied Physics Letters*, **86** (2), 021904 (2005).

[167] J Lloyd-Hughes, S K E Merchant, L Sirbu, I M Tiginyanu, and M B Johnston. "Terahertz photoconductivity of mobile electrons in nanoporous InP honeycombs", *Physical Review B*, **78** (8), 085320 (2008).

[168] V V Ursaki, I M Tiginyanu, O Volciuc, V Popa, V A Skuratov, and H Morkoç. "Nanostructuring induced enhancement of radiation hardness in GaN epilayers", *Applied Physics Letters*, **90** (16), 161908 (2007).

[169] A Burlacu, V V Ursaki, V A Skuratov, D Lincot, T Pauporte, H Elbelghiti, E V Rusu, and I M Tiginyanu. "The impact of morphology upon the radiation hardness of ZnO layers", *Nanotechnology*, **19** (21), 215714 (2008).

[170] J Lloyd-Hughes, E Castro-Camus, M D Fraser, C Jagadish, and M B Johnston. "Carrier dynamics in ion-implanted GaAs studied by simulation and observation of terahertz emission", *Physical Review B*, **70** (23), 235330 (2004).

[171] S Langa, J Carstensen, M Christophersen, H Föll, and I M Tiginyanu. "Observation of crossing pores in anodically etched n-GaAs", *Applied Physics Letters*, **78** (8), 1074-1076 (2001).

[172] E Estacio, H Sumikura, H Murakami, M Tani, N Sarukura, M Hangyo, C Ponseca, R Pobre, R Quiroga, and S Ono. "Magnetic-field-induced fourfold

azimuthal angle dependence in the terahertz radiation power of (100) InAs", *Applied Physics Letters*, **90** (15), 151915 (2007).

[173] T W Crowe, J L Hesler, R M Weikle, and S H Jones. "GaAs devices and circuits for terahertz applications", *Infrared Physics & Technology*, **40**, 175-189 (1999).

[174] T Yoshioka, S Takatori, P H Minh, M Cadatal-Raduban, T Nakazato, T Shimizu, N Sarukura, E Estacio, J V Misa, R Jaculbia, M Defensor, A Somintac, and A Salvador. "Terahertz emission from GaAs films on Si(100) and Si(111) substrates grown by molecular beam epitaxy", *Journal of Infrared, Millimeter, and Terahertz Waves*, **32** (4), 418-425 (2011).

[175] D Schoenherr, H L Hartnagel, S Hargreaves, R A Lewis, and M Henini. "Time-domain THz spectroscopy using acceptor-doped GaAs photoconductive emitters", *Semiconductor Science and Technology*, **23** (10), 105012 (2008).

[176] A Fleck, B J Robinson, and D A Thompson. "Characterization of defects in doped InGaAsN grown by molecular-beam epitaxy", *Applied Physics Letters*, **78** (12), 1694-1696 (2001).

[177] K Oe. "Characteristics of Semiconductor Alloy $GaAs_{1-x}Bi_x$", *Japanese Journal of Applied Physics*, **41** (Part 1, No. 5A), 2801-2806 (2002).

[178] M Yoshimoto, S Murata, A Chayahara, Y Horino, J Saraie, and K Oe. "Metastable GaAsBi alloy grown by molecular beam epitaxy", *Japanese Journal of Applied Physics*, **42** (Part 2, No. 10B), L1235-L1237 (2003).

[179] S Tixier, M Adamcyk, T Tiedje, S Francoeur, A Mascarenhas, P Wei, and F Schiettekatte. "Molecular beam epitaxy growth of $GaAs_{1-x}Bi_x$", *Applied Physics Letters*, **82** (14), 2245-2247 (2003).

[180] S Francoeur, M-J Seong, A Mascarenhas, S Tixier, M Adamcyk, and T Tiedje. "Band gap of $GaAs_{1-x}Bi_x$, $0<x<3.6\%$", *Applied Physics Letters*, **82** (22), 3874-3876 (2003).

[181] B Fluegel, S Francoeur, A Mascarenhas, S Tixier, E C Young, and T Tiedje. "Giant Spin-Orbit Bowing in $GaAs_{1-x}Bi_x$", *Physical Review Letters*, **97** (6), 067205 (2006).

[182] D G Cooke, F A Hegmann, E C Young, and T Tiedje. "Electron mobility in dilute GaAs bismide and nitride alloys measured by time-resolved terahertz spectroscopy", *Applied Physics Letters*, **89** (12), 122103 (2006).

[183] V Pačebutas, K Bertulis, L Dapkus, G Aleksejenko, A Krotkus, K M Yu, and W Walukiewicz. "Characterization of low-temperature molecular-beam-epitaxy grown GaBiAs layers", *Semiconductor Science and Technology*, **22** (7), 819-823 (2007).

[184] V Pačebutas, K Bertulis, G Aleksejenko, and A Krotkus. "Molecular-beam-epitaxy grown GaBiAs for terahertz optoelectronic applications", *Journal of Materials Science: Materials in Electronics*, **20** (S1), 363-366 (2009).

[185] G Molis, R Adomavičius, A Krotkus, K Bertulis, L Giniūnas, J Pocius, and R Danielius. "Terahertz time-domain spectroscopy system based on femtosecond Yb:KGW laser", *Electronics Letters*, **43** (3), 190-191 (2007).

[186] V Pačebutas, A Bičiūnas, K Bertulis, and A Krotkus. "Optoelectronic terahertz radiation system based on femtosecond 1 μm laser pulses and GaBiAs detector", *Electronics Letters*, **44** (19), 1154-1155 (2008).

[187] M Henini, J Ibáñez, M Schmidbauer, M Shafi, S V Novikov, L Turyanska, S I Molina, D L Sales, M F Chisholm, and J Misiewicz. "Molecular beam epitaxy of GaBiAs on (311)B GaAs substrates", *Applied Physics Letters*, **91** (25), 251909 (2007).

[188] K Radhanpura, S Hargreaves, R A Lewis, and M Henini. "The role of optical rectification in the generation of terahertz radiation from GaBiAs", *Applied Physics Letters*, **94** (25), 251115 (2009).

[189] M Shafi, R H Mari, M Henini, D Taylor, and M Hopkinson. "Electrical properties of nitrogen-related defects in n-type GaAsN grown by molecular-beam epitaxy", *Physica Status Solidi (c)*, **6** (12), 2652-2654 (2009).

[190] J Ibáñez, R Oliva, M De La Mare, M Schmidbauer, S Hernández, P Pellegrino, D J Scurr, R Cuscó, L Artús, M Shafi, R H Mari, M Henini, Q Zhuang, A Godenir, and A Krier. "Structural and optical properties of dilute InAsN grown by molecular beam epitaxy", *Journal of Applied Physics*, **108** (10), 103504 (2010).

[191] I A Buyanova, W M Chen, B Monemar, H P Xin, and C W Tu. "Effect of growth temperature on photoluminescence of GaNAs/GaAs quantum well structures", *Applied Physics Letters*, **75** (24), 3781-3783 (1999).

[192] S R Kurtz, A A Allerman, C H Seager, R M Sieg, and E D Jones. "Minority carrier diffusion, defects, and localization in InGaAsN, with 2% nitrogen", *Applied Physics Letters*, **77** (3), 400-402 (2000).

[193] M Shafi, R H Mari, A Khatab, M Henini, A Polimeni, M Capizzi, and M Hopkinson. "Deep levels in H-irradiated $GaAs_{1-x}N_x$ ($x < 0.01$) grown by molecular beam epitaxy", *Journal of Applied Physics*, **110** (12), 124508 (2011).

[194] H Ahn, Y-P Ku, C-H Chuang, C-L Pan, H-W Lin, Y-L Hong, and S Gwo. "Intense terahertz emission from *a*-plane InN surface", *Applied Physics Letters*, **92** (10), 102103 (2008).